ADDITIVE MANUFACTURING OF GRADED MICROSTRUCTURES FOR AEROENGINE COMPONENTS

By

BONNIE ATTARD

A thesis submitted to University of Birmingham in partial fulfilment of the requirements for the degree of DOCTOR OF PHILOSOPHY

Department of Metallurgy and Materials
College of Engineering and Physical Sciences
The University of Birmingham

March 2022



UNIVERSITY OF
BIRMINGHAM

University of Birmingham Research Archive

e-theses repository

This unpublished thesis/dissertation is copyright of the author and/or third parties. The intellectual property rights of the author or third parties in respect of this work are as defined by The Copyright Designs and Patents Act 1988 or as modified by any successor legislation.

Any use made of information contained in this thesis/dissertation must be in accordance with that legislation and must be properly acknowledged. Further distribution or reproduction in any format is prohibited without the permission of the copyright holder.

Abstract

The microstructure formed after laser powder bed fusion (L-PBF) depends on the thermal gradient and solidification rate with the complex physical interactions of the melt pool and heat flow also impacting the solidifying structure. Due to the layer-by-layer methodology applied in L-PBF, modifying these factors is possible and an area of growing research. Thus, the microstructure itself can be seen as a variable tool to be controlled through processing parameters, allowing L-PBF to be harnessed to move towards the generation of functionally graded microstructures and the formation of components with structures which are fully optimised for their application. This work explores the feasibility of additively manufacturing tailored Inconel 718 microstructures by varying process parameters and scanning strategies, to modify the mechanical properties and performance. This investigation focuses on controlling the heat input and thermal history through process parameter manipulation; notably the heat input parameters (power, scan speed, and hatch spacing) and island scanning parameters (island size, shift, and island overlap). Preliminary investigations into the use of base plate heating at 400ºC with the objective of moving from columnar to equiaxed growth were also made.

The changes in preferred orientation, morphology and grain size were fully characterised and compared using scanning electron microscopy, electron back scatter diffraction and X-ray diffraction. The solidification cell size was quantified to estimate the effect of the process parameters on the cooling rates. Both grain size and preferred orientation were successfully tailored through scanning parameter modification and separately through base plate heating. Based on these obtained microstructures, graded microstructures were generated using subtle modifications in the island strategy.

The viability of using scanning strategies to modify the mechanical properties of Inconel 718 through variations of microstructure was then investigated in more detail. Mechanical testing indicated that the scanning strategy can be used to generate functionally graded specimens; larger grains and more [001] preferred alignment resulting in lower Young's modulus and strength or smaller grains with a reduced preferential [001] orientation along the build direction increased the Young's modulus and strength. Digital image correlation showed that strain in graded structures was concentrated in highly textured areas. The ductility was limited by the entrainment of thin Al oxides folded in the melt pool which were investigated in more detail. Further investigation into the high temperature isothermal oxidation resistance of the microstructurally variant components was made. The mass gain behaviour was found to be broadly similar between the different conditions after 504 h and comparable to wrought Inconel 718 but following sub-parabolic oxidation kinetics possibly attributable to the formation of an underlying Nb rich layer.

Acknowledgements

I would like to express my sincere gratitude to my supervisors Dr. Sam Cruchley, Dr. Yu-Lung Chiu and Prof. Moataz Attallah for their encouragement, guidance, and support throughout these years without which this work would not have been possible. Thank you all so much for giving me the opportunity to work in this exciting field.

I also owe thanks to collaborators in this work namely; Dr. Christoph Beetz and Dr. Mustafa Megahed at ESI for their contribution in the grain modelling supporting in this work and Dr. Ellies Muyupa, Dr. Alex Forsey and Dr. Richard Moat at the Open University for their support with digital image correlation.

I would also like to thank Dr. Rachel Jennings, Dr. Amanda Field and Dr. Luke Carter for their guidance and support when I was still trying to find my way in additive manufacturing. Special thanks also go to Dr. Ubaid Ur Rehman Ghori for his assistance in electron microscopy and Mr. Jas Singh for technical assistance. Thank you as well to everyone in the AMPLab group for their support. I would also like to offer my heartfelt thanks to Emily Lewis; our chats over madeira cake were very anticipated, Anastassia Milleret, Anastasia Vrettou and Zakareya Mohamed for their friendship and valuable discussions through the years. This work took place during a uniquely strange time and moving back home halfway through was a huge challenge. I would like to express my gratitude to Prof. Ing. Glenn Cassar at the University of Malta for providing me with facilities to finish my oxidation work and give special thanks to all the staff at the DMME laboratories for their assistance in this last part of the journey post-pandemic; Ing. James Camilleri and Ing. Mary Grace Micallef, Mr Noel Tonna, Mr Daniel Dimech, Ms. Christabelle Tonna and Ms. Jeanelle Arpa for their support with the technical aspects. Thanks also go out to prof. Joseph Buhagiar for his assistance initially in finding this doctoral opportunity.

Finally, I would like to thank my amazing family and my friends for giving me their constant and invaluable moral support, understanding and encouragement throughout this project. You have my heartfelt gratitude for your patience and understanding during this time. I don't think I would have gotten here without you all. Finally, thanks go out to Stephane Role for the shoulder to lean on during this time and for being there for me during this journey and through all the numerous curveballs in this long road.

This work was funded through the Engineering and Physical Sciences Research Council (EPSRC) for the PhD Scholarship and funding endorsed by DSTL.

Publications

Sections of this work have been published in a peer-reviewed publication and book:

B. Attard, A. Hussein, M.M. Attallah, Chapter 19: New Materials Development, in: Fundamentals of Laser Powder Bed Fusion of Metals, Eds A. du Plessis, I. Yadroitsev, I. Yadroitsava, E. MacDonald 1st ed. Elsevier, (2021), pp 529-562

BA wrote the review related to laser powder bed fusion of functionally graded materials, microstructural grading in laser powder bed fusion, compositional grading in laser powder bed fusion. AH wrote the review related to functional materials. BA, AH and MMA reviewed and edited the manuscript.

B. Attard, S. Cruchley, Ch. Beetz, M. Megahed, Y. Chiu, M.M. Attallah, Microstructural Control during Laser Powder Fusion to Create Graded Microstructure Ni-Superalloy Components, Additive Manufacturing, 36 (2020) 101432 https://doi.org/10.1016/j.addma.2020.101432

BA conceived and designed the experiment, performed the experiments, interpreted data, wrote, and reviewed the manuscript. CB performed the grain modelling; MM assisted in interpretation of the grain modelling data and wrote the results related to grain modelling. SC, YC and MMA reviewed the manuscript, assisted in the interpretation of the data, and provided supervision.

The following sections of this work are in preparation for publication:

Chapter 5: **B. Attard,** S. Cruchley, Y. Chiu, M.M. Attallah, Application of baseplate heating in L-PBF of IN718 to control the columnar to equiaxed transition

BA conceived and designed the experiment, performed the experiments, interpreted data, wrote and reviewed the manuscript. SC, YC and MMA reviewed the manuscript and assisted in the interpretation of the data and provided supervision.

Chapter 6: B. Attard, S. Cruchley, Y. L. Chiu, E. Muyupa, A.N. Forsey, R.J. Moat, M. M. Attallah, Using Laser Powder Bed Fusion to Create Functionally-Graded Inconel 718 Superalloy Microstructures: Characterisation of Local Mechanical Properties and Defect Formation

BA conceived and designed the experiment, performed the experiments, interpreted data, wrote, and reviewed the manuscript. EM, AF, and RM provided experimental facilities for digital image correlation, assisted with the analysis of digital image correlation results and reviewed the manuscript. SC, YC and MMA reviewed the manuscript and assisted in the interpretation of the data and provided supervision.

Chapter 7: B. Attard, S. Cruchley, Y. L. Chiu, M. M. Attallah, The effect of altering scanning strategies in laser powder bed fusion on oxidation of Inconel 718 superalloy

BA conceived and designed the experiment, performed the experiments, interpreted data, wrote, and reviewed the manuscript. SC reviewed the manuscript and assisted in the interpretation of the data and provided supervision. YC and MMA reviewed the manuscript and provided supervision.

The following conference talks have resulted from this work:

B. Attard, S. Cruchley, Y. Chiu, M.M. Attallah, The utility of laser powder bed parameters and deposition strategies in creating functionally graded microstructures in IN718, Materials Science and Technology, (2018)

B. Attard, S. Cruchley, Y. Chiu, M.M. Attallah, The utility of deposition strategies in controlling the microstructure in IN718, Enlighten Conference Metal Powder-based Additive Manufacturing, (2018)

B. Attard, S. Cruchley, Y. Chiu, M.M. Attallah, The utility of laser powder bed parameters and deposition strategies in controlling the build microstructure in IN718, National Student Conference in Metallic Materials (2018)

Table of Contents

Abstract i

Acknowledgements ii

Publications iii

Table of Contents v

List of Symbols and Abbreviations xi

List of Figures xiv

List of Tables xxii

CHAPTER 1. Introduction 1

1.1 Overview of Inconel 718 applications and manufacturing routes 1

1.2 Additive manufacturing 3

1.3 Aim and Objectives 7

1.4 Thesis outline 7

CHAPTER 2. Literature review 9

2.1 Physical phenomena in additive manufacturing 9

2.2 Solidification in additive manufacturing 12

2.2.1 Heat flow and thermal gradient 12

2.2.2 Undercooling 14

2.2.3 Solidification rate 15
2.2.4 Solidification theory 16
2.2.5 Cooling rate 18
2.3 Metallurgy of IN718 19
2.3.1 Microstructure of AM IN718 22
2.3.2 Segregation 24
2.3.3 Heat treatment 26
2.4 Functionally graded microstructures in additive manufacturing 28
2.4.1 Functionally graded materials 28
2.4.2 Modifying microstructure through heat input parameters 29
2.4.3 Modifying the microstructure through scanning strategies 37
2.4.4 Effect of heating and cooling the substrate 48
2.5 Microstructural modification to change mechanical properties 49
2.6 Effect of microstructural modification on oxidation performance 52
2.7 Summary and research gaps 55
CHAPTER 3. Experimental procedure 57
3.1 Materials 57
3.1.1 Powder chemical composition 58
3.1.2 Powder flowability 58

3.1.3 Powder shape considerations 59

3.1.4 Base plate 59

3.2 Concept Laser M2 Powder Bed Fusion 59

3.2.1 Machine Set-up 59

3.2.2 Specimen manufacture details 61

3.2.3 Heated baseplate 65

3.2.4 Post processing: sample removal and sectioning 65

3.2.5 Post processing: heat treatment 66

3.3 Characterisation 66

3.3.1 Metallurgical sample preparation 66

3.3.2 Density and porosity measurements 67

3.3.3 Microscopy 67

3.3.4 Electron backscatter diffraction 68

3.3.5 Etching 69

3.3.6 X-ray diffraction 69

3.3.7 Hardness measurements 69

3.4 Mechanical testing 70

3.4.1 Room temperature tensile testing 70

3.4.2 Digital image correlation tensile testing 70

3.5 Isothermal oxidation testing 71

3.5.1 Furnace set-up 71

3.5.4 Cross-section preparation and characterisation 71

CHAPTER 4. Microstructural control during L-PBF to create graded microstructure Ni-superalloy components 73

4.1 Abstract 73

4.2 Introduction 74

4.3 Experimental Procedure 77

4.3.1 Fabrication 77

4.3.2 Characterisation 80

4.3.3 Numerical modelling 82

4.4 Results and Discussion 85

4.4.1 Effect of island size 86

4.4.2 Effect of island shift 89

4.4.3 Effect of scan strategy 92

4.4.4 Effect of island overlap 92

4.4.5 Influence of laser heat input parameters 92

4.4.6 Cooling rates 94

4.4.7 Numerical modelling results 95

4.4.8 Graded Blade 100

4.4.9 Effect of heat treatment 102

4.5 Conclusion 105

CHAPTER 5. Application of baseplate heating in laser powder bed fusion of Inconel 718 to control the columnar to equiaxed transition 106

5.1 Abstract 106

5.2 Introduction 106

5.3 Experimental Procedure 109

5.3 Results and Discussion 110

5.4 Conclusion 115

CHAPTER 6. Using L-PBF to create functionally graded Inconel 718 Microstructures: characterisation of local mechanical properties and defect formation 116

6.1 Abstract 116

6.2 Introduction 117

6.3 Materials and Methods 119

6.4. Results and Discussion 122

6.4.1 Microstructural analysis 122

6.4.2 Tensile performance 126

6.4.3 Digital image correlation 132

6.4.4 Fractography 135

6.5 Conclusion 143

CHAPTER 7. The effect of altering scanning strategies in laser powder bed fusion on the oxidation of Inconel 718 145

7.1 Abstract 145

7.1 Introduction 147

7.2 Material and Methods 148

7.3 Results and Discussion 150

7.3.1 Initial microstructure 150

7.3.2 Oxidation Kinetics 152

7.3.3 Surface oxidation 155

7.3.4 Cross-sectional analysis 165

7.4 Conclusion 172

CHAPTER 8. Conclusion and future work 174

8.1 Conclusion 174

8.2 Future work 177

REFERENCES 181

List of Symbols and Abbreviations

Symbol	Definition
σ_Y	Yield strength
γ	Austenite
h	enthalpy
K_p	oxide growth rate constant
$L1_2$	primitive cubic structure
n	rate exponent
n_g	Nucleation density/rate
Q	heat source power density
T	Temperature
t	Time, oxidation time
v	heat source movement speed
V_T	Isothermal velocity
V_{tip}	Tip growth velocity
γ'	gamma prime
γ''	gamma double prime
δ	Delta-phase, Ni3Nb
Δm	oxidation mass gain per unit surface area
ΔT	total undercooling
ΔT_C	constitutional undercooling
ΔT_K	kinetic undercooling
ΔT_R	undercooling due to the curvature at the solid/liquid interface
ΔT_{TH}	thermal undercooling
ε	Cooling rate
θ	angle between the surface normal of the solidification front and the laser scanning direction
λ	material conductivity
ΔT_n	undercooling at the nucleation temperature
α	equiaxed grain radius,
g_g	grain volume fraction
ρ	density

Abbreviation	Definition
3D	Three dimensional
AC	Air cooled
AM	Additive manufacturing
B.D	Building direction
bcc	Body centred cubic
BiD	Bidirectional
BSE	Back scattered electron
CA	Cellular automaton
CAD	Computer aided drawings
CDRS	Cross-directional rastering
CET	Columnar-to-equiaxed transition
CFD	Computational fluid dynamic
CH	Cross-hatched
DA	Double-aged
DAS	Dendrite arm spacing
DED	Directed energy deposition
DIC	Digital image correlation
E	Young's modulus
E.D	Energy density
EB-CHR	Electron beam cold heart refining
EB-PBF	Electron beam powder bed fusion
EBSD	Electron backscatter diffraction
EDS	Energy dispersive spectroscopy
ESR	Electro-slag remelting
FC	Furnace cooled
fcc	Face centred cubic
FGM	Functionally graded material
G	Thermal gradient
GIAB	Glancing Incidence Asymmetric Bragg
H	Homogenisation
HIP	Hot isostatic pressing
ICP-OES	Inductively coupled plasma - optical emission spectrometry
IN718	Inconel718
IP	Island parallel
IPF	Inverse pole figure
LAM	Local area misorientation
LoF	Lack of fusion
L-PBF	Laser powder bed fusion

M.U.D	Multiples of uniform distribution
ND	Normal direction
PBR	Pilling Bedworth ratio
R	Solidification rate
SDAS	Secondary dendrite arm spacing
SDRS	Single direction rastering
SE	Secondary electron
SEM	Scanning electron microscope
ST	Solution treated
STL	Stereolithography
UTS	Ultimate tensile strength
VAR	Vacuum arc remelting
VIM	Vacuum induction melting
WEDM	Wire electrical discharge machining
WQ	Water quenched
XRD	X-ray diffraction

List of Figures

Figure 1.1: IN718 in turbofan engines for aerospace propulsion [5,6]. 2

Figure 1.2: General processing route for IN718 aerospace components [3,8,9]. 3

Figure 1.3: (a) the grain size variation of a dual microstructure forging [18] together with (b) schematic representation of a dual microstructure heat treatment assembly [19]..... 5

Figure 1.4: Schematic representation of a general L-PBF set-up. 6

Figure 2.1: (a) Marangoni flow with melt movement towards from the hot laser spot towards the colder rear area with spattering from the ejection of low viscosity liquid and (b) melt evaporation and the effect of recoil on the melt pool [32]. 11

Figure 2.2: Temperature contour plot for 316L stainless steel melt pool determined through finite element analysis modelling [33]. 13

Figure 2.3: Heat source movement direction and growth rate at different melt pool positions. 16

Figure 2.4: Schematic solidification map showing the different solidification morphologies forming with changes in G and R. 17

Figure 2.5: (a) changes in G and R for IN718 in EB-PBF depending on solidification time, together with (b) solidification structure and melt pool isotherms [50,56]..... 18

Figure 2.6: Variation of Laves phase morphology with cooling rates of (a) 500 K/s (b) 1000 K/s (c) 2000 K/s and (d) 4000 K/s [57]..... 19

Figure 2.7: (a) showing γ" and γ′ for solution treated and double-aged IN718, together with (b) the crystal structure of γ" phase, (c) showing needle-like delta phase growing into the grains and (d) the rate of hardening during ageing at 650ºC for a grain size of 60 μm [16,76–78]. 21

Figure 2.8: (a) Optical micrograph for typical L-PBF IN718 with epitaxial growth visible between melt pools, together with secondary electron micrographs of (b) the columnar grain structure, (c)

slender columnar grains together with (d) angled epitaxial grains and (e) solidification cells showing elemental segregation around their boundaries [85]. 23

Figure 2.9: Growth direction of columnar grains for (a) and (b) L-PBF with different length to depth ratio melt pools resulting in vertical alignment and close vertical alignment respectively. Curves marked with I, II and III represent consecutive melt pool boundaries along the scan track [13]..... 24

Figure 2.10: Precipitates observed in AM IN718 with (a) showing interdendritic eutectic solidification products such as Laves phases and some niobium carbides with a higher magnification shown in (b) [14] while (c) shows square shaped Ti and Nb rich carbides for as-built microstructures [61]. 26

Figure 2.11: Functionally graded microstructure [106]. 29

Figure 2.12: Graded IN718 with an inverse pole figure map for a columnar microstructure with large coarse grains alternating together with a fine-grained matrix. Laser beam heat input parameters used for each microstructure are shown [124]..... 30

Figure 2.13: (a) The change in grain size and alignment with different welding speeds [46] together with (b) the predicted solidification rate at different welding speeds [47]..... 31

Figure 2.14: (a) IPF maps for microstructures obtained at different power levels in DED using a speed of 200 mm/s [131], together with (b) a process map for the dominant microstructure with different laser speeds and powers for CMSX-4 [111]..... 33

Figure 2.15: Showing (a) the dependence of penetration depth on power density and interaction time and (b) dependence of melt pool depth on beam power and scanning speed [136,138]..... 35

Figure 2.16: Showing changes in melt-pool profile with different electron beam parameters for (a) a point profile and (b) a line profile together with (c) the effect of different melt pool profiles on texture through IPF mapping [139]. 36

Figure 2.17: Schematic representation of some of the (a-g) common scanning strategies in L-PBF together with (h-i) parameters which can be varied within the strategies themselves..... 38

Figure 2.18: Change in grain tilt angle to the B.D showing IPF maps for (a) unidirectional and (b) bidirectional strategies with respective pole figures in (c) and (d), with (e) showing a schematic representation of the potential dendrite growth directions applicable for a bidirectional strategy and (f) a cell colony with growth from secondary arms at 45° [53,150,153]. 40

Figure 2.19: (a) Change in texture characteristics with different scanning strategies for IN738LC [148] together with (b) "quasi-random" crystal structure observed with a 67° rotation in a bidirectional strategy for CoCrMo [129]. 42

Figure 2.20: IPF maps for scanning strategies with a 67° layer rotation for a bidirectional strategy with XY and XZ cross-sections for (a) and (b) respectively together with an island strategy with XY and XZ cross-sections for (c) and (d) respectively. (e) shows the cross-section for a single track melt pool. [87]. 43

Figure 2.21: (a) IPF map with respect to the build direction of an XY cross-section showing the effect of the chessboard island scan pattern on large scale grain arrangement together with pole figures for (b) strongly textured area and (c) less defined textured zone [155]. 44

Figure 2.22: Effect of various scanning strategies used in EB-PBF to obtain (a and d) a columnar microstructure, (b and e) an equiaxed microstructure and (c and f) a transversely oriented microstructure [156]. 45

Figure 2.23: Strategies for (a) long hatch length and (b) short hatch length together with (a and d) respective IPF maps and (e) mechanical behaviour for different hatch lengths and (f) simulated behaviour with increasing hatch length [51,160]. 47

Figure 2.24: (a) grain size distribution for single direction rastering (SDRS, unidirectional) and cross-directional rastering (CDRS, cross-hatch) and (b) stress-strain curves for the different conditions [151]. 48

Figure 2.25: Mechanical properties for IN718 test samples made using EB-PBF [125]. 52

Figure 2.26: Dependence of the relative oxide height on the deviation of the grain from the ⟨111⟩ [186]. 53

Figure 3.1: Powder size distribution for BATCH1 and BATCH2. 57

Figure 3.2: (a) M2 concept laser set-up and (b and c) laser in operation during a build. 60

Figure 3.3: (a) Tensile bar orientation with respect to build direction and dimensions together with (b) typical build plate set up with multiple bars in different conditions. 64

Figure 4.1: (a) Island scanning strategy, (b) island parallel strategy (c) island overlap, (d) bidirectional and (e) cross-hatching scanning strategies and (f) island size together with island shift parameters. 78

Figure 4.2: Thermal model computational domain demonstrating 2 hatches. 84

Figure 4.3: (a) Diffractograph for IN718 powder compared to the control condition and texture coefficient obtained for (b) different scanning parameters and (c) laser parameters. Dotted line indicates the texture coefficient for the control condition. 86

Figure 4.4: IPF maps in XY and XZ planes together with corresponding pole figures for builds using a (a) 3 mm island size, (b) a 5 mm island size and (c) a 7 mm island size. 88

Figure 4.5: Variation in cumulative line fraction percentage distributions over grain diameters with island size in (a) the transverse direction and (b) along the build direction. 89

Figure 4.6: IPF maps in XY and XZ planes together with corresponding pole figures for (a) SHIFT4 and (b) CONTROL together with (c) corresponding variation in cumulative line fraction distribution against grain diameter for both cases and (d) the variation in island scanning order between SHIFT4 and the CONTROL. 91

Figure 4.7: (a) Temporal evolution of melt pool depth and (b) temperature gradient. 95

Figure 4.8: Numerical results of isothermal velocity versus temperature gradient for L-PBF. 96

Figure 4.9: Evolution of Hunt criterion during solidification for different nucleation densities. 97

Figure 4.10: Grain structure at $g_g = 0.0066$, $g_g = 0.66$ and fully solidified for nucleant densities of

$n_g = 0.2 \times 10^{16}$ m^{-3}, $n_g = 0.4 \times 10^{16}$ m^{-3} and $n_g = 0.8 \times 10^{16}$ m^{-3}. 98

Figure 4.11: Microstructure resulting from unidirectional scan strategies. 4 hatches, the first is always on the left and 4 layers are modelled. 99

Figure 4.12: Microstructure resulting from unidirectional scan strategies for 3 different island sizes (1 mm, 3 mm and 7 mm). The cross section shows grains resulting from 4 hatches, the first is always on the left with 4 consecutive layers are modelled..... 100

Figure 4.13: (a) The GRADEDBLADE specimen with (b) corresponding XZ cross-section IPF map along B.D and pole figures for (c) a 3 mm island size, (d) a 4 mm layer shift, (e) XZ cross-section IPF map along the transverse direction and (f) corresponding variation in cumulative line fraction distribution against grain diameters for the graded and monolithic conditions. 101

Figure 4.14: (a) The as-built microstructure with cell and grain boundaries delineated by Nb-C films and minute Laves particles at the cell boundaries together with the corresponding IPF map, (b) dissolution of the carbide films at the cell boundaries after heat treatment at 980ºC together with the corresponding IPF map and (c) the grain diameter distribution against cumulative line fraction plot. 104

Figure 5.1: Effect of solidification rate and thermal gradient on the CET for IN718. Dotted vertical red line indicates the absolute maximum expected solidification rate based on the scanning speed used in this work. A general indication of the expected processing window for this work is shown by a dotted red box. Original figure without data comparison from [139]. 108

Figure 5.2: Convex hull deviation maps for (a) the CONTROL condition, (b) the condition manufactured at an E.D 3.89 J/mm^2, (c) the E.D at 3.89 J/mm^2 together with a heated baseplate and (d) the CONTROL condition together with a heated baseplate, together with (e) the local misorientation map for the CONTROL condition with heated baseplate. 111

Figure 5.3: Representation of the ratio of deviation from the convex shape with the area % covered for the (a) CONTROL, (b) heated baseplate CONTROL, (c) $E.D_{3.89}$ and (d) heated baseplate $E.D_{3.89}$ conditions. 113

Figure 6.1: IPF maps for tensile bars for the (a) ISLAND7 (b) SHIFT4 and (c) ISLAND3 conditions with (d) a comparison of the changes in grain diameter along the B.D compared to previous work [161] on small build volumes and pole figures for (e) the ISLAND7 (f) the SHIFT4 and (g) the ISLAND3 conditions. 123

Figure 6.2: Change in melt pool depth with distance along the island. 126

Figure 6.3: Area% consisting of different crystallographic orientations aligned with the build direction for large build volumes (15×15×90 mm) conducted in this work compared to small build volumes (10×10×10 mm) conducted in Chapter 4 [161]. 128

Figure 6.4: Box and whisker plots for (a) 0.2% σ_y, (b) ultimate tensile strength and (c) ductility for monolithic conditions. Dashed lines indicate the values prescribed per ASTM B637-18 [99]. Representative stress-strain curves for the different monolithic conditions are shown in (d). 130

Figure 6.5: Schmid factor maps for large build volumes for the ISLAND7 and ISLAND3 conditions. 131

Figure 6.6: Showing the (a) schematic illustration of the grading applied for the GR_ISLAND condition with the failure point demarked, and an IPF map for (b) the central region, (c) the cumulative grain size distribution for the different ends and central region together with (d) the strain map over the area prior to failure with arrows marking the origin of failure and (e) the average strain over the length of the specimen prior to failure. 134

Figure 6.7: Representative fractographs showing an overview of the fracture surface for the (a) CONTROL and (b) ISLAND3 conditions with areas of lack of fusion marked by arrows together with (c) showing steps in the fracture surface as circled and (d) showing micro-void coalescence. 136

Figure 6.8: Representative fractographs for flat defects in (a) and (b) with boxes showing wrinkles and slip bands, together with (c) EDS composition map with orange showing Al and green showing Ni, (d) flat defect with a Ti enriched particle and (e) a flat defect with an Al elongated oxide. Arrows mark Al oxides. Corresponding chemical composition of points of interest is denoted. 137

Figure 6.9: (a) Failure point for the GRADEDISLAND condition with corresponding defect on the other half in (b)..... 141

Figure 6.10: (a) Representative SEM for discontinuities along the melt pool. Some oxidation along grain boundaries is visible and occurred after heat treating together with (b) secondary emission micrograph for top melt pool surfaces with EDS maps for (c) aluminium and (d) oxygen and optical micrographs for single layer melt pool cross sections for (e) a single track and (f) a 20 by 90 mm area. 143

Figure 7.1: Coupon orientation with respect to the build direction. 149

Figure 7.2: IPF maps for (a) ISLAND7, (b) CONTROL and (c) ISLAND3 together with (d) cumulative grain size distribution along the build direction for the different conditions and (e) orientation directions perpendicular to the surface being oxidised. 151

Figure 7.3: Mass gain values for the different conditions. 152

Figure 7.4: Arrhenius plot of parabolic K_p values comparing various superalloys from literature to the K_p values obtained in this work. Insert shows a high resolution of the points at 850 ºC. Adapted from [184]..... 155

Figure 7.5: SE micrographs for the surface oxide morphology of IN718 oxidised in air at 850ºC for time intervals between 24 h to 504 h for the ISLAND7, CONTROL and ISLAND3 conditions.. 157

Figure 7.6: SE micrographs of (a) Fe and Ni rich area for the CONTROL after 264 h (b) the wrinkled oxide structures after 24 h for the CONTROL specimen together with (c) Cr rich oxide nodule observed for ISLAND7 after 96 h and (d) faceted structures after 264 h on the CONTROL specimen after spallation and the chemical composition of specific areas of interest. 158

Figure 7.7: High resolution SE micrographs for the surface oxide grain structure of IN718 oxidised in air at 850ºC for 504 h for the (a) CONTROL and (b)ISLAND7 conditions with (c) showing a higher magnification of position 2 which is thought to consist of (Ni,Fe)Cr_2O_4 spinel structures. 160

Figure 7.8: High resolution SE micrograph for the surface oxide grain structure of IN718 oxidised

in air at 850ºC for 504 h for the (a) ISLAND7 condition together with corresponding EDS maps for (b) Cr, (c) Ni and (d) Fe. 161

Figure 7.9: EDS maps for an area of spall in the ISLAND3 condition after 264 h, showing in (a) the SE micrograph with a grain boundary passing through the spalled region together with elemental composition maps for (b) O, (c) Al, (d) Ti, (e) Nb, (f) Mo, (g) Fe (h) Cr and (i) Ni..... 162

Figure 7.10: Representative diffractographs for (a) the CONTROL condition at each oxidation interval, together with representative diffractographs for the (b) ISLAND7 and (c) ISLAND3 conditions at all time intervals..... 164

Figure 7.11: Representative BS micrographs for the ISLAND7, CONTROL and ISLAND3 conditions following oxidation in laboratory air at 850ºC for 504 h. Features of interest are marked. 166

Figure 7.12: BSE micrograph and EDS maps for the ISLAND7 condition after 504 h, showing the elemental distribution of the oxides and underlying segregation. 169

Figure 7.13: Variation in chemical composition along the cross-section for (a) Cr and O where dotted line indicates base material Cr composition, (b) Nb and Mo, (c) Fe, Ni Al and Ti and (d) the respective BS micrograph. Specimen under consideration was ISLAND7 after 504 h..... 171

List of Tables

Table 2.1: Nominal chemical composition of IN718 [67]. 20

Table 2.2: Heat treatments applied to L-PBF IN718 and mechanical properties obtained. 27

Table 2.3: Mechanical properties for IN718 with different predominant texture orientations. 50

Table 3.1: Powder size values for BATCH1 and BATCH2. 58

Table 3.2: Overview of laser heat input parameters. 62

Table 3.3: Scanning strategy parameters. Each condition had one scanning parameter varied from the control condition as highlighted. 63

Table 3.4: Overview of parameters used for mechanical graded coupons. 65

Table 3.5: Parameters used for heated baseplate experiments. 65

Table 4.1: The chemical composition of the IN718 powder used and the ASTM B637 [99] specified composition range of IN718. 77

Table 4.2: Scanning strategy parameters used. Each condition had one scanning parameter varied from the control condition as highlighted. 79

Table 4.3: Laser heat input parameters used. 80

Table 4.4: IN718 properties used for the thermal modelling and grain growth simulations. 84

Table 6.1: The chemical composition of the IN718 powder used compared to ASTM B637 [99]. 120

Table 6.2: Scanning strategy parameters. 120

Table 7.1: Parabolic K_p and cubic K_c oxidation rate constants for the different condition compared to other work on AM IN718. Adjusted R^2 values for this work were all above 0.97. 154

CHAPTER 1. Introduction

This chapter introduces Inconel718 (IN718) and provides a brief background on its typical applications and standard manufacturing routes. Additive manufacturing (AM); specifically, laser powder bed fusion (L-PBF), is then introduced together followed by the aim and objectives and an outline of this doctoral work.

1.1 Overview of Inconel 718 applications and manufacturing routes

IN718 is an aero-engine alloy widely used up to 650ºC [1]. This stems from its good mechanical properties at both room and elevated temperatures coupled with its high corrosion and oxidation resistance within this temperature range [1]. IN718 is commonly used in the hot sections of turbofan engines – specifically as turbine discs, stator vanes and structural cases as is shown in Figure 1.1 [1]. In these applications, it needs to maintain good mechanical properties at temperatures approaching 50% of its melting temperature (1370 – 1430ºC), maintain good creep resistance coupled with fatigue and oxidation resistance [2]. Other non-aerospace applications include compressor rotors in land-based turbine engines, cryogenic storage tanks, and oil and gas production machinery [3,4].

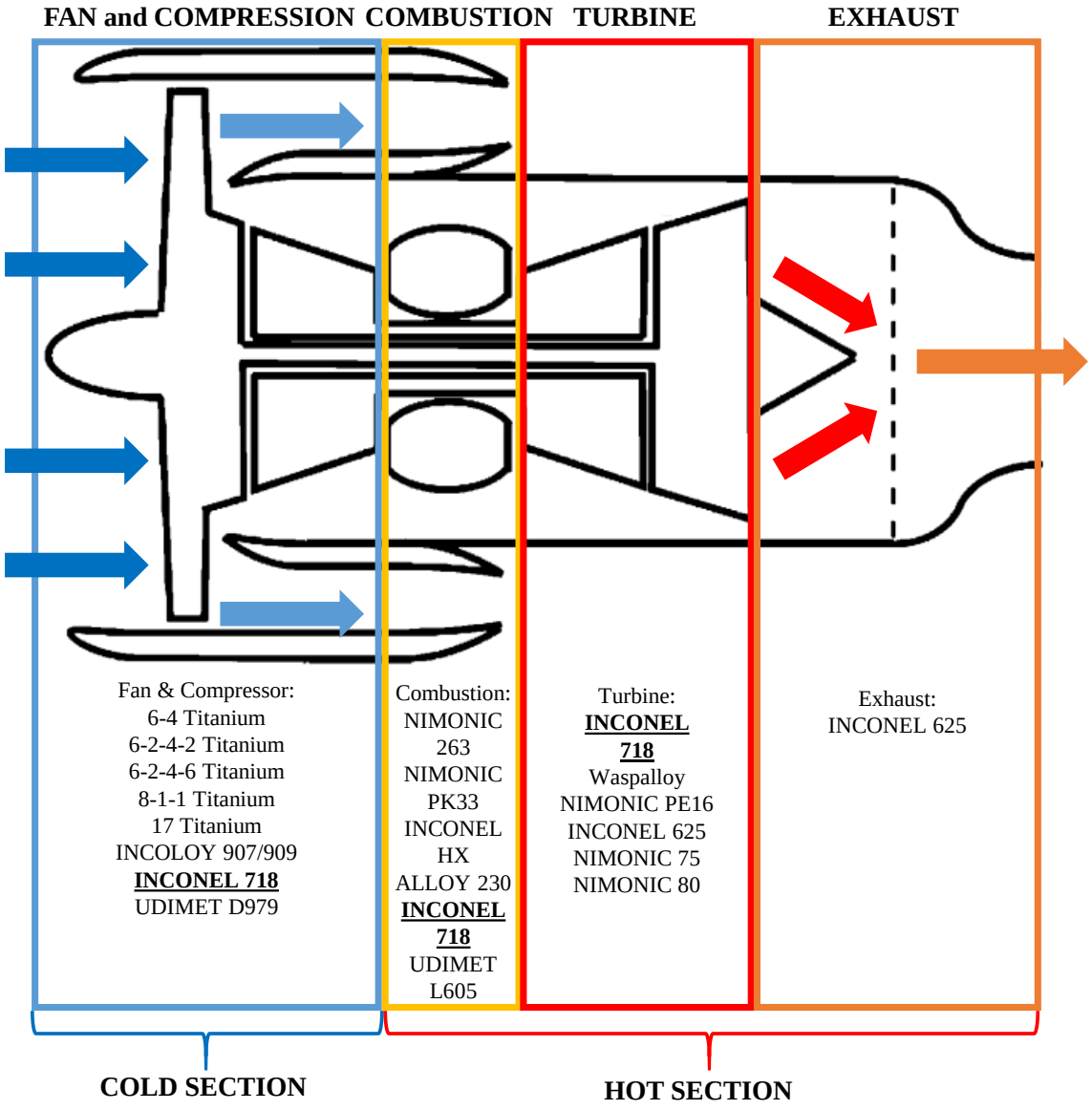


Figure 1.1: Schematic diagram for a short-ducted, non-mixing turbofan engine showing the use of IN718 for aerospace propulsion [5,6].

The typical processing route for IN718 is depicted in Figure 1.2. Typically, large ingots are fabricated using vacuum induction melting (VIM) in a refractory crucible to remove low-melting point contaminants [3]. The melt is then deoxidised before adding reactive elements such as Al and Ti [3]. Once the desired composition is achieved, the ingot is then remelted to reduce solidification defects caused during VIM [3]. Remelting can be done through vacuum arc remelting (VAR), electro-slag remelting (ESR) or electron beam cold heart refining (EB-CHR) [3]. The final

components are then made through either [1,3,7]:

i. *investment casting;* for complex shapes such as vanes and stator components. The reduction in strength associated to the casting process is acceptable as these components are governed by stiffness and limitations of wall thickness and radii.

ii. *forming*; for simpler geometries subject to high dynamic loads and fatigue loading such as turbine discs. Critical rotating components are made using hot die forging and friction welding to obtain good mechanical properties and fine-grained interfaces.

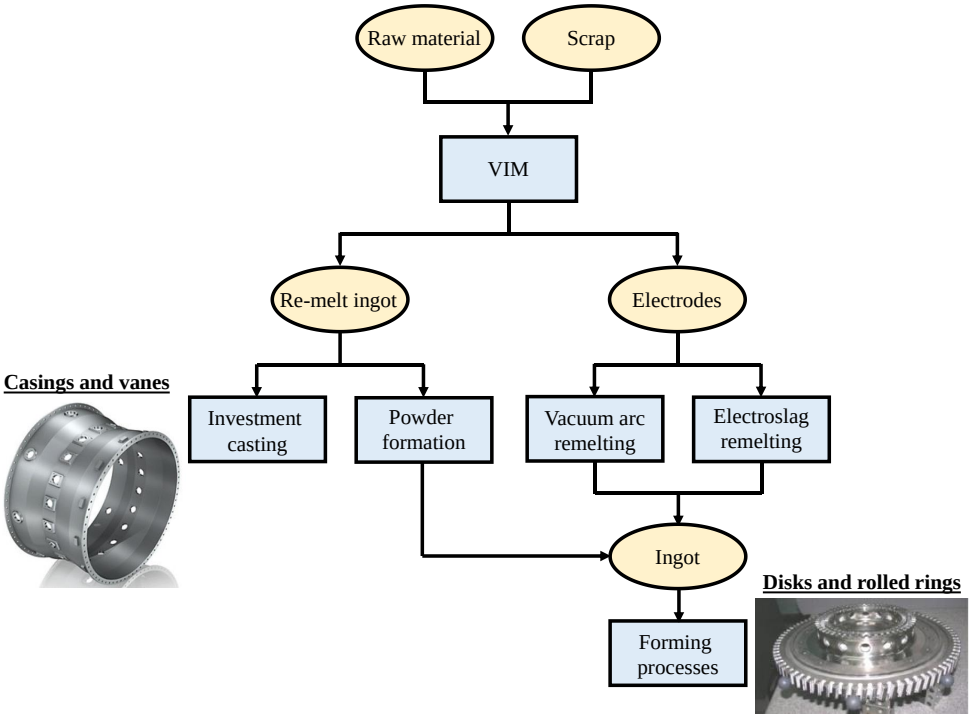


Figure 1.2: General processing route for IN718 aerospace components [3,8,9].

1.2 Additive manufacturing

Metal additive manufacturing is the process of making metallic components directly from three dimensional (3D) computer aided drawings (CAD), where a 3D CAD file is sectioned into a stereolithography (STL) file consisting of incremental layers of the CAD model [10]. These layers are then incrementally melted using a precisely moving high energy heat source, to melt the metal powder in the required shape [11].

AM enables the production of parts with complex designs which cannot be made through standard

machining processes such as internal cooling channels and topologically optimised geometries [8,10,11]. While powder atomisation for AM can be expensive, the conventional processing of components through the forging and machining route mapped out in Figure 1.2 is also costly and results in a very high degree of waste [8]. For instance for the manufacturing of a 5 kg F-101 compressor disc an initial ingot size of 95 kg is required [12]. Machining of IN718 further poses challenges due to work hardening resulting in excessive cutting temperatures and tool wear reducing the tool life [8,13]. Investment casting is time consuming and tends to result in inferior mechanical properties compared to forming and machining due to the high degree of elemental segregation characterising these processes [14,15]. Due to the slow precipitation kinetics characteristic of IN718, it is weldable and therefore an ideal candidate for AM [16–18]. Using AM can also be useful for further optimisation of the properties of such components. For instance, dual microstructure Ni-based superalloy discs consisting of a small grain size at the bore and a large grain size at the rim (Figure 1.3 (a)) are used to obtain superior mechanical performance. Such discs are obtained by applying a complex heat treatment involving insulation of the bore section as shown in Figure 1.3 (b). The use of AM and the layer-by-layer building method for such techniques allows the parameters to be changed during processing, hence affecting the microstructure. Thus, such dual microstructures to be obtained in situ without the need for a complex heat treatment stage.

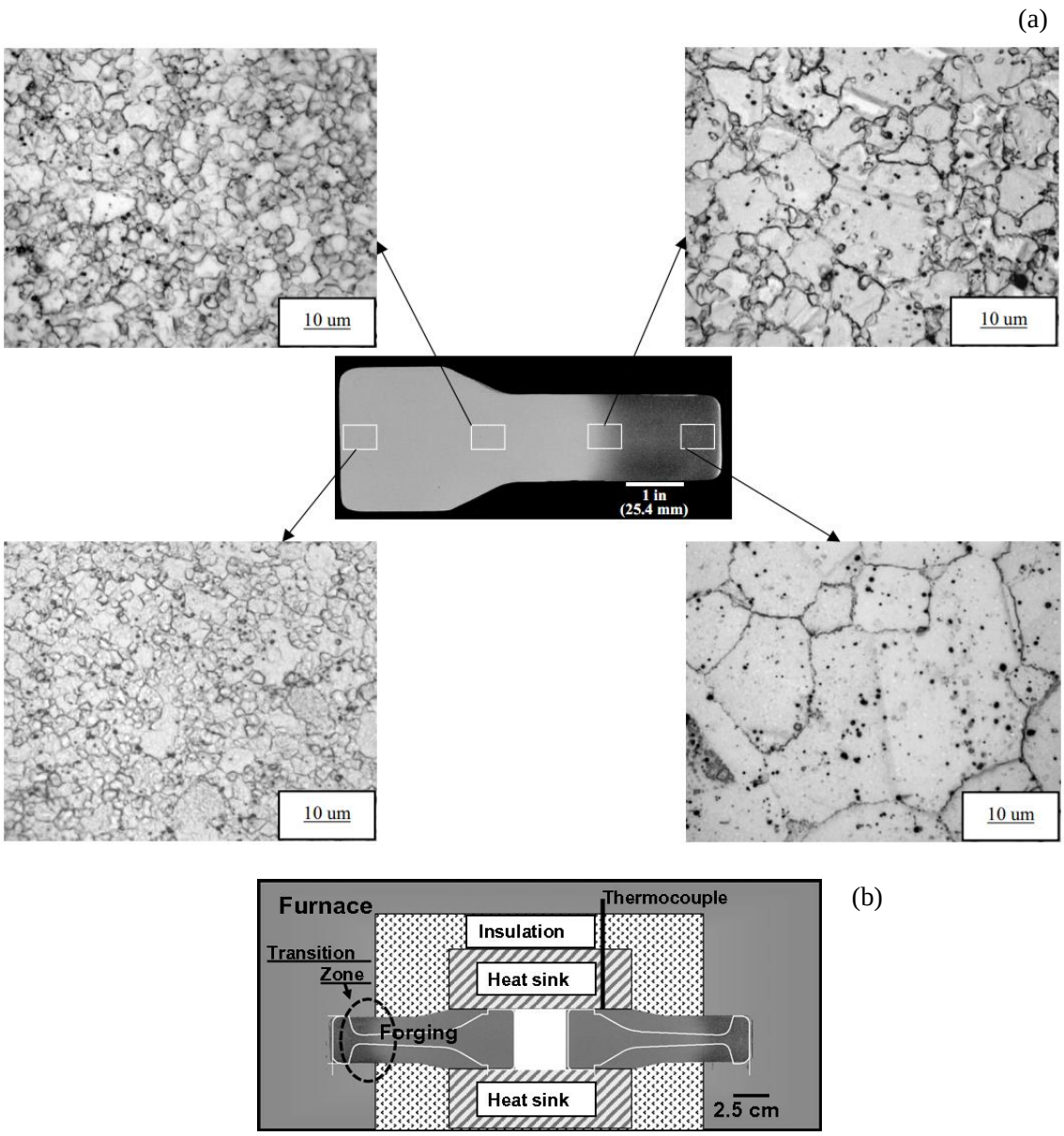


Figure 1.3: (a) the grain size variation of a dual microstructure forging [19] together with (b) schematic representation of a dual microstructure heat treatment assembly [20].

There are many techniques commonly used in the metal AM field – the scope of the current work is on laser powder bed fusion, though achievements using other techniques such as electron beam powder bed fusion (EB-PBF) and direct energy deposition (DED) will also be discussed. The other techniques themselves are reviewed in more depth by Frazier et al. [10], Debroy et al. [14], Ngo et al. [21] and Singh et al. [22].

The L-PBF process works by slicing a 3D model of the component into multiple layers which are

then sequentially melted in a powder bed using laser irradiation under an inert gas; typically argon [23–25]. L-PBF systems are generally set up as shown in Figure 1.4, with the powder being placed in a powder reservoir and components being built on a build plate or substrate, mounted on a build platform. A laser source deflected by a series of lenses and a galvanometer or scanning mirror moves along the surface to scan the required geometry [24]. The path that the heat source moves through during AM is referred to as the scanning strategy [24]. Between layers, the build plate will move down by the specified layer thickness and a recoater blade will spread powder from the reservoir to the substrate. The laser will then melt the subsequent layer. During this process some of the underlying layers may be remelted and solidified [24]. After manufacturing components are cut off the substrate using wire electrical discharge machining (WEDM) [24]. A heat treatment may be applied prior to or after part removal from the build plate.

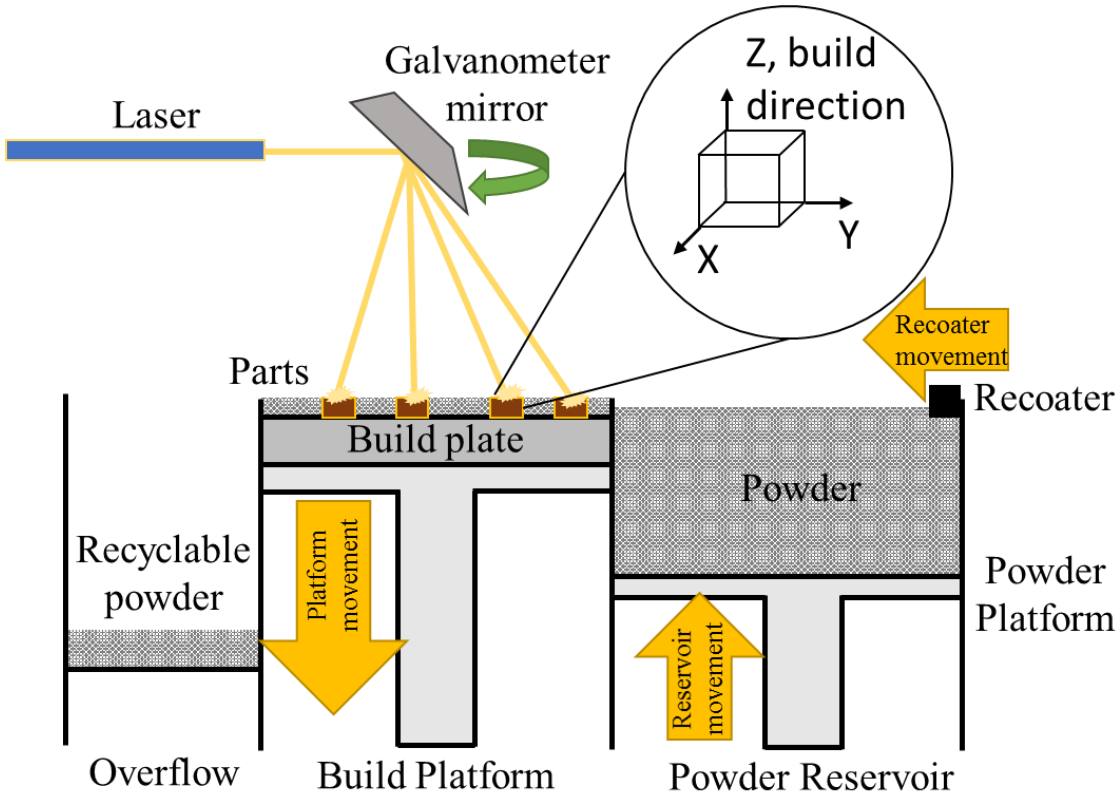


Figure 1.4: Schematic representation of a general L-PBF set-up.

1.3 Aim and Objectives

The aim of this work is to modify the microstructure of IN718 through L-PBF and determine the effect of these microstructural changes on the mechanical properties at room temperature and the high temperature oxidation behaviour. This aim will be achieved through the fulfilment of the following objectives:

1. Determine the response of the microstructure to different laser heat input parameters while still obtaining dense components
2. Compare the response of the microstructure using laser heat input parameters to that obtained by changing scanning parameters within the island scanning strategy and comparing that to changes obtained through other established strategies commonly discussed in literature such as the bidirectional and cross-hatching strategies.
3. Investigate whether baseplate heating can be a good alternative method to move from columnar to equiaxed growth.
4. Determine whether these microstructural modifications can be used to generate differences in mechanical properties.
5. Apply these techniques to generate functionally graded microstructures and determine the mechanical behaviour of such components at room temperature.
6. Investigate whether these changes in microstructures can be successfully used to modify the high temperature oxidation performance for L-PBF IN718.

1.4 Thesis outline

This research project investigates and evaluates the application of microstructural engineering through L-PBF applied to IN718.

In Chapter 2, a background on the metallurgy of IN718 is given together with a description of the physical variables governing solidification. The literature on the use of L-PBF in modifying the solidification conditions and thus the microstructure is then critically reviewed and the effect of microstructural engineering on the mechanical properties and the high temperature oxidation performance is discussed. Finally, the research gaps are identified and outlined.

In Chapter 3, the experimental procedure is outlined, specifying the powder used, building procedure, laser parameters and scanning strategies. The post-heat treatments, sample preparation, sample characterisation and mechanical testing procedures are also detailed.

Chapter 4 focuses on the feasibility of manufacturing tailored microstructures through varying process parameters namely the scanning strategy and laser heat input. The effects obtained for both approaches are compared. A suitable heat treatment was applied to obtain the required hardness and reduce segregation but maintain the different microstructures generated. The solidification cell size was quantified to estimate the influence of the process parameters on the cooling rate. A numerical grain growth model was applied to the scanning strategies used and the mechanism behind the differences was discussed. Based on the obtained monolithic microstructures, graded microstructures were obtained through the modification of subtle parameters within the island strategy itself.

Chapter 5 is a preliminary exploration of the application of base plate heating in conjunction with L-PBF of IN718 to transition from columnar to equiaxed growth. The effect of base plate heating is investigated in correlation with the use of two different laser heat input parameters and the differences in microstructure and hardness are discussed.

Chapter 6 investigates the feasibility of using laser scanning strategies rather than heat input parameters to modify the mechanical properties through changes in the microstructure. The effect of larger build volumes is discussed and the generation of a functionally graded condition solely altering the parameters in the scanning strategy is demonstrated. The validation of the theory postulated for the grain growth model is also discussed. The limiting factors to the performance are also discussed in detail together with elucidation of the physical factors affecting the process.

Chapter 7 determines whether the different microstructures obtained are enough to affect the oxidation performance at elevated temperatures and whether this will fructify in any significant improvements. The performance of L-PBF conditions is compared to the performance of wrought material. The cross-sections after long term exposures of 504 h are also analysed and discussed.

In Chapter 8 the main conclusions from this work are outlined and discussed and the future work is presented.

CHAPTER 2. Literature review

This chapter details the literature related to the physical and solidification phenomena in AM processes, the metallurgy of IN718 and how this differs after L-PBF processing. This chapter also includes a critical review on the progress in the field of microstructural control of grain orientation and size using additive manufacturing and how this can be used to change the mechanical properties and the oxidation performance of IN718. Gaps in the existing literature are highlighted and further discussed.

2.1 Physical phenomena in additive manufacturing

The melt flow behaviour in L-PBF is crucial as it will affect a component's solidification structure. The molten metal must wet the previously processed layer and upon solidifying, the surface must be smooth enough to enable further powder layering without forming cave-like throughs which can result in porosity [26,27]. The melt behaviour is related to:

i. *Surface tension and Rayleigh instabilities:* where surface tension will reduce surface energy by binding melted particles and forming a smoother surface, reducing the free energy of the system by reducing the surface area [26,28]. This results in an overall increased surface contact which transfers the heat faster and increases the cooling rate.
ii. *Viscosity:* changes in viscosity as the temperature changes from the liquidus to the solidus temperature influence the melt pool shape, smoothness, and density.
iii. *Wettability:* gives a measure of how well the liquid metal maintains contact to the underlying solid metal. Balling will occur when the molten material does not wet the underlying solid which will lead to significant porosity. This occurs due to surface tension and results in a rough and bead-shaped surface reducing the part density. When the total surface area of the melt pool is larger than that of an equivalent diameter sphere with the same volume, balling occurs [29]. Thus long melt pools having a length to diameter ratio larger than 2.1-3.14 tend to ball [26,29]. This ratio may be also affected by the laser scanning strategy where for very short raster lengths, the previous track may not have become fully solid yet which in turn results in a melt pool width

effectively spanning a number of scanning tracks leading to a more stable melt pool behaviour [26].

iv. *Oxidation:* increased oxygen content in the build chamber results in changes to the melt pool shape by affecting the direction of melt pool convection. Melt pool convection current direction is dependent on the temperature coefficient of surface tension and oxygen will decrease the surface tension of the melt pool and affect its dependency on temperature [30]. This will change the direction of Marangoni flow and therefore the melt pool shape [30]. Oxygen can also result in oxidation of alloying elements such as Fe and Al, leading to a reduction in surface quality and the formation of brittle oxides. Furthermore, liquid metals do not easily wet surface oxide films which can result in poor interlayer bonding and eventual failure [26,29,31,32]. Even relatively low oxygen concentrations (>1%) have been found to severely increase the balling behaviour due to oxidation of the liquid melt pool and oxidation of the surface [33].

v. *Absorption:* Laser absorptivity values depend on material composition, the laser wavelength and polarisation, the temperature, roughness, and reflectivity of the medium. Any residual oxygen in the chamber will change the absorptivity values and can even reduce laser beam absorption [34]. Further complexity stems from the fact that the absorptivity may also change with time during exposure to the laser source due to melting and with different power density [34]. The higher the absorption of the laser is, the easier the process will be to control as the variation in melt pool flow behaviour is reduced [26].

vi. *Marangoni convection:* During melting, temperature gradients form in the melt pool surface together with surface tension; the magnitude of such effects depending on temperature [26]. The rapid melt flow motion resulting from these gradients is known as Marangoni flow (shown in Figure 2.1 (a)) [26,35]. Through Marangoni flow, the heated liquid under the laser spot will move towards the rear end of the melt pool which increases the melt pool depth and recirculates the melt flow [35]. Due to the localised boiling caused by the laser, low viscosity liquid metal may be ejected creating spatter as shown in Figure 2.1 (a) [24,35]. When the melt is flowing from the centre to the edge of a melt pool, a flattened surface will form which reduces the chance of cave-like pores

forming [36,37]. Oxygen contamination can severely alter this melt flow behaviour resulting in humped melt pool solidification [26].

i. *Evaporation:* During laser processing, the temperature of the powder will be higher than the melting temperature of the material, which can lead to boiling and evaporation of the low boiling point constituents such as Al [31]. When this occurs, the powder particles rapidly expand and generate a recoil pressure on the melt pool as shown in Figure 2.1 (b) [31]. The vapour recoil pressure will create a melt pool surface depression below the laser [35]. Recoil pressure together with Marangoni flow help in further cooling the melt through evaporative and radiative surface cooling but will influence the stability of the melt pool [27,35]. Excessively high recoil pressures may cause melt expulsion as shown in Figure 2.1 (b) [31]. If even more energy is inputted into the melt pool, the vapour will form a plasma which could change the absorptivity along the melt pool depth and also affect powder denudation behaviour [31,35]. For alloys consisting of elements with a considerably lower boiling point and high vapour pressure such as Al in IN718, preferential evaporation of this element can occur [38,39]. The evaporated element will quickly condense in the powder bed or melt pool due to the low temperature of the build chamber leading to micro-segregation or porosity [38–41].

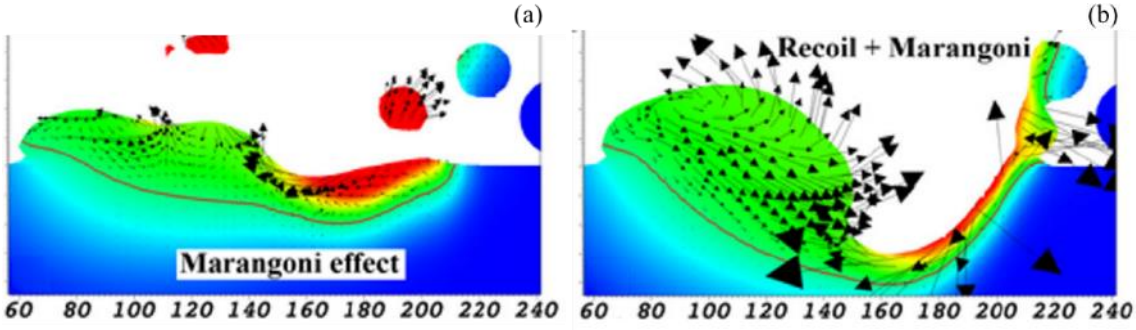


Figure 2.1: (a) Marangoni flow with melt movement towards from the hot laser spot towards the colder rear area with spattering from the ejection of low viscosity liquid and (b) melt evaporation and the effect of recoil on the melt pool [35].

2.2 Solidification in additive manufacturing

Solidification of a melt pool in AM, starts through nucleation which can be divided into homogenous (spontaneous) nucleation or heterogenous nucleation off preferred sites such as prior deposited layers or particles in the melt [42]. A large energy barrier must be overcome for homogenous nucleation to occur and the degree of undercooling must be very high, thus in AM heterogeneous nucleation is prevalent leading to epitaxial solidification where the grain structure of a new layer is a continuation of growth of the structure of the previous layer [29,42]. For epitaxial solidification to occur, the substrate or previous layer must be partially remelted to promote growth from the previously formed grains [29].

Due to the high energy interaction from the laser, heating and melting under the laser spot is extremely rapid followed by equally rapid cooling upon laser movement away from the area [43]. Laser processes, especially L-PBF, are non-steady state processes characterised by cooling rates between 10^5 to 10^6 K/s [14,36,44,45], with small melt pools ≤1 mm, thus making solidification very rapid with high chemical and thermal gradients [43]. The substrate acts as a heat sink further increasing the cooling rate, resulting in the formation of a rapidly solidified microstructure with refined grains and sub-grain structures compared to traditional solidification processes like casting [43]. The size and shape of the grains, extent of chemical segregation and the distribution of defects such as pores and cracks are all dependent on the melt pool solidification behaviour as will be discussed [42].

2.2.1 Heat flow and thermal gradient

The substrate in L-PBF acts as a heat sink and therefore the heat flow is predominantly oriented downwards towards it. The heat flow direction will determine the preferred solidification direction for any newly forming sub-grain structures (cells or dendrites) [46]. The influence of the substrate progressively decreases with increasing component height, resulting in a progressive increase in peak temperature of deposited layers as one moves up until a steady state is reached [14,47]. This directional heat flow results in a grain morphology predominantly aligned parallel with the building direction [46]. If the heat flow direction is equal in all directions grain growth will no longer be aligned with the build direction, as the growth rate would be similar in all directions forming

randomly oriented grains [46].

The thermal or temperature gradient (*G*) at the solid/liquid interface is the difference of temperature in the melt pool moving in the interface of the liquid towards the solid [48]. The thermal gradient is strongly affected by convective flow in the melt pool and depends on the material properties, manufacturing process, the heat input time during solidification as well as the position in the melt pool where this is measured [36,42,48]. Near the heat source axis, the temperature will be the highest, decreasing to a minimum value at the solid-liquid interface of the melt pool as shown in Figure 2.2 [14,36]. The temperature gradient gradually decreases as one moves away from the top of the melt pool [45]. It is also very dependent on laser power; Li et al. [45] measured an increase from 10.6ºC/µm to 21.7ºC/µm with a 150 W power increase. Speed was observed to have a small effect on temperature gradient which were not comparable to changes in power [45].

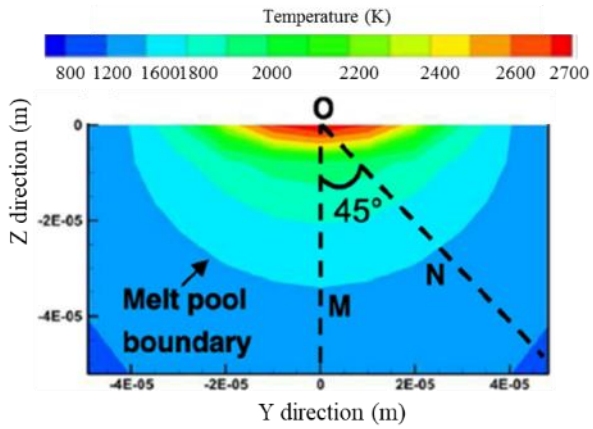


Figure 2.2: Temperature contour plot for 316L stainless steel melt pool determined through finite element analysis modelling [36].

2.2.2 Undercooling

Undercooling refers to the difference between the liquidus temperature of the alloy with nominal composition and the actual temperature of the melt. The total undercooling (ΔT) and the solid-liquid interface consists of [42]:

$$\Delta T = \Delta T_{TH} + \Delta T_C + \Delta T_R + \Delta T_K \qquad \textit{Equation 2.1}$$

where:

ΔT_{TH}: refers to the thermal undercooling.

ΔT_C: refers to the constitutional undercooling.

ΔT_R: is the undercooling due to the curvature at the solid/liquid interface.

ΔT_K: refers to the kinetic undercooling.

The kinetic undercooling is associated with the driving force required for solidification and related to the rate at which atoms become attached to the solid – for metals this tends to be very small (~1 K). The undercooling due to the curvature at the solid/liquid interface (referred to as the capillary effect) occurs when the liquid to solid transformation is supressed due to the additional surface energy needed to create a curved surface. This may be significant due to the fine structures being created. The thermal undercooling represents the degree to which the liquid is cooled below the equilibrium freezing temperature and may be considerable for high-speed solidification processes. The constitutional undercooling of the melt is in general the larger contributor to Equation 2.1. In alloys such as IN718, constitutional undercooling due to solute rejection caused from different solid and liquid solubilities of alloying elements will result in an inverted temperature gradient [42]. A boundary layer enriched in solute ahead of the solidification front will form due to elemental segregation [42]. The undercooling present in the melt means that unstable cellular or dendritic growth occurs. The fast solidification rates characteristic of the L-PBF process will further exacerbate this phenomenon as there is insufficient time for the liquid and solid to undergo diffusion and reach equilibrium conditions [42]. Significant undercooling can result in the formation of

equiaxed structures.

The degree of undercooling depends on the temperature gradient and the growth rate. It will influence the type of solidification sub-structures being formed (e.g. cells vs dendrites) and the extent of segregation. A large degree of undercooling in the melt will make it easier for homogenous nucleation to occur, resulting in equiaxed dendritic growth. The mode of growth will depend on the conditions at the interface and may be divided into planar, cellular or dendritic (columnar/equiaxed) morphologies [42].

2.2.3 Solidification rate

The solidification or growth rate (R) is the rate at which the solid/liquid interface in the melt pool advances. R will vary across the melt pool interface, with solidification on average occurring at a normal to the solid/liquid interface along the maximum thermal gradient [42]. The solidification rate is directly related to the heat source movement speed (v) by [42,49]:

$$|\mathbf{R}| = |\mathbf{v}| \cdot \cos(\theta) \qquad \textit{Equation 2.2}$$

where:

θ is the angle between the surface normal of the solidification front and the laser scanning direction.

Through Equation 2.2, at the surface of the melt pool if the solidification front is normal to the surface, the growth rate would be 0 at $\theta = 90^{o}$, while at $\theta = 0^{o}$, along the weld centreline the growth rate would be equal to the heat source movement rate, as shown schematically in Figure 2.3 [42,49]. Along the melt pool centreline, the growth rate of the solid and the release rate of latent heat are at a maximum, with the solidification rate decreasing as one moves towards the weld pool edges [42,50,51]. Upon solidification, the liquid will change phase to solid, releasing an amount of energy related to the latent heat of fusion. Thus, a critical growth rate exists beyond which the minimal thermal gradient at the centreline is not able to dissipate the generated heat of fusion quickly enough and the temperature in the surrounding liquid is increased [42]. If the growth rate is above this critical value, the weld pool shape will become more elongated and tear drop shaped as observed

for L-PBF and the maximum growth rate will be more sluggish than the heat source movement speed [42,51,52]. The higher the laser movement speed is, the less elongated the grains become, tending towards a more equiaxed structure at very fast solidification rates [14,53]. At very fast solidification rates, undercooling will also be very high and equiaxed dendritic growth becomes progressively easier.

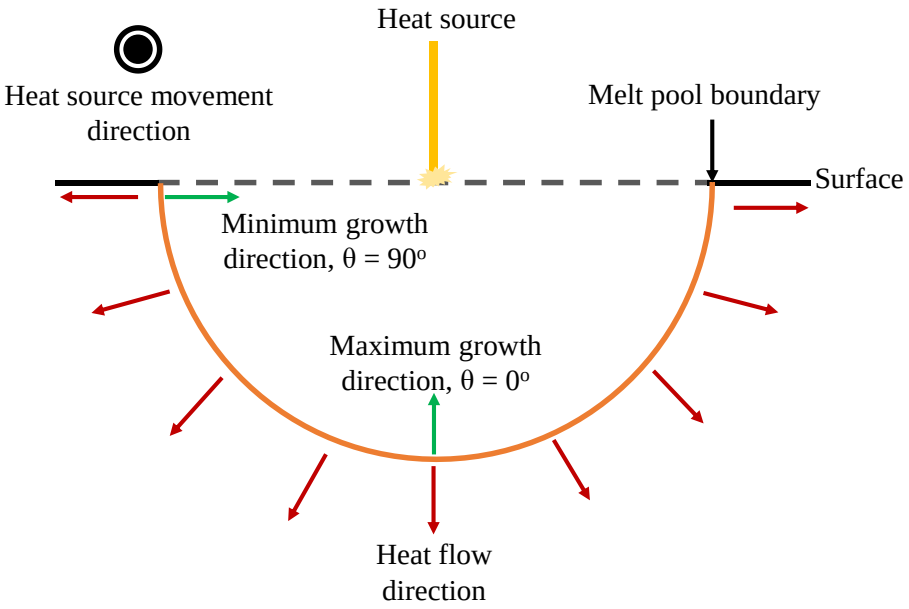


Figure 2.3: Heat source movement direction and growth rate at different melt pool positions. Adapted from [14].

2.2.4 Solidification theory

A low ratio of *G/R* (i.e. low temperature gradient and high solidification rate), favours the formation of equiaxed dendrites while a high ratio (high temperature gradient and low solidification rate) favours the formation of columnar/cellular dendrites, moving towards planar growth at very high *G/R* ratios as shown in Figure 2.4 [42,54,55]. Epitaxial growth will occur when columnar dendrites or cells maintain their growth orientation through melt pool boundaries [56].

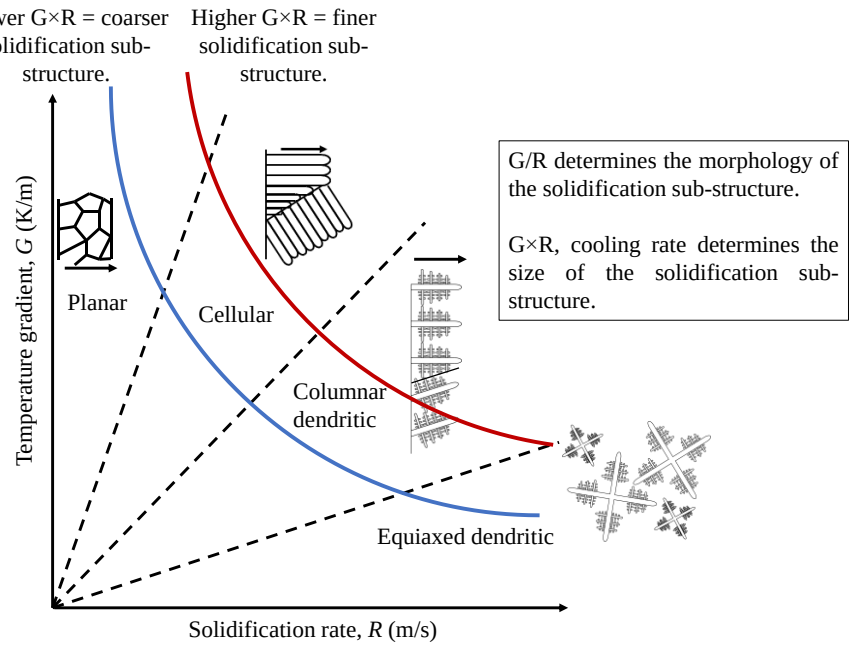


Figure 2.4: Schematic solidification map showing the different solidification morphologies forming with changes in G and R. Adapted from [57].

Columnar and cellular growth is driven by the steep temperature gradients resulting from the heat flow towards the substrate and is commonly observed for L-PBF [36,54,56,58]. In cellular growth, the cell orientation will be aligned with the direction of highest heat flow, while for columnar dendritic growth, growth will occur along the easy growth directions for the crystal with the heat flow direction determining which of the directions is currently active [42]. In fcc (face centred cubic) metals there are three equivalent orthogonal crystal directions; [100], [010] and [001] and the easy growth directions are along these directions. This arises due to either anisotropy in the surface energy of the solid-liquid interface or how easy it is for atoms to attach to the interface of different crystallographic planes or a combination of both factors [59].

Thus, during solidification grain selection occurs, where grains whose 〈001〉 direction is closely aligned with the normal to the solidification front outgrow other less optimally aligned grains [42]. If the primary growth orientation is along the [100] direction, the secondary growth orientation could be along [010] or [001] [42,60]. If the heat flow direction is most closely aligned with the [100], growth will be along that direction. When the direction of heat flow changes e.g. due to a change in laser movement, the 〈001〉 direction most closely aligned with the new heat flow

direction will grow preferentially which can lead to a 90° change in orientation between melt pools [60]. Columnar or cellular structures with similar orientations grow in bundles and when two bundles with different orientations intersect, a grain boundary is formed [56].

G and *R* vary with solidification time as shown in Figure 2.5 (a). Initially, the temperature gradient will be very high with a low solidification rate promoting the formation of columnar dendrites approximately perpendicular to the solidification front and aligned with the heat flow direction, as shown in Figure 2.5 (b) [53,61]. As the liquid front advances with further solidification and the melt pool shrinks, the temperature gradient decreases and the solidification velocity rapidly increases (Figure 2.5 (a)) [61]. The grain morphology will become equiaxed with decreases in the *G/R* ratio as shown in Figure 2.5 (b) resulting in a transition from cellular/columnar growth to equiaxed growth between the bottom and top part of the melt pool [53,61].

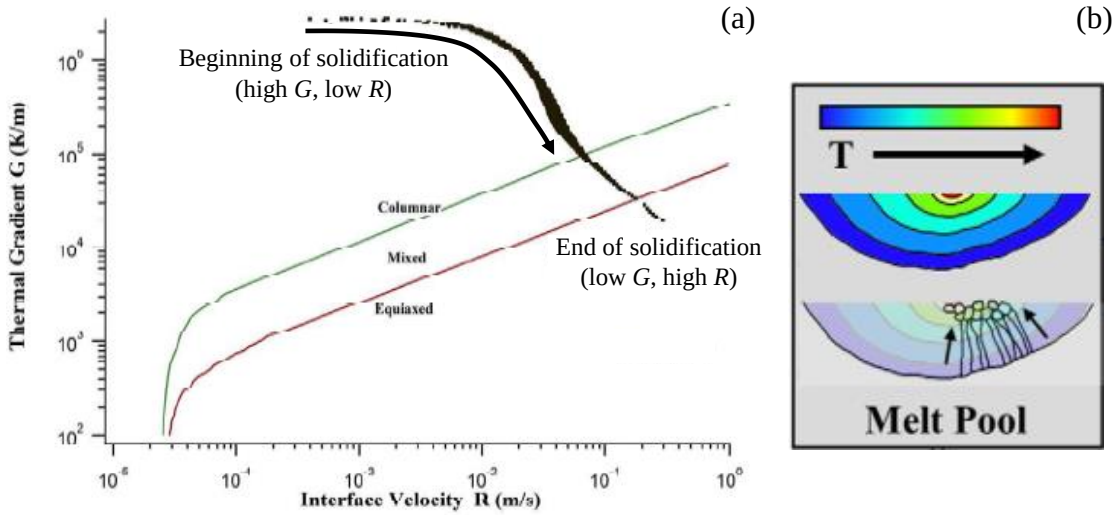


Figure 2.5: (a) changes in G and R for IN718 in EB-PBF depending on solidification time, together with (b) solidification structure and melt pool isotherms [53,61].

2.2.5 Cooling rate

The cooling rate is equivalent to the product of $G \times R$. The faster the cooling rate, the finer the solidification structure, resulting in a smaller cell size or a finer dendrite spacing [14,51]. The cooling rate also affects the solute diffusion lengths for segregation; with higher cooling rates resulting in a lower amount of segregation as shown in Figure 2.6 (a to d) for IN718 [51,62]. In AM, very high cooling rates are associated with a progressive decrease in long-chained Laves

formation [62].

Substrates in L-PBF often do not only have one component built on them – usually they are as densely packed as possible to optimise cost. The inter-layer time will affect the cooling rate of the parts being built [63–66]. Longer times between layers in DED have been reported to result in a reduction of epitaxial growth and an increase in yield strength (σ_Y) and micro-hardness [65,67]. In L-PBF the cooling rate will be higher than parts manufactured using DED, in part due to the higher scanning speeds employed and also due to the larger expected part density on a substrate coupled with delays due to the recoating stage. This is still affected by part geometry as with increases in part height it was still reported that the part temperature overall increased [44,47,66,68].

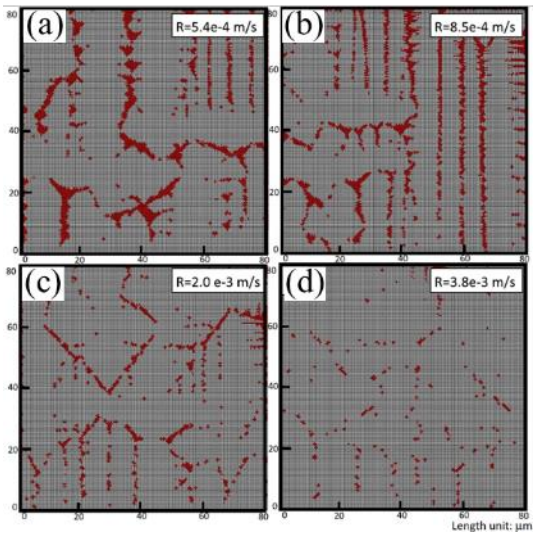


Figure 2.6: Variation of Laves phase morphology with cooling rates of (a) 500 K/s (b) 1000 K/s (c) 2000 K/s and (d) 4000 K/s [62].

2.3 Metallurgy of IN718

The nominal chemical composition of IN718 is given in Table 2.1. The microstructure of IN718 consists of an austenitic (γ) fcc based crystal Ni matrix, stabilised by Fe, Cr and Mo which have atomic radii close to the Ni atom and provide solid solution strengthening [12]. Cr forms a protective oxide surface layer to improve the oxidation resistance [69,70]. Small additions of boron and carbon improve the creep rupture strength of the alloy, with boron improving grain boundary cohesion and reducing grain boundary diffusion and carbon combining with Ti or Nb to form carbides to further

inhibit dislocation motion [70,71].

Table 2.1: Nominal chemical composition of IN718 [72].

Chemical composition of IN718 (wt.%)												
Ni	Fe	Cr	Mo	Nb	Ti	Al	Co	Cu	C	Si, Mn	P, S	B
50-55	Bal.	17-21	2.8-3.3	4.75-5.5	0.65-1.15	0.20-0.80	≤1.0	≤0.3	≤0.08	≤0.35	≤0.015	≤0.006

IN718 is a precipitation strengthened alloy. In precipitation strengthened alloys, precipitates interfere with the deformation process through a combination of lattice mismatch resulting in coherency strain strengthening together with the precipitate itself offering resistance to dislocation motion through it by order strengthening [2,73–75]. The precipitate size will determine whether precipitate shearing or Orowan looping is predominant [2,73–75]. IN718 relies on the formation of coherent gamma double prime (γ") precipitates and small amounts of gamma prime (γ') precipitates through ageing as its main strengthening mechanism. This structure is typically obtained through a double-ageing heat treatment and is shown in Figure 2.7 (a). Al and Ti are both required for the formation of γ' while Nb is required for the formation of γ" [70].

γ" is an elongated and disc shaped phase with a thickness of around 10 nm and a diameter of around 30 to 50 nm as shown in Figure 2.7 (a) [2,76,77]. It has a composition of Ni_3Nb with a coherent body centred cubic (bcc) tetragonal $D0_{22}$ structure as shown in Figure 2.7 (b) [2,53]. The γ" phase is responsible for the excellent high temperature properties of the material due to the low number of slip planes available in this phase [12]. The strength and hardness of IN718 will increase with increasing γ" particle size up to a peak value as shown in Figure 2.7 (d) [69]. The phase is metastable between temperatures of 500 to 900°C, with a solvus temperature of 900 to 920°C [2]. After long exposure times over 650°C, it will transform into needle-like δ phase consisting of Ni_3Nb (shown in Figure 2.7 (c)) [69,76,78]. The sluggishness of the precipitation of δ allows the precipitation of γ" to occur first, up to temperatures of 700°C. δ forms at grain boundaries or at stacking faults in γ" particles, growing into the grain in a needle or plate-like form. Higher residual strains in the lattice increase the δ precipitation rate and change the particle morphology from needle-like to globular form as the needle-like particles are broken into small globular pieces. There have been contradicting reports on δ phase; when δ forms, the Nb will be used for its formation rather than γ"

strengthening phases and the needle-like morphology of the phase together with its incoherency with the matrix can result in an increased brittleness [69,76,78,79]. However δ has been reported to be beneficial in small quantities to reduce the amount of grain growth during heat treatment and grain boundary sliding during high temperature creep and for intergranular δ, increases in ductility have been reported [17,80].

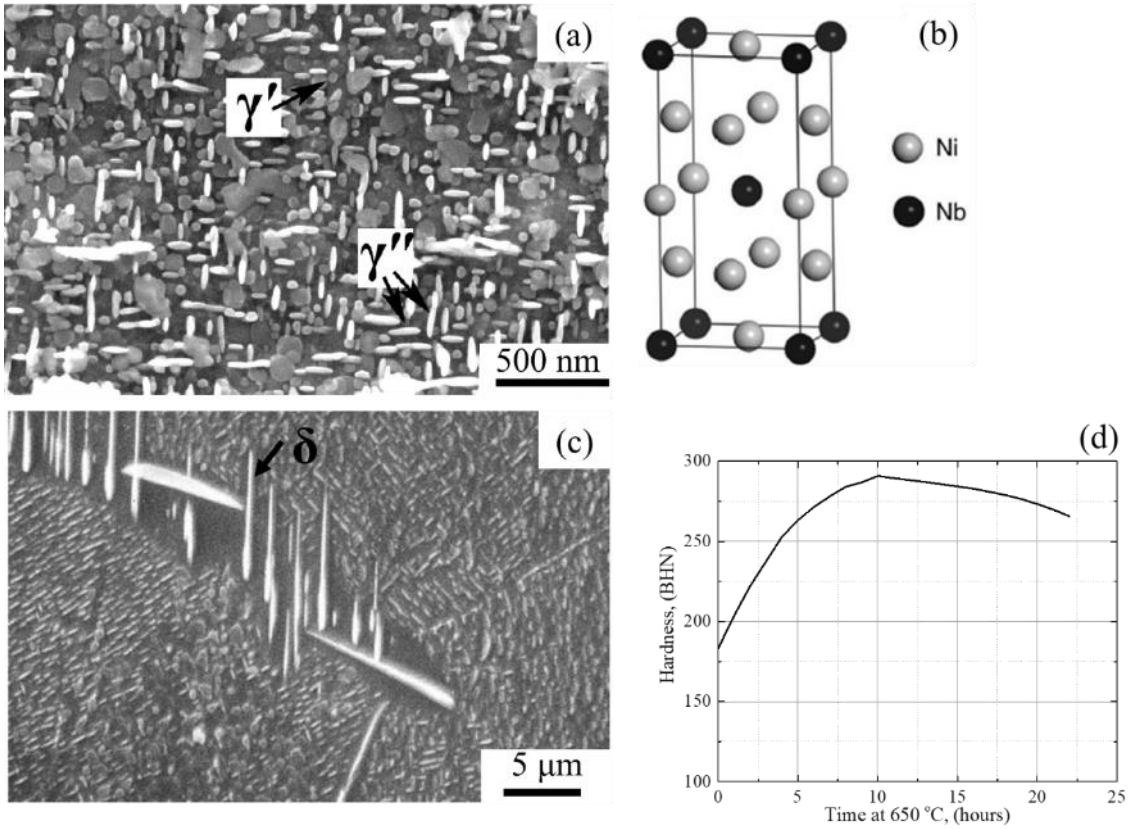


Figure 2.7: (a) showing γ" and γ′ for solution treated and double-aged IN718, together with (b) the crystal structure of γ" phase, (c) showing needle-like delta phase growing into the grains and (d) the rate of hardening during ageing at 650ºC for a grain size of 60 µm [17,81–83].

Small amounts of γ' are also present in double-aged IN718, this is a secondary strengthening phase with a composition of Ni_3(Al or Ti) forming a coherent phase with the γ matrix and stable between 600 and 900ºC [12]. The phase has a primitive cubic structure ($L1_2$) with Al atoms at the cube corners and Ni atoms at the centre of the faces [12,53]. Larger atoms such as Ti and Nb can substitute for the Al atoms [12]. These precipitates often align along the elastically soft ⟨100⟩ direction and can be cubic or spherical in form (the spherical form is shown in Figure 2.7 (a)) [12]. The γ' phase

has a lower coherent strain with the gamma matrix compared to the γ" phase and thus results in lower potential hardening [81].

2.3.1 Microstructure of AM IN718

The microstructure formed during solidification significantly affects mechanical properties and resistance to failure mechanisms [14]. Due to the high cooling rate in L-PBF, typically γ" and γ' are absent or not present in sufficiently high amounts in as-built structures resulting in a low tensile strength and a relatively high ductility [15,60]. For processes where the cooling rate is more sluggish, such as DED, spheroidal γ" has been observed together with γ' as particles around 20 nm in size [53,63,66]. For L-PBF, due to the numerous parts on a substrate by the time the layer is rescanned the part is already much cooler. Furthermore, extra time for cooling is available while the powder recoating process occurs which further reduces the heat retention. Thus, formation of appreciable γ" is more difficult for L-PBF due to the lower component temperatures compared to DED.

The microstructure obtained for IN718 after L-PBF is shown in Figure 2.8 (a to e). Typically, IN718 microstructures after L-PBF consist of an elongated grain morphology aligned with the build direction growing epitaxially through different layers as shown in Figure 2.8 (a) with a columnar dendritic or cellular substructure as shown in Figure 2.8 (b to d) [23,60,84]. The high cooling rate coupled with the high thermal gradient in L-PBF tends towards the formation of the cellular substructure where the growth of secondary dendrite arms is supressed; with cell diameters ranging between 100 to 1000 nm as shown in Figure 2.8 (e) [60]. Across melt pool boundaries cells tend to grow either epitaxially maintaining the same orientation or through a 90^{o} orientation change, growing along the easy crystallographic growth directions for the crystal [60,85].

Cellular growth in L-PBF can enhance pinning of dislocation movement by particles pinning the dislocations at the cell boundaries or the cell boundaries themselves moderately reducing the degree of slip in the substructure [86–89]. Boundaries in between cells have been observed to maintain the overall crystallographic direction with only a very small misorientation ($<10^{o}$) being present in between cells making up the same colony [85]. Cellular boundaries have been reported to consist of dislocation structures about 100 to 300 nm thick. Due to the rapid solidification and thermal

stresses generated during L-PBF, slightly distortion of the crystal plane occurs which is not significant enough to create a high angle grain boundary resulting in the dislocations observed at the cell boundaries [85,90].

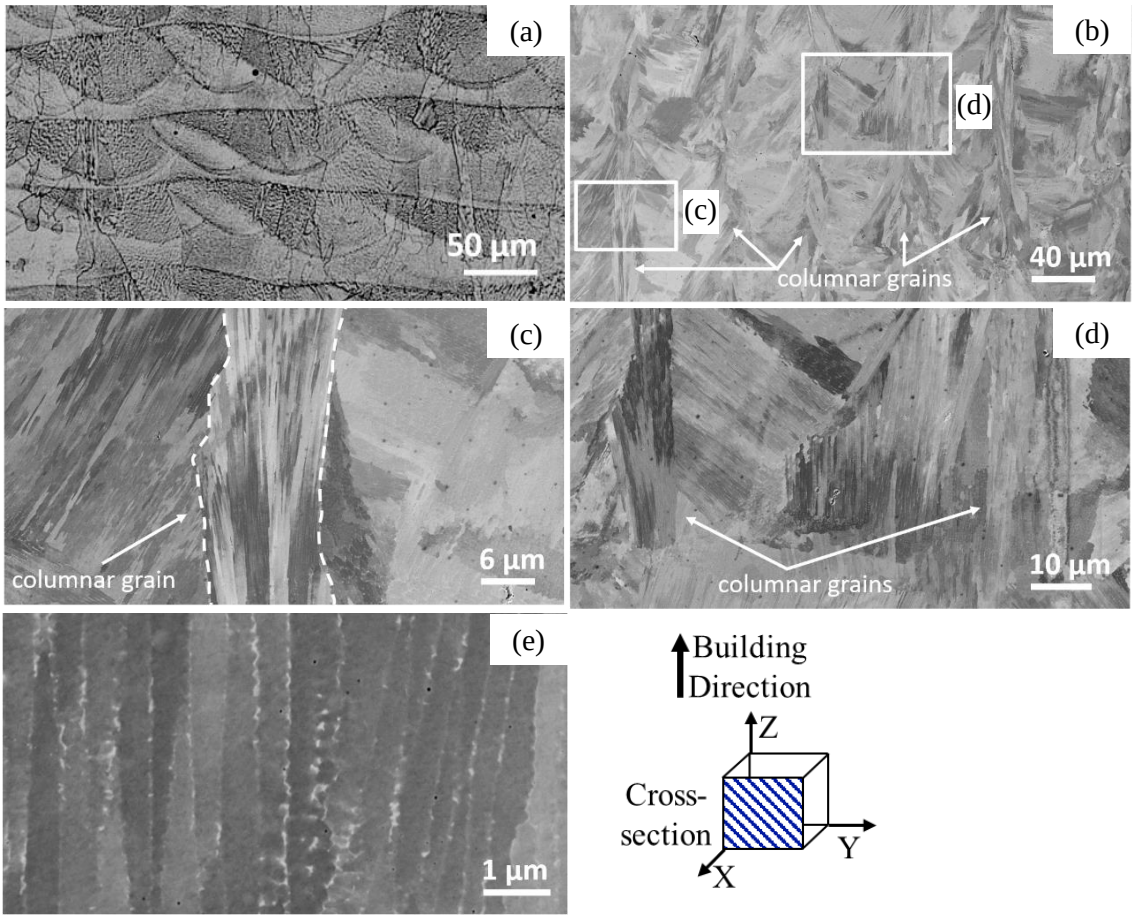


Figure 2.8: (a) Optical micrograph for typical L-PBF IN718 with epitaxial growth visible between melt pools, together with secondary electron micrographs of (b) the columnar grain structure, (c) slender columnar grains together with (d) angled epitaxial grains and (e) solidification cells showing elemental segregation around their boundaries [90].

The grain orientation is dependent on the melt pool shape; specifically, on the solid-liquid interface. Grains grow from the melt pool boundary towards the centre of the melt pool parallel to the direction of maximum heat flow [14]. In L-PBF, the melt pools have a high length to depth ratio due to the high speed of the process with a near-flat or flat solidification front as shown in Figure 2.9 (a and b) [14]. This results in columnar grains which grow vertically, with their 〈001〉 direction parallel to the building direction (B.D) [14]. If a grain grows in any one layer with a 〈001〉 direction normal

to the slightly inclined melt pool, it will be tilted away from the build direction by θ and when the beam is reversed for the next pass this grain will be even further aligned from the direction of maximum growth by 2θ [14]. This will result in these grains being even less favourably oriented [14]. Although grains with orientations close to the maximum temperature gradient at the trailing edge of the melt pool have a growth advantage in an individual layer, this advantage is not retained over multiple layers due to the beam rotating and the beam travel direction reversing [14]. Thus over multiple layers, grains aligned with their 〈001〉 direction parallel to the build direction will be on average more closely aligned with the maximum temperature gradient for the build (rather than that for a single pass) which in turn means they grow faster [14]. At intermediate laser speeds the melt pools may have a more intermediate shape between a flat front and a curved front. In such cases there may be a tilt in the grain growth direction where the grains are aligned with the direction of maximum heat flux as observed by Thijs et al. [91], Dovgyy et al. [92] and Helmer et al. [93].

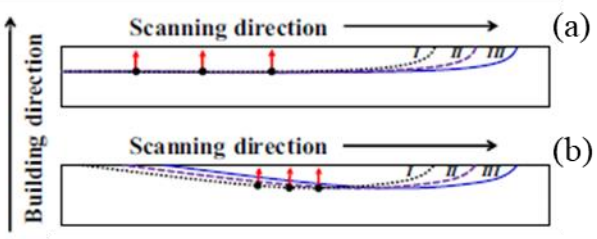


Figure 2.9: Growth direction of columnar grains for (a) and (b) L-PBF with different length to depth ratio melt pools resulting in vertical alignment and close vertical alignment respectively. Curves marked with I, II and III represent consecutive melt pool boundaries along the scan track [14].

2.3.2 Segregation

Additional phases can also be observed in IN718 after AM due to the large number of alloying elements with varying melting temperatures and solubilities in the alloy together with the non-equilibrium solidification conditions of the AM process resulting in constitutional undercooling and therefore elemental segregation. Retained strain after quenching was observed to accelerate the precipitation kinetics for such phases [1]. Some of these phases include [12,16,94–100,18,60,66,69,70,76,77,80]:

i. *Laves phases;* shown in Figure 2.10 (a and b) which form in the interdendritic areas as eutectic compounds, having over 20.61 wt.% Nb. These phases together with areas rich

in Nb carbides decrease the mechanical properties by acting as crack initiation sites due to their brittle nature [76] and are often observed when elemental segregation occurs. The phase forms as irregularly shaped elongated globules or as platelets with a hexagonal unit cell or a long-chained morphology visible with severe segregation.

ii. *Metal carbides and borides;* the small amounts of carbon and boron in IN718 combine with reactive elements such as Al, Ti, Nb, Cr or Mo to form carbides or borides residing on the γ-grain boundaries. The chemical composition can be MC, $M_{23}C_6$, M_7C_3 or M_3B_2. The carbides are normally found in interdendritic regions with the $M_{23}C_6$ carbide being observed to precipitate at the grain boundaries inhibiting grain boundary sliding. Long chained Laves phases and niobium carbides formed in interdendritic regions are deleterious for the mechanical properties due to their brittle nature [62,77]. Square shaped carbides have also been observed in AM with a centre of a lighter alloy [101]; most likely Ti with a Nb exterior as shown in Figure 2.10 (c) [66].

iii. *Alumina;* has been reported by Popovich et al. [76] and Deng et al. [60] in the form of small particles in the IN718 matrix – attributed to the oxidation of Al in the alloy during L-PBF processing or powder processing.

During solidification, elements such as Nb, Mo, Si etc will diffuse to the remaining liquid phase due to a different solid solubility between the liquid and solid phases [53,62,102]. Due to the rapid cooling rate present in L-PBF, segregation will occur in the order of; liquid → γ+liquid → γ +NbC+liquid → γ +NbC+Laves [15,60]. The result is that the dendrite/cell interiors are rich in austenite but depleted of Nb and Mo while the concentration of these elements in the liquid will increase substantially during solidification [53,62,90]. Near the end of solidification, the sub-grain structures will join and the remaining liquid will be separated into isolated discrete areas which will form a eutectic phase made out of gamma, Nb carbides and Laves [15,62]. The degree of segregation is dependent on the cooling rate as cooling rate determines the sub-grain structure size [62]. The formation of long chained Laves phases occurs at low cooling rates and high amounts of segregation, while at high cooling rates any Laves phase formed will be in the form of small discrete particles [62,103]. The orientation of the Laves phase has been reported to affect the mechanical behaviour of the particle upon loading with granular Laves particles being less prone to crack [77].

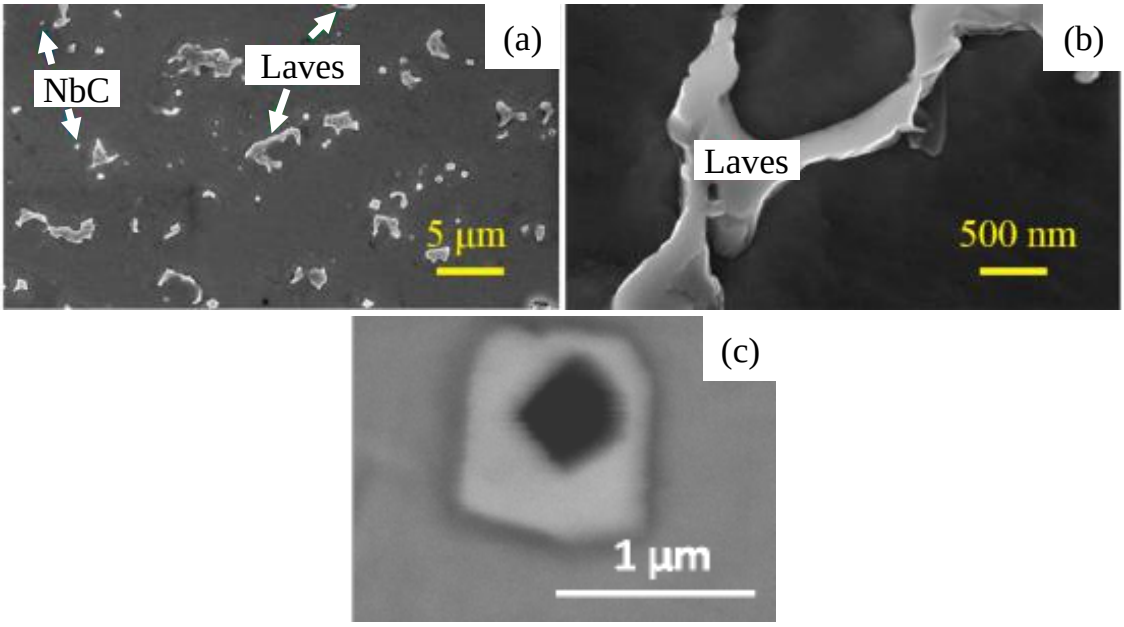


Figure 2.10: Precipitates observed in AM IN718 with (a) showing interdendritic eutectic solidification products such as Laves phases and some niobium carbides with a higher magnification shown in (b) [15] while (c) shows square shaped Ti and Nb rich carbides for as-built microstructures [66].

2.3.3 Heat treatment

The heat treatment required for precipitation hardening of IN718 consists of a solution treatment between 924 to 1010ºC for a minimum of 30 minutes followed by cooling at a rate equivalent or faster than air cooling [104]. A two-step ageing treatment is then required at 718 ± 14ºC for 8 h and 621 ± 14ºC to reach a total precipitation time of 18 h [104]. The tensile and hardness properties obtained after this ageing treatment are outlined in Table 2.2. The static recrystallisation temperature for IN718 is between 1025 and 1050ºC, thus any homogenisation treatment to induce recrystallisation needs to be carried out above this temperature in addition to the solution treatment and ageing treatment [105]. The two-phase heat treatment is applied to ensure preferential precipitation of γ'' followed by γ' at the lower end of the temperature and avoid precipitation of large amounts of δ. Typically, for a fully heat-treated alloy, the volume of γ' is usually around 4 to 5 % and the volume of γ'' is around 15 to 20% [69,106].

Post-build heat treatments are generally required after L-PBF of IN718 to reduce segregation and induce the precipitation of γ' and γ'' strengthening phases [2]. Furthermore, heat treatment reduces the dislocation density existing in the components; the high dislocation density and sub-grain

boundaries in AM components prevent dislocation movement and crack tip relaxation which can result in a poor elongation to failure compared to a wrought product [98]. Post-build heat treatments are effective at removing the residual stress, with stress after direct aging calculated to be ~99% of the as-built condition, decreasing down to ~22% after solution treatment and disappearing completely after a high temperature homogenisation treatment [60]. Heat treatments described in literature consist of several combinations with, for instance a hot isostatic pressing (HIP) cycle to close any pores, followed by a homogenisation treatment, solution treatment and double-ageing treatment; resulting properties are detailed in Table 2.2. Applying a direct ageing treatment to as-built components results in a high strength but also a low ductility [60,107]. Applying a high temperature homogenisation treatment improves the ductility at the cost of some of the strength.

Table 2.2: Heat treatments applied to L-PBF IN718 and mechanical properties obtained.

Heat treatment	0.2% σ_Y (MPa)	Young's modulus (GPa)	Ultimate tensile strength (MPa)	Elongation to failure (%)	Ref.
Wrought, per BS637_18/AMS 5662	1034	208	1275	12	[15,104]
As-Cast	758-915	-	862-1090	5-11	[14,15]
L-PBF, As-built	600	200	990	36	[60]
L-PBF, 850°C/2 h, AC	668 - 875	138 - 190	884 -1153	7 - 17	[76]
L-PBF, HIP at 1180°C/3 h/150 MPa, FC	481-645	183-188	788 - 1025	34 - 38	[76]
L-PBF, DA at 720°C/8 h, 620°C /8 h AC	1200	210	1400	15	[60]
L-PBF, ST at 980°C/1 h, WQ, DA 720°C/8 h, 620°C/8 h	1180-1186	190	1400-1440	18.5-23.5	[7,60]
L-PBF, H at 1080°C/1 h, WQ, DA 720°C/8 h, 620°C/8 h	1190	220	1370	25	[60]
L-PBF, H at 1080°C/1 h, WQ, ST 980°C/1 h, WQ, DA 720°C/8 h, 620°C/8 h	1200	210	1375	24	[60]
L-PBF, HIP at 1180°C/3 h/150 MPa/ H at 1065°C/1 h, AC, DA 760°C/10 h, 650°C/8 h, AC	1065-1045	188-190	1376-1272	15-19	[76]
WQ: water quenched	H: homogenisation		ST: solution treatment		
DA: double-aged	AC: air cooled		FC: furnace cooled		

2.4 Functionally graded microstructures in additive manufacturing

2.4.1 Functionally graded materials

A functionally graded material (FGM) is defined by the variation of a structural element or material ingredient gradually or discontinuously over the volume of a component [108]. The idea behind the concept is to incorporate incompatible functions into the volume of one part [108]. Some examples would be the integration of good high temperature mechanical performance on one end with a good fatigue crack propagation resistance on the other end of a component [108]. Functional grading can be applied through changes in composition, geometrical structure or microstructure [109,110].

Microstructure plays a critical role in determining the material behaviour – typically for commercial applications microstructural characteristics are homogenised to remove any non-uniformity. By treating the microstructure as a variable which varies depending on the positional requirements, varying material characteristics can be integrated into one component to achieve an optimal performance tailored for a specific application or environment. The preferred grain growth direction for metals is parallel to the direction of maximum heat flow which is affected by a number of features as a component is being built [91]. Due to the ability in AM to alter the deposition parameters in-situ during a build, the heat flow direction, thermal gradient and solidification conditions can be altered thus altering the microstructure being generated in-situ. For instance, Popovich et al. [111] successfully managed to generate a functionally graded component having an outer shell made of small equiaxed grains and an inner core made out of long elongated and highly textured grains as shown in Figure 2.11. The aim behind this design was to ensure that during thermomechanical fatigue testing, any cracks moving in towards the core would be deflected from the continuous movement along the transverse plane in the component [111]. Modifying the microstructure can be done through different approaches in AM as will be subsequently discussed. The use of modelling techniques to predict the microstructure being formed and move through the columnar-to-equiaxed transition (CET) has been often combined with experimental methods to generate functionally graded or microstructurally optimised components. A significant amount of work has been done modelling the CET in AM but falls out of the scope of this review; some notable works can be found elsewhere [112–121].

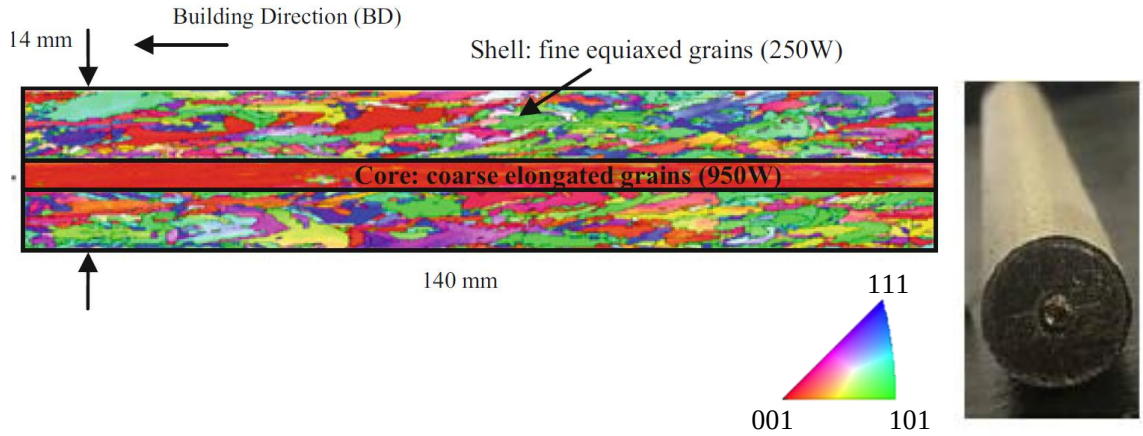


Figure 2.11: Functionally graded microstructure [111].

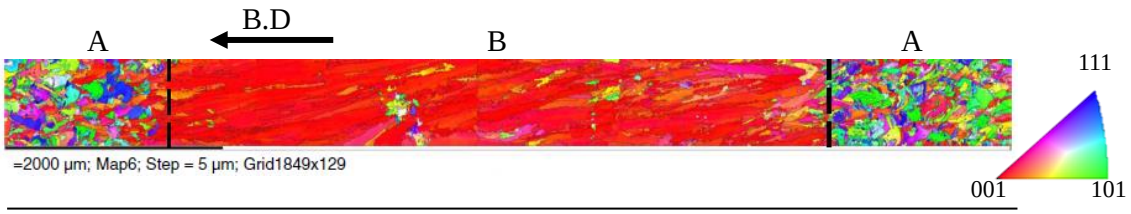
2.4.2 Modifying microstructure through heat input parameters

A straightforward method of determining the processing parameter window is through the application of the energy density equations. The energy density (E.D) for L-PBF is used to measure the heat input of a set of processing parameters. A number of metrics exist such as the line E.D, area E.D and volumetric E.D. For L-PBF as the layer thickness is usually kept constant, the area E.D can be used which is given by Equation 2.3:

$$Energy\ Density\ (J/mm^2) = \frac{Power\ (W)}{Scan\ speed\ (mm\ s^{-1}) \times scan\ spacing\ (mm)} \qquad \textit{Equation 2.3}$$

This takes into account the effect of power, speed and hatch spacing and can be used to define a viable processing window for a material where full consolidation will occur [122]. For nickel superalloys the minimum area E.D above which full consolidation is expected is 1.7 J/mm^2 [122]. This does not mean that the energy density can be increased infinitely – very high energy densities will result in turbulence and the evaporation of low melting point alloying elements resulting in the entrapment of this metal vapour in the melt leading to very large pores. From a microstructural perspective changes in E.D have been associated with an increased hardness in IN718 [52,91]. This is attributed to some form of γ' precipitation due to the numerous heating and cooling cycles applied during the build [52,91]. Increasing the energy density has also been related to an increase in cell spacing denoting a decreased cooling rate [36].

While the E.D is helpful to define a general processing window, not all the factors which affect a build's microstructure are considered [123]. Other important factors affecting the microstructure such as the scan strategy, island size and island overlap for island scan strategies, focus diameter and angle of the laser beam, defocusing of the energy source, part positioning and changes in baseplate temperature are not taken into account [124]. The effect of some of these factors has been derived elsewhere and work is ongoing to account for the full effect of such factors within melt pool models [123,125–127]. Furthermore, varying the individual parameters such as power, scan speed and scan spacing while keeping a constant E.D will still affect the melt pool width and depth resulting in variations in the microstructure and therefore the mechanical properties [114,124,128]. In fact, Popovich et al. [129] demonstrate this concept very clearly as shown in Figure 2.12. The same E.D is used to manufacture an entire component but through variations in both power, scanning speed, hatch spacing and layer spacing together with beam profile, the microstructures obtained are drastically different, varying from a columnar to a "quasi-equiaxed" structure [129]. Similar principles (same E.D, different combinations of speed and scan spacing) have been applied to EB-PBF by Körner et al. [130] with significant changes in microstructure obtained. Thus, the effect of power, speed and hatch spacing on the microstructure will be separately considered.



Zone	Laser Power (W)	Scanning speed (mm/s)	Hatch spacing (mm)	Layer thickness (µm)	Beam diameter (µm)	Beam distribution
A	250	700	0.12	50	80	Gaussian
B	950	320	0.5	100	100	Flat top

Figure 2.12: Graded IN718 with an inverse pole figure map for a columnar microstructure with large coarse grains alternating together with a fine-grained matrix. Laser beam heat input parameters used for each microstructure are shown [129].

2.4.2.1 Effect of speed

A slower scanning speed in AM is associated with grains being more aligned with the building direction and with wider columnar growth and a coarser microstructure overall [49,91,93].

Scanning speed was used by both Körner et al. [130] and Helmer et al. [93] in EB-PBF to obtain different solidification structures, where at low speeds a columnar structure was observed while at high speeds the structure became equiaxed. It was also reported that with changing scanning speed, the grain aspect ratio changed going from aspect ratios of 7 at low speed to 1.3 at high speed [93]. Similar findings were reported for welding, with higher welding speeds resulting in more equiaxed grains at the centre of the weld pool even with increasing beam current and voltage together with reductions in grain size as shown in Figure 2.13 (a) [49]. Increases in scanning speed directly increase the solidification interface velocity and higher speeds are associated with a higher solidification rate as shown in Figure 2.13 (b) which in turn affects the cooling rate and the *G/R* ratio and therefore also the microstructure morphology [50]. Higher speeds have also been associated with the generation of higher residual thermal strains in the material from the relatively higher solidification rate, which can lead to thermal cracking in both dendritic and inter-dendritic regions [52].

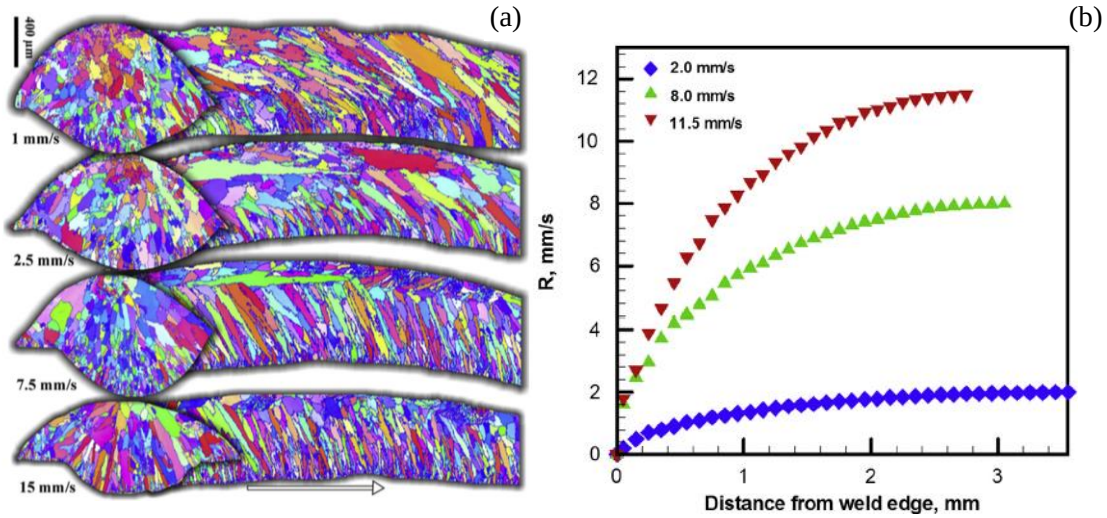


Figure 2.13: (a) The change in grain size and alignment with different welding speeds [49] together with (b) the predicted solidification rate at different welding speeds [50].

2.4.2.2 Effect of hatch spacing

The effect of hatch spacing on the microstructure is still not fully understood with conflicting effects being observed by different authors. Increasing the hatch spacing i.e. reducing the level of overlap between melt tracks, was associated with a reduction in grain size and a change in preferred

orientation for TiAl-TiB_2 specimens using L-PBF [131]. The lower degree of overlap resulted in a reduced heat input, which in turn accelerated the solidification of the material and reduced the thermal gradient and therefore the *G/R* ratio [131]. Conversely, other authors have observed that at lower hatch spacing values (i.e. more overlap between scans), the cooling rate was higher (temperatures are higher and therefore heat is lost at a faster rate) resulting in a finer cellular structure compared to scans made using a less overlap between scans [132]. Altering the hatch spacing can result in increases in porosity or solidification cracking if the amount of overlap is not enough or is too high [133–135].

2.4.2.3 Effect of power

High laser powers are associated with the formation of larger and more aligned grain morphologies with low laser power generating a mix of coarse and fine grains in DED while significant increases in power generate a highly textured angled coarse microstructure as shown for inverse pole figure (IPF) maps in Figure 2.14 (a) [14,136]. The increase in laser power also exacerbates the segregation present in IN718 with use of higher laser power in DED associated with larger undesirable eutectic phases such as Laves phases and NbC films [53,136]. A higher degree of segregation is also visible in L-PBF in conjunction with higher laser power and coarse columnar growth [52,76,129]. A higher laser power in DED was observed to result in a lower tensile strength overall attributed to the larger overall grain size [137]. Analogous effects were observed with increases in electron beam current in EB-PBF, where when the current was increased, the equiaxed zones got much smaller and columnar growth was more prevalent [135].

This is in direct contradiction with modelling results presented by Kurz et al. [46] shown in Figure 2.14 (b) and Bontha et al. [138], where it can be seen that from a theoretical perspective with increasing power, the structure should tend to be more equiaxed as the thermal gradient according to modelling data at higher powers should be lower therefore promoting equiaxed growth. Conversely Li et al. [45] measure a distinct increase in thermal gradient with an increase in laser power for simulations of Al melted using L-PBF. This discrepancy could be due to the fact that melt pool behaviour tends to be very complex and local fluctuations in thermal gradient due to Marangoni flow and nucleation density due to the injected powder will affect the solidification mechanics [136]. It can also be observed that the grains depicted in the low power condition in

Figure 2.14 (a) are still to an extent columnar in the layer and that due to the high misalignment with the B.D and changes in between layers of the heat source orientation, a "quasi-equiaxed" structure is obtained with grain orientation changing but the structure still undergoing epitaxial growth rather than true homogenous nucleation. Variation in grain alignment is still present in between layers, but within layers the grains are mostly aligned with the heat source movement at low powers. At high power, even though a bidirectional movement strategy is used, the grain tilt to the build direction remains constant. At higher power, the melt pool depth will increase which in turn increases remelting leading to more and easier epitaxial growth between layers which may result in alternate layers growing from a secondary preferred growth direction (e.g. [010] instead of [001]) to keep the same grain tilt direction.

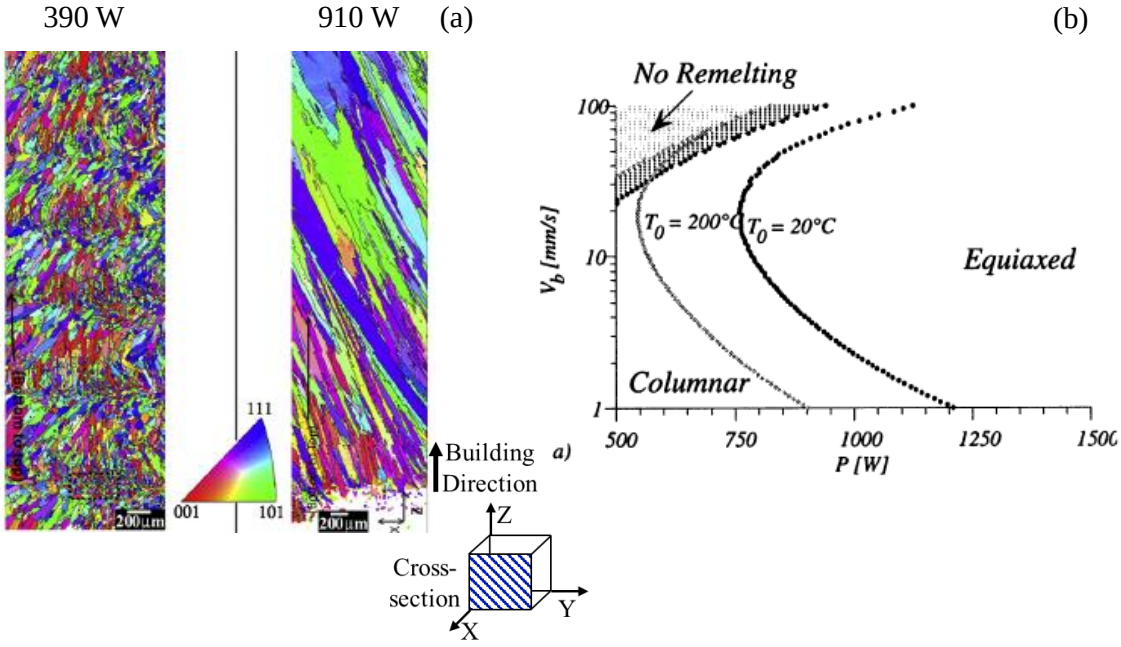


Figure 2.14: (a) IPF maps for microstructures obtained at different power levels in DED using a speed of 200 mm/s [136], together with (b) a process map for the dominant microstructure with different laser speeds and powers for CMSX-4 [116].

2.4.2.4 Effect of heat input parameters on melt pool

Melt-pool shape is one of the major aspects affecting the microstructure morphology. Deep melt-pools result in a high degree of remelting and therefore easy columnar epitaxial growth. An excessively deep melt-pool can lead to the entrapment of vapour from low melting point elements

forming keyhole porosity. Overly shallow melt-pools on the other hand are mainly associated with a reduced degree of remelting thus resulting in a reduction of the epitaxial growth occurring but can result in lack of consolidation defects. The angle of the solidification front will determine the angle of the 〈001〉 with respect to the B.D as the tilt angle of the unit cell will vary with the tilt angle of the normal to the solidification front [139]. This is important as it will affect which predominant crystallographic planes are parallel to the loading direction. The melt-pool dimensions and solidification front orientation will be dependent on the laser heat input parameters used during the process.

Guo et al. [128] reported that with increasing power and decreasing laser speed, melt pools tend to increase in depth and to elongate along the laser scan direction as there is more time available for heat transfer to occur along the transverse direction. Melt pool width and depth were found to increase linearly with increasing power during L-PBF by Metelkova et al. [140]. Li et al. [45] also observed an increase in melt pool width, depth and length for increases in laser power through simulation; with width and depth increasing linearly with increases in power and melt pool length increasing non-linearly with power. The increase in width with power was experimentally confirmed by Shah et al. [137] and by Sadowski et al. [141] with increasingly high powers leading to a larger line width with the effect being more predominant at lower speeds [141]. This dependence of microstructure morphology on the melt pool shape has been used by Gokcekaya et al. [142] to alter the texture generated during L-PBF through alterations of heat input parameters.

Laser beam speed has a significant impact on melt pool width – melt pools formed using the same power density have similar depths of penetration but those with a longer interaction time are wider. Wider melt pools were found by Keshavarzkermani et al. [16] to contain angled grains converging to the top middle of the melt pool rather than grains aligned with the build direction. At high speeds (i.e. short interaction time) variations in power are not very effective in increasing the melt pool depth [141,143]. An increase in power becomes more effective at increasing melt pool depth as the interaction time increases (i.e. reduced speed) as shown in Figure 2.15 (a and b) [141,143]. Metelkova et al. [140] observed that changes in laser traversing speed resulted in a non-linear variation in the melt pool width and depth with an exponential relationship between speed and melt pool depth, and very large changes especially at low laser movement speed. Li et al. [45] observed

through simulation that with increases in laser speed, the melt pool shape overall got smaller i.e. width, length and depth decreased significantly. Excessively high speeds are linked with melt pool instability with irregularly spaced laser tracks and open porosity at the surface and potential splashing of liquid metal out of the melt pool [27,45].

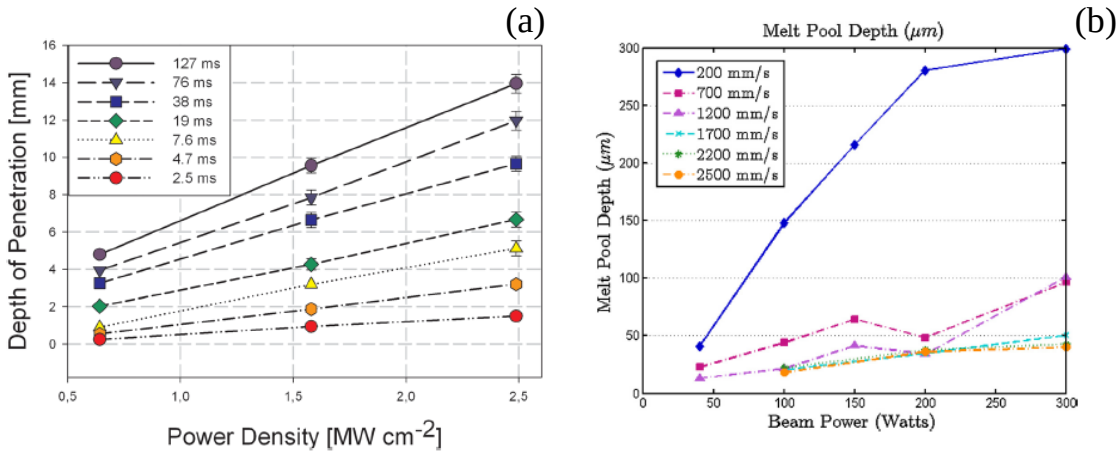


Figure 2.15: Showing (a) the dependence of penetration depth on power density and interaction time and (b) dependence of melt pool depth on beam power and scanning speed [141,143].

A combination of electron beam current and electron beam speed was used by Dehoff et al. [144] in EB-PBF to locally change the melt pool shape and thus control the microstructure obtained as shown in Figure 2.16 (a to c). Both the speed and current are varied simultaneously to change the weld-pool XY profile from a point mode shown in Figure 2.16 (a) associated with a more randomly oriented grain growth to a line profile shown in Figure 2.16 (b) is associated with columnar growth in EB-PBF. In the line profile, the melt pool solidification front would be flatter, thus the normal to the solidification front would be along the build direction resulting in columnar growth [14]. For a point mode, the solidification front is expected to be more curved resulting in grains at different angular orientations forming in the melt pool [14]. These two modes were used to locally control the grain orientation to the B.D as shown in Figure 2.16 (c). Conversely, Körner et al. [130], observed that for melt pool XZ profiles with a pronounced spherical border, a highly aligned columnar grain morphology formed and melt pools which were very wide and nearly flat resulted in equiaxed morphologies. The electron beam speed for the nearly flat melt pools was much higher than the speed used for melt pools with a spherical border [130]. This would induce a much higher

solidification rate leading to lower G/R values and thus tending towards a more equiaxed structure [42,49,54,55]. Conversely, for the work done by Dehoff et al. [144] the grain growth is likely still epitaxial but due to the changes in solidification front curvature the grain alignment to the build direction is changed resulting in a more random orientation along the B.D. A similarly inspired approach by Sofinowski et al. [145] uses the angle of the laser beam to the surface to induce changes in the microstructure by altering the solidification front angle in L-PBF. This provides very effective results in changing the grain orientation along the transverse direction but still resulting in epitaxial growth. However, along the build direction, there is still a prevalent orientation; in this case ⟨011⟩ due to the grain tilt induced. Changing the laser angle to the surface might be challenging on a conventionally designed system, in addition to the fact that the approach is only effective in changing the preferred orientation in the transverse direction rather than the building direction.

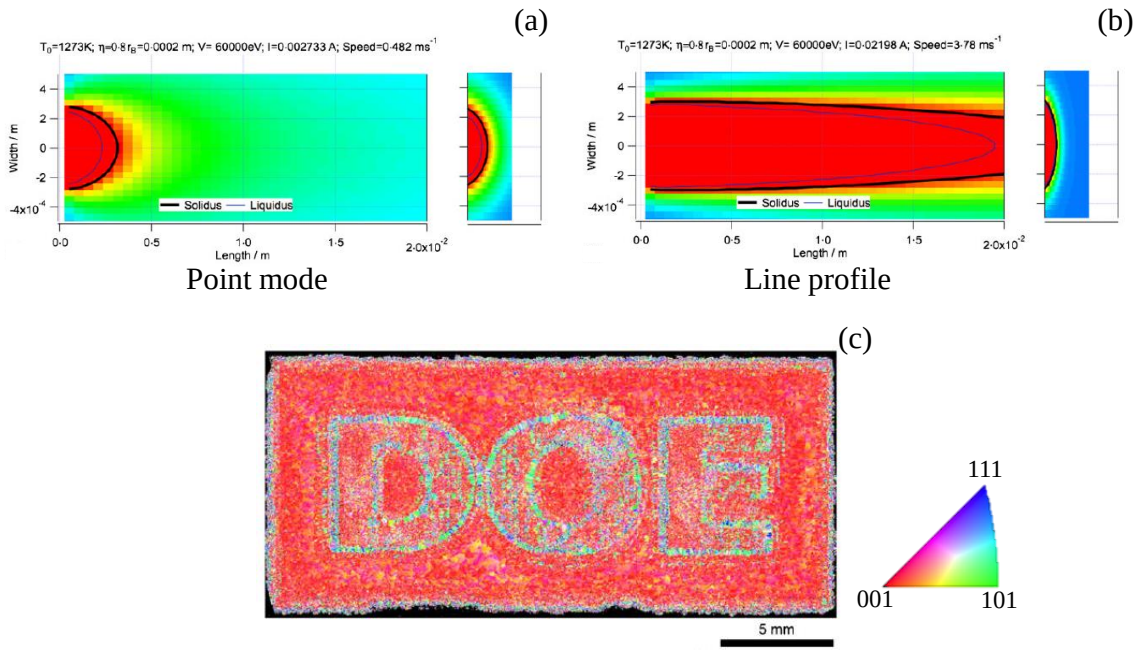


Figure 2.16: Showing changes in melt-pool profile with different electron beam parameters for (a) a point profile and (b) a line profile together with (c) the effect of different melt pool profiles on texture through IPF mapping [144].

2.4.3 Modifying the microstructure through scanning strategies

Altering heat input parameters can negatively affect the quality and density of components made. Certain materials may be susceptible to forming unexpected intermetallic phases or precipitates at high laser energy inputs due the increased amounts of elemental segregation [91]. Porosity may also increase due to insufficient consolidation or evaporation of low melting point elements.

The heat source movement will impact the amount of heat transmitted to the component and the dissipation of the thermal energy collected by the component being built – affecting both the thermal gradient and solidification rate indirectly. Scanning rasters can also be repeated over already solidified areas to refine the solidification microstructure by remelting, inducing recrystallisation or apply in-situ heat treatments [51,146–149]. Selected typical scanning strategies for PBF and the nomenclature used in this work are shown in Figure 2.17. Some work has been done on using the laser scanning strategy to modify the microstructure and will be reviewed here. The existing work, however, has mostly been focused on rudimentary scanning strategies such as the unidirectional and bidirectional strategies. Other more complex strategies such as island scanning strategies are popular as they have been reported to result in a reduction of residual stresses [150–152] but the effect of altering the parameters of these strategies themselves have not yet been fully investigated.

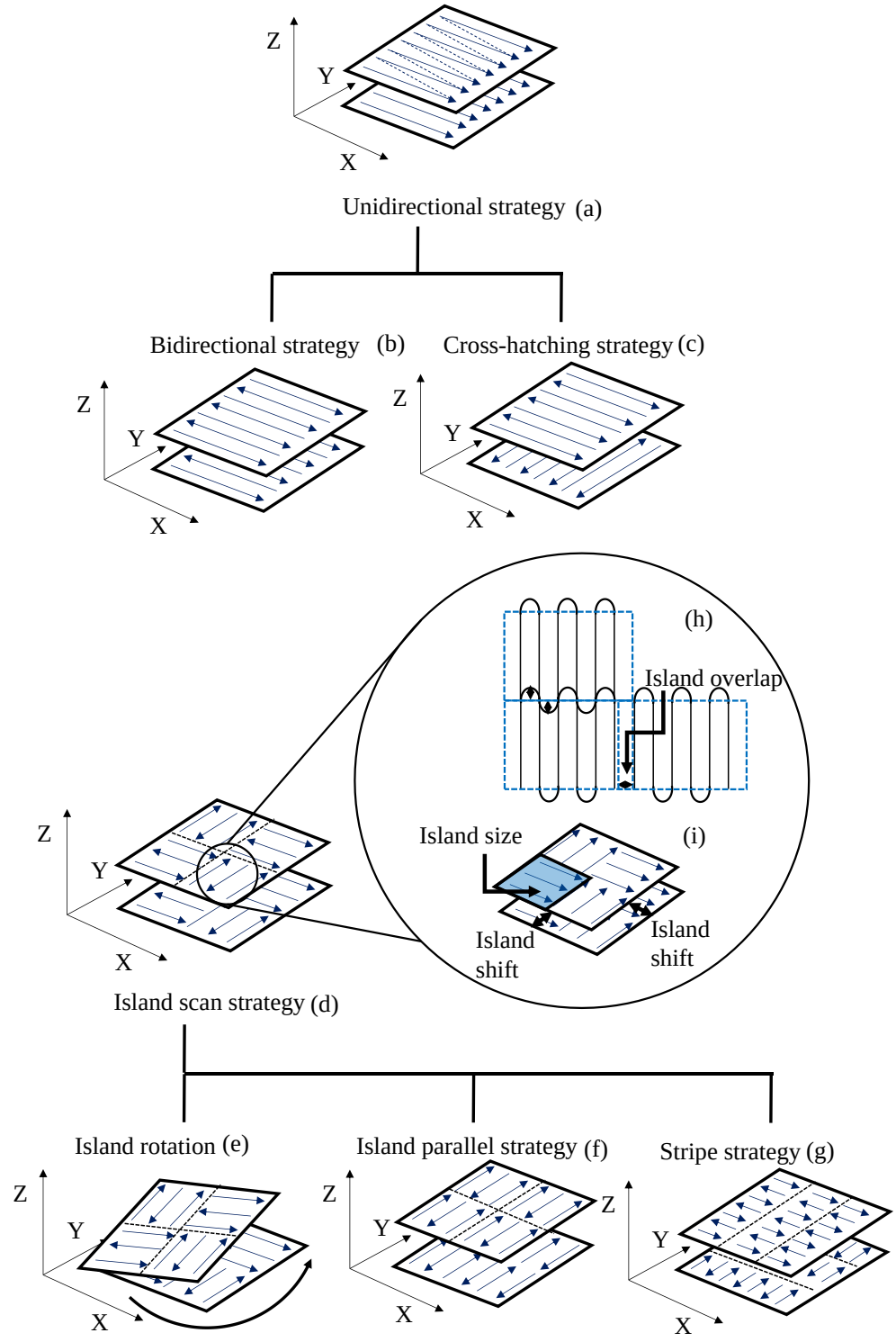


Figure 2.17: Schematic representation of some of the (a-g) common scanning strategies in L-PBF together with (h-i) parameters which can be varied within the strategies themselves.

The laser movement affects the tilt direction of the resulting grain structure [51]. Thijs et al. [91] and Dovgyy et al. [92] both observed that the grain growth direction follows the laser motion, where if the laser is moved from left to right the grains will also be slanted from left to right. This effect was also observed by Geiger et al. [153] and Kunze et al. [154] for IN738LC with the 〈001〉 crystal directions being aligned with the B.D and in most cases with the laser scanning direction. Altering laser motion from unidirectional to bidirectional motion in DED was used to change the angle between the build direction and preferential growth axis from 30° to alternating at ±45° with a distinct zig-zagging feature of grains as shown in Figure 2.18 (a to d) [136,155]. The alteration in angle is unexpected as one would expect a variation of ±30°. A distinct change in grain size can also be observed in Figure 2.18 (a and b) with the grain size increasing when moving from a unidirectional strategy to a bidirectional strategy [155]. Grain size has also been observed to increase when moving between a unidirectional strategy without rotation between layers towards a unidirectional strategy with a 90° rotation between layers [156]. This contradicts results obtained through modelling where Li et al. [157] found that between these two strategies there was not a significant change in grain size but rather that grain shape changed varying from a crescent shape for the unidirectional strategy to a linear shape observed for the bidirectional strategy. In their work there was no indication of whether the preferential alignment along the build direction was affected although the differences in shape would indicate that the heat flow direction along the B.D changes.

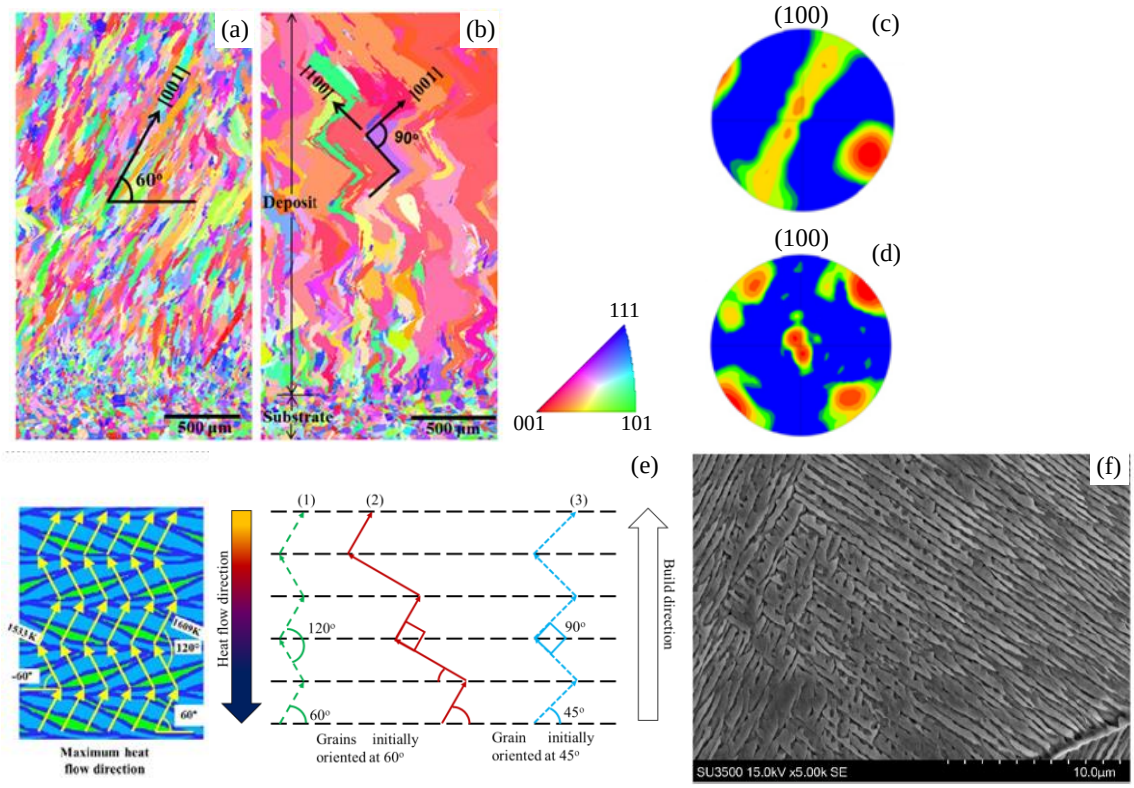


Figure 2.18: Change in grain tilt angle to the B.D showing IPF maps for (a) unidirectional and (b) bidirectional strategies with respective pole figures in (c) and (d), with (e) showing a schematic representation of the potential dendrite growth directions applicable for a bidirectional strategy and (f) a cell colony with growth from secondary arms at 45° [56,155,158].

For the unidirectional strategy, the heat flow is perpendicular to the trailing edge of the melt pool resulting in a 30° tilt to the build direction [158]. For the bidirectional strategy, the rotation between each successive raster will result in a change in favoured angle from 30° to -30°, and if growth were to follow the ±30° approach, the angle between the dendrite trunks of the neighbouring layers would be 120° with the B.D as shown in pattern 1 in Figure 2.18 (e) which can not occur in an experimental scenario [158]. If the primary dendrites of neighbouring layers were to grow perpendicularly to each other with the primary dendrites of the second layer growing preferentially off the secondary dendrites of the previous layer, the dendrite growth direction will deviate about 30° from the maximum heat flow direction as shown in pattern (2) in Figure 2.18 (e) [158]. This large misalignment makes such a growth scenario unfeasible [158]. Solidification pattern 3 in Figure 2.18 (e) has a similar mechanism as pattern 2 (with primary dendrites growing perpendicularly to primary dendrites in the previous layer along the easy growth directions), but the dendrite growth

is aligned to around 45° with the build direction which means that there is a deviation of only about 15° with the heat flow direction in all the layers resulting in a much smaller overall average deviation from the heat flow direction [158].

Wang et al. [56] observe something similar where the cellular growth is observed to be in general aligned at ±45° to the building direction. Cells may alternate orientation by 90° from their previous growth direction by making use of the secondary 〈001〉 growth direction [56,85]. In fact, growth of adjacent cells on the slightly developed secondary arms of a neighbouring cell colony were observed and are marked in Figure 2.18 (f) confirming work by Wei et al. [158]. The growth in this direction is theorised to occur as it conserves the crystal orientation between the neighbouring melt pools thus needing a lower nucleation energy for epitaxial growth [159]. Thus, the change in growth angle required between one melt pool and the other is minimised [159]. This deviation in solidification angle from the build direction can result in the development of a [011] fibre texture along the B.D rather than the typical [001] texture due to the alignment of the [001] at 45° to the B.D [56,159].

The movement of grains with the motion of the laser can be harnessed to easily modify the texture in the transverse direction (XY plane). Dovgyy et al. [92] documented that for the fcc CoCrFeMnNi alloy with the cross-hatch strategy, the rotation between layers accounted for cross-wise layer epitaxial growth resulting in two fibre textures at right angles to each other forming a cube texture. Thijs et al. [48] observed that a 90° rotation in scanning strategy between layers results in the formation of a cube texture as opposed to a fibre texture which forms when no rotation is present. Geiger et al. [153] observed that a bidirectional strategy with a 90° angle rotation between layers (cross-hatch) resulted in a cube texture where all the 〈001〉 crystal axes were aligned with the x, y and z axes of the laser motion. Rotating the entire strategy by 45° degrees, resulted in a 45° rotation of the texture [153]. Using a 67° rotation between layers reduced the layer overlap and imparted randomisation in the XY plane; the 〈001〉 directions were no longer oriented along the x and y directions of the build, while there was still an alignment of the [001] with B.D (Figure 2.19 (a)) [153]. This contradicted observations by Zhou et al. [134], where a consecutive 67° rotation of a bidirectional strategy results in an overall “quasi random” crystallographic texture with grains still appearing elongated somewhat but not aligned along any particular direction as shown in Figure

2.19 (b). However, it is difficult to determine whether the IPF orientation shown is with the B.D or not.

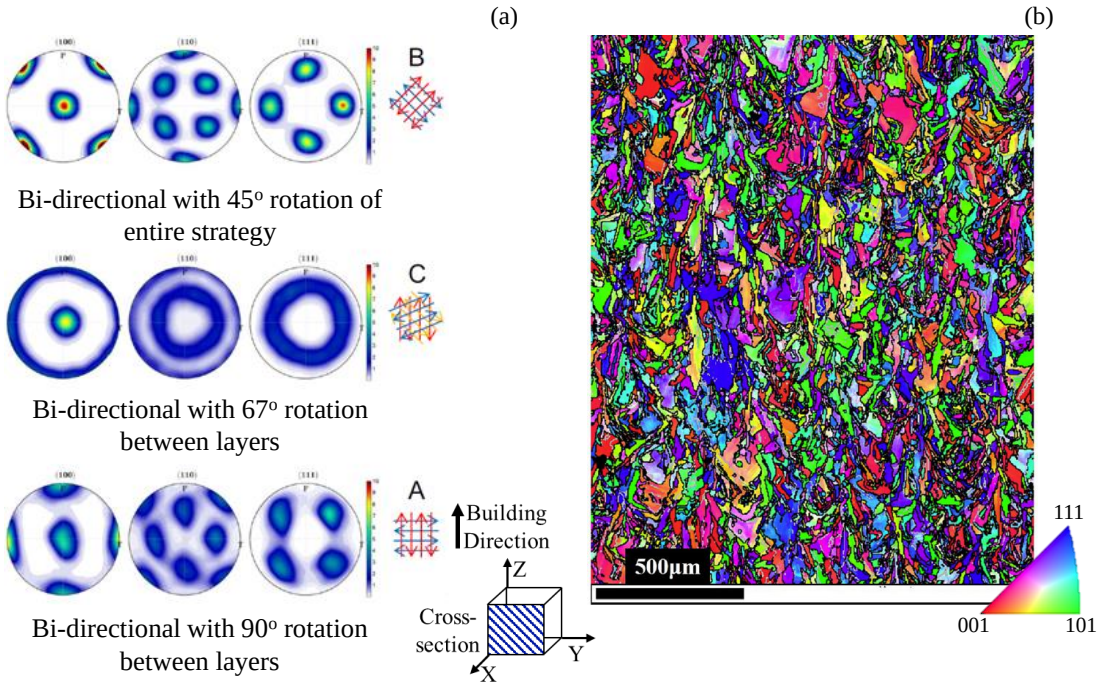


Figure 2.19: (a) Change in texture characteristics with different scanning strategies for IN738LC [153] together with (b) "quasi-random" crystal structure observed with a 67° rotation in a bidirectional strategy for CoCrMo [134].

Dovgyy et al. [92] compared the effect of a 67° rotation between a bidirectional raster strategy shown in Figure 2.20 (a and b) to an island strategy shown in Figure 2.20 (c and d). While a columnar grain morphology was obtained for both conditions, the crystallographic direction aligned with the build direction was the [011] rather than the usually observed [001] direction. The growth direction of the grains and cells for a single track are shown in Figure 2.20 (e) which showed that several grains had a distinct angle of about 45° to the build direction except the grains in the middle of the track which were aligned with the build direction. Normally the grains aligned with the build direction would continue to grow preferentially and dominate the structure, but due to the rotations applied between layers and between the islands themselves, the heat flow direction was continuously changed [56,158]. Thus the grain growth angle to the heat flow direction is minimised by a 45° angle to the B.D as with the case for a bidirectional strategy [56,158]. The use of an island strategy in combination with the consecutive 67° rotation further increased the intensity of the [011] orientation as shown in Figure 2.20 (c and d) due to side branching of cells between boundaries of

adjoining islands [92]. In this way the grains extended through several islands and the grain size along the XY plane also increased.

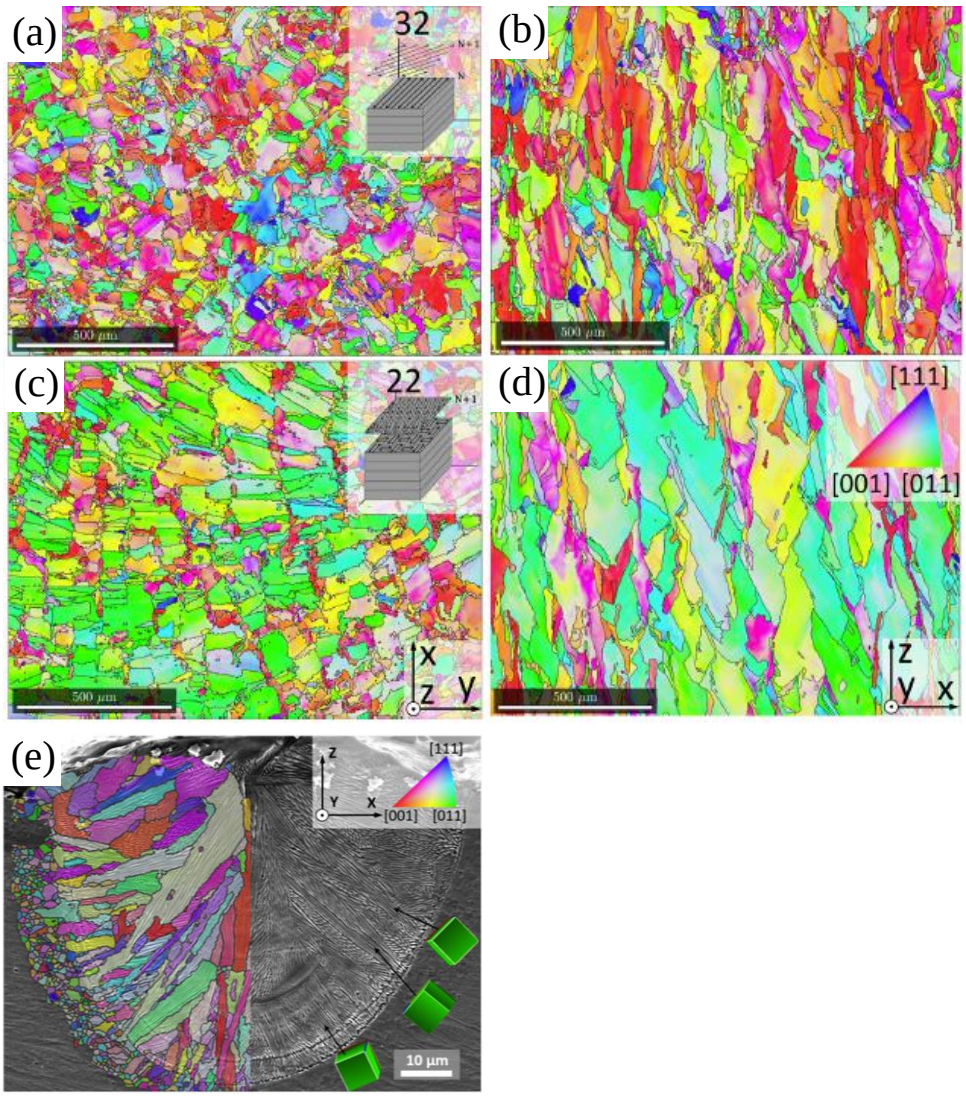


Figure 2.20: IPF maps for scanning strategies with a 67° layer rotation for a bidirectional strategy with XY and XZ cross-sections for (a) and (b) respectively together with an island strategy with XY and XZ cross-sections for (c) and (d) respectively. (e) shows the cross-section for a single track melt pool. [92].

The island strategy was found by Carter et al. [160] to result in a large-scale pattern of coarse columnar grains interspersed with a fine grained region where the island overlap occurred for CM247LC, as shown in Figure 2.21 (a). The elongated columnar grains were found to have a high multiples of uniform distribution (M.U.D) value and a rotated [001] cube texture (parallel to the laser vector rotation) as shown in Figure 2.21 (b) while the fine-grained regions had a lower cube

texture intensity with a deviation in angle from the B.D as shown in Figure 2.21 (c). Due to the relatively small island size and the relatively high laser scanning speed (between 400 mm/s to 2000 mm/s), the melt pool length could have been considerable where the trailing edges of the melt pool were close to the edges of the island [160]. The trailing edges of the melt pool are curved which would in turn result in a change in direction of the heat flow leading to a significant change in orientation of the last solidifying grains [14,160]. Conversely in work by Dovgyy et al. [92], this large scale patterning was not visible for island chessboard strategies potentially due to the rotation being applied.

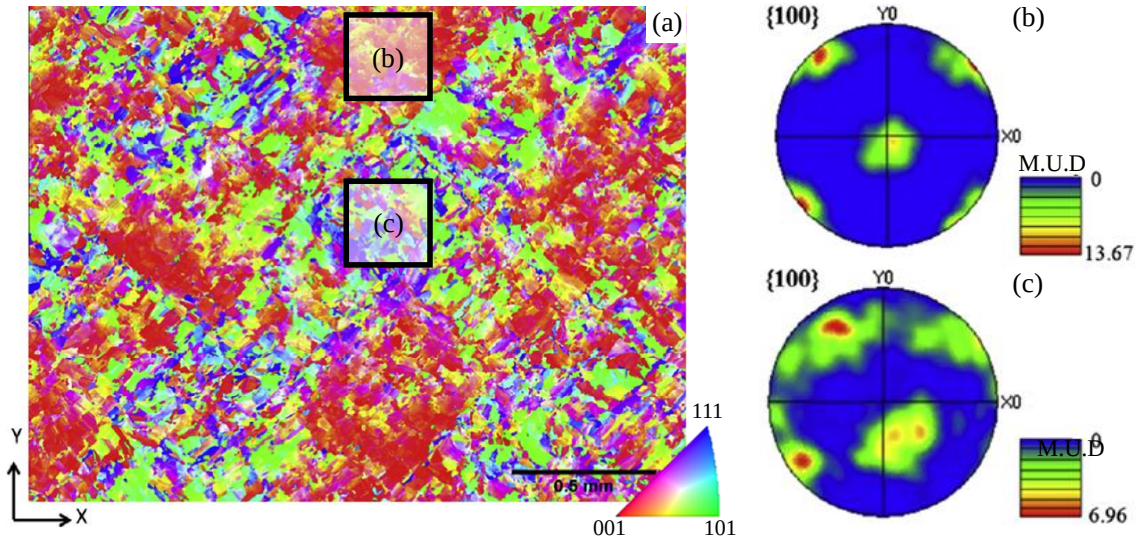


Figure 2.21: (a) IPF map with respect to the build direction of an XY cross-section showing the effect of the chessboard island scan pattern on large scale grain arrangement together with pole figures for (b) strongly textured area and (c) less defined textured zone [160].

An attempt at using scanning strategy in EB-PBF to control microstructure has been made by Dehoff et al. [161] – although the strategies and beam parameters used in their work are not available for analysis. Through some variation of parameters, different grain structures were obtained going from grains very aligned to the B.D towards a disorganised structure with a random alignment as shown in Figure 2.22 (a to f) [161]. The authors indicated that a transverse grain alignment was obtained with one of the strategies used i.e. grains having their axis aligned with the XY scanning plane rather than the B.D [161]. This is attributed to the solidification front moving at the same speed of the electron beam which seems unlikely with the high speeds considered in EB-

PBF [42,51,52]. However, as specific parameter combinations were not provided it is not clear why this behaviour occurred. It could be that the grain morphology has a curvature as has been observed by other authors when changing scanning strategy [157]. Helmer et al. [93] using EB-PBF applied the scanning strategies to alter the solidification direction and were able to switch from columnar to "quasi-equiaxed" growth through a periodic layer rotation. Spot scanning rather than rastering has also been used in EB-PBF to vary the microstructure for instance moving from a columnar structure towards an equiaxed structure or changing the grain size of the columnar grains obtained [162,163]. Alternating the raster order through the use of varying line order numbers has also been used in EB-PBF by Karimi et al. [135] to promote the formation of equiaxed grains, although this also resulted in the formation of a large amount of solidification cracks and shrinkage porosity in the specimens generated. Lei et al. [164] use a combination of line offset variation and heat input parameter variation to modify the microstructure in EB-PBF.

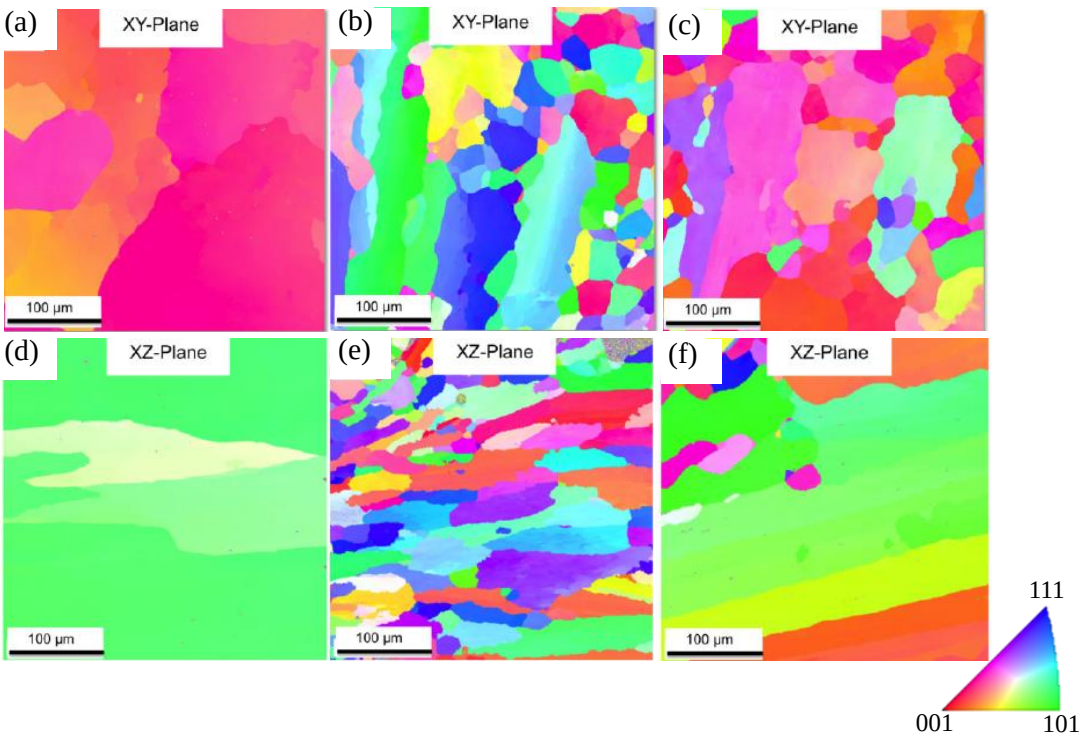


Figure 2.22: Effect of various scanning strategies used in EB-PBF to obtain (a and d) a columnar microstructure, (b and e) an equiaxed microstructure and (c and f) a transversely oriented microstructure [161].

Hatch length has been reported to affect the microstructure generated, with shorter hatch lengths being associated with the formation of aligned columnar structures as shown in Figure 2.23 (b and d) and longer hatch lengths associated with the increased formation of stray grains as shown in Figure 2.23 (a and c) [54]. Small stray grains could develop in between columnar grains attributed to regions of low temperature gradients, rapid cooling and fast solidification rate [54,115,116]. This also translates to a difference in mechanical performance with specimens produced using a long hatch length having a better mechanical performance compared to a short hatch length as shown in Figure 2.23 (e) [165]. The reason behind this large difference in microstructure was not further investigated – though the shorter hatch lengths would be expected to heat up the material more as the laser takes less time to arrive at the adjacent melt pool [166,167]. This would lead to a slower solidification rate and therefore larger sub-grain structures, coarser grains and overall worse mechanical properties [168]. Shorter hatch lengths require less time for the beam to return to the initial position, thus consecutive melt pools can overlap producing a wider melt pool – this has been observed through simulation [167] and is thought to lead to a higher amount of epitaxial growth and therefore a higher degree of alignment. For a longer hatch length, the heat transfer will be quicker and the previous melt pool has already solidified producing smaller melt pools and thus a reduction of epitaxy in the microstructure [167,169]. A higher degree of heating will also reduce the solidification rate, promoting further epitaxial columnar growth [14,53]. Furthermore, the underlying material has a longer time to cool with a longer hatch length, which in turn results in subsequent hatches not melting through as many previously solidified layers reducing the epitaxial growth [54]. This would result in overall finer microstructural and sub-microstructural features and a lower texture intensity [54]. Supporting results were also obtained by Wang et al. [56] this time due to thinner cross-sections resulting in a shorter hatch length and thus a reduced cooling rate and a higher degree of alignment with the B.D. Using the island strategy parameters such as the island size could be modified to leverage such an approach and applied to potentially modify the mechanical properties.

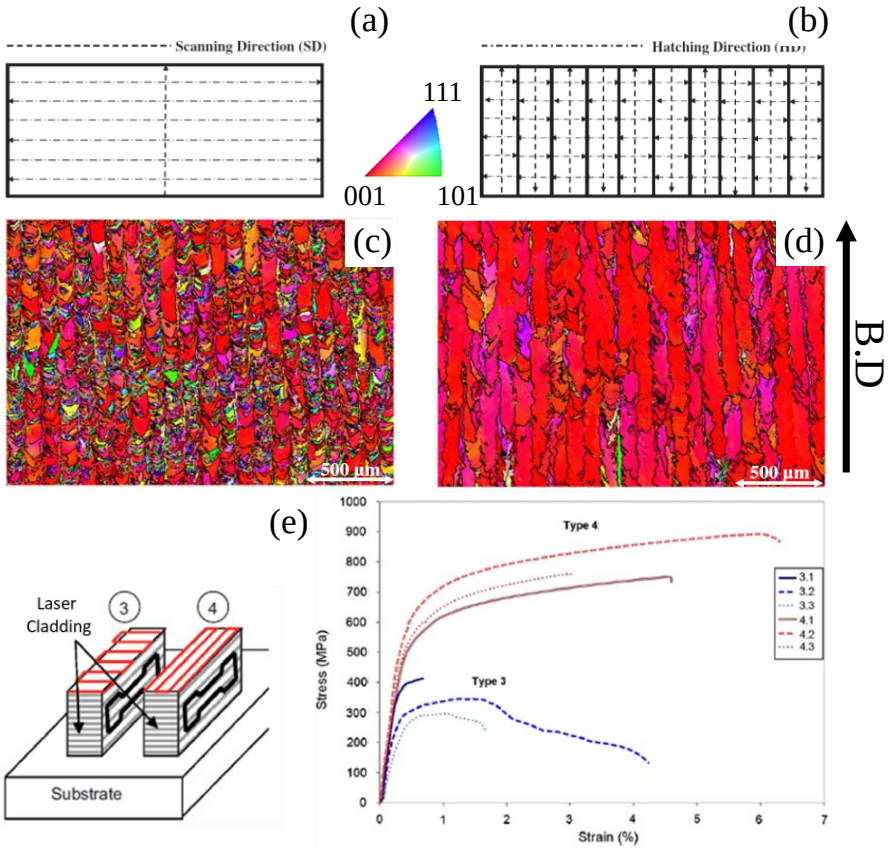


Figure 2.23: Strategies for (a) long hatch length and (b) short hatch length together with (a and d) respective IPF maps and (e) mechanical behaviour for different hatch lengths and (f) simulated behaviour with increasing hatch length [54,165].

Evidence of the effect of scanning strategy on the grain size distribution of IN718 is shown in Figure 2.24 (a). Liu et al. [156] compare a unidirectional strategy to a cross-hatch strategy. Both the strategies used resulted in the formation of a bimodal grain size distribution but the difference between the smallest and largest grain size peaks was larger for the unidirectional strategy. Samples having larger grains generated using the unidirectional strategy were found to fail through transgranular crack propagation while for unidirectional cross-hatching strategies where the grain size was nominally smaller, the samples exhibited mixed mode failure [156]. The difference in failure modes was attributed to larger grains being more favourable as sites for crack propagation due to weaker strain hardening effects in such grains. This resulted in uneven deformation leading to differing dislocation densities in adjacent grains of differing size which in turn results in different levels of stress hardening [156]. The mechanical properties obtained through the two strategies also

differ in σ_Y and ductility as shown in Figure 2.24 (b) [156].

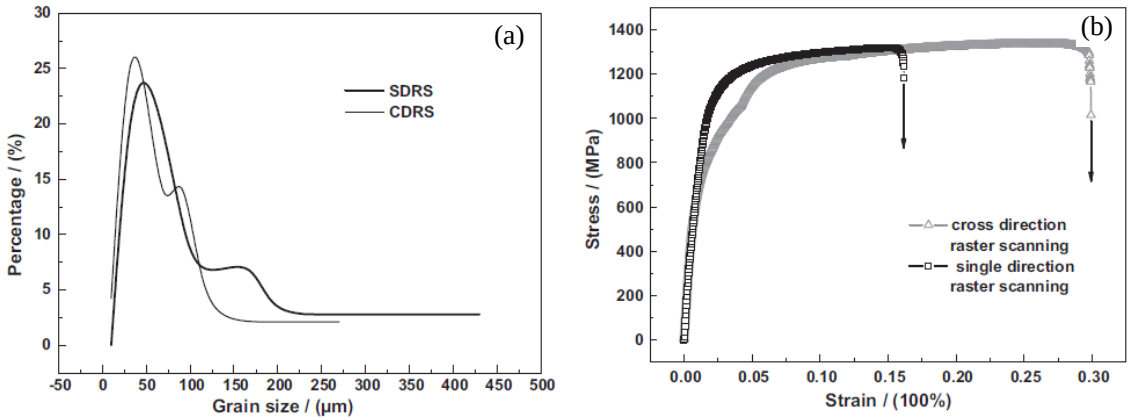


Figure 2.24: (a) grain size distribution for single direction rastering (SDRS, unidirectional) and cross-directional rastering (CDRS, unidirectional cross-hatch) and (b) stress-strain curves for the different conditions [156].

The modification of the texture and grain size along the build direction for L-PBF is still challenging, with many works reporting a change in the transverse direction rather than along the build direction. Modification of laser heat input parameters can also be used to directly induce equiaxed or "quasi-equiaxed growth", but this can result in decreases in the specimen quality. Modification of the scanning strategy itself has been used to alter the preferred orientation along the XY plane, however altering the preferred orientation along the B.D for L-PBF is still difficult. Changes to relatively disruptive scan strategies such as the island scanning strategy have not yet been fully investigated and thus provide an interesting avenue of further research in microstructural control through altering the scanning strategy rather than the laser heat input parameters.

2.4.4 Effect of heating and cooling the substrate

The thermal gradient is affected by the rate of heat flow through the baseplate. Thus, by heating or cooling the baseplate a change in temperature gradient will occur which in turn affects the solidification conditions. Chen et al. [102] show that improving the cooling of the baseplate significantly increases the columnar alignment of the grains as the result of an increase in thermal gradient. One must consider that the parts fabricated here are relatively low in build height – being only about 5 mm high and this could affect the magnitude of such an effect as with increasing build height the efficiency of the baseplate in acting as a heat sink would be reduced especially with the

low thermal conductivity characteristic of IN718. In fact, in the study by Chen et al. [102] comparing water cooling with air cooling of the baseplate, a very swift reduction in cooling rate was observed as the build height increased beyond the initial layers in direct contact with the substrate. The effect of baseplate temperature has been quantified in processing maps for columnar to equiaxed transitions by Gäumann et al. [116]. To promote columnar growth, the temperature of the baseplate needs to remain as low as possible while baseplate heating will promote true equiaxed growth through a reduction in temperature gradient [116]. Baseplate heating can also be used to perform in-situ heat treatments during a building process although factors such as oxygen pick up, cracking and powder sintering need to be considered [170].

2.5 Microstructural modification to change mechanical properties

From an application perspective, part positioning on the plate should be optimized to obtain the highest part density for the given build envelope – part orientation in the build chamber has been associated with a 160% change in the energy consumed during the process [171]. Nickel alloys are known to have anisotropic properties along different crystallographic directions [14]. Ni is inherently anisotropic with a Zener anisotropy between 2.43 and 2.48 [172,173]. For Ni single crystals, the elastic moduli along the three principal crystallographic directions are 119.8 GPa along the [100], 200.8 GPa along the [011] and 259.2 GPa along the [111] [172,174]. For different orientations aligned with the build direction the Schmid factor will also vary depending on orientation [175]. This shows that with predominant {011} and {111} alignments to the loading direction, the σ_Y and Young's modulus (E) should increase.

The difference in mechanical properties in practice with different predominant textures is shown in Table 2.3. The ⟨001⟩ direction has a lower strength compared to other predominant crystal directions. The ductility tends to be better for predominant ⟨001⟩ alignment as can be seen in Table 2.3. On the other hand, the ⟨001⟩ alignment is more favourable for creep performance in nickel based alloys favouring a very long stress rupture life [154,176,177]. At elevated temperatures, creep for Ni-based alloys is controlled by {111}⟨112⟩ slip and will not strain harden, while ⟨001⟩ and ⟨111⟩ oriented crystals favour multiple slip systems which results in a long rupture life due to strain hardening [177]. Crystals oriented for single slip systems will undergo a large rotation before an

additional slip system becomes active which means a large amount of primary creep with high strain occurs with a short rupture life [177]. Grains oriented for multiple slip will need little or no rotation before the onset of secondary creep resulting in low creep amounts and a long creep life [177].

Thus part orientation, specifically with respect to the expected loading direction and B.D in conjunction with the anisotropy exhibited by IN718, will also affect the mechanical properties of the component [7,11,51,60,178,179]. Being able to modify the preferential texture along the loading direction is beneficial as it allows efficient component placement on substrates in addition to optimal mechanical properties. Furthermore, being able to tailor the mechanical properties allows components to be optimised for applications by considering the microstructure of the parts themselves as a variable. Limited studies have investigated the tailoring of the microstructure to obtain graded components with mechanical property grading using L-PBF.

Table 2.3: Mechanical properties for IN718 with different predominant texture orientations.

Crystal orientation to load direction	Heat treatment	Test temperature (°C)	0.2% Yield strength (MPa)	Young's modulus (GPa)	UTS (MPa)	Elongation to failure (%)	Ref.
Random, forged	ST 954°C/1 h, PHT 718°C/8 h & 621°C/total 18 h	650	1000	-	1500	20	[78]
Vertical	HIP 1160°C/ 3 h, ST 955°C/1 h, PHT 720°C/8 h & 620°C/total 18 h	RT	1034	-	1365	28.7	[179]
Horizontal			1055	-	1407	21.6	
〈001〉	As-built	RT	531	113	866	21	[129]
Quasi-random			668	173	1011	22	
Horizontal	As-built	RT	807	-	1051	22	[178]
			816		1085	19	[23]
Vertical			675	-	957	28	[178]
			737		1010	20.6	[23]

RC: recrystallisation treatment ST: solution treatment PHT: precipitation hardening treatment RT: room temperature

Körner et al. [130] observed that for highly columnar IN718 microstructures manufactured using EB-PBF, there was a distinct difference between the transverse (XY) and longitudinal (XZ) direction in Young's modulus. Columnar structures were found to have a Young's modulus of

127 GPa parallel to the building direction and 159 GPa perpendicular to the build direction [130]. Samples which had an equiaxed morphology were found to have a Young's modulus of 183 to 189 GPa in both directions [130]. Conversely the yield strength and ultimate tensile strength (UTS) for the highly aligned columnar samples was found to be higher than that obtained for equiaxed samples as can be seen in Figure 2.25 which is unexpected [130]. This might indicate that there might be other factors at play such as porosity – in fact, samples with an equiaxed morphology were found to have a lower life to failure compared to their columnar counterparts coupled with a large variability in ductility which may be associated with premature failure through the inclusion of defects such as porosity or segregation.

The idea of microstructural optimisation was successfully applied by Im et al. [176] in IN718 to generate a highly oriented 〈001〉 crystal structure similar to a directionally solidified microstructure using EB-PBF. This was done through the application of a high temperature applied to the powder bed and differences to the focus offset [176]. The idea behind this work was to obtain an improved creep performance. In fact at temperatures of 650ºC and loads of 700 MPa, the structure was successfully engineered to provide a higher creep performance to a comparably wrought product [176]. In L-PBF, Wang et al. [180], compare the use of an island strategy to a strip strategy, which did not result in highly significant difference in the mechanical properties along the build direction or the transverse direction for the different strategies used.

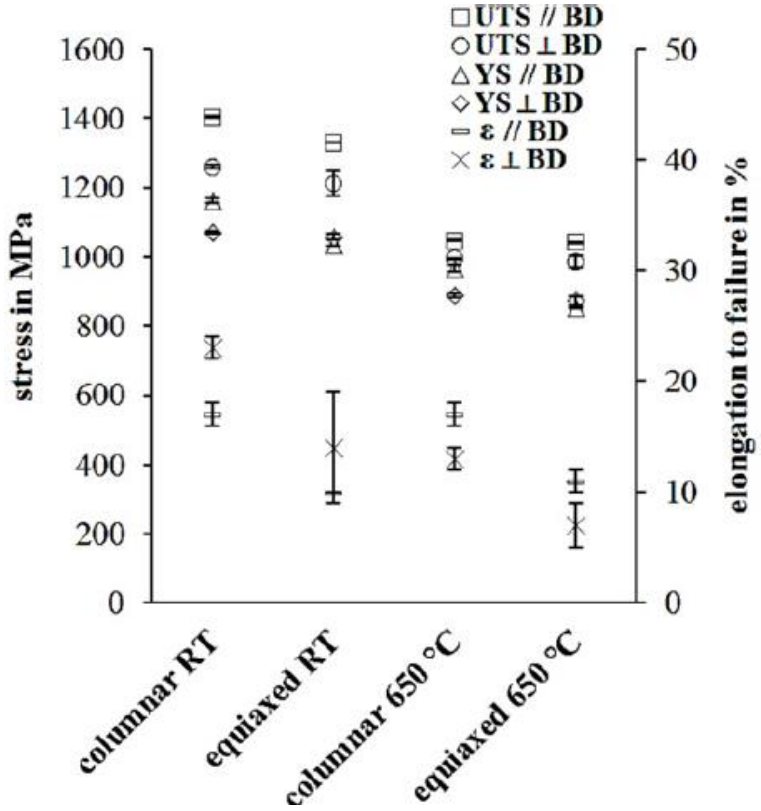


Figure 2.25: Mechanical properties for IN718 test samples made using EB-PBF [130].

2.6 Effect of microstructural modification on oxidation performance

Oxidation is one of the more important factors affecting the high temperature performance of materials. Through oxidation, a loss of cross-sectional area occurs together with the formation of intergranular oxide compounds. Oxidation has been shown to reduce the time to crack initiation, and accelerate the fatigue crack growth rates thus reducing the fatigue life [181–183].

According to Giggins and Petit [184], IN718 is a group II type of Ni-Cr-Al based alloy; it consists of ~19 wt.% of Cr which forms an adherent and protective (up to 1000 ºC) Cr_2O_3 scale at the alloy surface together with discontinuous Al_2O_3 particles underneath upon exposure to elevated temperature oxidising conditions [185]. TiO_2 intergranular phases have also been observed for oxidation of IN718 by Calandri et al. [79]. The formation sequence of the Cr, Al and finally Ti oxides has been explained in detail elsewhere [79]. Beneath the chromia layer, a Cr depleted zone has also been reported [186]. Enrichment of the near-surface area in Nb has been documented for

IN718 oxidised between 850 to 950°C [79,187]. Conversely, Li et al. [186] document the formation of NbO rather than Nb below the chromia layer. This Nb enriched layer is thought to reduce the oxidation rate [188]. The minor alloying elements such as Al, Ti, Nb and Mn will affect the oxide formation kinetics deviating the oxidation kinetics from those observed for pure Cr_2O_3 formation [189].

Grain boundaries act as short-circuit diffusion pathways for oxygen in Cr and grain boundary diffusion is faster than lattice diffusion [190]. Below 1000°C, grain boundary diffusion is also more prevalent as grain boundaries have an irregular atomic arrangement and will act as preferred oxidation sites [186]. This does however depend on the chemical composition and the rate at which the protective Cr oxide is established [191]. Thus, the amount of grain boundaries impinging the surface should influence the oxidation rate. The initial oxidation rates for Ni based superalloys have been observed to also be affected by the orientation of the surface grains [186,192–194]. Wang et al. [192] performed studies on Haynes 230, oxidised at 900°C for 5 minutes in air to determine the initial oxidation behaviour on different grain orientations as is shown in Figure 2.26.

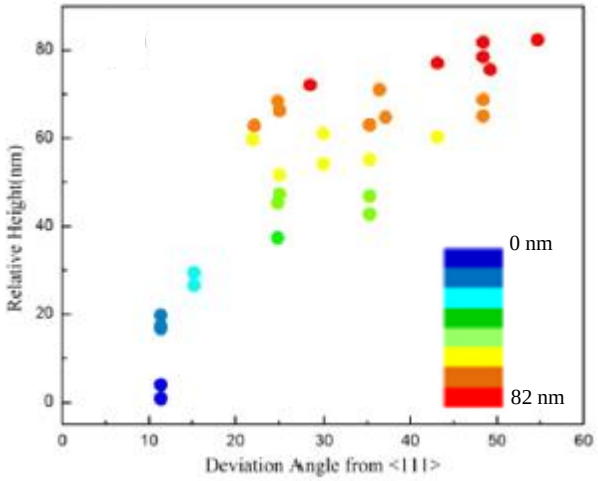


Figure 2.26: Dependence of the relative oxide height on the deviation of the grain from the ⟨111⟩ [192].

They found that the oxidation rates are dependent on the deviation of the grain orientation from the ⟨111⟩ direction, with grains which are aligned to the ⟨111⟩ direction being more oxidation resistant [192]. Conversely, they found that grains presenting the (001) face to the oxidation surface tended to have a higher overall oxide thickness indicating that the oxidation rate for these orientations was

in fact more compared to grains with a (111) orientation to the normal direction as is shown in Figure 2.26. Grains with a (011) orientation perpendicular to the normal direction (ND) were found to have an intermediate oxidation rate [192]. This effect is thought to be related to the planar density of the different orientations; resulting in the formation of large oxide grains which reduce the oxidation rate or small oxide grains which yield a high number of oxide grain boundaries accelerating the oxidation rate [192]. This has also been observed for Cr and Ni, where the oxide thickness was found to be different between individual grains with a different orientation [190,193]. The authors suggest that this behaviour is due to the formation of high diffusivity grain boundaries on the film forming on the (001) faces and low diffusivity, coherent twin grain boundaries forming on the (111) faces [193].

2.7 Summary and research gaps

The microstructure generated during L-PBF is dependent on several complex physical factors related to the melt pool behaviour and its interaction with the heat source, the heat flow behaviour, thermal gradient, and solidification rate. The interaction of these factors is known to influence the final microstructure. Due to the layer-by-layer building methodology prevalent in L-PBF, modifying these factors and their interaction with the forming microstructure is possible and is an area of growing research. The consensus after L-PBF is to homogenise the microstructure through heat treatment or HIP to obtain uniform mechanical behaviour. If the microstructure itself is seen as a variable tool to be controlled through processing parameters, then L-PBF can be actively harnessed to move away from using heat treatments for homogenisation towards the generation of functionally graded microstructures and components with structures which are fully optimised for their application. Graded microstructures for IN718 are already used in aeroengine disc applications using a complex heat treatment to optimise properties for the inner and outer section of the disc. Microstructural control using L-PBF can be a valuable tool in further simplifying the production and optimisation of such components.

Most of the successful work on microstructural control is focused on the effect of varying heat processing parameters to vary the thermal gradient and solidification rate directly. While this is possible, in L-PBF porosity is still an issue using such means and parameters need to be carefully considered to avoid overheating, incomplete consolidation, segregation and solidification cracking during the process. In processes such as EB-PBF, varying the microstructure is relatively easy since the heat input parameters can be varied on a spatial basis, and this has been successfully applied to transition from columnar to equiaxed growth. However, in L-PBF this remains a challenge, especially when modifying the texture and grain size along the build direction. The high thermal gradients, partly due to the high scanning speeds and the heat sink effect of the unheated base plate coupled with the small melt pools make transitioning to equiaxed growth very difficult. The following research gaps are evident from existing literature:

i. The laser scanning path is a viable option to influence the heat flow direction and the solidification rate. While a limited amount of work has been done on established common laser movement strategies such as unidirectional strategies, bidirectional and

cross-hatching strategies, the effect of the island strategy commonly used in L-PBF is still not well investigated with several possible subtle alterations which can be made to such a strategy to further modify the heat flow and thus affect the microstructure. This strategy offers a more evenly distributed heat input and thus can reduce the effect of variations in cross-sectional area over a component.

ii. Furthermore, while varying the microstructure along the transverse direction has been achieved to a certain extent, the grains generated are still aligned with the build direction and tailoring the crystal structure in this direction is still a challenge.

iii. The studies observed in L-PBF still exhibited epitaxial growth, but due to the application of different strategies or heat input parameters, the tilt angle of the grains to the build direction was modified rather than the formation of true equiaxed growth. This is not a transition from columnar to equiaxed growth. The use of a heated baseplate has been shown to be effective for DED in inducing the CET but has not been yet extensively investigated for L-PBF of IN718.

iv. The feasibility of successfully using scanning strategies or baseplate heating in modifying the mechanical properties along the B.D still needs to be further investigated. Furthermore, the effect of modifying the scanning parameters in one specimen to create microstructurally graded components with varying mechanical properties has also not been fully determined.

v. Although some work has been done on the effect of texture on the initial oxidation behaviour, it has not yet been elucidated whether these variations in initial oxide thickness can be effectively used to reduce the oxidation rate over long term exposures at elevated temperatures. An investigation into the effect of combined texture and grain size modifications on the oxidation performance is also lacking. The high variability of the microstructures produced by the process may also affect the oxidation performance which has not been investigated in detail.

CHAPTER 3. Experimental procedure

3.1 Materials

Two batches of argon gas atomised IN718 spherical powder supplied by LPW Technology LTD (UK) were used for this work. The first batch (BATCH1) was used for metallographic samples discussed in Chapter 4 and Chapter 5 while the second batch (BATCH2) was used for manufacturing mechanical test coupons and oxidation testing coupons discussed in Chapter 6 and Chapter 7. BATCH1 had been used for 5 previous builds prior to this study. The powder size distributions were measured as per ASTM B822-17 [195] using laser diffraction methods for both batches and are shown in Figure 3.1 and Table 3.1. A difference in size distribution was observed and thus the powder spreading characteristics were further analysed. The powder from BATCH1 had a higher size distribution likely due to the increase in melt bonding and spatter formation contributing to an increase in powder size. Both powder batches were sieved prior to use.

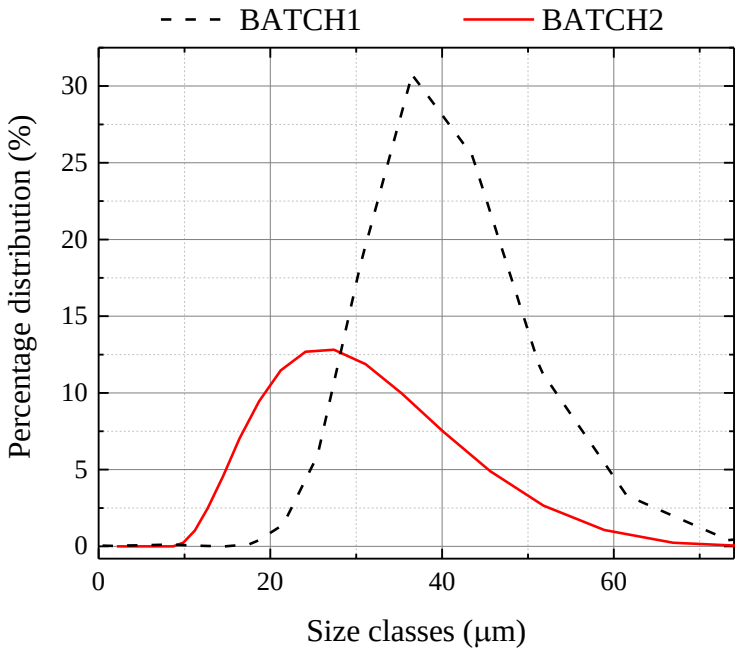


Figure 3.1: Powder size distribution for BATCH1 and BATCH2.

Table 3.1: Powder size values for BATCH1 and BATCH2.

	D10 (µm)	D50 (µm)	D90 (µm)
BATCH1	25.93	35.02	48.34
BATCH2	16.9	27.7	44.7

3.1.1 Powder chemical composition

The chemical composition of the powder was analysed externally at AMG Advanced Metallurgical Group, using inert gas fusion and combustion analysis for quantification of N, O, C and S (accuracy of 0.001 wt.%) and inductively coupled plasma - optical emission spectrometry (ICP-OES) for quantification of the remaining elements with an accuracy of 0.005 wt.%. The quantities for these elements were found to be within the limits established by ASTM B637-18 [104].

3.1.2 Powder flowability

To remove any agglomerates resulting from previous processing, the powders were sieved using 63 µm sieves prior to analysis and use. The bulk density and tap density of the powder were measured using a calibrated 25 cm^3 copper container and a calibrated PCE BT2000 mass balance. For the tap density vibrations were applied to the filled container, and the container was refilled as needed until no more powder could be added after which its mass was measured. Hall flow measurements were applied to both batches. Hall flow measurements were carried out as per B213-17 [196] using the static flow method. The average bulk density of the powder was found to be 4.34 to 4.57 ± 0.01 gcm^{-3} and tap density of 4.9 to 5.02 ± 0.02 gcm^{-3}. The Hausner ratio for the powder used here was of between 1.12 and 1.10 indicating an excellent flowability. An average Hall flow rate of 12 s to 15.3s /50g was obtained.

As BATCH1 had already been used previously, its powder flowability was measured using the Schulze Shear ring test method in addition to the Hall flow test method to ensure sufficient spreading for building purposes. Shear ring measurements were performed on the Schulze Shear Ring RST-XS tester using a normal pre-shear load of 6000 Pa, 3 shear levels and 1 measurement per shear level. The flowability of the powder was quantitatively characterised using the FFC ratio

of the consolidation stress to the unconfined yield strength. Typically, an FFC above 10 indicates that the powder is free flowing. The FFC ratios obtained here were of 48 and 49 indicating free flow. During building no issues were observed with powder flow with either of the powder batches used.

3.1.3 Powder shape considerations

The powder structure and morphology was analysed using a Hitachi TM3000 scanning electron microscope (SEM) in back scattered electron (BSE) mode. Energy dispersive spectroscopy (EDS) analysis using an accelerating voltage of 15 kV was employed to investigate areas of interest. The powder used here was largely spherical with a dendritic microstructure from the fast-cooling rate during gas atomisation.

3.1.4 Base plate

The base plate used for majority of this work was a stainless-steel sand blasted plate. For work where single layer melt pools were investigated a nickel alloy (IN625) baseplate was used to obtain similar thermal properties to the IN718 powder to ensure that the single layer melt pools were a good representation of what would occur with melt pools on a Ni based component.

3.2 Concept Laser M2 Powder Bed Fusion

3.2.1 Machine Set-up

An M2 Concept laser-powder bed fusion system was used as shown in Figure 3.2 (a). All processing was done under a continuous feed of argon (< 0.1% O_2). The system consisted of a handling chamber where the build set-up and powder sieving operations were carried out and a processing chamber where the build itself was processed. The set-up was equipped with a 400 W Yb-fibre laser in continuous wave mode with a maximum build envelope of 250 mm by 250 mm by 280 mm (L×W×H). The maximum scanning speed of the set-up was 7000 mm/s with a laser spot size of ~60 μm having a gaussian irradiance profile. A flexible rubber recoater blade was used for powder spreading operations during the build. This was changed prior to each build to ensure proper powder spreading.

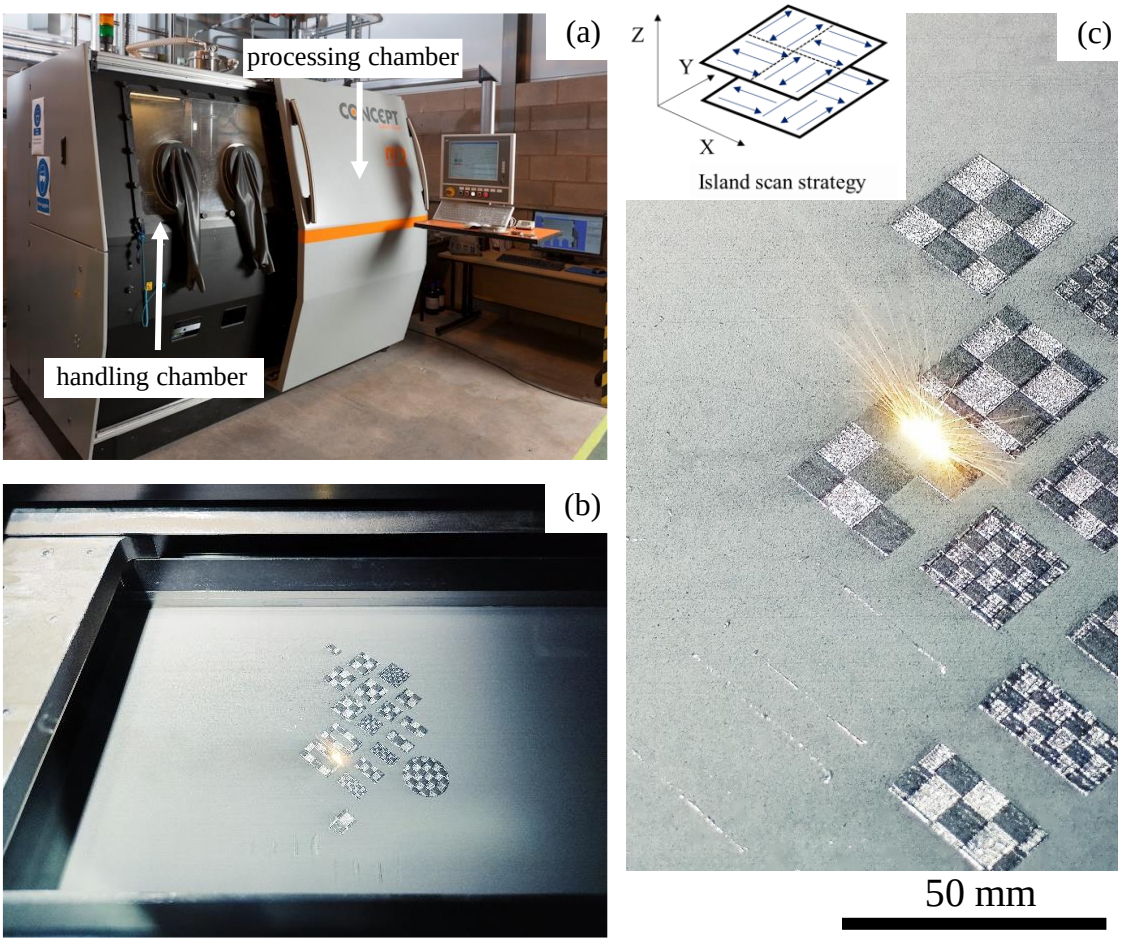


Figure 3.2: (a) M2 concept laser set-up and (b and c) laser in operation during a build, together with a schematic of the associated island scanning strategy shown in the insert in (c).

A representative image of a typical build process is shown in Figure 3.2 (b and c). During set-up, a substrate is affixed to the build platform and the powder is sieved through a 63 µm sieve into the powder reservoir in the handling chamber at the left side of the machine shown in Figure 3.2 (a). Once the set-up is complete, the entire assembly is moved to the processing chamber on the right-hand side of the machine shown in Figure 3.2 (a). A sliced 3D computer aided design file (known as a stereolithography file) containing the part files is then uploaded to the machine and the processing parameters such as the laser heat input parameters and details related to the scanning strategies are entered. The build process has been previously described in Chapter 1.2.

3.2.2 Specimen manufacture details

The "default" scanning strategy unique to the Concept laser system is defined as an island scanning strategy depicted in Figure 2.17 (d). This is the strategy is shown for the layers visible in Figure 3.2 (b and c). It consists of partitioning the surface area into 5 mm islands (where the island size is shown in Figure 2.17 (i)) which are then scanned in a random order within the layer with a 90^{o} rotation between neighbouring islands. There is a 1 mm by 1 mm shift in both the X and Y directions for the island pattern between consecutive layers (shown in Figure 2.17 (i)). The edges of the islands overlap by a default value of 0.0225 mm (as depicted in Figure 2.17 (h)). The subsequent layer is then rescanned in a similar random order. A layer thickness of 30 μm was used throughout this work. A control condition optimised for a high density was defined using this "default" island scanning strategy manufactured using a power of 263 W, scan speed of 1500 mm/s and a scan overlap of 0.075 mm for comparison purposes. This condition is defined as the CONTROL condition in this work and known to produce high density components from previous work [197] .

A study on the effect of the laser parameters and scanning parameters on the grain size and texture was performed by manufacturing monolithic cubes (10×10×10 mm) through two sets of experiments.

To investigate the effect of laser heat input parameters, the scanning strategy used was the "default" island scanning strategy. For these specimens the power, scanning speed and hatch spacing were then varied as shown in Table 3.2 to encompass a range of energy densities. The experimental parametric matrix was defined by using a design of experiment approach with a five-level central composite rotatable response surface design to encompass the range of energy densities selected. The energy density was calculated using Equation 2.3. The energy density values used here represent the area energy density since the layer thickness was kept constant throughout all experiments. Not all parameter combinations obtained specimens which were fully dense. Only parameter combinations yielding an Archimedes density of higher than 8.19 g/cm^3 were considered for further investigation and characterisation.

Table 3.2: Overview of laser heat input parameters.

Power (W)	Speed (mm/s)	Hatch spacing (mm)	Energy Density (Jmm^{-2})
50	1000	0.075	0.67
150	2000	0.06	1.25
150	1000	0.03	5.00
188	2500	0.075	1.00
188	1500	0.045	2.78
188	1500	0.075	1.67
188	2500	0.045	1.67
225	2000	0.09	1.25
225	2000	0.03	3.75
225	3000	0.06	1.25
225	1000	0.06	3.75
225	2000	0.06	1.88
263	2500	0.045	2.33
263	2500	0.075	1.40
263	1500	0.075	2.33
263	1500	0.045	3.89
300	2000	0.06	2.50
300	1000	0.06	5.00
240	1200	0.063	3.17
263	1500	0.060	2.92
263	1500	0.075	2.33

To investigate the effect of scanning parameters, the power, scan speed and hatch spacing were kept constant at 263 W, 1500 mm/s and 0.075 mm respectively, selected for optimised density (>99.5%). The scanning strategies were then varied, and an overview of the various modified scanning parameters is listed in Table 3.3. In the test conditions, individual scanning parameters such as the scanning strategy itself, the island overlap, the island size and the island shift were varied individually from the CONTROL condition. Single layers were produced using scanning parameters denoted as CONTROL, ISLAND3 and ISLAND7 in Table 3.3 to facilitate the measurement of the melt pool dimensions. These consisted of 1 scan track, 1 island and a single layer of 90 mm by 20 mm.

Proof of concept scaled-down, hollow turbine blades with dual grading were made using the ISLAND3 strategy outlined in Table 3.3 to manufacture the blade section of the components. The

fir root tree section was made using the SHIFT4 condition. This component is referred to as the GRADEDBLADE in this work.

Specimens for oxidation testing were made in the form of cuboids having dimensions of 20 mm by 20 mm by 10 mm which were then sliced in 1 mm slices along the XZ plane using wire electrical discharge machining (WEDM) to investigate the effect of texture and grain size on the oxidation behaviour. These samples were then sliced in 1 mm thick slices. The conditions investigated for the oxidation work were the CONTROL, ISLAND3 and ISLAND7 conditions outlined in Table 3.3.

Table 3.3: Scanning strategy parameters. Each condition had one scanning parameter varied from the control condition as highlighted.

	Scanning Strategy				
Test condition designation	Laser scan path	Island size (mm)	Island shift in X and Y directions between each layer (mm)	Island overlap (mm)	Testing
CONTROL	Island	5	1	0.0225	Tensile, Oxidation
SHIFT4	Island	5	**4**	0.0225	Tensile
ISLAND7	Island	**7**	1	0.0225	Tensile, Oxidation
ISLAND3	Island	**3**	1	0.0225	Tensile, Oxidation
OVERLAP2.5	Island	5	1	**0.05625**	No
BiD	**Bidirectional**	None	None	None	No
CH	**Cross-hatched**	None	None	None	No
IP	**Island parallel**	5	1	0.0225	No

Tensile specimens were then manufactured as square bars having dimensions of 15 mm by 15 mm by 90 mm as shown in Figure 3.3 (a). The bars were manufactured in such a way that the build direction was parallel to the tensile axis. The modification of the alignment along the build direction depends on the heat flow direction and for L-PBF due to the prevalent effect of the build plate acting as a heat sink this is difficult to modify. Modifying the orientation in the XY direction is easier as

the crystals tend to be oriented according to the scanning direction. Thus, it was deemed of more scientific value to investigate the more challenging aspect along the B.D rather than how the grains align with laser movement. A typical build plate set up for mechanical test coupons used in this work is shown in Figure 3.3 (b). Monolithic conditions optimised for high texture/large grain size and low texture/smaller grain size were made using parameters as outlined in Table 3.3.

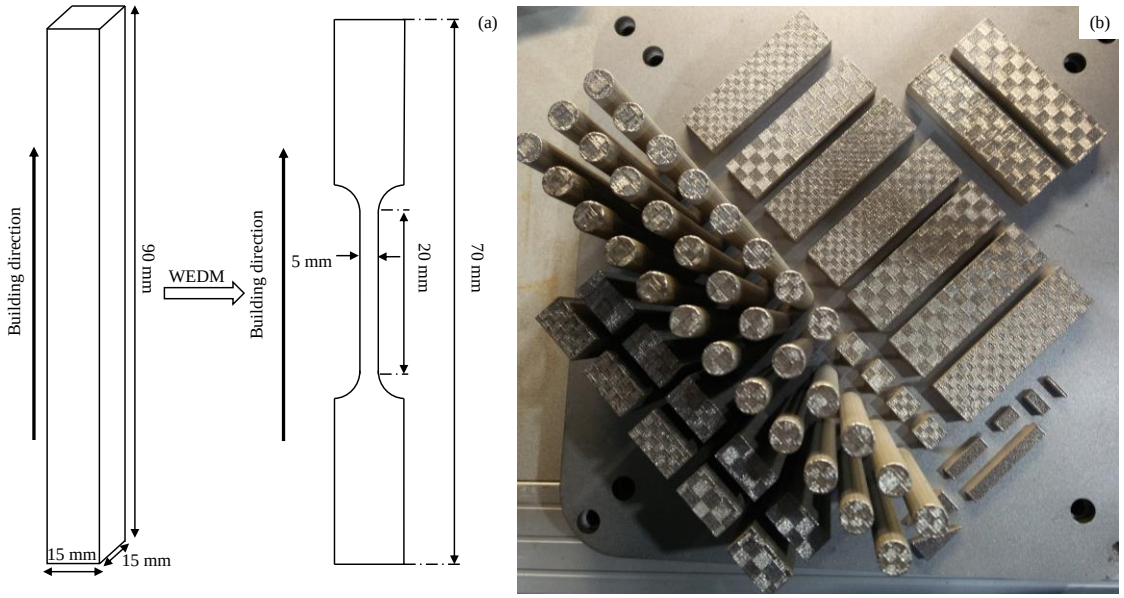


Figure 3.3: (a) Tensile bar orientation with respect to build direction and dimensions together with (b) typical build plate set up with multiple bars in different conditions.

Dual graded specimens were made of different monolithic conditions having one end optimized for large grain size and texture along the build direction and the other end optimised for a low texture/small grain size along the build direction. The grading was varied going from a low texture/smaller grain size towards a higher texture/larger grain size to avoid epitaxial growth of larger grains into the finer grained structure [129]. Details of the parameters used for the manufacture of these bars are given in Table 3.4.

Table 3.4: Overview of parameters used for mechanical graded coupons.

Test condition designation	Grading 1	Grading 2	Mechanical testing
GR_ISLAND/SHIFT	SHIFT4	ISLAND3	Tensile
GR_ISLAND	ISLAND7	ISLAND3	Tensile, DIC,

3.2.3 Heated baseplate

For L-PBF the base plate will act as a major heat sink. Most established systems allow heated baseplate capability up to 150 to 200 ºC for stress relieving purposes. L-PBF processes are characterized by a very high thermal gradient which makes it very difficult to move to homogenous nucleation and equiaxed growth. A heated baseplate would reduce the thermal gradient to facilitate the columnar to equiaxed transition. Thus, a set of experiments using a heated baseplate was carried out. The baseplate consisted of an IN625 plate of dimensions 60 × 60 mm which was heated to a temperature of 400 ± 5ºC for 1 h before commencing the experiment and the temperature maintained during the building process. The aim of this experiment was to investigate the effect of heating the bed and thus reducing the thermal gradient in the build direction on the reduction of columnar growth. The specimens were simple cubes of dimensions 10 × 10 × 10 mm and the parameters included in this experiment are listed in Table 3.5.

Table 3.5: Parameters used for heated baseplate experiments.

Test condition designation	Laser scan path	Power (W)	Scan speed (mm/s)	Hatch spacing (mm)
CONTROL	Island	263	2500	0.075
$ED_{3.89}$	Island	263	1500	0.045

3.2.4 Post processing: sample removal and sectioning

Coupons were removed from the substrates using a wire electrical discharge machine. XZ and XY planar cross-sections were prepared for all parameter conditions. Tensile bars were heat treated after removal from the plate as will be described in Section 3.2.5. These bars were then sliced using the WEDM to obtain the dog bone shape as per a modification from ASTM E8M [198] with a gage length modified to be 5 mm wide and 20 mm long and 1 mm thick as shown in Figure 3.3 (a). This cutting procedure eliminated the rough as-built surface texture which is known to affect the mechanical properties negatively to allow focus on the microstructural impact on the mechanical properties. The oxidation specimens were heat treated as detailed in Section 3.2.5 and then sliced

into 1 mm thick coupons from the original cuboids in parallel to the build direction (XZ cross-sections) using a Struers Accutom 5 precision saw with water cooling.

3.2.5 Post processing: heat treatment

A heat treatment was applied to a CONTROL specimen of 10 × 10 × 10 mm as per ASTM B637-18 [104]. The heat treatments were applied using an LTD atmospheric furnace using a solution treatment temperature of 980ºC for 1 hour followed by water quenching – the relatively low solution treatment temperature in comparison to the recrystallisation temperature for IN718 of 1020 to 1050ºC [105] was chosen to retain the microstructure generated [199]. The coupon was then double-aged at 720ºC for 8 hours followed by furnace cooling to 620ºC and aged for a further 10 h followed by air cooling. Confirmation of the retained original microstructure was obtained prior to further heat treatment. Coupons used for mechanical testing and oxidation testing were then also heat treated as per the procedure described here to obtain the γ' and γ" precipitates required for strengthening of the microstructure and enable comparison to structures used in application.

3.3 Characterisation

All measurements in this work denote mathematical averages of a normally distributed data set unless otherwise specified with the variability given by ± in the measurement showing a difference of 1 standard deviation.

3.3.1 Metallurgical sample preparation

XZ and XY cross-section metallographic samples for all the test conditions and oxidation specimens were mounted in resin and metallographically polished to a mirror-like finish using 0.04 μm colloidal silica solution. Prior to microscopic characterisation this resin was then removed. Oxidation specimens were polished to this finish from both sides and the edges and corners were chamfered to reduce stress concentrations and polished.

The flat tensile dog bone specimens were prepared using a Sharmic™ vibratory bowl polisher to remove any machining marks followed by metallographic polishing of 1 side. The other side was retained with the original finish which offered a textured surface to be used as a speckle pattern for

digital image correlation.

3.3.2 Density and porosity measurements

Archimedes density measurements were performed as per ASTM B962-17 [200] in ethanol at room temperature (~20°C). The coupons considered here had a density of 8.19 g/cm^3 and over (the density of IN718 is listed as 8.19 g/cm^3 [201]) as measured through the Archimedes method – the variations in density may be related to the different precipitates in the alloy formed after heat treatment.

The Archimedes measurements were confirmed using optical microscopy on XZ cross-sections with a minimum area of 1.5 mm^2 over 3 different locations. The coupons considered to be dense through Archimedes measurements were remeasured using optical microscopy as Archimedes measurements tend to overestimate density with holes being filled with powder [91] – and only coupons with a density of over 99.5% of the total area measured were considered to be nominally dense. These coupons were then further characterised as will be described.

3.3.3 Microscopy

Optical microscopy was carried out on specific regions of interest such as weld pools using a Zeiss Axioscope 5 microscope. Low resolution electron microscopy was carried out using a Hitachi TM 3000 Plus on regions of interest such for as powder characterisation, as-built surface features and for cell-size measurements.

High resolution scanning electron microscopy was performed where required such as on fracture surfaces and microstructural specimens using a field emission Tescan Mira 3 SEM equipped with a wide field view camera with an accelerating voltage of −15 kV and a variable working distance and spot size. Secondary electron (SE) and corresponding BSE images were taken where required. EDS measurements were carried out on regions of interest using an accelerating voltage of −30 kV and a working distance of 15 mm.

SEM on oxidation coupons was performed using a field emission Zeiss Merlin Gemini SEM using both secondary electron and backscatter electron signals. Energy dispersive spectroscopy was used for chemical analysis of areas of interest and chemical mapping. Cross-sectional analysis of the oxide scale thickness and chemical composition was performed for each condition at 504 h.

3.3.4 Electron backscatter diffraction

Electron backscatter diffraction (EBSD) measurements were carried out using a step size of 1.5 μm and a scan size of ~1000 μm by ~800 μm to generate IPF maps for microstructural specimens. For the GRADEDBLADE condition, the grid sizes required were larger. A step size between 3 and 4 μm together with a scan size of 11661 μm by 1479 μm was used for the blade section while the fir root tree was scanned using a scan size of 6083 μm by 5362 μm and a step size of 7 μm.

The grain size measurements were calculated on a comparative basis due to the non-parametric (i.e. the distribution of data does not fit a fixed set of probability distributions) grain size distribution. Grain diameter was calculated along the build direction and along the transverse direction where required considering grains that had diameters equal to 4 points or more as the grain size in general was much larger than this. To directly compare the grain size distributions effectively, the line intercept method was used in both the build direction and transverse directions according to ASTM E112-13 [202] on EBSD maps. The grain diameter distributions were then plotted as cumulative grain fractions of the intercept line versus the grain diameter values for both XY and XZ cross-sections. These curves can be used to directly correlate the distribution in grain diameters (shown on the X axis) covering a certain line percentage (shown on the Y axis). Aspect ratio values were calculated by dividing the average grain diameter along the XZ by the average grain diameter along the XY cross-sections.

Texture measurements such as pole figures and IPF maps were generated from the EBSD scans. These were then used to compare preferential alignment of the unit cell between different conditions. A qualitative comparison of the grain misorientations was made from the IPF maps obtained for the different structures by comparing the area percentages covering 3 equal ranges of misorientation closely assigned with the main crystallographic directions. Multiples of uniform distribution measurements for texture components were obtained after contouring using a half width of 10º and a cluster size of 5º. The MTEX [203] MATLAB toolbox was used to reconstruct grains and calculate convex hull based shape parameters for the grains. The convex hull is a polygon whose shape encloses and contains all the points making up an entity – in this case a grain. Grains which approach a rounded and equiaxed shape tend to have a very low deviation from their convex hull, while grains which are less rounded and more irregular in shape will tend to give higher

deviation values from their convex shape. Local area misorientation maps were also generated where required to determine any effect on the misorientation within grains.

3.3.5 Etching

Cell size measurements were performed for selected dense conditions using the line intercept method on XY and XZ cross-sections. Prior to measurement the surfaces were electrolytically etched using a 10% potassium hydroxide and H_2O solution at 3 V direct current for 10 seconds. A minimum of 1800 cells were measured per condition. Melt pool measurements of the top surface were also carried out on etched coupons for single layer specimens after etching the surfaces with Kalling's etchant for 3 seconds.

3.3.6 X-ray diffraction

X-ray diffraction (XRD) measurements were performed on the XY cross-sections for microstructural specimens taken at a height between 3 mm and 4 mm using a Bruker D2 Phaser XRD system equipped with a Co source for θ-2θ angles, between 45º and 120º, a step size of 0.02º and scanning an area of 19.66 cm^2. The measurements were then converted to the Cu equivalent. The texture coefficients for each condition were calculated by calculating the ratio between the intensity of the (002) to the (111) reflections.

The surfaces before and after oxidation were investigated using X-ray diffraction with a Rigaku Ultima IV diffractometer with CuK_α radiation operated in the Glancing Incidence Asymmetric Bragg (GIAB) configuration. An angle of incidence of 3º was used with a step size of 0.05º and a scan speed of 1º per minute in the range of 30º to 100º. The tube acceleration voltage was – 40 kV and the tube current was 40 mA.

3.3.7 Hardness measurements

Hardness measurements were carried out using a Buehler VH1202 machine equipped with a Vickers indenter, a load of 1 kg and a dwell time of 10 s to compare as-built to solution treated and double-aged conditions. The position of the hardness indents was selected in such a way as to leave enough distance to avoid the interference of the underlying strain field of previous measurements. Further hardness measurements were done to compare specimens manufactured using a heated

baseplate using a Buehler VH1202 machine equipped with a Vickers indenter, a load of 5 kg and a dwell time of 10 s. These hardness measurements were done in parallel with the build direction along the height of the specimens. There was an amount of scatter in the hardness data collected due to the variability in the microstructure and relatively large grain size typical of AM components. To compensate for this, a relatively high load was used to ensure that the strain field under the indenter would be large enough to sample several grains.

3.4 Mechanical testing

3.4.1 Room temperature tensile testing

Room temperature tensile tests were conducted as per ASTM E8M [198] on monolithic specimens of interest as specified in Table 3.3. The elastic part of the test was performed using strain control at a strain rate of 0.015 min^{-1}. For this part of the curve the extension was measured using an extensometer. Beyond the elastic limit of the curve, the strain rate was increased to 0.4 min^{-1} and extension measurements were tabulated using the machine head displacement values.

3.4.2 Digital image correlation tensile testing

Tensile testing with digital image correlation (DIC) was performed on the GRADEDISLAND condition. The test was performed on an Instron universal testing machine in displacement control using a 0.002 min^{-1} strain rate – equating to a cross-head displacement rate of 0.1 mm/min. The strain was measured using a knife edge extensometer and in-situ DIC. Images were acquired using a Nikon D850 camera with 32 megapixels was used in conjunction with an Opto Engineering TC16M012 2:1 magnification telecentric lens at an acquisition rate of 0.1 Hz. These images were converted from raw format using Matlab into 16 bit grayscale tiff images and analysed using Davis 8.4 by LaVision [204]. The images were analysed after correcting for lateral shifting and using a least square correlation function for displacement measurement in both the y-direction (loading direction) and the x-direction (lateral direction). Three seeding points were used per analysis and the image time series was analysed with respect to the previous image. A smoothing algorithm using gaussian linear smoothing and adjacent averages was applied to reduce noise in the strain maps obtained.

3.5 Isothermal oxidation testing

3.5.1 Furnace set-up

Isothermal oxidation tests in laboratory air were performed using a Nabertherm horizontal metal tube furnace at 850 ± 10ºC for times up to 504 h. Prior to starting the tests, the furnace was calibrated using a K-type thermocouple over a period of 24 h at the oxidation temperature. The specimens were placed in dehydrated covered alumina boats during the test.

Oxidation tests were conducted on the conditions exhibiting a low texture and high texture namely; the ISLAND3, ISLAND7 and CONTROL conditions as described in Table 3.3. The samples were prepared to a build direction (XZ) cross-section. The sample dimensions (length, width, and thickness) were measured thrice using a Vernier calliper followed by degreasing in ethanol and drying. A high precision Sartorius Me5 micro-balance (±0.001 mg) was used to obtain mass gain measurements. Initial mass measurements for the specimens were obtained prior to starting the tests. Repeated (3 times) mass measurements were obtained at intervals of 0 h, 24 h, 48 h, 96 h, 264 h and 504 h. The mass change per unit area after each interval was calculated and used to calculate the oxidation rate constants.

Samples were placed in the centre of the pre-heated furnace which reached temperature within 10 minutes of sample placement. Upon test conclusion, the furnace was switched off and opened and the samples were cooled in the furnace at a cooling rate varying between 8.2ºC/min in the first 10 minutes to 5ºC/min as the specimens approached 600ºC. Cooling to below 650ºC took ~20 minutes. Mass gain measurements were taken upon cooling. Samples and alumina crucibles were placed in a sealed desiccant container upon reaching room temperature.

3.5.4 Cross-section preparation and characterisation

Cross-sectional analysis of the oxide scale thickness and chemical composition was performed for each condition and oxidation duration. This required the protection of the brittle surface oxide on the sample during the coupon preparation procedure. Specimens were sputter coated with a thin gold layer followed by Ni-plating using a Watt's bath electrolyte solution (710 ml deionised water, 30 g boric acid, 190 g Ni sulphate and 40 g Ni chlorate) at a temperature between 30 and 60ºC using

a hot-plate with a current density between 1-10 $A.dm^{-2}$ for a total of 20 minutes. Once plated, coupons were mounted using Struers Durocit-3 resin and sectioned using Struers Accutom 5 precision cut-off machine and metallographically polished to a 0.04 μm finish using OP-S solution for around 5 minutes. SEM and EDS line and map measurements were performed on near-surface regions to gage oxide thickness and analyse diffusion for the different alloying elements.

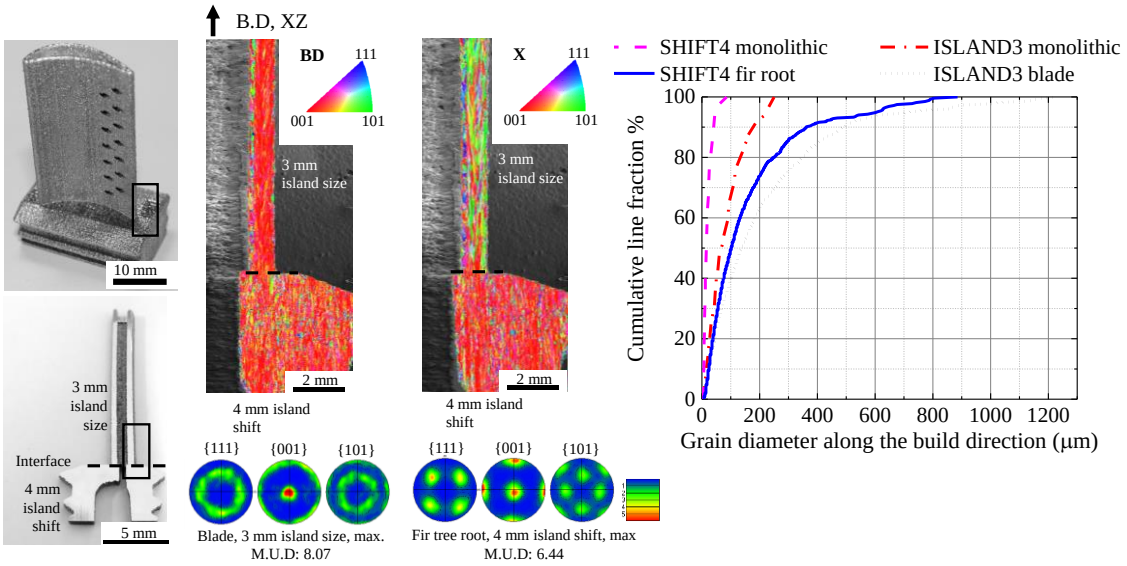
CHAPTER 4. Microstructural control during L-PBF to create graded microstructure Ni-superalloy components

4.1 Abstract

This work explores the feasibility of additively manufacturing tailored microstructures through varying process parameters, to eventually control the mechanical properties and performance. The investigation focuses on controlling the heat input and thermal history during laser-powder bed fusion of IN718 through process parameter manipulation; notably the heat input parameters (power, scan speed, and hatch spacing) and island scanning parameters (island size, shift, and island overlap). The changes in preferred orientation, morphology and grain size were characterised in both the transverse and build cross-sections using scanning electron microscopy and electron back scatter diffraction, while the texture development was comparatively characterised using X-ray diffraction. The solidification cell size was quantified to estimate the influence of the process parameters on the cooling rates. This was also rationalised using a thermal model resolving the scan characteristics to provide the transient temperature distribution to a numerical grain growth model. Based on the obtained microstructures, graded microstructures were generated using the island strategy and identical laser parameters throughout but changing subtle features such as the island size and shift. A suitable post-process heat treatment was applied to retain the tailored microstructures, while obtaining the required hardness.

Keywords: L-PBF; Ni-Superalloys; modelling; solidification; texture.

Graphical abstract:



4.2 Introduction

Inconel 718 is widely used for critical applications requiring a material able to resist high temperatures and stresses such as aircraft engines and nuclear reactor components [1]. IN718 is very difficult to machine due to its high hardness and tendency to work harden, requiring high cutting forces which in turn exacerbates the work hardening experienced by the alloy [13]. However, the slow precipitation kinetics of the alloy make IN718 weldable and therefore an ideal candidate for AM [1,16]. AM has been focused on mimicking the microstructures obtained through conventional manufacturing techniques such as forging, by employing heat treatment to promote recrystallization and remove epitaxial growth and the associated texture produced during the AM process. The layer-by-layer building concept inherent to AM allows the heat input and thus thermal gradient and solidification rates to be changed during the process leading to differing solidification conditions resulting in different solidification microstructures [38]. This means that microstructural features such as grain size, morphology and texture can be modified during fabrication by changing deposition parameters to potentially introduce microstructural grading. Microstructural grading is already being applied for dual microstructure turbine discs. A complex heat treatment is applied to provide a gradual grading in grain size from a small grain size at the bore of the disc which is at lower temperatures moving gradually towards larger grains at the rim where higher temperatures

are expected [19,205]. The ability to use AM for a similar application would mean that microstructural grading could be applied to more complex part geometries to obtain the desired texture or grain size.

Grading can be performed using various approaches such as using laser heat input parameters or particulate refinement as reviewed by Oliveira et al. [38]. A clear example of such grain orientation control was demonstrated by Dehoff et al. [144] using EB-PBF where the electron beam heat input parameters were changed actively to switch from a line to a point heat source and thus obtain mis-oriented grains at a very specific location. A dependence of the level of texturing on the laser heat input parameters; specifically power in DED has been observed by Parimi et al. [136] where a higher power resulted in a much more defined texture compared to microstructures made using lower power. Similarly using EB-PBF and modifying deflection speed and line offset, Körner et al. [130] managed to switch the microstructure from columnar to equiaxed. The effect of modifying the laser heat input parameters was further demonstrated by Popovich et al. [76,129] using laser-powder bed fusion, where 2 power levels were used to manufacture a dual grain structure; varying between a highly textured and large grain size and a much smaller quasi-equiaxed grain morphology. However, grading a microstructure by varying the laser heat input parameters can negatively impact the mechanical properties by introducing porosity and defects into the melt [76,111,178].

Varying the scanning strategy has also been shown to affect the grain orientation. The scan direction in DED has been shown to affect dendrite orientation with unidirectional scans exhibiting a fibre texture aligned at 60^{o} to the build direction and bidirectional scans exhibiting a cube texture with the dendrites being aligned at 45^{o} to the B.D [155]. A similar effect has also been observed in L-PBF by Thijs et al. [91]. Geiger et al. [153] observed a variation in texturing and grain size with different cross-hatch angles. However, the texture variation was only observed in the transverse axes indicating that along the build direction grains would still have the less favourable (001) alignment [153]. Wan et al. [206], investigated bidirectional and cross-hatching scan strategies where the scan strategy was found to affect the amount of texturing found in the specimens. They found that using a cross-hatched strategy resulted in a higher degree of texturing compared to a bidirectional scan strategy [206]. This was also supported by work done by Sun et al. [159] using both cross-hatching and bidirectional strategies. Liu et al. [156] observed that the unidirectional

scanning strategy in laser solid forming was found to encourage a more columnar mode of growth when compared to the cross-hatching strategy which also resulted in differing grain sizes leading to a differing performance in tensile testing. While unidirectional, bidirectional and cross-hatching strategies are both viable strategies for L-PBF, it has been documented that using the island scan strategy results in an overall lower amount of residual stresses as the heat input is more uniformly distributed across the surface [150,151]. This also means that changes in the cross-sectional area will not affect the heat input as much. The effect of varying island scanning parameters such as island size, island overlap and island shift on microstructural features such as texture, grain size and morphology is currently not well understood. An understanding of the effect of these parameters on the grain morphology (equiaxed or columnar), size and preferred orientation along the build direction would provide an alternative method towards microstructural grading while still using laser parameters optimized for high density.

Simulations are attractive tools enabling the virtual investigation of a printed component's expected temperature distribution. This can used to calculate the undercooling and solidification rate and thus the corresponding as-built microstructure and thermal history. This information together with a suitable nucleation model enables cellular automaton (CA) methods to predict grain growth during solidification [207]. Some researchers couple CA with a computational fluid dynamics (CFD) model of the melt pool [158,167,208]. Both CFD and CA require extensive computational resources, so only small domains can be studied. Solving the three-dimensional conduction equation by reducing melt pool details is an alternate attractive option for coupling with CA to increase the domain size [114,209].

The scope of this study is to investigate the effect of varying scanning strategies and laser parameters both experimentally and numerically on the preferred growth orientation along the build direction which to date has been challenging, the microstructural morphology and grain size. The novelty here is to explore the available tools for microstructure control in terms of the island scanning strategy effect on the solidification in addition to supporting this using a thermal model to further investigate grain growth. Micro-segregation for as-built components remains an issue as discussed by Oliveira et al. [40] therefore the viability of such strategies will be further confirmed through the application of a heat treatment tailored to retain the obtained microstructure while obtaining the required hardness for double-aged IN718 and reducing the effect of brittle particles as much as

possible.

4.3 Experimental Procedure

4.3.1 Fabrication

An M2 Concept Laser L-PBF system using pre-alloyed gas atomised IN718 powder (Ø 10 to 45 μm, ASTM B637-18 [104]) was used to create 10 ×10×10 mm cubes. The powder composition is shown in Table 4.1.

Table 4.1: The chemical composition of the IN718 powder used and the ASTM B637 [104] specified composition range of IN718.

Element (wt.%)	Ni	Cr	Fe	Nb	Mo	Ti	Al
IN718 powder	52.15	19.24	18.47	5.19	3.11	1.03	0.44
IN718 ASTM B637-18 [104]	50-55	17-21	bal.	4.75-5.50	2.80-3.30	0.65-1.15	0.20-0.80

All processing was done under a continuous feed of argon (< 0.1% O_2). The CONTROL scanning strategy (Figure 4.1 (a)) consisted of partitioning the surface into 5 mm islands which were then scanned in a random order (within the layer) with a rotation of 90º between consecutive islands. Between each consecutive layer there was a 1 mm by 1 mm shift in both the X and Y directions (Figure 4.1 (f)) and an island overlap (Figure 4.1 (c)) of 0.0225 mm. The subsequent layer was then rescanned in the same random order. A layer thickness of 30 μm was used throughout this work.

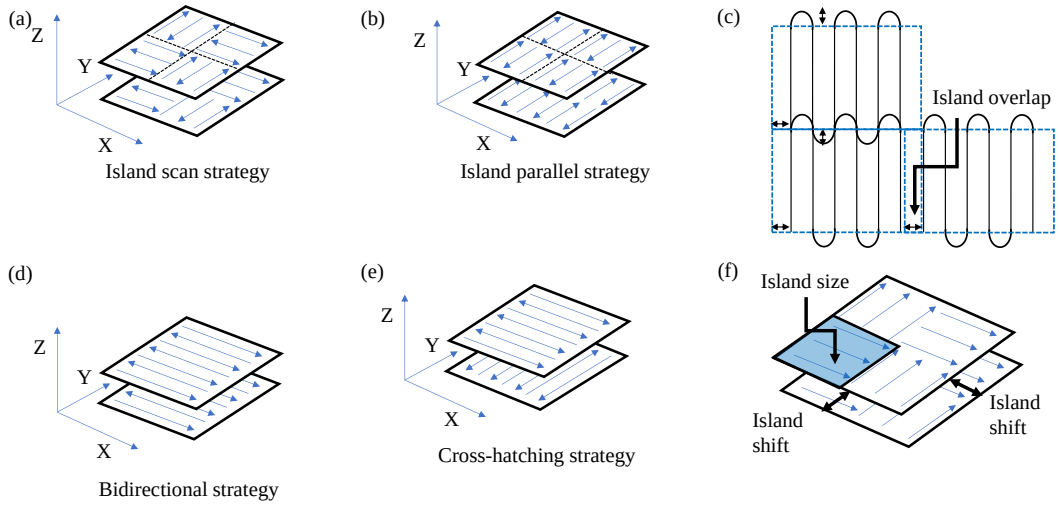


Figure 4.1: (a) Island scanning strategy, (b) island parallel strategy (c) island overlap, (d) bidirectional and (e) cross-hatching scanning strategies and (f) island size together with island shift parameters.

The effect of laser parameters and scanning parameters on the grain size and texture was investigated by manufacturing monolithic coupons through two sets of experiments as follows:

i. To investigate the effect of scanning parameters, the power, scan speed and hatch spacing were kept constant at 263 W, 1500 mm/s and 0.075 mm respectively, selected for optimised density (>99.5%). The strategies used here are outlined in Figure 4.1 and an overview of the various modified scanning parameters is listed in Table 4.2. In the test coupons, individual scanning parameters such as the scanning strategy itself (Figure 4.1 (b, d, e)), the island overlap (Figure 4.1 (c)), the island size and the island shift (Figure 4.1 (f)) were varied individually from the control condition. A CONTROL coupon manufactured using scanning parameters optimised for high density was made for comparison. In addition, 2 single-layer coupons were produced using scanning parameters denoted as ISLAND3 and ISLAND7 in Table 5 having a length of 90 mm and a width of 20 mm. These were used to measure the time required for scanning individual islands and a single layer.

Table 4.2: Scanning strategy parameters used. Each condition had one scanning parameter varied from the control condition as highlighted.

Test condition designation	Scanning Strategy				
	Laser scan path	Island size (mm)	Layer-wise island shift in X and Y directions (mm)	Island overlap (mm)	Post-processing
CONTROL	Island	5	1	0.0225	None
SHIFT4	Island	5	**4**	0.0225	None
ISLAND7	Island	**7**	1	0.0225	None
ISLAND3	Island	**3**	1	0.0225	None
OVERLAP2.5	Island	5	1	**0.05625**	None
BiD	**Bidirectional**	None	None	None	None
CH	**Cross-hatched**	None	None	None	None
IP	**Island parallel**	5	1	0.0225	None
STA	Island	5	1	0.0225	**Solution treatment and aging heat treatment**

ii. To investigate the effect of heat input parameters the scanning strategy used was that used to manufacture the CONTROL condition as defined in Table 4.2. For these specimens the power, scanning speed and hatch spacing were then varied as shown in Table 4.3 to encompass a range of energy densities. The energy density was calculated using Equation 4.1. The energy density values used here represent the area energy density since the layer thickness was kept constant throughout all experiments.

$$\text{Energy Density (J/mm}^2) = \frac{\text{Power (W)}}{\text{Scan speed (mm s}^{-1}) \times \text{hatch spacing (mm)}} \qquad \textit{Equation 4.1}$$

Table 4.3: Laser heat input parameters used.

Power (W)	Scanning Speed (mm/s)	Hatch Spacing (μm)	Energy Density (J/mm^2)
225	2000	60	1.88
263	1500	75	2.33
300	2000	60	2.50
263	1500	60	2.92
263	1500	45	3.89

A demonstrative proof of concept of a scaled-down, hollow turbine blade was manufactured using the island strategy and a power of 263 W, scan speed of 1500 mm/s and a hatch spacing of 0.075 mm. While such aerofoils are typically made out of single crystal, crack susceptible, high gamma prime alloys such as MAR M 247 and CMSX-4, this geometry was chosen to determine whether the trends observed are also applicable to more complex geometries than a simple cube shape, as this will affect the thermal behaviour of the component [210,211]. The information gained from this work is aimed to be the groundwork for application and modification in AM building strategies for more complex alloy systems in application if then required. The fir-tree root geometry of the blade was made using the 4 mm shift in the X and Y directions between each layer (SHIFT4 in Table 4.2) and a 5 mm island size while the blade geometry was made using a 3 mm island size and 1 mm shift in the X and Y directions (ISLAND3 in Table 4.2). This condition will be referred to as GRADEDBLADE. The strategy parameters were selected on a basis of which monolithic condition provided the largest changes in grain size and texture and were varied from the bottom to the top of the turbine blade to create a dual-graded microstructure and avoid epitaxial growth of larger grains into the finer grained structure [129]. The region where the parameters were changed from one condition to another contained a 120 μm overlap to ensure bonding between the 2 conditions.

4.3.2 Characterisation

Archimedes density measurements were performed as per ASTM B962-17 [200] in ethanol at room temperature (~20ºC). These measurements were confirmed using optical microscopy on XZ cross-sections with a minimum area of 1.5 mm^2 over 3 different locations. All coupons considered here had a density of 8.19 g/cm^3 and over (the density of IN718 is listed as 8.19 g/cm^3 [201]) as measured through the Archimedes method – the variations in density may be related to the different

precipitates in the alloy formed after heat treatment. Coupons were over 99.5% dense as measured using optical microscopy.

XZ and XY plane cross-sections were prepared for all test conditions. The specimens were sectioned using electrical discharge machining, mounted in resin and metallographically polished to a mirror-like finish using 0.04 μm colloidal silica solution. X-ray diffraction measurements were performed on the XY cross-sections at a 4 mm height using a Bruker D2 Phaser XRD system equipped with a Co source for θ-2θ angles, between 45° and 120° using a step size of 0.02° and scanning an area of 19.66 cm^2. The measurements were then converted to the Cu equivalent. The preliminary texture coefficients for each condition were calculated by calculating the ratio between the intensity of the (002) to the (111) reflections. This was done to obtain a high throughput measurement for benchmarking. Hardness measurements were conducted using a Buehler VH1202 machine equipped with a Vickers indenter, a load of 1 kg and a dwell time of 10 s.

Scanning electron microscopy was performed using a field emission Tescan Mira 3 SEM equipped with a widefield view camera on regions of interest for the as-built control and heat-treated coupons. Cell size measurements were performed for selected conditions using the line intercept method on XY cross-sections. Prior to measurement, the surfaces were electrolytically etched using a 10% potassium hydroxide and H_2O solution at 3 V direct current for 10 seconds. A minimum of 1800 cells were measured using the line intercept method. Melt pool measurements of the top surface were also carried out on etched coupons.

EBSD measurements were performed using a step size of 1.5 μm and a scan size of 1000 μm by 800 μm to generate inverse pole figure maps and pole figures. Multiples of uniform distribution measurements for texture measurements were obtained after contouring using a half width of 10° and a cluster size of 5°. For the GRADEDBLADE condition, the grid sizes required were larger. A step size between 3 and 4 μm together with a scan size of 11661 μm by 1479 μm was used for the blade section while the fir root tree was scanned using a scan size of 6083 μm by 5362 μm and a step size of 7 μm. The grain size measurements were calculated on a comparative basis due to the non-parametric grain size distribution. To directly compare the grain size distributions effectively, the line intercept method was used in both the build direction and transverse directions according to ASTM E112-13 [202] for intercepts equivalent to 4 points or more (i.e. 6 μm). The grain diameter

distributions were then plotted as cumulative grain fraction of the intercept line versus the grain diameter values for both XY and XZ cross-sections. These curves can be used to directly correlate the distribution in grain diameters (shown on the X axis) covering a certain line percentage (shown on the Y axis). Aspect ratio values were calculated by dividing the average grain diameter along the XZ by the average grain diameter along the XY cross-sections.

Heat treatments were applied as per ASTM B637-18 [104] to coupons built using the CONTROL condition to observe whether the grain texture would be retained after a successful solution treatment, as observed by Chlebus et al. [199]. The heat treatments were applied using an LTD atmospheric furnace using a solution treatment temperature of 980ºC for 1 hour followed by water quenching – the relatively low solution treatment temperature was chosen to retain the microstructure generated. These coupons were then double-aged at 720ºC for 8 hours followed by furnace cooling to 620ºC and ageing for a further 10 h and air cooled. The coupons were then electrolytically etched using a 10% potassium hydroxide and H_2O solution at 3 V direct current for 10 seconds to compare with the control as-built condition which was similarly etched.

4.3.3 Numerical modelling

A thermal model was used to assess scan strategies and their influence on heat distribution by solving the conduction equation (Equation 4.2) in a sample domain. Two time grids were used; one was coarse (dt =1 ms) resolving large scale temperature evolution in the sample geometry, the other is was much finer ($d\,t$ = 10 μs) to resolve the temperature distribution and its changes in the vicinity of the laser. Likewise, the spatial resolution was based on a relatively coarse (dx = 66 μm) grid spanning the computational domain, while the other grid dynamically calculated based on the melt pool length. The melt pool length was sub-divided into 3 computational cells. The fine grid was gradually coarsened with a sufficiently large border around the melt pool to capture fine scale temperature differences.

$$\rho \frac{dh}{dt} = \nabla \cdot (\lambda \nabla \mathrm{T}) + Q \qquad \textit{Equation 4.2}$$

where:

ρ is density in kg/m^3,

h is enthalpy in J/kg,

t is time in seconds,

λ is material conductivity in W/mK,

T is temperature in K

and Q is heat source power density in W/m^3.

The laser was modelled as a Gaussian surface heat source. The variance of the power distribution was defined to correspond to that of the laser used in the M2 Concept laser. The power was scaled by an absorption coefficient of 0.45 and the peak temperature was capped at the alloy's boiling temperature. It is assumed that the processing chamber reaches a steady state temperature of 373 K during printing, which is defined as a Dirichlet boundary condition to the domain boundaries and is also defined as an initial thermal condition for all simulation. The conduction equation is solved iteratively in a finite volume framework. The ESI Additive Manufacturing suite of tools was used.

The spatial and temporal temperature distributions were supplied to the solidification grain structure modeling algorithm based on work done by Mosbah et al. [212]. A grain envelope was computed and defined by the forefront of primary, secondary and tertiary dendritic tips. Each forefront of the dendrite tips was tracked using a Lagrangian particle spaced using the secondary dendrite arm spacing (SDAS). SDAS can be calculated based on the cooling rate and hence changes during runtime. The temperature range between liquidus and solidus was used to identify the melt pool. The tips' growth velocity is calculated using a kinetic model, taking the local undercooled melt pool into account (Equation 4.3, adapted from [213]). Constant values for Equation 4.3 have been interpolated from data obtained by Kundin et al. [213] for values in between 180 J/m and 360 J/m. Interactions between the tips and grains in their vicinity are computed. Randomly distributed nucleation spots are used with constant nucleation density (n_g) that nucleate at a mean undercooling of 3.5 K with a deviation of 2.0 K. The material properties which were used are summarized in Table 4.4.

$$v_{tip} = (5.8 \times 10^{-8}) \cdot \Delta T^{2.7} \qquad \textit{Equation 4.3}$$

where:

v_{tip} is the tip growth velocity in m/s,
and T is the temperature in K.

Table 4.4: IN718 properties used for the thermal modelling and grain growth simulations.

Solid density (kg/m^3)	8000
Liquid density (kg/m^3)	7400
Solid thermal conductivity (W/mK)	15
Liquid thermal conductivity (W/mK)	28.5
Solid specific heat capacity (J/kgK)	600
Liquid specific heat capacity (J/kgK)	750
Absorption coefficient for IN718 [214]	0.45
Solidus temperature (K)	1533
Liquidus temperature (K)	1609
Boiling temperature (K)	3186
Secondary arm spacing (m)	5×10^{-6}

For the thermal model a cuboid computational domain of size $(x, y, z) = (1.5 \times 0.5 \times 0.9)$ mm was used. The first layer was assumed at height $z = 0.03$ mm corresponding to the layer thickness used in the experimental work. The layer thickness for the successive layers was also $\Delta z = 30$ µm. Laser spot size at the surface was assumed to be $d_L = 63.5$ µm, scan speed $v_L = 1.5$ m/s, laser power $P_L = 263$ W, hatch spacing $\Delta y = 75$ µm. An example of the thermal model computational domain for 2 hatches is shown in Figure 4.2.

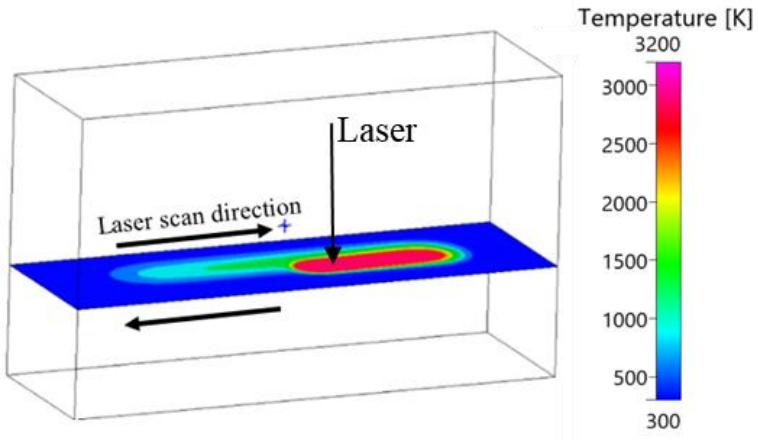


Figure 4.2: Thermal model computational domain demonstrating 2 hatches.

4.4 Results and Discussion

Representative XRD patterns obtained for the powder and for the control coupon are shown in Figure 4.3 (a). The reflections for γ (Ni-Cr-Fe) and γ' (Ni_3 (Al, Ti)) coincide, although it is expected that the amount of γ' and γ" will be low due to the sluggish precipitation kinetics of IN718 [136]. In fact, the hardness obtained for the as-built conditions ranged between 310 and 330 HV_1 – typical for non-heat treated IN718 [199]. The low hardness further supports that the precipitation of γ' and γ" was minimal after L-PBF as the kinetics of precipitation for these phases are too sluggish to precipitate with the high cooling rates typical of L-PBF. The diffraction peaks shifted by about 0.2° higher after L-PBF processing compared to the powder, indicating a reduction in the distance between the lattice planes and thus some distortion in the lattice which is expected due to the high cooling rates in L-PBF leading to an amount of residual stress. No significant developed peaks corresponding to Laves phase were observed here but this could be attributed to a combination of a relatively high step size and low resolution not resolving low intensity reflections from the background signal.

There is a distinct change in the texture coefficient (defined as the ratio of the intensity of the (002) to the (111) reflections), when compared to the powder diffractograph due to the columnar growth occurring during fabrication. The texture coefficient for the CONTROL condition was found to be 4.14 while for the powder it was found to be 0.35. With various laser and scanning parameters, the intensity of the texture coefficient was found to vary as can be seen in Figure 4.3 (b and c) indicating differing levels of columnar growth. By changing the scanning parameters and strategies, the resultant heat flux direction and magnitude can be changed thus impacting the orientation of the preferential [001] solidification direction for fcc materials as will be further discussed.

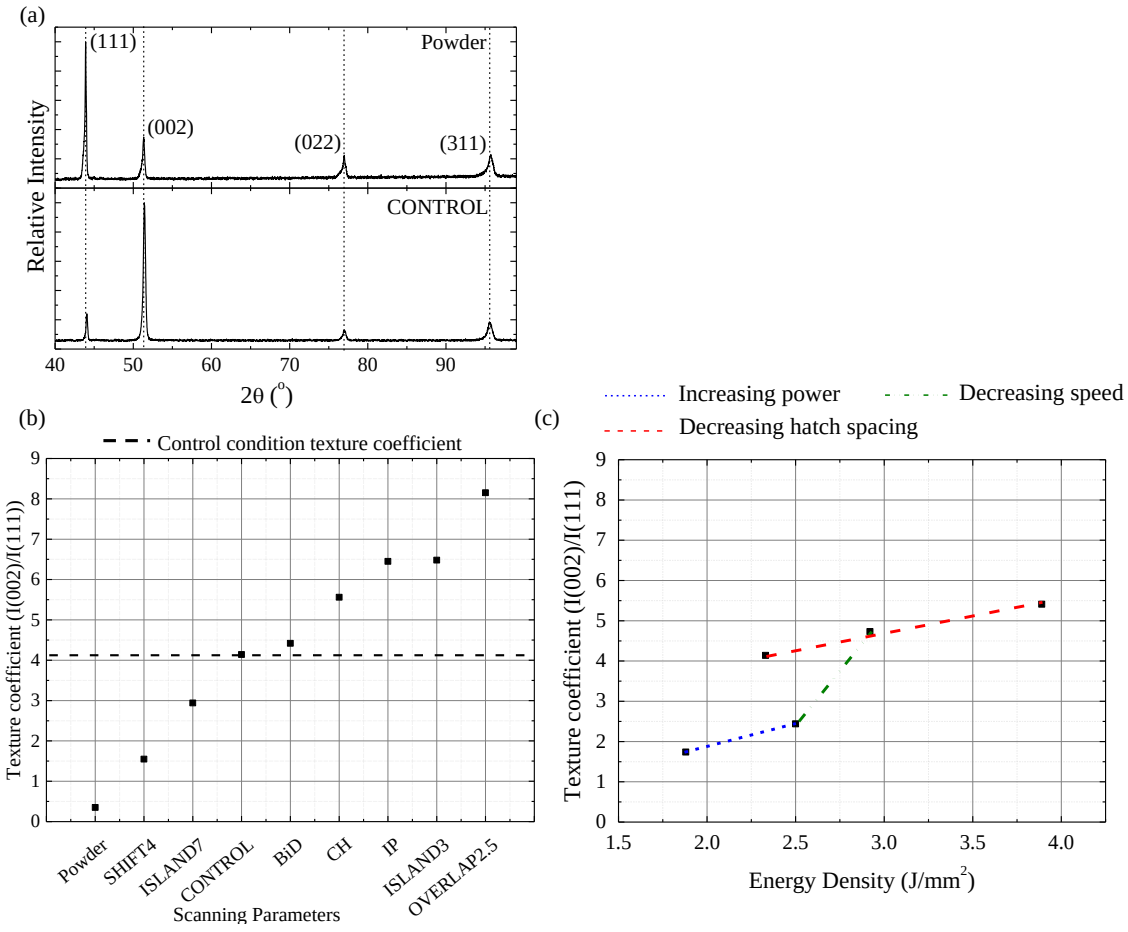


Figure 4.3: (a) Diffractograph for IN718 powder compared to the control condition and texture coefficient obtained for (b) different scanning parameters and (c) laser parameters. Dotted line indicates the texture coefficient for the control condition.

4.4.1 Effect of island size

The texture evolved for strategies using a 3 mm island size is very pronounced, as can be observed in Figure 4.4 (a). The intensity of this texture decreases as the island size increases as shown in Figure 4.4 (b and c). This is further corroborated by the texture coefficient obtained through XRD which varies from 6.48 for a 3 mm island size build, decreasing to 4.14 at a 5 mm island size (CONTROL) to 2.94 at a 7 mm island size; showing that columnar growth along the B.D is present but much reduced with increasing island size. A rotation of the (001) pole was evident in the pole figures with the 7 mm island size condition having a tilt angle of the (001) pole of around 20° to the B.D and 3 mm island size condition having a tilt angle between the (001) pole and the build direction

of only about 6°. The [001] growth direction is aligned with the direction of greatest resulting heat flux between the horizontal and vertical heat flows, resulting in a growth direction that is generally tilted downwards in varying degrees [136,156,215]. The change in tilt angle has been found to occur due to a change in the solidification front tilt angle and is associated with higher cooling rate [139]. For the 3 mm island size, the grains were found to have an average aspect ratio of 2.62, while once a larger island size is used, the aspect ratio progressively decreased to 1.07 for a 5 mm island size to 0.81 for a 7 mm island size and a larger number of small "stray" grains can be observed in between scan tracks.

This effect can be compared to the effect of changing hatch length observed by Nadammal et al. [54]. With a short hatch length, the IN718 microstructure was observed to be increasingly more columnar compared to a long hatch length [54]. With a longer hatch length it was found that the columnar growth tended to be interrupted by the nucleation of stray grains within and between the columnar grains [54]. Hatch length is largely dependent on the part geometry – with larger areas resulting in longer hatch lengths if a simple unidirectional or bidirectional rastering strategy is used. Varying the island size, largely eliminates the effect of part geometry and heat input is more uniform along the area being scanned.

With a smaller island size, the laser will need a shorter time to perform a single line scan compared to a larger island size which would increase the laser pre-heat effect as is further described in the numerical modelling results in Section 4.4.7. This would mean that the previously melted adjacent scan tracks would contribute more to pre-heating of the subsequent melt track. The duration for the laser to scan a single 3 mm island was measured to be around 0.095 s, while for a 7 mm island this was found to be around 0.335 s. These times were obtained from the larger single layer cross-sectional area (20 mm by 90 mm) coupons for accuracy. The total time required to scan a single 7 mm island size layer was measured and found to be less overall (~12 s) than that required for a 3 mm island size (~19 s) due to the higher number of islands required with a smaller island size. For instance, for a 10 mm side square there would be ~11 islands with a 3 mm island size compared to ~2 islands using a 7 mm island size requiring less time for movement of the laser between islands. Thus, smaller islands will have heat being inputted over a longer time frame compared to larger island scanning strategies. Therefore, cooling of parts built with a smaller island size will also be slower as the layer processing time is overall longer.

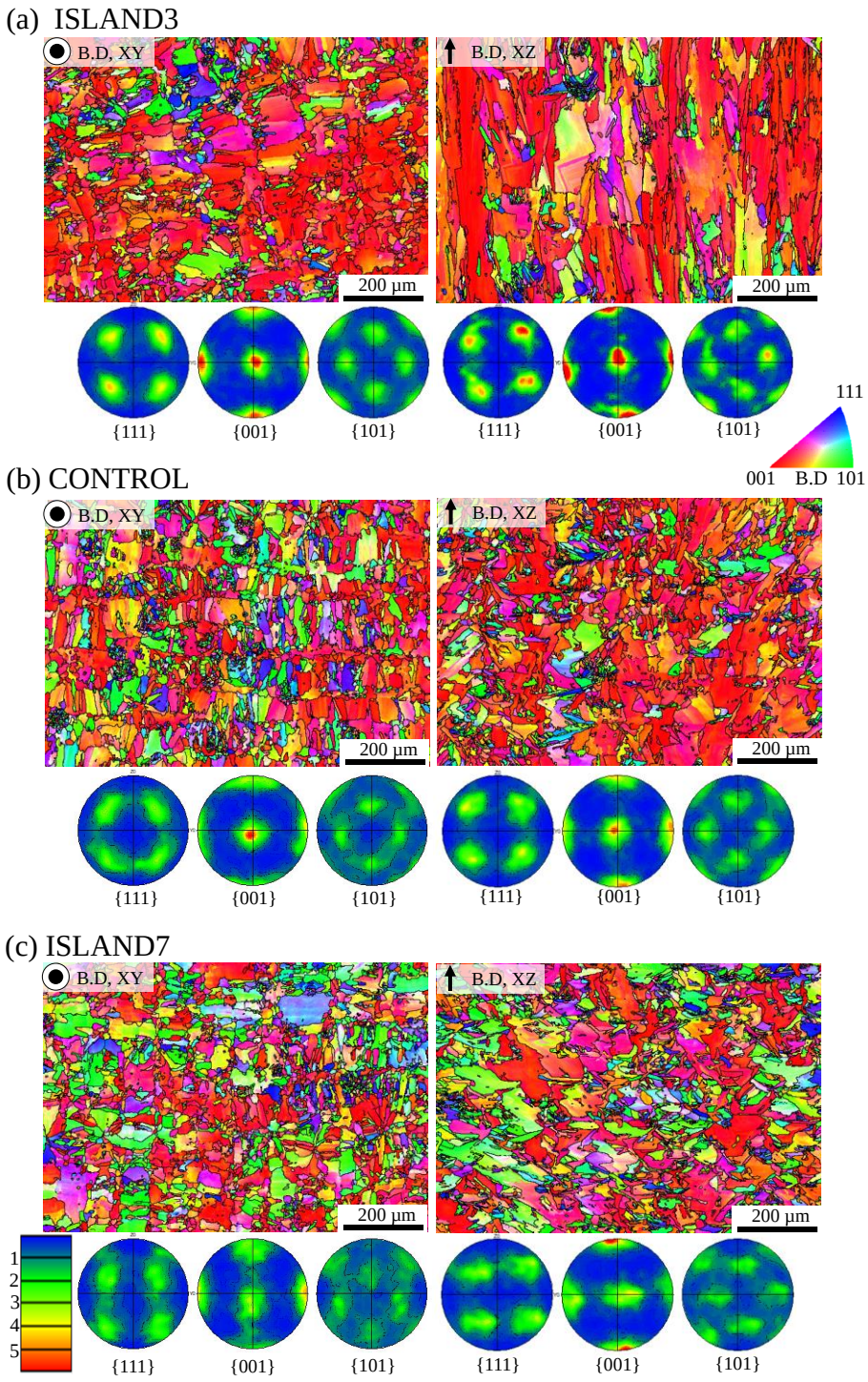


Figure 4.4: IPF maps in XY and XZ planes together with corresponding pole figures for builds using a (a) 3 mm island size, (b) a 5 mm island size and (c) a 7 mm island size.

In the transverse direction the grain diameter distributions are relatively similar (Figure 4.5 (a)). As can be seen in Figure 4.5 (b), ISLAND3 builds lead to a higher percentage of grains having larger diameters along the build direction compared to ISLAND7, showing that as the island size decreases grains tend to be more elongated along the B.D indicating a higher degree of epitaxial growth along the (001). Conditions having a high texture coefficient overall had a larger grain size which should affect mechanical properties.

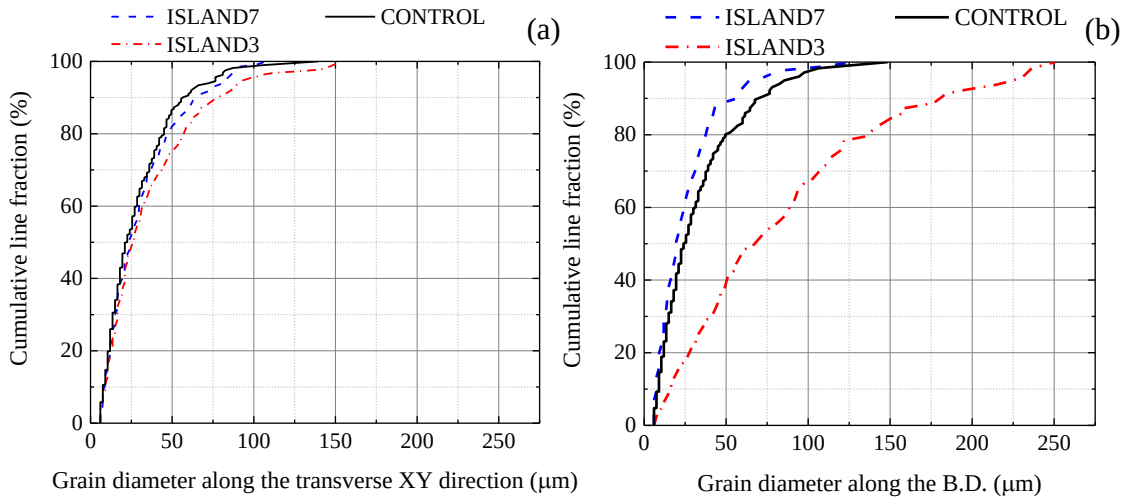


Figure 4.5: Variation in cumulative line fraction percentage distributions over grain diameters with island size in (a) the transverse direction and (b) along the build direction.

4.4.2 Effect of island shift

When applying a layer shift of 1 mm or a layer shift of 4 mm combined with an island size of 5 mm, the overall effect should be similar as the overall pattern would still be shifted by 1 mm. However, as shown in Figure 4.6 (a and b) a difference in texture is clearly visible. For shifts of 4 mm, the grains in the XY and XZ plane appear to have a very low texture along the B.D and in the XZ plane the grains are curved instead of columnar. For a shift of 1 mm in the XY plane the grains appear more aligned with their [001] crystallographic direction to the B.D while in the XZ plane columnar growth is more prevalent. The texture coefficient obtained for SHIFT4 was of 1.55 while with a 1 mm shift (CONTROL) the coefficient was of 4.14 further confirming the decrease in columnar growth with an increase in layer shift. While the grain size distribution for these 2 conditions is quite similar in the XY plane, the difference is mostly visible in XZ plane with the

4 mm shift having overall a distribution of smaller grains in the XZ axis. This is further demonstrated by the decreasing aspect ratio going from 1.07 for the CONTROL condition to 0.71 for the SHIFT4 condition.

The nature of this effect is clear when one considers the island strategy shown in Figure 4.6 (d). Within a layer, the islands will be scanned in a random order, however the order in which the islands are scanned is not changed between each layer, as the same random order is used in each layer. Therefore, when shifting the subsequent layer by 1 mm in X and Y directions, the scanned island is for all intents and purposes still overlapping the subsequent island and will be scanned in the same order, meaning that cooling rates and therefore solidification rates will follow a fixed cyclic routine. For the 4 mm island shift, the corresponding island in the layer will have nearly moved off the original island after the first layer and the order in which the islands are scanned will vary in a more random way which will in turn break up the cyclic solidification routine as with every 2nd layer the scanning order on the subsequent layer is pseudo-randomised again. This will also affect the heat flux in the -Z direction and in turn influence the preferential [001] growth direction. This effect would be very prone to be affected by the geometry of the part being scanned as the shifting here corresponds to 40% of the cube's length of 10 mm. For larger scanning areas the increase in shift might be less effective at disrupting the scanning order between layers while for thin sections (i.e. < 1 mm) the effect might be irrelevant due to the limited cross-sectional area. Furthermore, with larger areas, the laser may take longer to reach adjacent islands as it is scanning which may further reduce the effectiveness of changing island shift thus it is important to consider the cross-sectional area of the part being scanned.

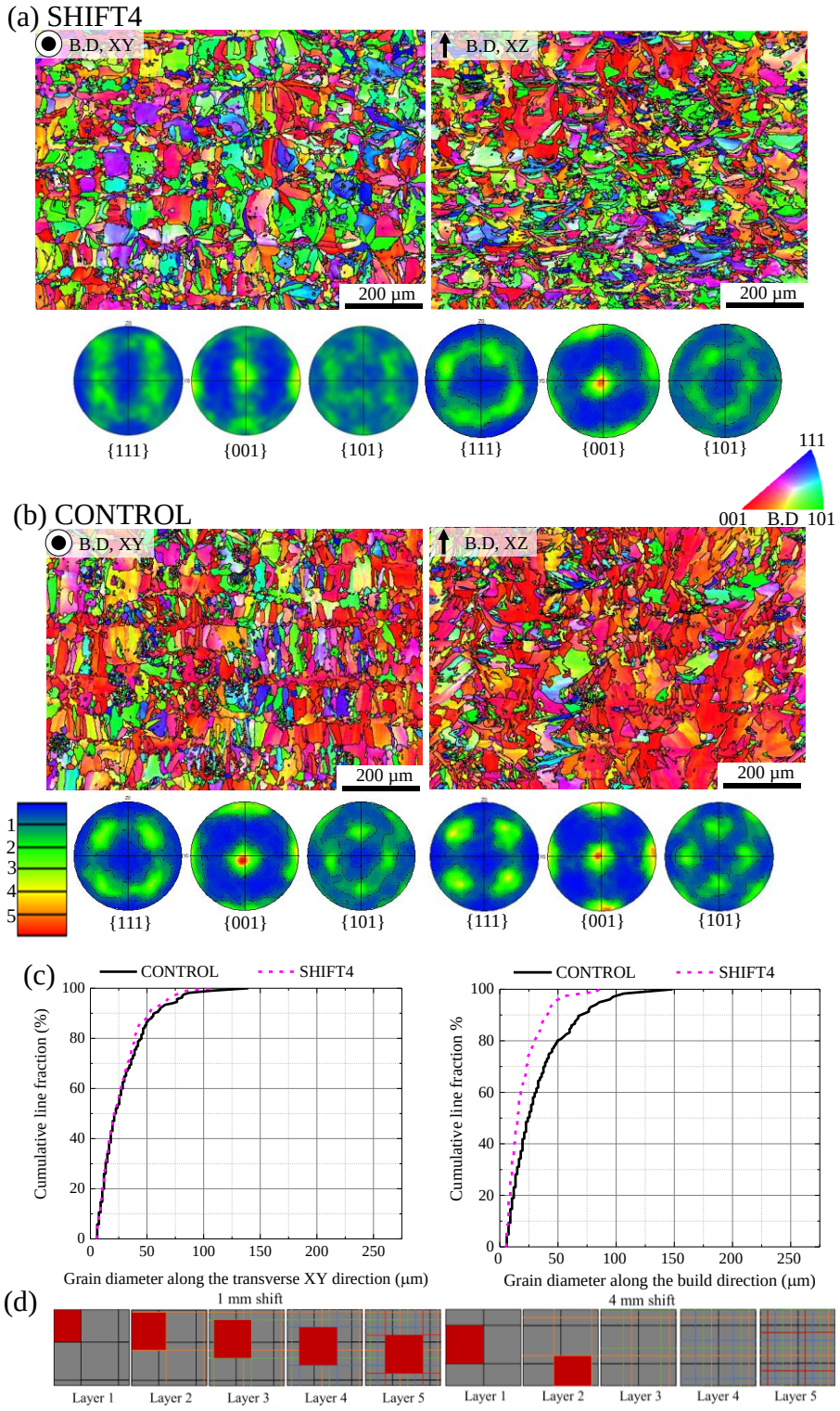


Figure 4.6: IPF maps in XY and XZ planes together with corresponding pole figures for (a) SHIFT4 and (b) CONTROL together with (c) corresponding variation in cumulative line fraction distribution against grain diameter for both cases and (d) the variation in island scanning order between SHIFT4 and the CONTROL.

4.4.3 Effect of scan strategy

The scanning strategy itself was found to also affect the texturing coefficient to an extent as can be seen in Figure 4.3 (b). The CONTROL condition used an island scan strategy and had a texture coefficient of 4.14. Changing the strategy to a bidirectional strategy increased the texture coefficient slightly to 4.42. Using the cross-hatching strategy increased the coefficient to 5.56. A similar effect for the cross hatching strategy was observed by Wan et al. [206] and Thijs et al. [216]. The island parallel strategy (i.e. no 90^{o} rotation between islands but a 90^{o} rotation between layers), which essentially mimics the cross hatch strategy, further increased the coefficient to 6.45 indicating that the change in island orientation can be further used to increase or decrease the epitaxial growth to a certain extent in conjunction with laser scanning parameters. The island parallel strategy could be used to improve the heat distribution in parts while generating specimens with a more pronounced [001] texture.

4.4.4 Effect of island overlap

Increasing the island overlap to 0.05625 mm, i.e. by 2.5 times the original value, affects the texture coefficient increasing it to 8.15 as shown in Figure 4.3 (b), indicating that the preferred orientation of the unit cell becomes much more pronounced. With a larger island overlap the amount of epitaxial growth will be more as the laser vector will rescan a larger section of the island and thus re-melt a larger amount. At the island edges it has been reported that equiaxed misoriented grains tend to form as opposed to the more aligned grains forming in the centre of an island [160]. Increasing the overlap between islands will mean that a larger area of these small equiaxed grains at the island edges will be re-melted resulting in the resulting melt re-solidifying epitaxially facilitating columnar aligned growth.

4.4.5 Influence of laser heat input parameters

The area energy density as a unit will only give a rough indication of the amount of texturing to be expected as the individual laser parameters will each affect the texturing in varying amounts regardless of their specific energy density as can be seen in Figure 4.3 (c). In fact in work by Popovich et al. [111] the energy density was maintained constant while varying a number of parameters resulting in drastically different textures and grain sizes overall.

With an increase in power from 225 W to 300 W the texture coefficient (i.e. ratio between the (002) and (111) peak intensity) was increased somewhat from 1.74 to 2.44 for builds using a scan speed of 2000 mm/s and a hatch spacing of 0.060 mm. The melt pool depth measured for these 2 conditions was statistically similar with 49 ± 9 μm and 43 ± 9 μm observed for the 225 W and 300 W respectively. The melt pool width however was found to statistically (α of 0.01) increase from 106.8 ± 11.6 μm to 140.7 ± 21.9 μm. This behaviour is similar to measurements made by Sadowski et al. [141] where at 2200 mm/s – speeds close to those used here, between an increase in power from 200 W to 300 W, the increase in melt pool depth was very slight while the extent of increase in melt pool width was far more significant. An increase in melt pool width with a decrease in speed was also observed by Yadroitsev et al. [217].

The laser scan speed used for these builds was quite high at 2000 mm/s – builds using a lower speed of 1500 mm/s together and a power of 263 W and hatch spacing of 0.060 mm exhibited a much higher increase in texture coefficient to 4.73 indicating that the columnar growth was significantly more pronounced. A similar effect with decreasing laser speed has also been observed by Thijs et al. [91]. For this lower speed it was found that the melt pool depth increased slightly to 49.4 ± 6.9 μm – which was still quite close to the conditions at higher speed while the melt pool width again increased considerably to 161.6 ± 20.5 μm.

The change in texture co-efficient with increasing power was lower than that observed when decreasing the laser speed. The change in power was only of 75 W and may not have been high enough to result in a vast difference in texture coefficient. At a higher scanning speed, the cooling rate will increase, and the melt pool depth decreases as the laser will spend a shorter amount of time on a specific location, meaning the heat transfer with increasing power levels is not as efficient, thus increasing the solidification rate resulting in less time for epitaxial growth to take place, leading to a less columnar structure. Even though reductions in speed resulted in slightly deeper melt pools – the change in melt pool depth was found to vary to a lower extent than the change in texture coefficient and melt pool width between the different conditions.

Hatch spacing also affected the texture coefficient where, for coupons built using a power of 263 W and a scan speed of 1500 mm/s, decreasing the hatch spacing from 0.075 mm to 0.045 mm had the effect of increasing the texture coefficient to 5.41. The depths of the melt pools also statistically

significantly increased from 50.8 ± 10.1 μm to 66.7 ± 11.3 μm while the widths increased statistically significantly from 138.6 ± 23 μm to 173.4 ± 23.6 μm. In fact, it was previously observed by White et al. [218] that melt pool width is quite affected by the power, scan speed and especially scan spacing which supports the variable changes in width observed with different laser parameters. Dong et al. [132] observed that peak temperatures for scanning tracks were higher with smaller hatch spacing (i.e. more overlap) than peak temperatures obtained with a larger hatch spacing, weld pool width and depth also progressively increased with decreases in hatch spacing. A higher consecutive scan track temperature associated with decreases in hatch spacing would lead to a larger heat flow along the building direction thus increasing the preferential alignment along the building direction.

4.4.6 Cooling rates

The effect of scanning strategy on the cooling rate was quantified through cell size measurements. The cell size obtained for the CONTROL condition was of 740 ± 140 nm equating to a cooling rate of ~14.6×10^{5}°C/s, calculated using Equation 4.4 [219]:

$$\mathrm{DAS} = 80\varepsilon^{-0.33} \qquad \textit{Equation 4.4}$$

where:

DAS is the dendrite arm spacing taken equivalent to cell spacing (μm),
and ε is the cooling rate in °C/s.

The cooling rate obtained is close to what is generally observed for L-PBF processes due to the high cooling rates (>10^5 K/s) inherent to the L-PBF process [220]. The variation inherent to the measurement is significant as the cell size will also depend on the location in which the measurement was taken due to the cooling rate varying within the melt pool, influencing the growth direction of the cells themselves [159]. With the ISLAND7 condition the difference was not statistically significant compared to the CONTROL sample (cell size was of 730 ± 120 nm equating to a cooling rate of 15.1×10^{5}°C/s) due to the large variation in cell sizes present at different locations. However, for the ISLAND3 condition, the cell size obtained increased by a large margin to 920 ± 270 nm equating to a cooling rate of 7.4×10^{5}°C/s, which was found to be a statistically significant increase compared to the CONTROL and other conditions. This would further

corroborate that the cooling rate with a 3 mm island size was lower compared to a 5 mm and 7 mm island size also accounting for the increase in texture and overall increase in grain size. Between different island shifts the difference in cell size was not statistically significant – with the SHIFT4 condition having a cell size of 770 ± 190 nm as compared to the measurement obtained for the 1 mm shift CONTROL sample of 740 ± 140 nm. In this scenario, the overall cooling rate would still be very similar however as previously discussed the solidification cycle would be periodically broken up as the random order in which the islands are scanning is affected by the island shift.

4.4.7 Numerical modelling results

From the thermal simulation, the time resolved temperature field and melt pool depth were obtained at the centre of the domain, which also corresponds to the island centre. The position of the liquidus isothermal (T_L) as a function of time $z(t)$ and the temperature gradient at that position $G(t)$ was determined as shown in Figure 4.7. The melt pool depth and the thermal gradient do change with island size due the different in times required for the laser to return to the area being analysed.

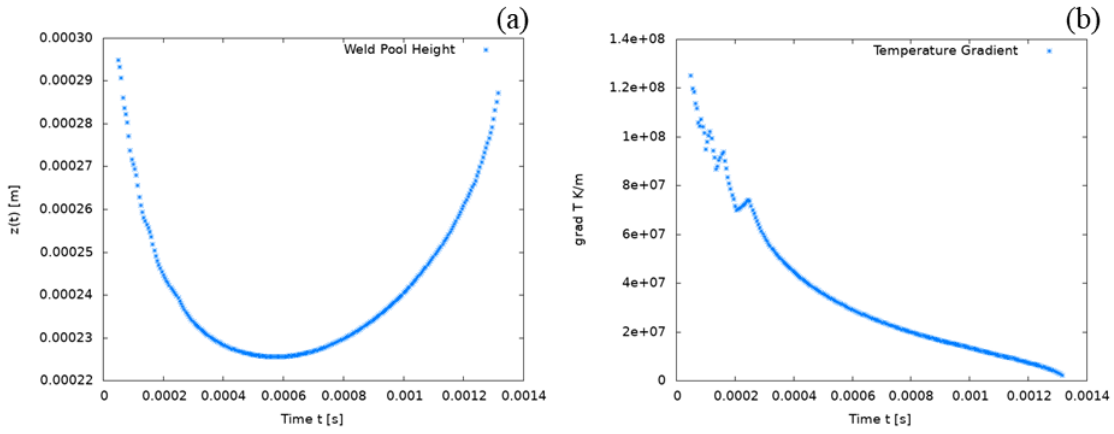


Figure 4.7: (a) Temporal evolution of melt pool depth and (b) temperature gradient.

Figure 4.8 shows the isothermal velocity vs. temperature gradient plot, $v_T(G)$ based on the numerical results obtained showing a cooling rate of approximately $Gv_T \approx 10^6\,\mathrm{K/s}$. When compared with isothermal velocities and temperature gradients reported for traditional manufacturing routes [59], L-PBF values are at least 1 order of magnitude higher.

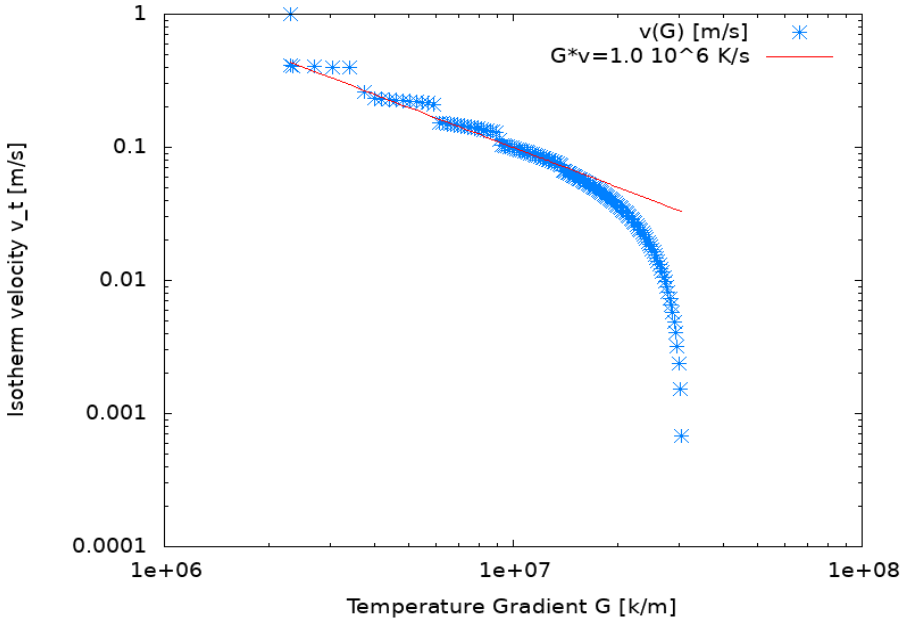


Figure 4.8: Numerical results of isothermal velocity versus temperature gradient for L-PBF.

To determine whether columnar or equiaxed grain structures in L-PBF would form, a criterion first developed by Hunt (Equation 4.5) was applied [112]. The grain structure should be fully columnar, if $g_g < 0.0066$ and is fully equiaxed if $g_g > 0.66$. With $G(t)$ and v_T the volume fraction of equiaxed grains nucleated in front of the columnar dendrites can be calculated as shown in Equation 4.5.

$$g_g = \frac{4\pi n_g \alpha^3}{3(k+1)^3 (v_T G)^3} \left[\left(\frac{v_T}{\alpha}\right)^{k+1/k} - \Delta T_n{}^{k+1} \right]^3 \qquad \textit{Equation 4.5}$$

where:

g_g is the grain volume fraction,

n_g is the nucleation density,

α is equiaxed grain radius,

v_T is the isothermal velocity,

G is the temperature gradient,

and ΔT_n is the undercooling at the nucleation temperature.

Figure 4.9 shows how the Hunt criterion changes during solidification and it can be seen that solidification would start at the edge of the melt pool with a very low Hunt criterion, indicating columnar growth.

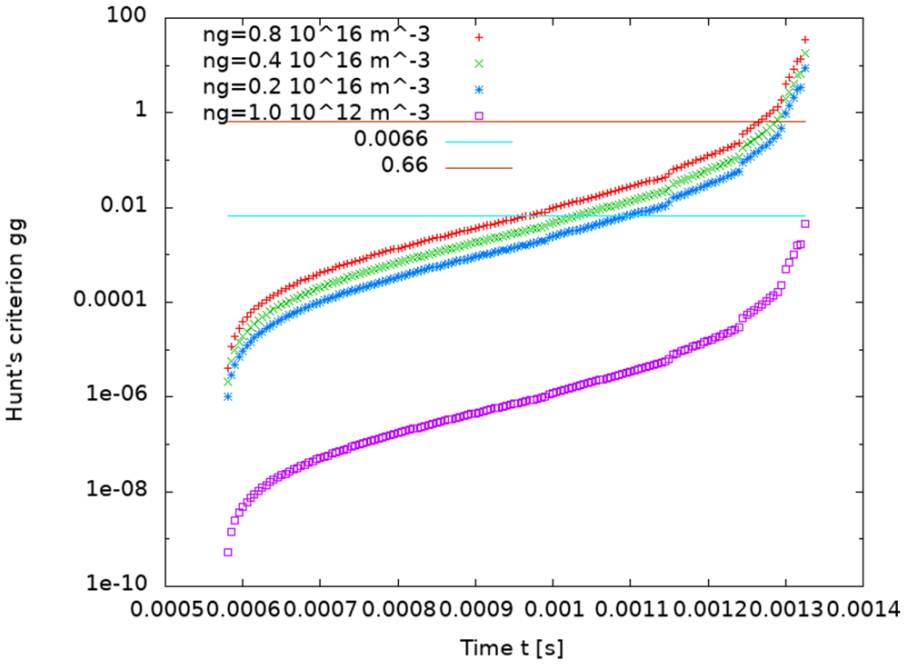


Figure 4.9: Evolution of Hunt criterion during solidification for different nucleation densities.

Nucleant density is known to be a factor controlling the microstructure generated [38]. In fact, refinement particles have been used in AM to increase the nucleant density and to transition from columnar to equiaxed growth [147,221–225]. To determine the influence of the nucleant density on the numerical results generated different nucleation densities were modelled. Three simulations each using different nucleation densities were compared in Figure 4.10. The substrate grain structure is arbitrarily defined using a random generator. The results confirm the regimes predicted by Hunt's criterion. For $g_g < 0.0066$ epitaxially grown columnar grains were obtained that transition to equiaxed grains once higher g_g values were reached.

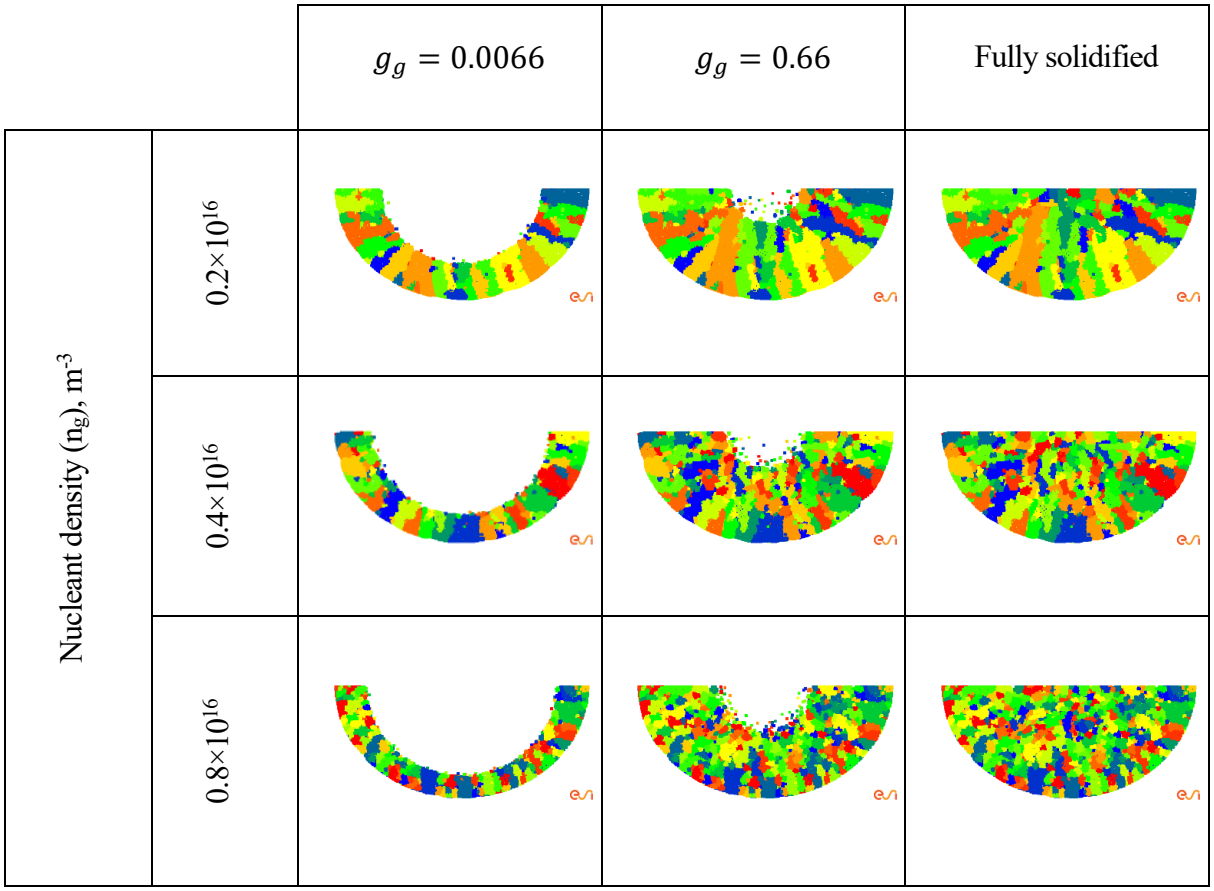


Figure 4.10: Grain structure at $g_g = 0.0066$, $g_g = 0.66$ and fully solidified for nucleant densities of $n_g = 0.2 \times 10^{16}$ m^{-3}, $n_g = 0.4 \times 10^{16}$ m^{-3} and $n_g = 0.8 \times 10^{16}$ m^{-3}.

The model was applied to a unidirectional scan scenario with 4 hatches and 4 layers. The width of the processed area (4 hatches) was 0.3 mm. With a solution domain width of 0.5 mm, 0.1 mm on either side of the processed area was considered. The heat distribution (Figure 4.2) supported the assumption that the region of interest was not affected by domain boundary conditions. The hatch length was 1 mm, so that the duration between hatches was short. Therefore, the first hatch of each layer was melted in cold material and the succeeding hatches in an increasingly warmer environment, resulting in an increasingly deeper melt pool as shown in Figure 4.11. In subsequent layers, the equiaxed grains in the region around the centerline of the melt pool of the previous layer were re-melted and the existing grains on the edge of the melt pool started growing again. If the melt pool was deep enough to reach the columnar grains, these were growing into the subsequent layer, resulting mostly in an overall columnar structure. Despite the main modelling uncertainty related to nucleation density, the observed remelting required for columnar growth was in line with

experimental observations.

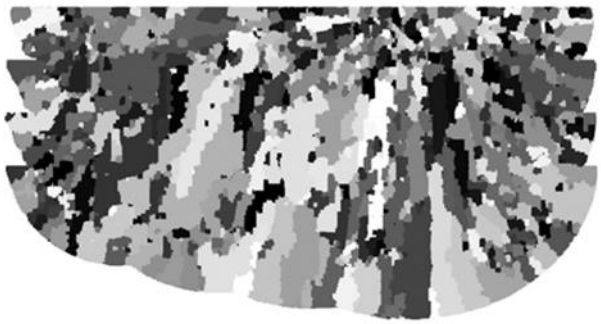


Figure 4.11: Microstructure resulting from unidirectional scan strategies. 4 hatches, the first is always on the left and 4 layers are modelled.

Assuming a given nucleation density of 11.4×10^{15} m^{-3}, the same unidirectional scan strategy and process parameters are used to investigate the influence of the different island sizes; namely varying the island size between 1, 3 and 7 mm. Kinetic model parameters were identical. Figure 4.12 compares the numerical grain structure for 4 hatches and 4 layers. It is directly visible that the 1 mm island exhibits more columnar grains as compared to 3 and 7 mm islands; which follows the experimental results of Figure 4.4. The numerical results show intermittent equiaxed grains that are mostly found between hatches for 1 mm island. The majority of equiaxed grains are re-melted when the laser comes back to process the next layer exposing the lower epitaxial grains that can continue their growth across several layers during solidification. As the island size increases the time interval before the laser comes back is longer, leading to a lower pre-heat for the newly deposited material. The melt pool depth decreases and more equiaxed grains remain to compete with the epitaxial grains leading to less columnar grains.

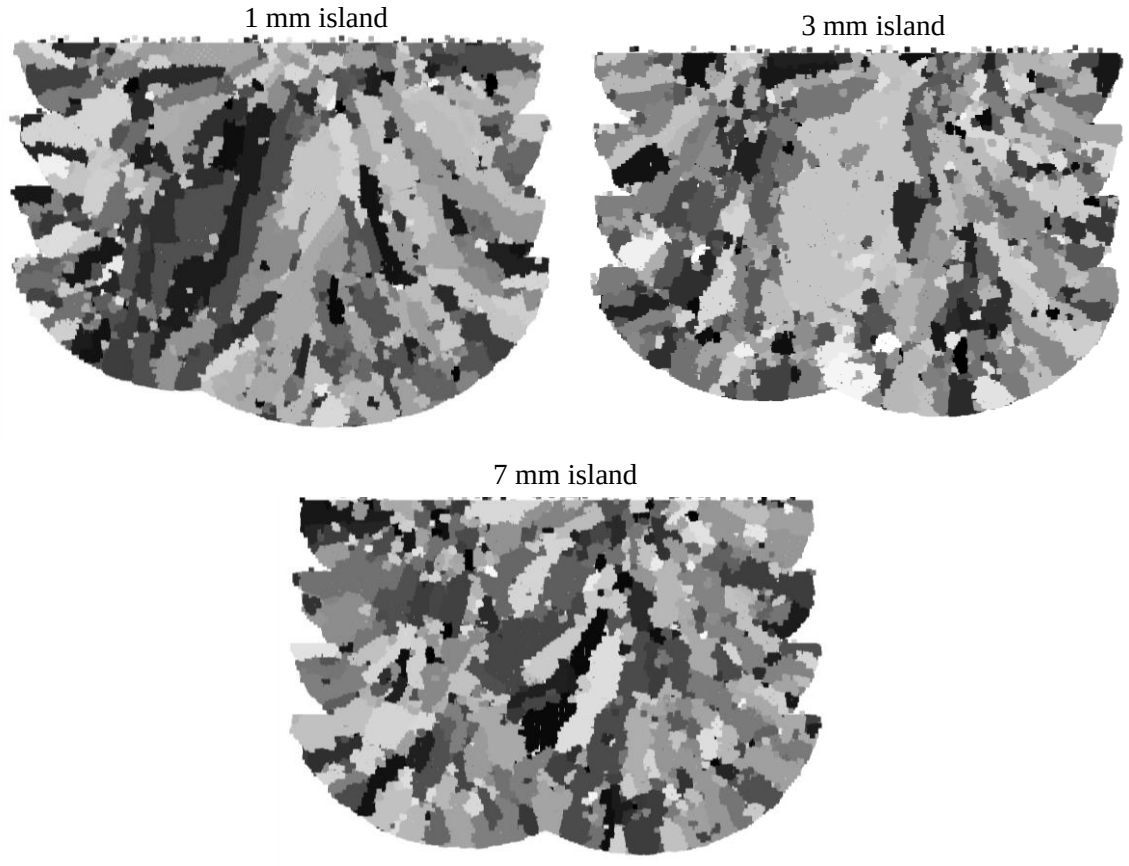


Figure 4.12: Microstructure resulting from unidirectional scan strategies for 3 different island sizes (1 mm, 3 mm and 7 mm). The cross section shows grains resulting from 4 hatches, the first is always on the left with 4 consecutive layers are modelled.

4.4.8 Graded Blade

The cross-section for the GRADEDBLADE is shown in Figure 4.13 (a) where the area analysed using EBSD is highlighted together with the interface and the differences in parameters used for the blade and fir-tree root sections. As can be seen from Figure 4.13 (b and e), the microstructure varies over the length of the component although the difference in texture variation between the 2 conditions is much less pronounced in comparison to the corresponding monolithic conditions shown in Figure 4.4 (a) and Figure 4.6 (a). The blade section has a fibre texture indicating that there is a strong alignment of the ⟨001⟩ crystallographic direction to the direction of thermal flux, however as opposed to the cube texture previously observed, in this case, the ⟨001⟩ and ⟨010⟩ crystallographic directions are not aligned with the X and Y axes of the build. This was evident

when observing the IPF maps along the X and Y axes of the build for the blade section shown in Figure 4.13 (e), where mainly the [011] direction was aligned with the transverse axes of the build. The alignment of the [001] crystallographic direction with the build direction is beneficial in scenarios where creep loading is present as the [001] direction performs better in creep loading scenarios [177]. The intense fibre alignment might be in part also due to the much smaller cross-sectional area of the blade resulting in a very intense heat flow across the B.D.

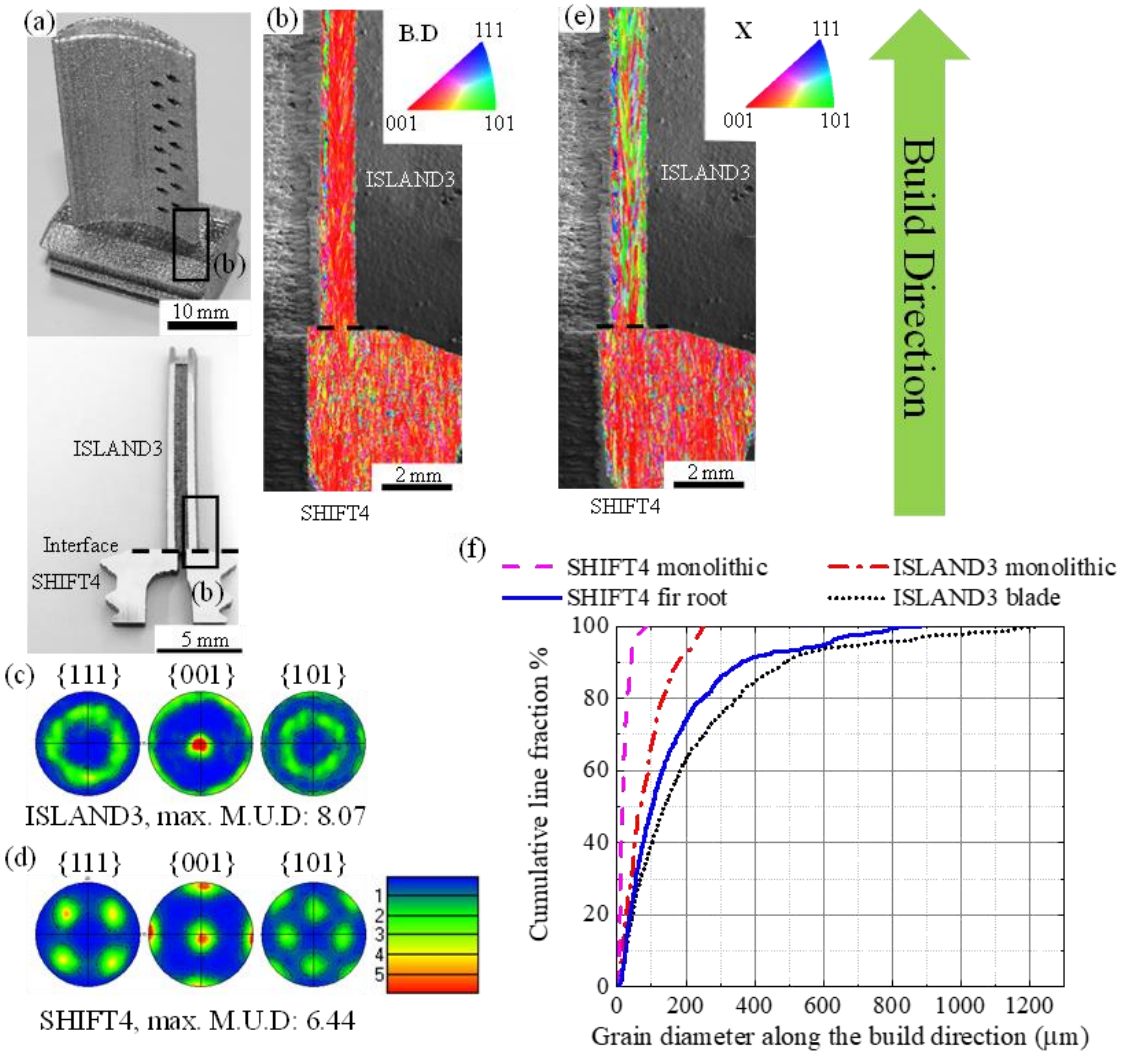


Figure 4.13: (a) The GRADEDBLADE specimen with (b) corresponding XZ cross-section IPF map along B.D and pole figures for (c) a 3 mm island size, (d) a 4 mm layer shift, (e) XZ cross-section IPF map along the transverse direction and (f) corresponding variation in cumulative line fraction distribution against grain diameters for the graded and monolithic conditions.

The fir-tree root was observed to have mainly a cube texture which is quite commonly observed in AM and was previously observed for monolithic conditions where the 〈001〉 directions were mostly aligned with the X, Y and Z axes of the build as shown in Figure 4.13 (d). The M.U.D intensity of both the blade section and the fir-tree root is in general higher than that observed for the monolithic cubes previously analysed with the blade section obtaining an M.U.D of 8.07 as compared to similar parameters used to manufacture the 10 cm side cubes which had an M.U.D of 7.91 along the XZ cross-section. The M.U.D values for the fir-root also varied slightly when compared to the monolithic condition with the fir-root section having an M.U.D of 6.44 and its monolithic counterpart having an M.U.D of 5.11 in its XZ cross-section.

There is a difference in the grain length along the build direction with the blade section having grains which are much more elongated than the fir-root section as can be seen from the cumulative area distribution vs line intercept curve shown in Figure 4.13 (f). The trends of the 2 graded regions follow to those of the monolithic conditions where the SHIFT4 results in lower elongation along the build axis when compared to the ISLAND3 condition.

The cross-sectional area being scanned will make a difference for the part being built as for smaller cross-sectional areas the thermal gradient of the area being scanned is expected to be higher when compared to larger cross-sectional areas leading to a higher heat flux along the build direction. Furthermore, the mechanic observed with a 4 mm layer shift in the monolithic samples where the texturing and grain size are reduced due to induced randomisation of the island scanning order is strongly dependent on the cross-sectional area being scanned and may change over different cross-sectional areas. In such a case use of a larger island size or different laser parameters might have been preferable to reduce the effect of cross-sectional area as much as possible.

4.4.9 Effect of heat treatment

The solution temperature chosen in this work was lower than the reported recrystallisation temperature of IN718 of 1020ºC for wrought IN718 and 1100ºC for AM IN718 [105,226]. In general, the microstructure of AM components is solution treated at temperatures higher than the recrystallisation temperature to remove any remnant of the typical columnar microstructure. Furthermore, the solution treatment is required in order to dissolve any niobium carbide films decorating cell and grain boundaries as these films may embrittle the material [103,136,227].

However, as discussed previously the scanning parameters used in AM can be modified to tailor a microstructure depending on its application thus a heat treatment is required where this microstructure is preserved.

Chlebus et al. [199] showed that the temperature of 980ºC is high enough to dissolve carbide films decorating cell and grain boundaries but that grain recrystallisation will only occur when the temperature is increased further. Thus, limiting the temperature to 980ºC during solution treatment should preserve the microstructure obtained during L-PBF while still meeting ASTM B637-18 conditions. A double-ageing treatment according to ASTM B637-18 [104] was then applied to precipitate γ' and γ'' and obtain the required strength and hardness. Further investigation into heat treatment temperatures below the recrystallisation temperature of IN718 and different durations could be carried out to determine an optimal heat treatment condition for additively manufactured parts e.g. to retain dislocation structures.

The hardness before heat treatment for the control condition was found to be 326.5 ± 7.6 HV1, close to the value of 297 ± 5 HV1 obtained by Chlebus et al. [199] and values between 290 and 300 HV20 obtained by Liu et al. [226]. Post-heat treatment, the hardness increased to 472.1 ± 11.5 HV1 due to the precipitation of γ' and γ''. The values shown agree with literature for the hardness of similarly heat treated IN718 where the values obtained lie between 450 and 460 HV [23,199]. Prior to heat treatment, the microstructure consisted of grain boundaries and cell boundaries delineated by carbide films, shown in Figure 4.14 (a) with small Laves particles observed in the cell boundaries as shown in the insert in Figure 4.14 (a). After heat treatment the carbide films in the grains disappeared and some carbides could be observed to decorate the grain boundaries as shown in Figure 4.14 (b). The grain size and texture were not found to change significantly as can be seen in Figure 4.14 with the grain structure still following the original scan track lines. The texture coefficient for the nominal condition after heat treatment was found to be 4.58 as opposed to 4.14 obtained prior to heat treatment indicating that the temperatures chosen were sufficiently low to retain the original texture and avoid recrystallization.

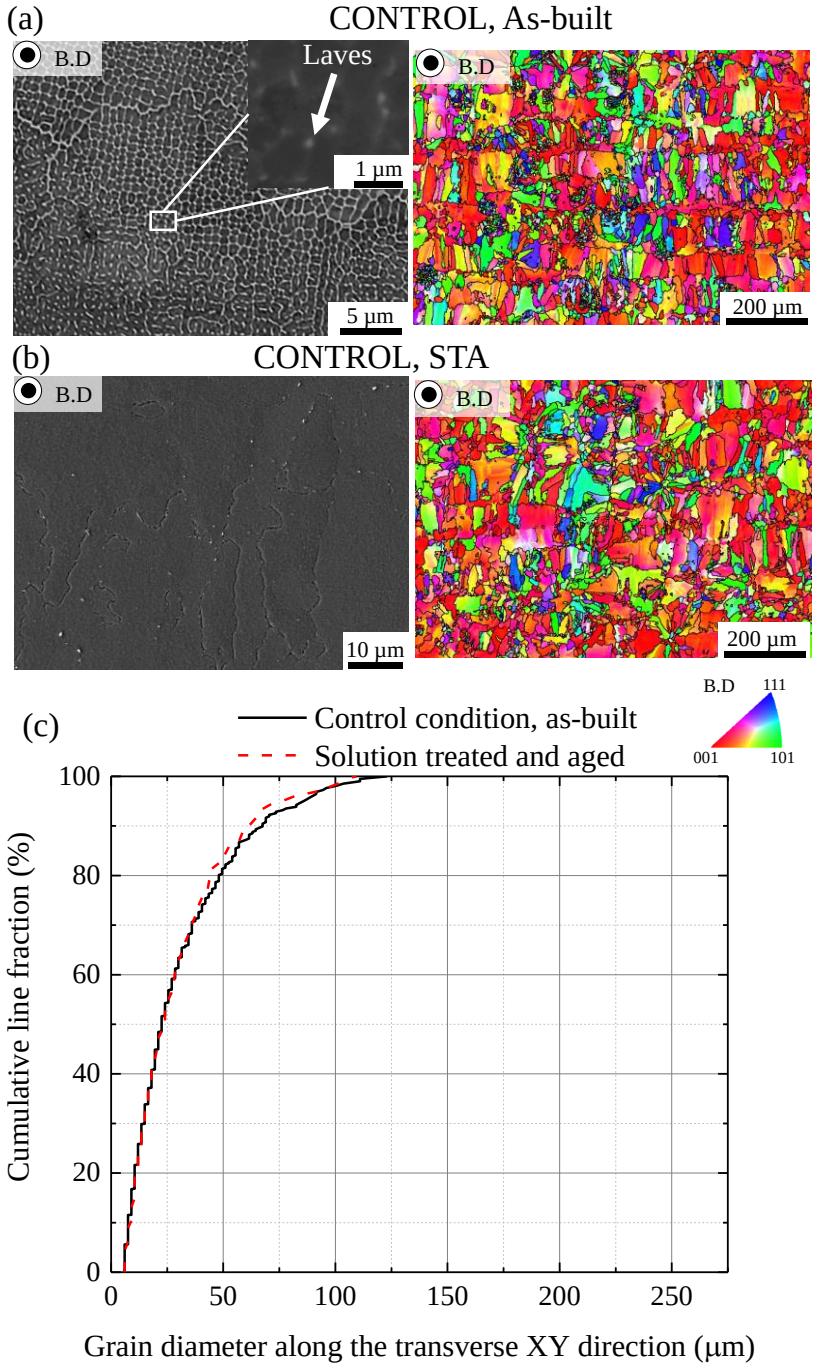


Figure 4.14: (a) The as-built microstructure with cell and grain boundaries delineated by Nb-C films and minute Laves particles at the cell boundaries together with the corresponding IPF map, (b) dissolution of the carbide films at the cell boundaries after heat treatment at 980ºC together with the corresponding IPF map and (c) the grain diameter distribution against cumulative line fraction plot.

4.5 Conclusion

Using different strategies and scanning parameters the solidification rates and thermal gradients can be modified to change the microstructure being obtained. By selecting optimised laser heat input parameters, the scanning parameters can be modified without impacting the porosity to modify the microstructure and mechanical properties. Using an island scanning strategy with a small island size, a highly columnar microstructure was obtained while still using the island scanning strategy but with a large island shift or larger islands a "quasi-equiaxed" structure was obtained. Through modelling it was found that the nucleant density in the melt pool plays a strong role in determining the ease of transition from columnar to equiaxed microstructures and that the level of pre-heat from previous melt tracks and the resulting melt pool depth play a key role in determining which grains are maintained or replaced, affecting the final microstructure generated. The increase in columnar growth with a reduction in island size was also observed through modelling.

These two microstructural morphologies were successfully applied to a proof-of-concept hollow turbine blade with a dual microstructure. Even though the area and volume of the specimen were different than the original monolithic test coupons the differences in microstructural morphology were still evident. However, the scanning strategy is directly affected by the cross-sectional area thus the scanning strategy parameters need to be carefully selected to ensure the effect of the sample geometry is as minimised as possible. A successful heat treatment was investigated and applied to maintain the microstructure obtained after L-PBF and improve the hardness through the precipitation of γ' and γ" to allow successful application of such components.

Further investigations are being carried out to obtain melt pool measurements in support of the consecutive increase in melt pool depth to support the grain growth model and investigate the effect of microstructural control on the local mechanical properties at the graded interface using digital image correlation. High temperature oxidation tests are currently ongoing to elucidate the effect of texture and microstructure control on the oxidation rates. These results are in preparation for future publication.

CHAPTER 5. Application of baseplate heating in laser powder bed fusion of Inconel 718 to control the columnar to equiaxed transition

5.1 Abstract

This work explores the feasibility of a heated baseplate in additive manufacturing of Inconel 718 to transition from columnar to equiaxed growth with the aim of reducing the anisotropy typical of such components and improving their mechanical properties. In this work, Inconel 718 specimens were manufactured using laser powder bed fusion with baseplate heating at 400ºC. These were compared to conditions without baseplate heating with a varying hatch overlap. The use of a heated baseplate results in a significant reduction in grain elongation coupled with an increase in local misorientation within the microstructure compared to no baseplate heating. The reduction in grain elongation occurs due to the formation of numerous small globular grains as opposed to the typical large epitaxial grain structure obtained after additive manufacturing. The decrease in grain elongation and increase in local misorientation contribute to an increase in hardness for conditions manufactured using a heated baseplate.

Keywords: laser deposition, solidification microstructure, electron backscattering diffraction, nickel alloys, columnar to equiaxed transition

5.2 Introduction

The microstructure formed during solidification significantly affects a material's mechanical properties and failure behaviour [14]. By treating the microstructure as a variable, different material properties can be optimised. Machining of IN718 poses a number of challenges due to work hardening during the cutting process but due to its slow precipitate formation and good weldability Inconel 718 is an ideal candidate for additive manufacturing [8,13,16–18]. The scope of the current work focuses on a sub-section of AM, specifically laser powder bed fusion. L-PBF has the potential through the modification of the laser heat source parameters and scanning strategy to change the variables governing the solidification process and therefore the microstructure as has been demonstrated in Chapter 4 [166].

Typically, the microstructure for IN718 after L-PBF consists of an elongated grain morphology aligned to the B.D, growing epitaxially through different layers with a columnar dendritic or cellular sub-structure [23,60,84]. The columnar-to-equiaxed transition shown in Figure 5.1 governs the grain morphology obtained during AM [46]. The parameters governing the growth mode are the temperature gradient at the solid/liquid interface (which is the difference of temperature in the melt pool moving in the interface of the liquid towards solid) and the solidification rate [116]. When the CET occurs, nucleation of the equiaxed grains occurs in the liquid ahead of the columnar zone.

The baseplate in L-PBF acts as the main heat sink during the process. By heating or cooling the baseplate, a change in heat flow, therefore thermal gradient and solidification rate occur. A high G and a low R will promote columnar growth, while a high R and low G will promote equiaxed growth [117]. The heat flow itself will determine the grain growth orientation; when the heat flux is equal in all directions the growth tends to be globular, while when the heat flux is unidirectional, the resulting growth will be elongated along the direction of highest heat flow, typically the build direction [46]. The grain morphology (cellular, columnar or equiaxed dendrites) can be modified through laser parameters such as power, hatch spacing and scan speed and scanning strategy as is comparatively shown in Figure 5.1.

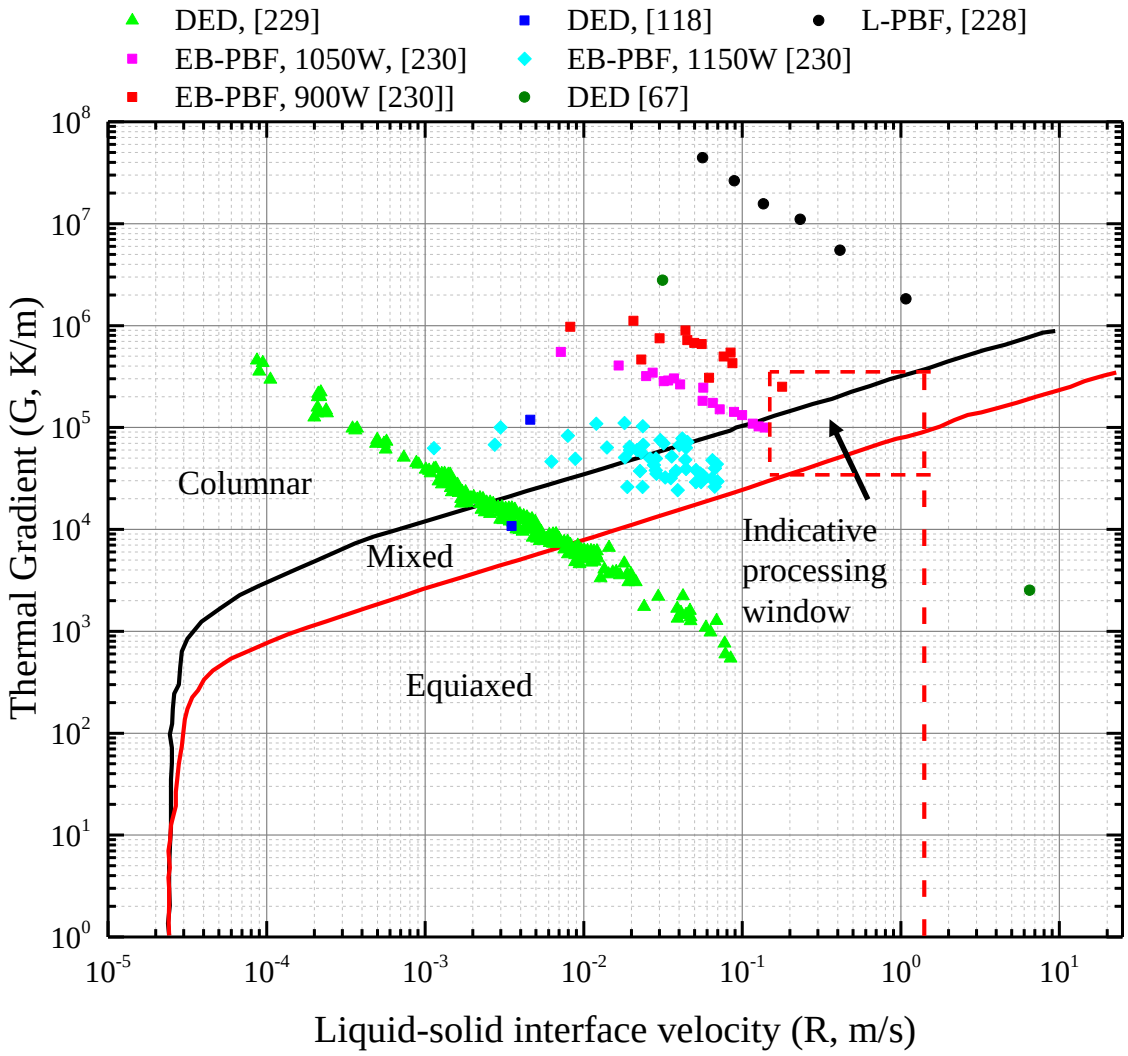


Figure 5.1: Effect of solidification rate and thermal gradient on the CET for IN718 through simulated data. Dotted vertical red line indicates the absolute maximum expected solidification rate based on the scanning speed used in this work. A general indication of the expected processing window for this work is shown by a dotted red box. Original figure without data comparison from [144].

For face-centred cubic metals, the primary growth orientation is along the [100] direction with the secondary growth orientation along the [010] or [001] directions [60]. If the heat flow direction is most closely aligned with the [100], growth will be columnar and along that direction. In fact, large columnar grains with a ⟨001⟩ direction in parallel to the B.D are typically observed following L-PBF. The effect of baseplate temperature has been quantified for DED by Gäumann et al. [116] where the effect of baseplate cooling was applied to grow single crystal structures through epitaxial growth. Increasing the cooling effect of the baseplate through additional cooling significantly

increases the columnar alignment of the grains as a result of the higher unidirectional heat flow leading to an increase in the temperature gradient [102]. L-PBF is typically characterised by rapid cooling rates and high thermal gradients as shown in Figure 5.1 caused by the large heat sink effect of the baseplate and thus characterised by very aligned columnar growth. The high thermal gradient makes it very difficult to transition from columnar to equiaxed growth. Baseplate heating is thought to promote equiaxed growth through a reduction in temperature gradient [116,150]. The aim of this work is to determine whether the use of a heated baseplate in L-PBF, is enough to modify the growth mode during solidification of IN718 to transition from epitaxial growth towards equiaxed growth.

5.3 Experimental Procedure

An M2 Concept Laser L-PBF system using pre-alloyed gas atomised IN718 powder (Ø 10 to 45 µm, with composition per ASTM B637-18) was used to create 10×10×10 mm cubes under a continuous feed of argon (< 0.1% O_2). The island scanning strategy used in this work is described in detail elsewhere [166]. The "CONTROL" coupons were made using a power of 263 W, a scanning speed of 1500 mm/s and a hatch spacing of 0.075 mm with a constant layer thickness of 30 µm. The scanning overlap was decreased from 0.075 mm to 0.045 mm to obtain a higher planar energy density increasing from 2.33 J/mm^2 to 3.89 J/mm^2 (denoted as $E.D_{3.89}$). The planar energy density was determined as detailed in [122]. Specimens were built using an unheated baseplate and a baseplate heated to 400 ± 5ºC. The absolute maximum expected solidification rate together with an indication of the thermal gradients for the parameters used in this work are shown in Figure 5.1. It is expected that the solidification rate is effectively lower than that demarked in Figure 5.1 due to the heat dissipation kinetics at high scanning speeds [231].

The specimens were sectioned along the build direction, mounted in resin and metallographically polished to a mirror-like finish. Hardness measurements were conducted using a Buehler VH1202 machine equipped with a Vickers indenter, a load of 5 kg and a dwell time of 10 s. Hardness measurements were done moving in parallel with the build direction along the height of the specimens. There was an amount of scatter in the hardness data collected due to the variability in the microstructure and relatively large grain size typical of AM components. To compensate for this, a relatively high load was used to ensure that the strain field under the indenter would be large enough to sample several grains. Scanning electron microscopy was performed using a field

emission Tescan Mira 3 SEM equipped with a widefield view camera on regions of interest. Electron backscatter diffraction measurements were performed using a step size of 1.5 μm and a scan size of 1000 μm by 800 μm. Larger scans were made for the CONTROL heated baseplate condition using a step size of 7 μm and a scan size of 3003 μm by 3605 μm. Multiples of uniform distribution measurements for texture components were obtained after contouring using a half width of 10° and a cluster size of 5°. The MTEX [203] MATLAB toolbox was used to reconstruct grains and calculate convex hull based shape parameters for the grains to quantify the deviation from columnar to equiaxed growth. The convex hull is a polygon whose shape encloses and contains all the points making up an entity – in this case a grain. Grains which approach a rounded and equiaxed shape tend to have a very low deviation from their convex hull, while grains which are less rounded and more irregular in shape will tend to give higher deviation values from their convex shape.

5.3 Results and Discussion

The differences between each of the grains for the different conditions and a fully convex shape are shown in Figure 5.2. The plots for the CONTROL condition and $E.D_{3.89}$ condition are shown in Figure 5.2 (a and b) respectively. For the CONTROL condition, the grain morphology consists of grains elongated along the B.D but also curved in the transverse direction. The larger grains in the specimen have a very irregular shape due to the epitaxial growth present between layers. This translates to a higher deviation from their convex hull. The smaller, rounder grains tend to have lower deviation values. This is also numerically represented in Figure 5.3 (a), where for the CONTROL condition, there is a significant percentage of the scanned area with high deviation values from the convex shape. With the $E.D_{3.89}$ condition shown in Figure 5.2 (b) and Figure 5.3 (c), the grain size increases progressively overall and there is a much higher degree of area covered by grains with elongated, irregular morphologies indicating a much higher degree of columnar growth. Similar observations for a decrease in hatch spacing have been made by Balbaa et al. [232]. While some small areas of globular grains are visible, these are present to a much lesser extent compared to the CONTROL condition.

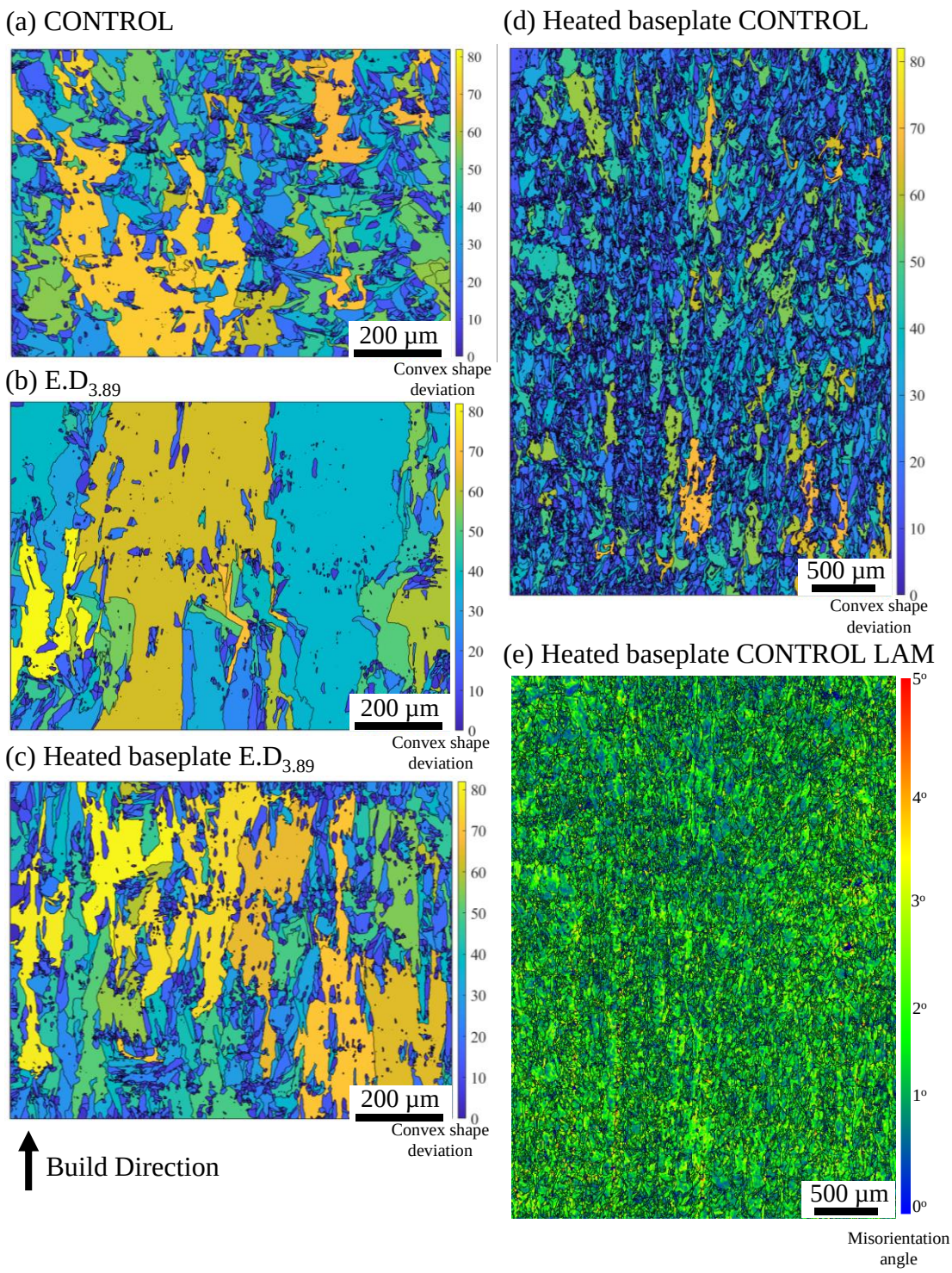


Figure 5.2: Convex hull deviation maps for (a) the CONTROL condition, (b) the condition manufactured at an E.D 3.89 J/mm^2, (c) the E.D at 3.89 J/mm^2 together with a heated baseplate and (d) the CONTROL condition together with a heated baseplate, together with (e) the local misorientation map for the CONTROL condition with heated baseplate.

The solidification rate is primarily dependent on the laser movement speed [42,49], with the maximum solidification rate occurring at the centre line of the melt pool. The laser movement speed was not modified which means that the maximum expected solidification rate was not changed. Through a decrease in hatch spacing moving from the CONTROL condition to $E.D_{3.89}$, there will be a higher degree of remelting promoting epitaxial growth and increasing the difference in temperature between the melt (which is being reheated more often) and the solid. This would translate also to an increase in the thermal gradient over the solidification front. The increased heat input into the melt pool for $E.D_{3.89}$ will also mean that the magnitude of heat flux towards the substrate will be very large which results in grains which are closely aligned in parallel to the B.D, together with a very aligned cellular sub-structure.

The application of a heated baseplate results in a distinct change in the grain size and grain morphology. In the $E.D_{3.89}$ condition with baseplate heating, a mixed mode of growth is present as opposed to the predominant columnar growth observed without a heated baseplate, and the grain size decreases substantially as shown in Figure 5.2 (c). While there is still overall a predominant columnar morphology, there is an increase in the number of very small purely equiaxed grains visible in Figure 5.2 (c) having a very low deviation from the convex hull. While there is still a significant percentage of area with relatively high deviation from a convex shape as shown in Figure 5.3 (d), this is already much reduced compared to the case without baseplate heating shown in Figure 5.3 (c). Through EBSD analysis it was found the small equiaxed grains formed are not oriented favourably with the easy growth direction with a significant number of them having ⟨111⟩ or ⟨011⟩ orientations to the B.D. This also results in reduction of the M.U.D value with a value of 5.94 being obtained for this condition compared to 12.41 obtained for the analogous condition without baseplate heating.

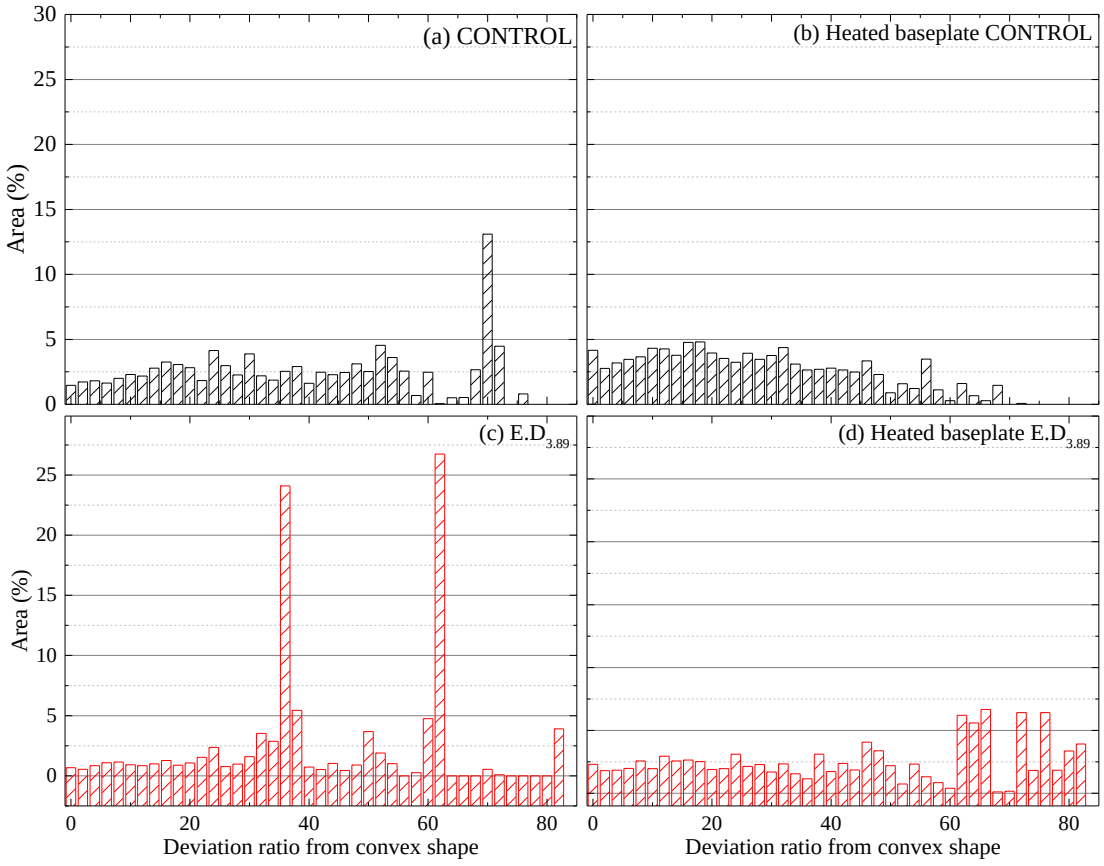


Figure 5.3: Representation of the ratio of deviation from the convex shape with the area % covered for the (a) CONTROL, (b) heated baseplate CONTROL, (c) $E.D_{3.89}$ and (d) heated baseplate $E.D_{3.89}$ conditions.

The addition of baseplate heating is enough to disrupt this predominant columnar growth mode and result in the formation of small equiaxed grains in the microstructure even for the $E.D_{3.89}$ condition where the resulting thermal gradient is quite high due to the opposing effect of a reduced scan spacing (translating to more overlap). This effect is even more evident when baseplate heating was used to manufacture the CONTROL condition as shown in Figure 5.2 (d) and supported by a further reduction in M.U.D from 5.50 to 4.11. Some elongated grains with a highly irregular shape are still visible but the number and amount along B.D is much less compared to conditions without baseplate heating. The shape of the grains overall is also much more uniform and more globular, tending towards smaller deviations from the convex hull shape as can be seen from the distribution for the deviation from convex hull shown in Figure 5.3 (b). A multitude of small round grains are visible as the thermal gradient is sufficiently reduced through baseplate heating coupled with the

inherently high solidification rates characteristic of L-PBF, for equiaxed growth to be initiated. While at the maximum solidification rate expected for this process would mean that a difference of 400ºC due to base plate heating should not have such a large effect, the solidification rate will vary within the melt pool. Thus, as one moves away from the centreline of the melt pool, where the solidification rate is lower, the reduction in temperature gradient from the heated base plate would become more significant as shown in Figure 5.1. The solidification rate also tends to be slower than the laser movement speeds for L-PBF due to the high movement speeds characterising the process [231].

An argument can be made that the formation of the small grains observed here is due to in-situ recrystallisation. The possibility of recrystallisation during L-PBF has been documented by Laleh et. al [233] for 316L stainless steel with a baseplate heated at 200ºC. The recrystallisation temperature for 316L is between 400 to 700ºC while that for IN718 is around 1020ºC [105]. In the work by Laleh et al. [233] following L-PBF the specimen structure consists of a high density of Σ3 grain boundaries. Local area misorientation (LAM) maps also indicate that the LAM in the bulk of the specimens is low following recrystallisation [233]. The LAM map for the heated baseplate CONTROL condition obtained here is shown in Figure 5.2 (e). A high misorientation is visible over the area scanned. The density of Σ3 grain boundaries was also not observed to increase in these specimens indicating that recrystallisation was not the underlying cause for the formation of the small equiaxed grains observed here. Further investigation could be done on a localised area of globular grains to confirm this.

The hardness measurements show that with a change in solidification mode, the mechanical properties can be improved which may be probably attributed to the change in grain size. The hardness for the CONTROL condition was 287 ± 2 HV_5 while that for the $E.D_{3.89}$ condition was 279 ± 5 HV_5. For heated baseplate, at $E.D_{3.89}$ the hardness increased to 287 ± 6 HV_5, while for the CONTROL condition with heated base plate, hardness increased further to 306 ± 6 HV_5. The hardness values observed here are for as-built IN718; thus, relatively low compared to double-aged IN718 but baseplate heating can be easily applied to other superalloy systems which do not require heat treatment. The increase in hardness would also be balanced out by a stress relieving treatment due to the heat ed baseplate reducing the dislocation density and thus hardness of the bulk.

5.4 Conclusion

In summary, the use of a heated baseplate in L-PBF can be applied to move from a columnar solidification mode to an equiaxed mode of growth. This has not been applied for IN718 in the context of L-PBF for altering the CET. While applying a heated baseplate can be useful to process crack prone alloys, applying it for alloys thought to be easily processable using L-PBF such as IN718 provides different benefits. The heated baseplate reduces the thermal gradient, which together with the relatively fast solidification rates leads to equiaxed nucleation and growth within the melt pool. Through this mechanism, an overall decrease in grain size and preferred orientation is observed which together contribute to a slight increase in hardness for specimens processed on the heated baseplate where the reduction in grain size is counteracted by essentially a stress relieving treatment from the baseplate heating being applied. The growth mode observed here is still within the mixed regime thus further work is needed to optimise the parameters to obtain a fully equiaxed structure and characterise the effect of a heated baseplate on the surface finish and density.

CHAPTER 6. Using L-PBF to create functionally graded Inconel 718 Microstructures: characterisation of local mechanical properties and defect formation

6.1 Abstract

This study investigates the viability of using scanning strategies rather than heat source parameters in laser powder bed fusion to modify the mechanical properties of Inconel 718 through variation of microstructure. Both grain size and preferred orientation were successfully tailored. Mechanical testing indicated that the scanning strategy can be used to generate functionally graded specimens; larger grains and more [001] preferred alignment resulting in lower Young's modulus and strength or smaller grains with a reduced preferential [001] orientation along the build direction increasing the Young's modulus and strength. Digital image correlation showed that strain in graded structures was concentrated in highly textured areas. The ductility was low due to lack of fusion defects which formed due to thin Al oxides folded and entrained in the melt pool. Such defects are known to form in casting but have not been discussed in depth in the context of AM. Melt pool motion due to Marangoni flow and recoil effects can be entraining young aluminium oxide films in the melt pool.

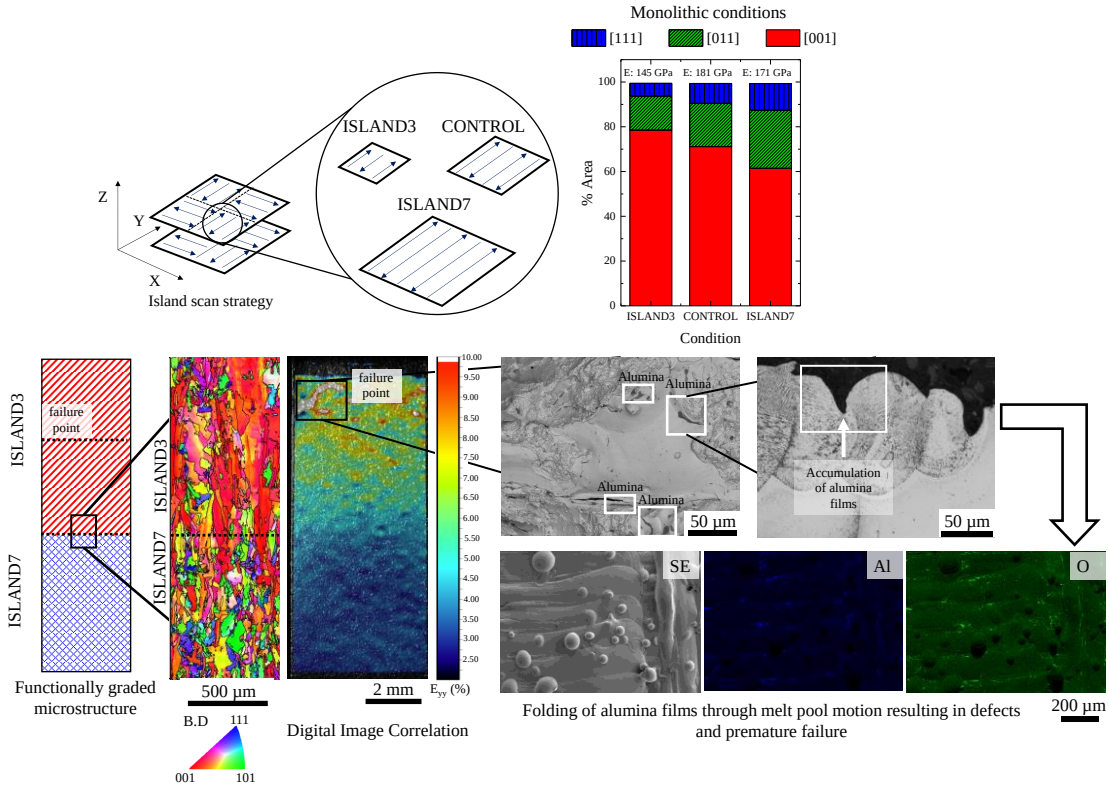
Highlights

1. Changes in scanning strategy were used to modify the microstructure in L-PBF of IN718
2. Graded microstructures were successfully generated with varying mechanical properties
3. Lack of fusion defects contributed to a reduced ductility
4. Origin of the defects was through entrainment of young Al oxide films

Keywords

Laser powder bed fusion, Ni-Superalloys, texture, stress/strain measurements, fracture behaviour

Graphical Abstract



6.2 Introduction

Inconel718 is one of the most used alloys for additive manufacturing of superalloys due to its slow precipitation kinetics and its low crack formation during AM which makes it a good candidate for laser powder bed fusion [234]. The high thermal gradient and cooling rates present in L-PBF produce a very different microstructure when compared to forging processes. Typically, IN718 microstructures after L-PBF consist of an elongated grain morphology with the {001} orientation aligned with the build direction, growing epitaxially through consecutive layers with a columnar dendritic or cellular substructure [23,60,84,235]. Across melt pool boundaries cells tend to grow either epitaxially maintaining the same orientation or through a 90º orientation change, growing along the easy crystallographic growth directions for the crystal [60,85]. Ni is inherently anisotropic with a Zener anisotropy between 2.43 - 2.48 [172,173]. The Schmid factor has been reported to vary from 0.5 for a predominant {001} orientation to 0.25 for a predominant {111} orientation

aligned with to the loading direction [175]. This translates to improved mechanical properties for {011} and {111} predominant orientations along the loading direction at room temperature, while {001} orientations along the loading direction are more favourable for a long stress rupture life at elevated temperatures [154,172,174,176,177]. The mechanical property anisotropy of IN718 after L-PBF due to the favoured alignment has been experimentally demonstrated in several works [84,129,178,179]. Part orientation, specifically with respect to the expected loading direction and building direction, will affect the mechanical properties of the component through the grain alignment in the part together with geometry [7,11,51,60,178,179]. The layer-by-layer building strategy fundamental to L-PBF means that the heat input and therefore the thermal gradient and solidification rate can be modified during the process. Features such as grain size, shape and orientation can be modified during fabrication by altering deposition parameters [168,205]. Being able to modify the preferential texture along the building direction is beneficial as it allows efficient component placement on substrates in addition to location specific, tailored properties. Some studies such as [129,153,180] have investigated the tailoring of microstructure to obtain graded components with mechanical property grading using L-PBF heat input parameters. While laser heat input parameters are effective at modifying the microstructure, excessive heat input drastically increases porosity and defects [76,111,129,178].

Limited studies have investigated the effect of the laser movement path on the mechanical properties. Geiger et al. [153] use different layer rotation angles between successive layers, to progressively change the texture from a cube-texture to a rotated cube-texture with a scanning angle of 45^{o} degrees to the main axes then to a fibre texture with a 67^{o} orientation between layers which also affected the mechanical properties [153]. While the texture intensity was modified in the transverse plane (i.e. orthogonal to the B.D), the preferred [001] alignment parallel to the B.D was still maintained. This alignment is dependent on the direction of greatest thermal flow which tends to be towards the substrate and rotation of successive layers will not necessarily affect the thermal flow orientation or its intensity. Changing the strategy from a bidirectional to unidirectional strategy, Wan et al. [206] found that the texture along the build direction could be reduced indicating that the directional solidification mechanism typical of L-PBF can be affected through the scanning strategy. The cross-sectional area and height were also found to be important factors affecting the microstructure with thinner cross-sections being affected more by grain nucleation from the part

sides and larger cross-sections being more columnar [236]. The build volume will affect the thermal flow and thus the microstructure. The effect of build volume on the microstructure generated has not been given a lot of attention with the focus typically being on small cubes. Previous work has been conducted by these authors [166] successfully changing the microstructure through scanning strategy for small build volumes.

The scope of this study is to investigate the mechanical behaviour of microstructural grading applied using varying laser scanning strategies. The effect of cross-sectional area and build volume will also be investigated in terms of the microstructure obtained together with the effect of elemental segregation.

6.3 Materials and Methods

An M2 Concept Laser L-PBF system using pre-alloyed gas atomised IN718 powder (Ø 10 to 45 μm, ASTM B637-18 [104]) was used to create flat bars with dimensions of 15 mm by 15 mm by 90 mm ($L \times B \times H$). The chemical composition for the powder is given in Table 6.1. Details with regards to the build parameters and the island scanning strategy employed here are given in Chapter 3. The power, scan speed and hatch spacing were kept constant at 263 W, 1500 mm/s and 0.075 mm respectively, selected for optimised density (>99.5%, [166]) together with a layer thickness of 30 μm. The specimens were manufactured with their B.D parallel to the tensile axis. All processing was carried out under a continuous feed of argon (< 0.1% O_2). Single layers were produced using scanning parameters denoted as CONTROL, ISLAND3 and ISLAND7 in Table 6.2 to facilitate the measurement of the melt pool dimensions. These consisted of 1 scan track, 1 island and a single layer of 90 mm by 20 mm.

Table 6.1: The chemical composition of the IN718 powder used compared to ASTM B637 [104].

Element (wt.%)	Ni	Cr	Fe	Nb	Mo	Ti	Al	O	C
IN718 Powder	52.01	19.90	17.96	5.27	2.97	0.95	0.55	0.02	0.04
IN718 ASTM B637-18	50-55	17-21	bal.	4.75 - 5.50	2.80 - 3.30	0.65-1.15	0.20-0.80	-	0.08 max

Dual graded specimens were manufactured; having one end optimized for a large grain size and texture aligned with the B.D and the other end optimised for a low texture aligned with the B.D and smaller grain size. The grading was varied going from a low texture/smaller grain size towards a higher texture/larger grain size to avoid epitaxial growth of coarse grains into the fine grained structure [129]. The parameters used for the manufacture of graded bars are given in Table 6.2. Coupons were removed from the substrate and heat treated as per ASTM B637-18 [104]. A solution treatment at a temperature of 980ºC for 1 hour was applied followed by water quenching and double-ageing at 720ºC for 8 hours followed by furnace cooling to 620ºC, with a 10 h hold time followed by air cooling. The relatively low solution treatment temperature in comparison to the recrystallisation temperature for IN718 of 1020 to 1050ºC [105] was chosen to retain the microstructure generated as confirmed in Chapter 4 [166].

Table 6.2: Scanning strategy parameters.

Test condition designation	Island size (mm)	Island shift in X and Y directions between each layer (mm)
CONTROL	5	1
SHIFT4	5	4
ISLAND7	7	1
ISLAND3	3	1
	Bottom grading	Top grading
GR_ISLAND/SHIFT	ISLAND3	SHIFT4
GR_ISLAND	ISLAND3	ISLAND7

After heat treatment, the tensile bars were contoured and sliced per ASTM E8M [198] in a dog bone shape with a gauge length of 5 mm by 20 mm with a 1 mm thickness. This procedure eliminated the rough as-built surface finish to allow focus on the microstructural impact on performance. The flat bars were polished using a vibratory bowl polisher followed by metallographic polishing of 1 side to a mirror-like finish using 0.04 µm colloidal silica solution.

Optical microscopy was used to obtain melt pool cross section measurements for single layer

specimens after etching the surfaces with Kalling's etchant for 3 seconds. These measurements were used to determine the melt pool depth along the length of an individual island. Energy dispersive spectroscopy measurements were performed of the melt pools at the surface of the specimens using a field emission Merlin Gemini scanning electron microscope equipped an EDS Ametek detector. Fractography was investigated using a field emission Tescan Mira 3 SEM equipped with a widefield view camera on regions of interest for the fracture surfaces after tensile testing using both secondary electron and backscatter electron signals. EDS was used for chemical analysis of areas of interest. EBSD measurements were performed using a step size of 1.5 μm and a scan size of 1000 μm by 800 μm to generate inverse pole figure maps and pole figures. Larger maps were carried out on the graded interface region for the GRADEDISLAND condition using a step size of 2.5 μm with a scan size of 2000 μm by 680 μm. Multiples of uniform distribution measurements for texture measurements were obtained after contouring using a half width of 10º and a cluster size of 5º. The grain size measurements were calculated on a comparative basis due to the non-parametric grain size distribution. To directly compare the grain size distributions effectively, the line intercept method was used in the B.D according to ASTM E112-13 [202] for intercepts equivalent to 4 points or more (i.e. 6 μm). The grain length distributions along the B.D were plotted as cumulative grain fraction of the intercept line versus the grain diameter. These curves can be used to directly correlate the distribution in grain diameters (shown on the X axis) covering a certain line percentage (shown on the Y axis).

Preliminary room temperature tensile tests were conducted as per ASTM E8M [198]. The elastic part of the test was performed using strain control at a strain rate of 0.015 min^{-1}. For this part of the curve the extension was measured using an extensometer. Beyond the elastic limit of the curve, the strain rate was increased to 0.4 min^{-1} and extension measurements were tabulated using the machine crosshead displacement values. Tensile testing with digital image correlation was performed on the GRADEDISLAND condition. The test was performed on an Instron universal testing machine in displacement control using a 0.002 min^{-1} strain rate – equating to a crosshead displacement rate of 0.1 mm/min. The strain was measured using a knife edge extensometer and in-situ DIC. Images were acquired using a Nikon D850 camera with 32 megapixels was used in conjunction with an Opto Engineering TC16M012 2:1 magnification telecentric lens at an acquisition rate of 0.1 Hz. These images were converted from raw format using Matlab and analysed using Davis 8.4 by

LaVision [204]. The images were analysed after correcting for lateral shifting and using a least square correlation function for displacement measurement in both the y-direction (loading direction) and the x-direction (lateral direction). Three seeding points were used per analysis and the image time series was analysed with respect to the previous image. A smoothing algorithm using gaussian linear smoothing and adjacent averages was applied to reduce noise in the strain maps obtained.

6.4. Results and Discussion

6.4.1 Microstructural analysis

The IPF maps obtained for the tensile bars are shown in Figure 6.1 (a to c) together with the cumulative line fraction curves shown in Figure 6.1 (d) compared to equivalent small build volumes obtained in previous work [166] for the SHIFT4, ISLAND3 and ISLAND7 conditions. With the larger build volumes used for the tensile bars, the grain length along the B.D increases overall for all conditions compared to that obtained for smaller build volumes in previous work [166]. Typically the average grain size tends to increase with build height, as the previously deposited layers will be at a temperature higher than room temperature, and thus as the build height increases some heat is expected to accumulate [66]. This in addition to the reduced heat sink effect of the baseplate as the height increases together with relatively the low thermal conductivity of IN718 will further increase heat accumulation, reducing the cooling rate and resulting in coarser grains.

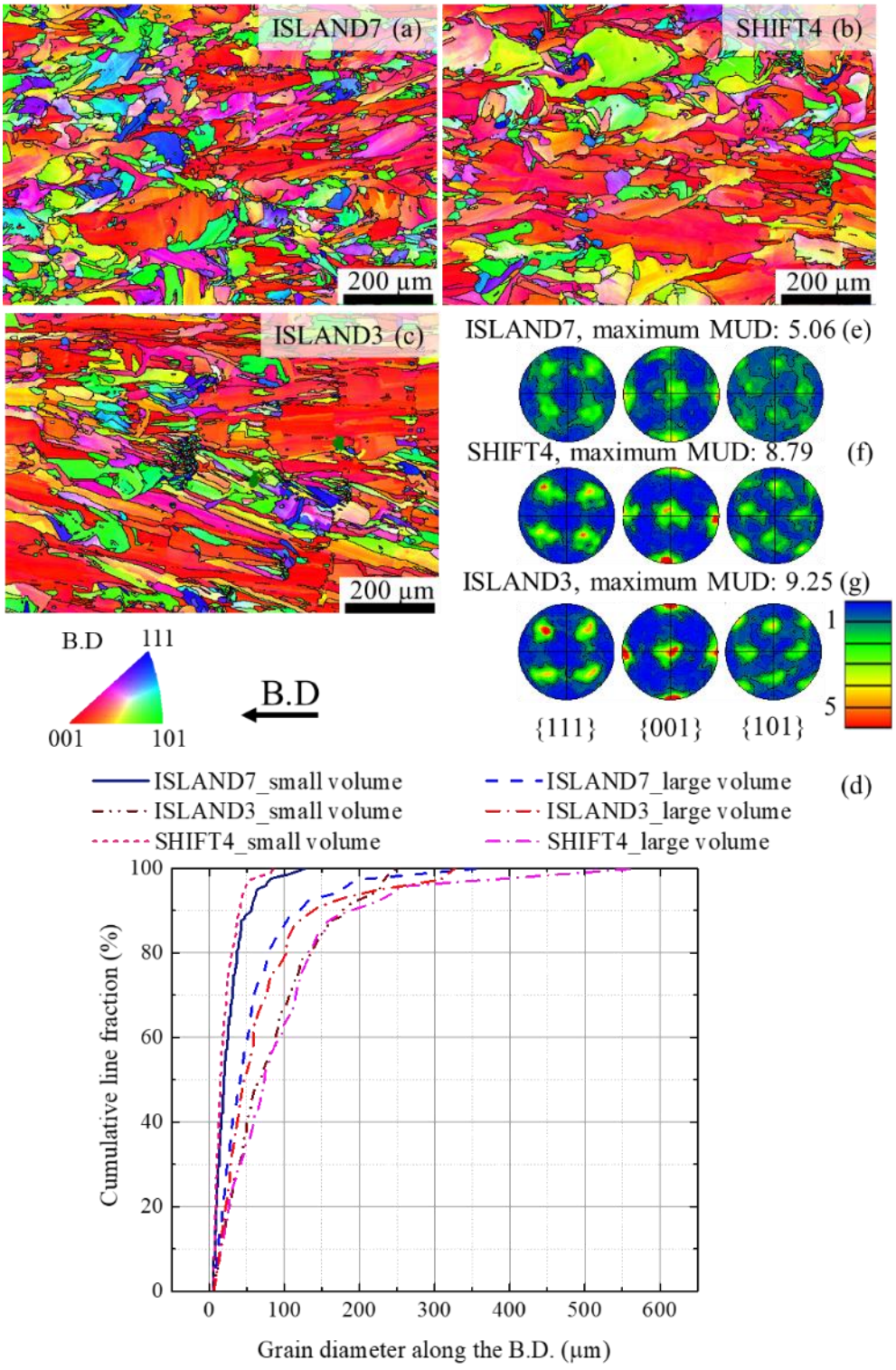


Figure 6.1: IPF maps for tensile bars for the (a) ISLAND7 (b) SHIFT4 and (c) ISLAND3 conditions with (d) a comparison of the changes in grain diameter along the B.D compared to previous work [166] on small build volumes and pole figures for (e) the ISLAND7 (f) the SHIFT4 and (g) the ISLAND3 conditions.

The ISLAND7 condition still has an overall smaller grain size than the ISLAND3 condition with larger volumes. However, the grain size along the build direction of the SHIFT4 condition exceeds that of the ISLAND3 condition for the large tensile bar volumes under investigation here. With large build volumes, the ISLAND3 condition still results in extremely elongated and directionally oriented grains as shown in Figure 6.1 (c). The microstructure obtained is comparable to microstructures obtained in directional solidification with grains extending beyond 1 mm along the B.D. Stray grains can be observed having unfavourable [111] or [011] growth orientations and being overcrowded by favourably oriented [001] grains. The ISLAND7 condition shown in Figure 6.1 (a) still has an amount of elongation and texturing but the grain size is smaller with significantly higher numbers of grains in [011] or [111] orientations aligned to the B.D.

Pole figures for each respective condition are given in Figure 6.1 (e to g). The ISLAND7 condition still has a lower texture than the ISLAND3 condition even with a larger build volume while the SHIFT4 condition approaches the higher texture seen for the ISLAND3 condition. An increase in columnar growth indicated by higher texture coefficients and longer grain lengths along the B.D occurs when moving to smaller island sizes. Increasing the island shift with small build volumes was reported [166] to reduce the grain size and preferential alignment overall however with large build volumes it appears that this effect is not effective. The underlying mechanism for this is described in Chapter 4 and would be expected to be dependent on the cross-sectional area scanned. The reduction of the alignment of the [001] axis to the build direction is quite difficult to achieve as the easy growth axis for cubic materials is along the [001] direction and this tends to align itself with the direction of highest thermal flux which lies along the B.D. Therefore, to change the alignment along the build direction one would have to change the direction of the resulting thermal flux. This is initially angled towards the base plate due to the initial effect of the base plate in providing a cooling effect and, for taller components, the insulative nature of the powder at the sides of the component reducing the heat flow towards the sides making heat flow through the previously solidified and cooled metal easier than through the powder. For the ISLAND7 condition, the faster heat loss from the lower exposure time to the laser coupled with the longer time between hatches will reduce the flow of heat towards the substrate thus reducing the alignment with the B.D. A similar effect has been observed in [92,158,206] where changes in the scanning strategy affected the thermal flow modifying the preferential alignment along the building direction. A difference in

texture strength is also evident – the ISLAND3 condition has an M.U.D value of 9.25; nearly double that observed for the 7 mm island size at M.U.D of 5.06. The texture observed for the ISLAND3 condition is a well-defined cube texture with the [001] axes aligned with the build direction and the X and Y directions of the build. For the ISLAND7 condition, the grains are somewhat oriented parallel to the build direction and the alignment with the X and Y directions of the build is less predominant.

It is important to note that the growth mode seen here is still columnar but the changes in scanning strategy are affecting the tilt of the grains along the B.D and the predominant heat flux direction. The grain orientation is dependent on the boundary between the solid and liquid phases in the melt pool. Grains will grow from the melt pool boundary towards the centre in parallel to the direction of maximum heat flow [14]. In L-PBF, melt pools have a flat or near-flat solidification front [14]. Typically, this results in columnar dendrites or aligned cells which grow with their 〈001〉 direction parallel to the building direction forming elongated columnar grains [14]. With a smaller island size, the heat flow will be concentrated in a much smaller area thus the thermal flow would be intense along the build direction compared to a larger island size. Furthermore, smaller island sizes require a longer laser on time on the overall component as the laser will need to move between numerous smaller islands further reducing the cooling rate as measured in Section 4.4.6. With a smaller island size, the duration between hatches will be shorter than with larger island sizes. The first hatch will be scanned in cold material, but with subsequent hatches the environment heats up as there is not enough time for heat dissipation to occur and it is thought through melt pool modelling that this would result in a consecutive increase in melt pool depth as the island progresses [166]. With larger islands this effect would be less evident as the laser needs to traverse a longer distance thus there is more time between consecutive hatches. This was confirmed through melt pool measurements in single layer melt pools shown in Figure 6.2 where with smaller island sizes there is an increase in the melt pool depth with distance along the island supporting modelling data Section 4.4.7. There is also a much higher degree of scatter in the measurements for melt pool depth as the island size decreases which could be an indication of melt pool instability. Changing island size is relatively unaffected by the cross-sectional area being scanned except for the heat input overall being higher as there will be a larger number of islands to complete but the relative difference between the 2 strategies is still effective with different cross-sections and build volumes.

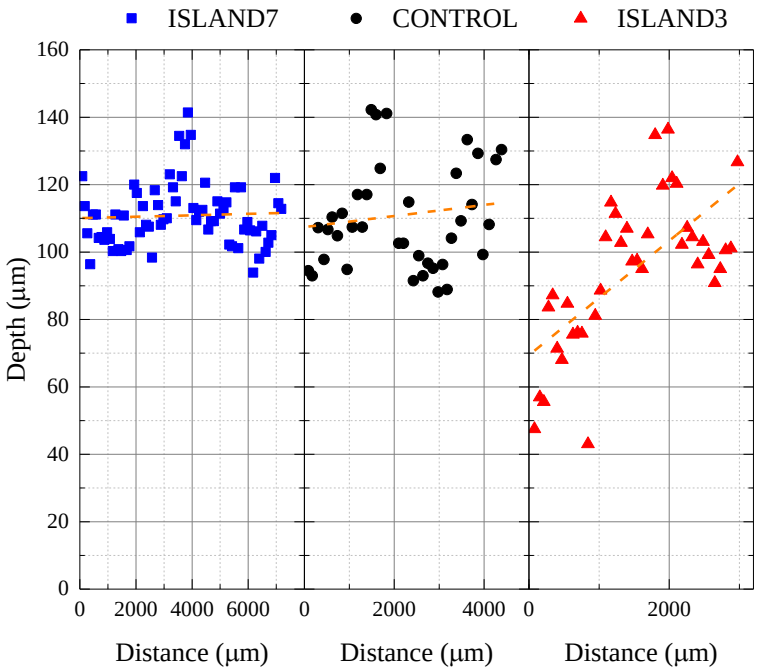


Figure 6.2: Change in melt pool depth with distance along the island.

The idea of consecutive changes in melt pool size being relevant for the microstructural morphology contradicts the hypothesis presented by Carter et al. [160] where the laser is equated to a moving band of heat and movement along individual hatches is not considered. Changes in the motion along a single hatch also have an important effect on the microstructure being generated. However in work by Carter et al. [160], a 5 mm island size was used where the effect while present is minimal, as significant changes in depth along an island only became evident as the island size is decreased to 3 mm. The consecutive increase in melt pool depth detailed for small island sizes can become important even in unidirectional or bidirectional scanning strategies if the cross-sectional area of the component is small due to the relatively quick return of the laser beam to the adjacent position.

6.4.2 Tensile performance

The Young's modulus obtained for the CONTROL condition was 181 ± 10 GPa. The ISLAND3 condition exhibited a reduction in Young's modulus to 145 ± 25 GPa. The Young's modulus for the SHIFT4 condition was 174 ± 22 GPa while for the ISLAND7 condition the Young's modulus was 171 ± 11 GPa. The Young's moduli observed for the CONTROL, ISLAND7 and SHIFT4 conditions were close to that observed for wrought IN718 at 208 GPa [15]. Ni is anisotropic and for Ni single crystals, the elastic moduli along the three principal crystallographic directions vary from

119.8 GPa along the [100], 200.8 GPa along the [011] and 259.2 GPa along the [111] directions [172,174]. The increased relative proportion of grains with their [100] oriented to the B.D for the ISLAND3 condition contribute to the decrease in modulus observed.

Figure 6.3 compares the area covered by different orientations for each strategy for the small volumes discussed in Chapter 4 compared to the large build volumes used for tensile bars under investigation here. It is evident that when changing the build volume to that of the larger tensile bars, the number of grains with [001] alignment to the build direction increases; this is most evident for the SHIFT4 condition where the [001] alignment is of similar level to that observed for the CONTROL condition. This is not surprising since the change in island shift is susceptible to changes in cross-sectional area being scanned. The effect of grain orientation in changing the Young's modulus is evident when considering Figure 6.3, where the ISLAND7, CONTROL and SHIFT4 conditions all have significant amounts of grains oriented with their [011] directions in parallel to the B.D which in turn results in the higher Young's modulus observed. The ISLAND3 condition nominally has the largest amount of [001] orientations parallel to the B.D which results in the lower Young's modulus. It is also evident that the changes in build volume do not lead to a massive change in the preferred orientation compared to the smaller build volume when modifying the island sizes.

Similarly heat treated IN718 built vertically was reported to have a modulus of 163 GPa while specimens inclined at 45^{o} to the build direction were reported to have a modulus of 188 GPa [199] and specimens with a predominant [011] orientation were reported to have a Young's modulus of 220 GPa [237]. Specimens made using EB-PBF but with an equiaxed microstructure were reported to have a Young's modulus of 183 GPa [130] which is quite close to the values observed for the CONTROL, ISLAND7 and SHIFT4 conditions. Young's modulus values of 125 GPa were reported for specimens with a predominant [001] orientation along the loading axis [237] which is closer to that observed for the ISLAND3 condition. Young's modulus values for the ISLAND7 and for the SHIFT4 condition were close to that obtained for the CONTROL condition. It is surprising that the ISLAND7 condition did not exhibit a marginally higher Young's modulus given that the percentage of [011] and [111] oriented grains increased – however there was some variability in the measurements which would make it difficult to detect small changes in Young's modulus.

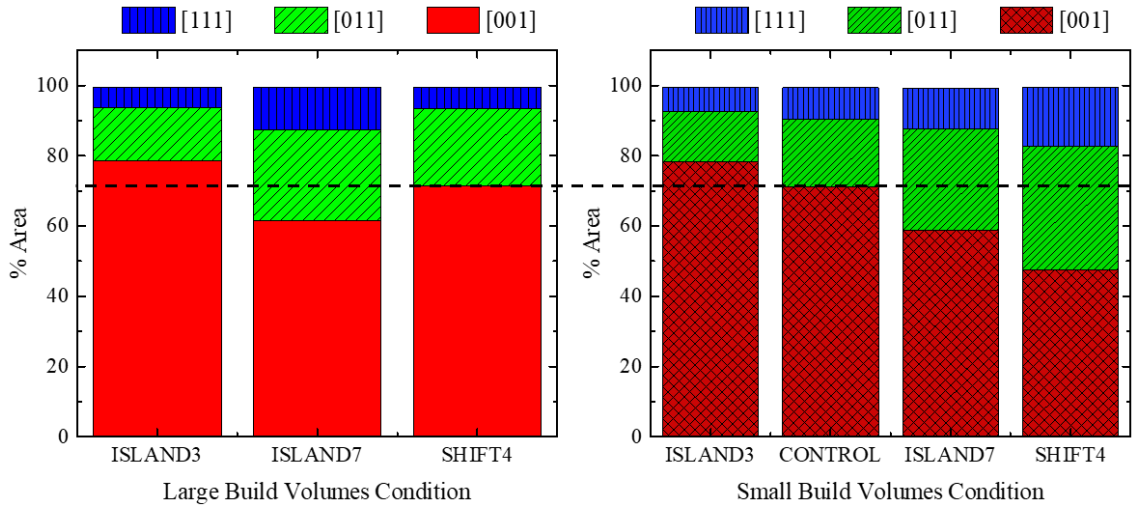


Figure 6.3: Area% consisting of different crystallographic orientations aligned with the build direction for large build volumes (15×15×90 mm) conducted in this work compared to small build volumes (10×10×10 mm) conducted in Chapter 4 [166].

For the graded conditions the average Young's moduli were 176 ± 28 GPa for the GR_ISLAND condition and 139 ± 40 GPa for the GR_ISLAND/SHIFT condition. The Young's modulus observed for the GR_ISLAND condition was higher than expected, since the grading also consisted of the ISLAND3 parameters. From a microstructural perspective the grains oriented with their [001] aligned to the build direction would elastically deform more than those which are not so aligned. However, grains which are not aligned with their [001] to the build direction (and axis of deformation) would restrict the movement of the preferentially oriented grains. For strain to occur the non-aligned grains would also have to be straining by the same amount, accounting for the Young's modulus values close to those of the ISLAND7 condition. Young's modulus measurements for the GR_ISLAND/SHIFT condition were lower, however as a much higher degree of predominant [001] preferred alignment was present for the SHIFT4 compared to the ISLAND7 condition a lower Young's modulus might have resulted. The measurements for GR_ISLAND/SHIFT were also prone to some significant variability which makes it difficult to make a meaningful conclusion.

The box and whisker plots for the mechanical properties for the monolithic conditions are shown in Figure 6.4 (a to c). The yield strength and ultimate tensile strength were observed to be as per the ASTM B637-18 [104] standard for double-aged IN718 for all conditions except the ISLAND3

specimens. The modulus, σ_y and UTS values observed here for the CONTROL and ISLAND7 conditions were quite close to values observed for IN718 optimally heat treated to maximise the effect of dislocation strengthening built along the horizontal plane by Gallmeyer et al. [238] demonstrating the efficacy of the scanning strategy modifications in optimising the mechanical properties. The average σ_y for the GR_ISLAND and GR_ISLAND/SHIFT were found to be 1142 ± 10 MPa and 1115 ± 37 MPa respectively. The average σ_y for the GR_ISLAND and GR_ISLAND/SHIFT were quite close to what was observed for the monolithic conditions. The UTS for the GR_ISLAND condition was 1312 ± 20 MPa and 1305 ± 43 MPa for the GR_ISLAND/SHIFT condition.

The ductility required by ASTM B637-18 for IN718 in the solution treated and double-aged condition is of 12% [104]. In this work, the ductility was lower than that required for the standard as shown in Figure 6.4 (c) and a large variability in ductility overall was observed indicating that premature failure was occurring which would also affect the UTS values obtained as work hardening would be limited.

The variability in measurements for σ_y and UTS observed here for is typical for AM due to the large variation in grain orientation and size within specimens. The σ_y will depend on a number of factors amongst which the preferred orientation, cell size, precipitate amount and grain size will affect to a certain extent [85,168,238]. The effect of cell size on the σ_y of as-built IN718 has been quantified by Gallmeyer et al. [238]. For these conditions, using cell sizes calculated in Chapter 4 for small build volumes it is expected that the cell size would contribute 256 MPa for the ISLAND7 condition, 243 MPa for the SHIFT4 condition, 252 MPa for the CONTROL condition compared to 201 MPa for the ISLAND3 condition, due to the larger cell sizes resulting from the slower cooling rate associated with the ISLAND3 condition. It is however not expected that the cell dislocation structure would contribute massively to the strength after solution treatment as the dislocation density would decrease due to the solution treatment stage.

The crystal orientation is also a factor to consider as dislocations will move through slip planes, and where these are not favourably orientated, a rotation of the plane or twinning will need to occur for slip to be more favourable. For fcc crystals, slip occurs along the ⟨110⟩ type directions in the {111} type planes. The changes in σ_y observed here were slight even though there were some distinct

differences in grain orientation and grain size between different conditions. The area of crystals with the [001] aligned to the build direction is still relatively high for both ISLAND3 and ISLAND7 conditions. While there is a difference in crystallographic orientation and grain size this may not be large enough to result in a statistically significant improvement in σ_y. For the ISLAND3 condition there is a tendency for a lower σ_y, although the variability in the measurement is quite high.

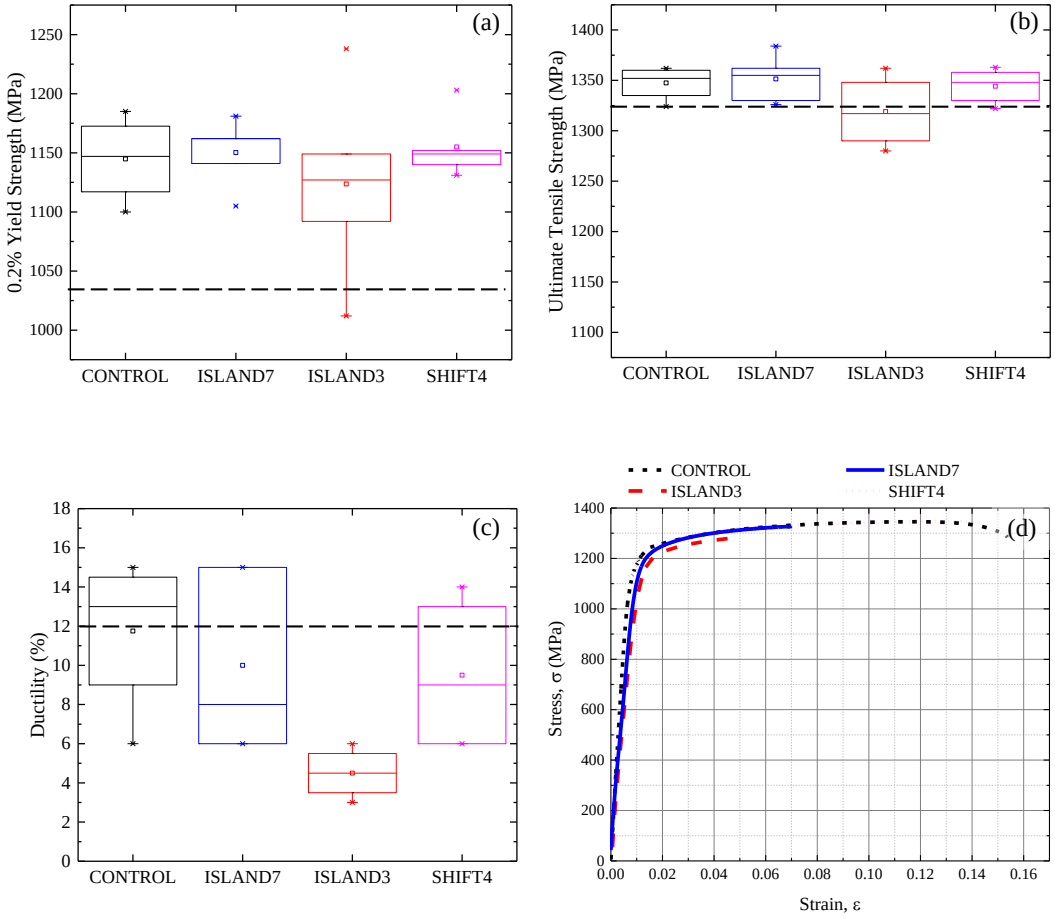


Figure 6.4: Box and whisker plots for (a) 0.2% σ_y, (b) ultimate tensile strength and (c) ductility for monolithic conditions. Dashed lines indicate the values prescribed per ASTM B637-18 [104]. Representative stress-strain curves for the different monolithic conditions are shown in (d).

The Schmid factor represents the resolved shear stress on a specific slip system. A higher Schmid factor corresponds to a higher resolved shear stress for slip and therefore a grain with a higher maximum Schmid factor is often considered easier to deform compared to a grain with a lower maximum Schmid factor [175]. The Schmid factor map data for ISLAND7 and ISLAND3 tensile

bars is shown in Figure 6.5. There is a difference in between the different conditions shown, with the ISLAND7 condition experiencing overall a higher area percentage of grains with a lower Schmid factor. However, both conditions have a relatively high proportion of area consisting of Schmid factors of 0.4 and higher which would explain the relatively similar yield strengths of both conditions. The other factor at play here is that the strength of IN718 is dependent on the precipitates forming after ageing which inhibit dislocation motion. This would have a much larger contribution strengthening compared to changes in the crystallographic structure.

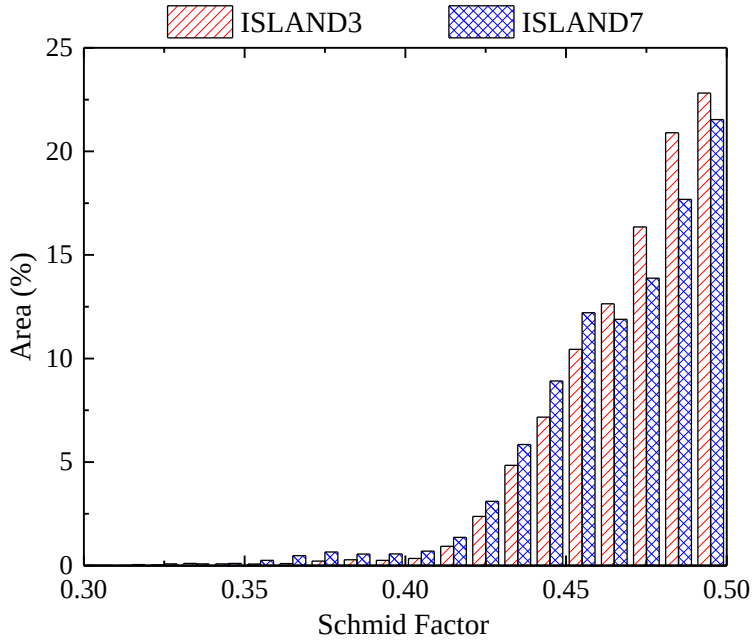


Figure 6.5: Schmid factor maps for large build volumes for the ISLAND7 and ISLAND3 conditions.

For the ISLAND3 condition, the UTS obtained is lower than the other conditions indicating that the larger cell size and grain size affect the mechanical properties as has been discussed. On the other hand, this low UTS could also be a direct result of premature failure brought about by a reduction in ductility from defects in the specimens acting as stress concentrators. In fact, representative stress-strain curves for these specimens shown in Figure 6.4 (d) clearly show that for the ISLAND3 condition there is no necking, with the specimen failing abruptly during the plastic deformation regime. For the ISLAND7 condition and SHIFT4 conditions there was a lot of variability between different specimens with some specimens showing a considerable region of strain hardening and some specimens having a limited region of strain hardening followed by abrupt failure. The UTS values for the GR_ISLAND and GR_ISLAND/SHIFT conditions were also

comparable to those obtained for the ISLAND3 conditions further supporting the fact the limited work hardening was occurring due to premature failure. The ductility for the ISLAND3 condition was also the lowest among all the processed conditions obtained (< 5%). Similar premature failure was observed for specimens which were graded where the ductility for the graded conditions was <5% and specimen failure was characterised by a short strain hardening region with no necking followed by abrupt premature failure; in the region scanned with the ISLAND3 parameters. The ductility for the ISLAND3 condition is also the lowest among all the processing conditions obtained (< 5%) with the graded conditions also having a similarly premature failure. The UTS values for the GR_ISLAND and GR_ISLAND/SHIFT conditions were also comparable to those obtained for the ISLAND3 conditions further supporting the fact the limited work hardening was occurring due to premature failure.

6.4.3 Digital image correlation

A schematic of the grading for the GRADEDISLAND condition together with the respective IPF map, grain size distribution and strain map are shown in Figure 6.6. The physical interface between the 7 mm island and the 3 mm island parameters is visible and delineated in Figure 6.6 (a and b). The grain size for the interface region was found to be overall smaller than the grain size measured at both ends and the 3 mm island strategy was effective at creating larger and more aligned grains. The interface area was rescanned and remelted twice in a small overlap region of 90 μm thick (equivalent to 3 layers) to ensure a good bonding between layers which may have disrupted the epitaxial growth through re-melting and the ensuing re-nucleation of the pertinent areas. The interface depicts a chaotic and gradual transition from one microstructure to the other with the absence of a distinct marked difference between regions. The large grains are growing epitaxially out of smaller favourably oriented regions in the interface zone. The gradual transition in morphology affects the transition in strain distribution as shown in Figure 6.6 (d and e) where the strain changes gradually, from an area exhibiting a low strain towards the area exhibiting a higher degree of plastic deformation. Popovich et al. [129] observed that for graded structures where the low energy input condition followed the high energy input condition, growth of the large [001] oriented grains would occur into the region of smaller more equiaxed grains extending up to 500 μm in length. This was not observed here as the condition producing larger grains was scanned after the condition producing smaller grains. In the work conducted by Popovich et al. [178] a sharp

transition could be observed from smaller, randomly oriented grains to larger aligned grains which also results in a drastic transition when the components are placed under load. Having a gradual interface means the mechanical properties gradually transition allowing a smoother strain distribution between the two areas. During tensile testing, the failure occurred in the monolithic ISLAND3 condition not at the interface. It is also worth noting that the strain does not appear to be uniformly distributed in each area with some areas exhibiting a higher degree of strain than others, likely due to the anisotropy exhibited by the crystal structure [239]. Grains which are favourably oriented for deformation would be undergoing a higher degree of micro-strain than grains which are not [239].

The strain map obtained through DIC together with strain measurements along the gage length are shown in Figure 6.6 (d and e). The top region built using the ISLAND3 parameters exhibited significantly higher strains compared to the ISLAND7 section. This was expected from the higher proportion of {001} oriented grains to the B.D obtained for the ISLAND3 condition. The image in Figure 6.6 (d) was taken just prior to failure and although the average ductility for this specimen was found to be ~5%, the ISLAND3 region exhibits local strain of around 8 to 9%, while the ISLAND7 condition exhibited around 3% local strain at failure. The specimen's failure origin is depicted by arrows in Figure 6.6 (d) and occurred around 4 mm into the ISLAND3 section. Failure did not occur in the interface region – indicating that the remelting of the region improved consolidation. Unfavourably oriented grains may also have constrained the deformation at the interface. The specimen exhibited overall a low ductility due to a defect in the area where failure occurred as indicated by fractographic surface investigations discussed in Section 6.4.4.

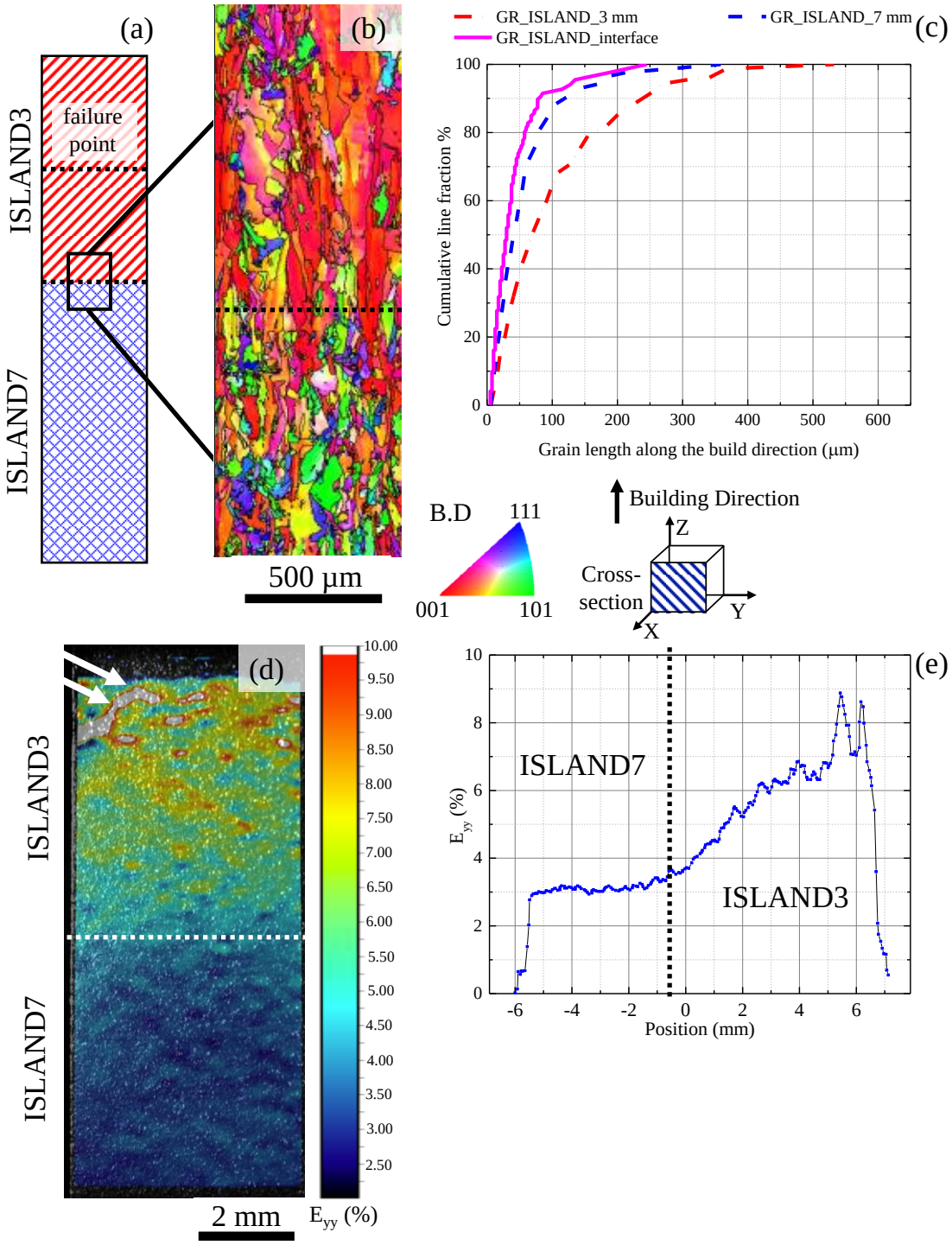


Figure 6.6: Showing the (a) schematic illustration of the grading applied for the GR_ISLAND condition with the failure point demarked, and an IPF map for (b) the central region, (c) the cumulative grain size distribution for the different ends and central region together with (d) the strain map over the area prior to failure with arrows marking the origin of failure and (e) the average strain over the length of the specimen prior to failure.

6.4.4 Fractography

Due to the characteristic limited ductility of the specimens reported in this work, detailed fractographic investigations were performed to investigate the reason behind the premature failure observed. Representative fracture surfaces are shown in Figure 6.7 and features from different monolithic and graded conditions are shown in Figure 6.8 and Figure 6.9. Even though full consolidation was obtained (density >99.95%) as shown also for typical fracture surfaces in Figure 6.7 (a and b), the failure of the specimens was still defect driven by small, localised areas where lack of fusion (LoF) occurred shown in Figure 6.8 (a to e).

Several fracture surfaces exhibited small step-like features along the surface as shown in Figure 6.7 (c). The formation of these step-like features is related to crack propagation along grain boundaries. The grain morphology of the specimens had some transverse grain boundaries perpendicular to the build direction as shown in Figure 6.1 (a to c). This would facilitate Mode I opening crack mechanics, where dislocations pile-up at grain boundaries during loading and facilitate micro-cracking along the grain boundaries [240]. The flat nature of some grain boundaries provides an easy crack propagation pathway during failure. Due to the relatively large grain size when compared to forged counterparts, crack propagation along the transverse grain boundaries is easier, resulting in areas where these step-like features are observed. The magnitude of the steps is between 10 and 25 μm while the average grain size along the transverse direction for the work conducted here is between 17 to 18 μm which is within the size range of the steps observed on the fractographs. Similar features have been observed elsewhere and also associated with localised failure along grain boundaries [178,241]. All the specimens also exhibit a dimpled fracture surface such as that shown in Figure 6.7 (d) with micro-void coalescence characteristic of relatively ductile metallic materials [240]. This together with the step-like features indicates there is a mixed mode of failure present, with transgranular failure active overall with some areas exhibiting failure along the grain boundaries.

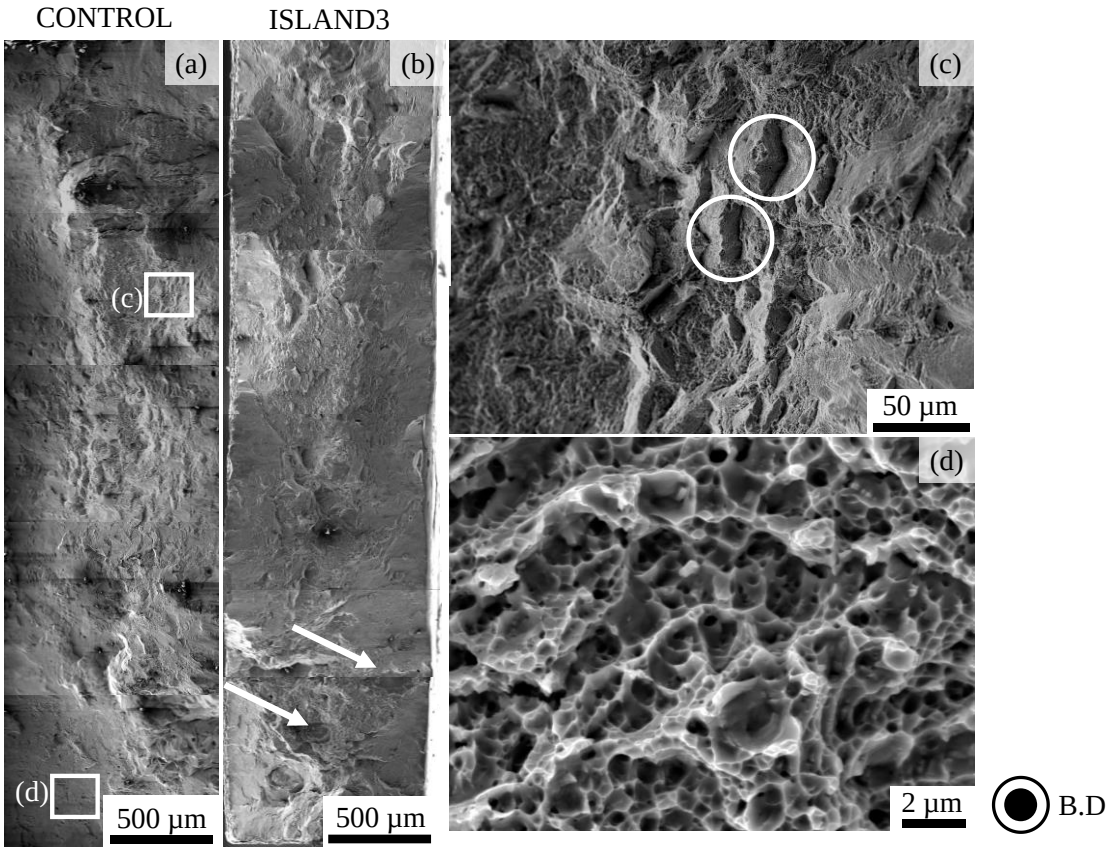
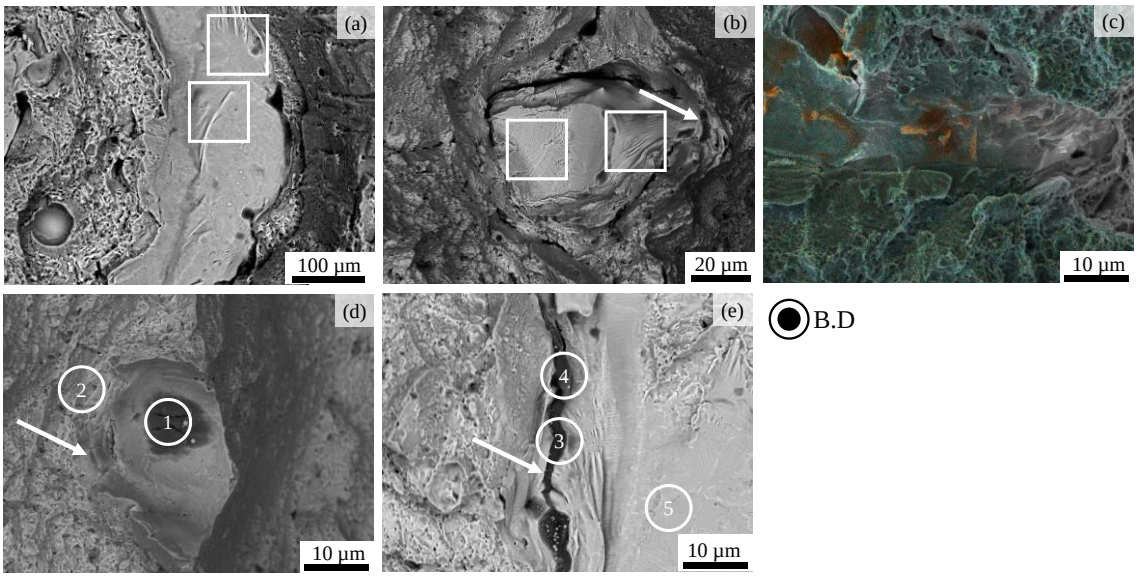


Figure 6.7: Representative fractographs showing an overview of the fracture surface for the (a) CONTROL and (b) ISLAND3 conditions with areas of lack of fusion marked by arrows together with (c) showing steps in the fracture surface as circled and (d) showing micro-void coalescence.

For specimens where the ductility was low (<5%), small and localised defects were observed in the fracture surface; representative images are shown in Figure 6.8 (a to e). Such specimens still exhibited micro-void coalescence indicating that the failure mode had not changed but that the defects were reducing the load bearing cross-section and acting as points of stress concentration. This was consistently the case for the ISLAND3 condition resulting in the prevalently low ductility values, but also sporadically observed with the other conditions resulting in the high variability of ductility observed. For specimens where such defects were not observed on the fracture surface, the ductility was higher at ~15% with some necking also observed in the corresponding stress-strain graph and meeting the ductility requirements set out in for solution treated and aged IN718 ASTM B637-18 [104]. The surface of such defects was characterised by a slight wrinkled appearance and several straight parallel lines as shown in Figure 6.8 (a, b and e). No evidence of dimpling was observed on the defects indicating that the defects were not part of the load bearing area.



Element (wt. %) Position	Ni	Cr	Fe	Nb	Ti	Al	Mo	O
1	42.4	23.4	17.9	0.7	14.5	0.4	0.3	-
2	53.8	19.8	17.9	2.7	1.1	0.3	1.8	-
3	26.0	11.5	9.8	2.3	3.5	22.9	1.3	19.1
4	13.4	7.8	5.5	1.4	5.6	31.3	0.7	28.7
5	49.1	18.9	17.7	4.6	1.0	1.0	2.6	-

Figure 6.8: Representative fractographs for flat defects in (a) and (b) with boxes showing wrinkles and slip bands, together with (c) EDS composition map with orange showing Al and green showing Ni, (d) flat defect with a Ti enriched particle and (e) a flat defect with an Al elongated oxide. Arrows mark Al oxides. Corresponding chemical composition of points of interest is denoted.

Fractographs taken at higher magnifications used in this work, such as Figure 6.7 (d), did not exhibit fracturing of Laves particles – thus the brittle fracture of any remaining Laves phase was not the primary reason behind the low ductility observed. The relatively low ductility and its high variability together with the evidence of micro-void coalescence indicate that failure was premature, and despite the specimens being nominally dense resulting from defects. The fracture surfaces were characterised by defects appearing to be from lack of fusion. LoF defects such as the ones observed here are a problem for tensile specimens tested along the building direction as the loading is applied perpendicular to the defect, opening it up [11]. Smaller build volumes in previous work [166] using identical parameters as those used here did not exhibit significant LoF porosity; the specimens were over 99.95% dense. The lack of consolidation observed in the large volumes investigated here is unexpected. Changes in island size have not been associated with an increase in porosity [242]. The

large build volumes also did not exhibit any significant porosity when examined optically prior to the test. The powder used for the manufacture of the tensile bar specimens was virgin powder with a very low oxygen content ~0.02 wt.%. The main difference to the microstructural coupons was that the build volume and cross-sectional area scanned increased and that a tensile load was applied.

Changes in cross-sectional area have been associated with increased porosity [178,243]. With a change in cross-section, it was reported that the smaller areas would be hotter than larger specimens because it would take less time for the laser beam to come back to the same location during a build [243]. However, with multiple specimens built on the same plate this would be less relevant because the specimens have enough time to cool down between layers. The recoating stage will also give further time for cooling. A larger cross-sectional area should be hotter in practice as the laser spends longer melting different areas in the cross-section. Melt pool depth measurements in this work support this; with depths of 126 μm recorded for large cross-sectional areas, compared to depths of 112 μm recorded for a single island and depths of 102 μm recorded for a single track for the ISLAND3 condition. For the ISLAND7 condition the cross-sectional area affected the melt pool depths much less with melt pool depths for large cross-sectional areas recorded at 112 μm, single islands recorded at 106 μm and single tracks having a depth of 107 μm. The melt pool depth also is overall higher for the ISLAND3 condition supporting the indication that these specimens are hotter compared to the ISLAND7 condition. In view of this it is not thought that the change in cross-sectional area is leading to a reduction in the heat input as the melt pools are getting progressively deeper with larger cross-sectional areas. The melt pool aspect ratios were found to be between 1.6 to 2 for the conditions investigated here. An aspect ratio between 1 and 2.5 indicates keyhole mode where the intensity of the laser in the centre is relatively high causing deep penetration which is reflected by the increase in melt pool depth [232]. Aspect ratios exceeding 2.5 shift the melt pool into severe keyhole mode, which can result in porosity at the bottom of the melt pool [232]. Such porosity would also have an irregular shape rather than the flat profile of the defects seen here. The defects seen here are not due to shallow melt pool depth as the depths recorded here are more than the thickness of two layers, thus sufficient remelting occurred. For specimens where lack of fusion due to insufficient melt pool overlap is occurring, the area where the lack of fusion occurred would be filled with remnant powder particles and characterised by shallow melt pools [232] which was also not the case here. Insufficient melting or denudation would also result in defects as strings along

the specimen surface as opposed to the individual scattered defects observed here.

The fractographs also exhibited areas with Al enrichment on the surface of the defects as shown through EDS mapping in Figure 6.8 (c) and adjacent to all the LoF defects as elongated dark Al oxides as shown using backscatter imaging in Figure 6.8 (b, d, and e). High amounts of oxygen were detected in these areas indicating that oxidation occurred either during the build or during powder production. EDS measurements of the matrix did not yield any noteworthy quantities of oxygen. It is not possible to completely avoid oxidation of the alloying elements in IN718. Al and Cr both require an extremely low partial pressure of oxygen to oxidise. Aluminium oxide film formation has also been reported in vacuum casting of Ni-turbine blades containing only 3.0 wt.% Al [244,245]. Small amounts of oxygen will be present in the argon shielding gas during L-PBF and during powder production forming very thin oxides [245,246].

Some areas enriched in Ti were also observed as shown in Figure 6.8 (d), exhibiting micro-cracking indicative of a brittle nature. Potentially this was a titanium carbide as the area is significantly darker than the surrounding area in the backscatter micrograph. The area adjacent to this enriched zone was again flat with faint parallel lines visible at the sides transitioning into the typically dimpled surface characteristic of ductile failure. The fact that powder was not observed embedded in the defects indicates that no powder was spread over that area to begin with. Furthermore, the defects were flat indicating that they were not due to the formation of open, "cave-like" pores on the surface as the laser was scanning.

The faint parallel lines observed on most of the defect surfaces shown in Figure 6.8 (a, b and e) are likely to be deformation twins forming on stretched alumina films [247]. The wrinkles observed on the defect surfaces shown in Figure 6.8 (a, b and e) can be attributed to the folding of the thin oxide film due to melt pool motion. Multiple folds due to melt pool motion would increase the film thickness enough to be detectable in EDS resulting in Figure 6.8 (c) [247]. The oxide films have two sides – a wetted side which is in contact with the molten metal and a non-wetted side which is in contact with the shielding gas [245]. The exposed side in fracture surfaces would be the dry non-wetted side of the oxide [245]. Zhang et al. [245] document the formation of intermetallic phases such as Laves and Nb-rich MC phases on the wetted surface of chromia and alumina based oxides in AM. The Ti carbide observed in Figure 6.8 (d) probably formed in this way as no Ti carbides

were observed in the powder. In fact, the surrounding matrix to the particle is flat with faint parallel lines visible indicating an oxide film was present.

The formation and entrainment of oxide films is frequently reported in casting of Ni-based superalloys, resulting in specimens which appear fully dense as the films are folded closed but showing similar defects on the fracture surface [247–250]. The formation of Al rich oxides has been documented in AM and welding of IN718 [241,251] and the formation of oxide layers on AM powders exposed to oxygen has also been documented [252,253]. In AM, it has been postulated that these films are one of the causes of component failure [254]. Similar aluminium based oxides have been observed in wire directed energy deposition for IN718 [245] – albeit the oxide films observed were much larger than those observed here and were deemed to have been already formed in the filler wire. The formation of alumina and titania films in AM of IN718 during DED has also been reported by Kim et al. [255] using laser engineered net shaping. Detailed investigation of such oxide films for L-PBF on IN718 have not been made.

Powder particles are surrounded by a thin native oxide layer on their surface. For IN718, it is expected that this would consist of chromia although minute alumina rich spots were observed on two powder particles from the sample investigated. No significant segregation of the other alloying elements was observed either on powder surface or cross-section. Vaporisation of chromia increases drastically at temperatures of ~1000ºC which is below the temperature required to melt IN718 [256]. Thus, it is expected that any chromia from the outer native oxide films on the powder would be volatised during the L-PBF process. Alumina vaporises at 3490ºC [257], thus any alumina oxides on the outer surface of the powder would remain in the melt contributing to the elongated oxides seen adjacent to the flat defects as the highest temperature induced by the heat source is around 3000ºC [234]. Spatter of powder being reincorporated in newly formed melt pools could also be contributing to the oxide films observed as spattered particles typically also contain a high degree of oxides on the surface [258–261]. The oxides formed through spatter are typically rounded as opposed to the elongated particles observed here [261]. Spatter particles can also lead to lack of fusion around them due to the low wettability of their oxidised surfaces [262]. The powder used here was virgin powder thus the incorporation of spatter would be limited only to that formed during the process itself and reincorporated into the melt. It is not thought that surface oxides on the powder and spatter were the sole contributors to the formation of the alumina films observed here.

Vaporisation of Al could be occurring during the build followed by its redeposition on the melt pool surface and the formation of a thin oxide layer on the surface of the melt pool [234]. The fact that the condition which is hotter (ISLAND3) suffered extensively from such oxide film formation would support that due to the increased heating, more Al vaporisation occurs resulting in these oxide films being more prevalent. A similar occurrence of Al evaporation and Hf evaporation and segregation at the melt pool sides has been observed by Wang et al. [39] for CM247 LC. If through melt pool motion from recoil and Marangoni flow [35], this film becomes folded on itself it would form a defect entrained in the melt [247]. Evidence of oxide folding for the GRADEDISLAND specimen at the location where failure commenced is shown in Figure 6.9 (a and b). The matching defect was observed in both the specimen halves with a roughened region from where consolidation occurred visible in the middle of a relatively flat defect. Through DIC, the origin of cracking was observed as marked in Figure 6.6 (d) and this correlated to the defect shown in Figure 6.9 (a and b).

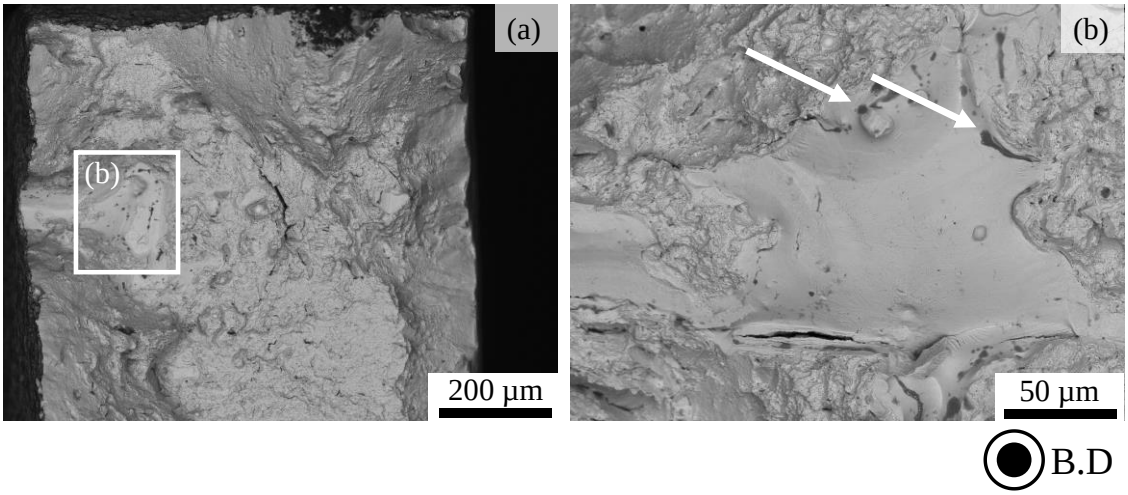


Figure 6.9: (a) Failure point for the GRADEDISLAND condition with corresponding defect on the other half in (b). Arrows mark elongated Al oxides.

While typically the melt pool surfaces were flat, some areas with deep troughs, namely at the edges of the islands and in-between hatches, were observed as shown in Figure 6.10 (a) where such oxides could easily become folded. EDS mapping of the top surface of an island shown in Figure 6.10 (b to d), demonstrated that there was elemental segregation occurring at the boundaries of the melt pools with aluminium and oxygen rich areas being detected at the edges of the melt pool boundaries and at the edges of individual islands accounting for the elongated oxides visible in the fracture surfaces. It is likely that these elongated oxides are not fully remelted during the subsequent scans

which results in them being entrained in the melt. Melt pool Marangoni flow contributes to the movement of these films to the sides of the melt pool [32]. It is thought that the flat defects result from films that have not entirely been moved to the sides or from oxidation of Al deposited at the surface through vaporisation. Single layer melt pools shown in Figure 6.10 (e and f) exhibit melt pools with depressions on the sides. These can be attributed to the Marangoni effect coupled with motion due to vapour recoil pressure from evaporating molten metal such as Al which has a low vaporisation temperature (~2470ºC) [27,31]. The troughs in the melt pools are reduced in depth with consecutive scans (Figure 6.10 (f)) due to the melt pool overlap but at the edges of the scan track some depressions may remain where it will be difficult for enough remelting to occur to remove the segregated oxides. IN718 is classified as being highly manufacturable through AM due to its low Al content resulting overall in a very low mass loss through vaporisation of the element [234]. However, the Al amounts present in the alloy are still enough to result in significant vaporisation affecting the reliability of such components.

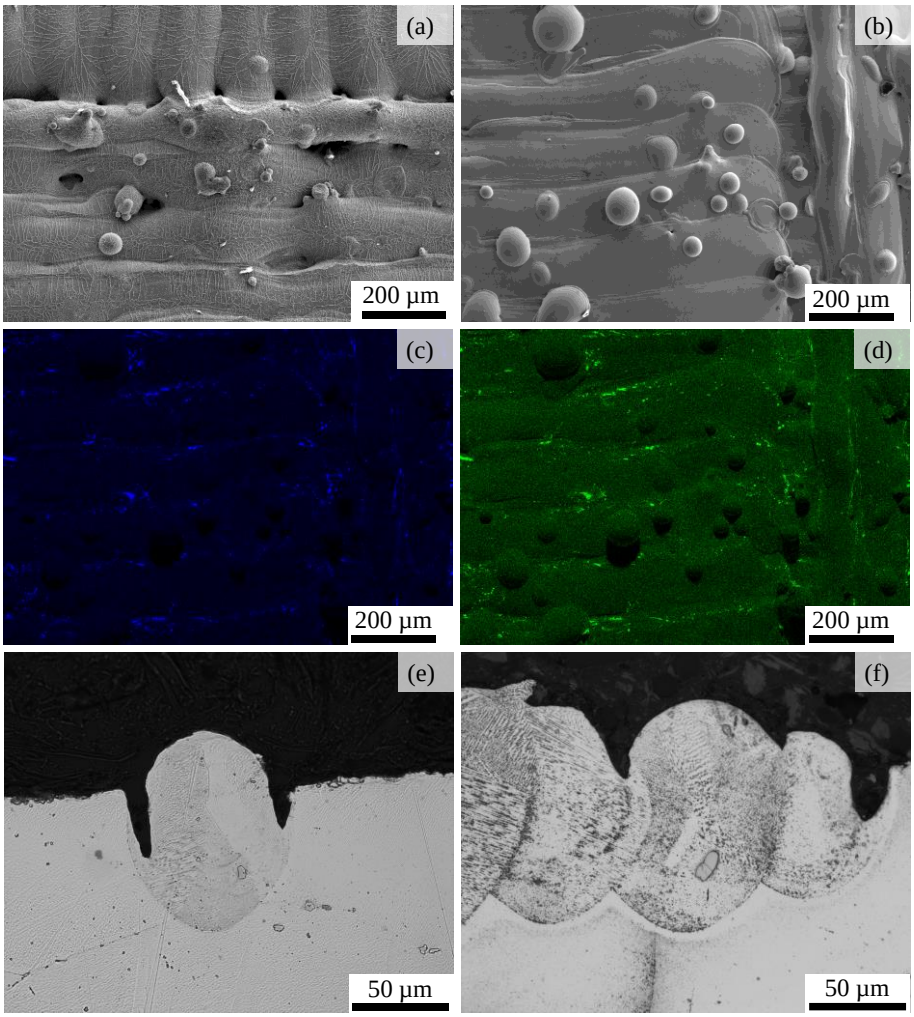


Figure 6.10: (a) Representative SEM for discontinuities along the melt pool. Some oxidation along grain boundaries is visible and occurred after heat treating together with (b) secondary emission micrograph for top melt pool surfaces with EDS maps for (c) aluminium and (d) oxygen and optical micrographs for single layer melt pool cross sections for (e) a single track and (f) a 20 by 90 mm area.

6.5 Conclusion

This work investigates the feasibility of using laser scanning strategies rather than heat source input parameters to modify the microstructure of L-PBF IN718. Through a modification of the island size and island shift the grain size, orientation, and morphology were successfully modified. This work also compares the microstructures generated for a relatively large build volume to that conducted in small (side 10 mm) cubes. With larger build volumes, the effect of island shift is negligible in changing the microstructure while modifying island size still presents significant differences along

the build direction which is difficult to achieve for L-PBF due to the highly directional heat flow along the build direction.

Mechanical testing of these components indicated that the scanning strategy can be used in generating monolithic conditions with varying properties and functionally graded specimens. Specimens having larger grains and higher relative proportions of grains with a [001] predominant orientation to the loading direction exhibited a lower Young's modulus, a lower strength and locally exhibited more micro-strain. These properties mean that when combined in a functionally graded component the behaviour of such structures will vary as was confirmed through digital image correlation. Thus, components can be optimised for different use case scenarios. The interface of these functionally graded specimens was also found to be sound with a gradual change in grain size over the interface and failure occurring 4 mm away from the interface in the monolithic section.

The ductility was relatively low and exhibited significant variability. Fractography revealed even though full consolidation was obtained (density >99.95%), the failure of the specimens was still defect driven due to the entrainment of Al oxide films in the melt reducing wettability and affecting consolidation between subsequent layers. All the defects exhibited aluminium enrichment and showed specific surface features such as wrinkling and slip bands. It is thought that the defects formed due to thin Al oxide films becoming folded and entrained in the melt pool through Marangoni flow and recoil in the melt pool. Such defects have been observed in casting of Ni superalloys but have not been discussed in depth in the context of laser powder bed fusion for Inconel 718. They are believed to occur due to the vaporisation and subsequent deposition of Al on the surface of newly formed melt pools.

CHAPTER 7. The effect of altering scanning strategies in laser powder bed fusion on the oxidation of Inconel 718

7.1 Abstract

The initial oxidation rate of Ni superalloys has been linked to the grain orientation and grain size as grain boundaries act as short-circuit diffusion pathways for oxygen in Cr and the oxidation rate may change with grain orientation. The microstructure produced after additive manufacturing processes such as laser powder bed fusion is dependent on the heat flow, thermal gradient, and solidification rate. Thus, using laser powder bed fusion both the grain size and preferred orientation can be tailored. The scope of this study is to determine whether such modifications affect the oxidation resistance of Inconel 718. The scanning strategy was used to obtain specimens with varying grain size and prevalent grain orientations. Isothermal oxidation at 850 ºC for 504 h was performed and oxidised specimens were characterised. The mass gain behaviour was broadly similar between the different conditions after 504 h and comparable to wrought Inconel 718 but following sub-parabolic oxidation kinetics. The specimen with the smallest grain size exhibited spallation after 96 h, while the specimens with a larger grain size exhibited spallation after 264 h. The smaller grained condition exhibited a higher degree of intergranular alumina penetration compared to the other conditions. All the conditions investigated here formed an underlying Nb rich layer which has been associated with an initial reduction of the oxidation rate with the kinetics moving from parabolic to cubic.

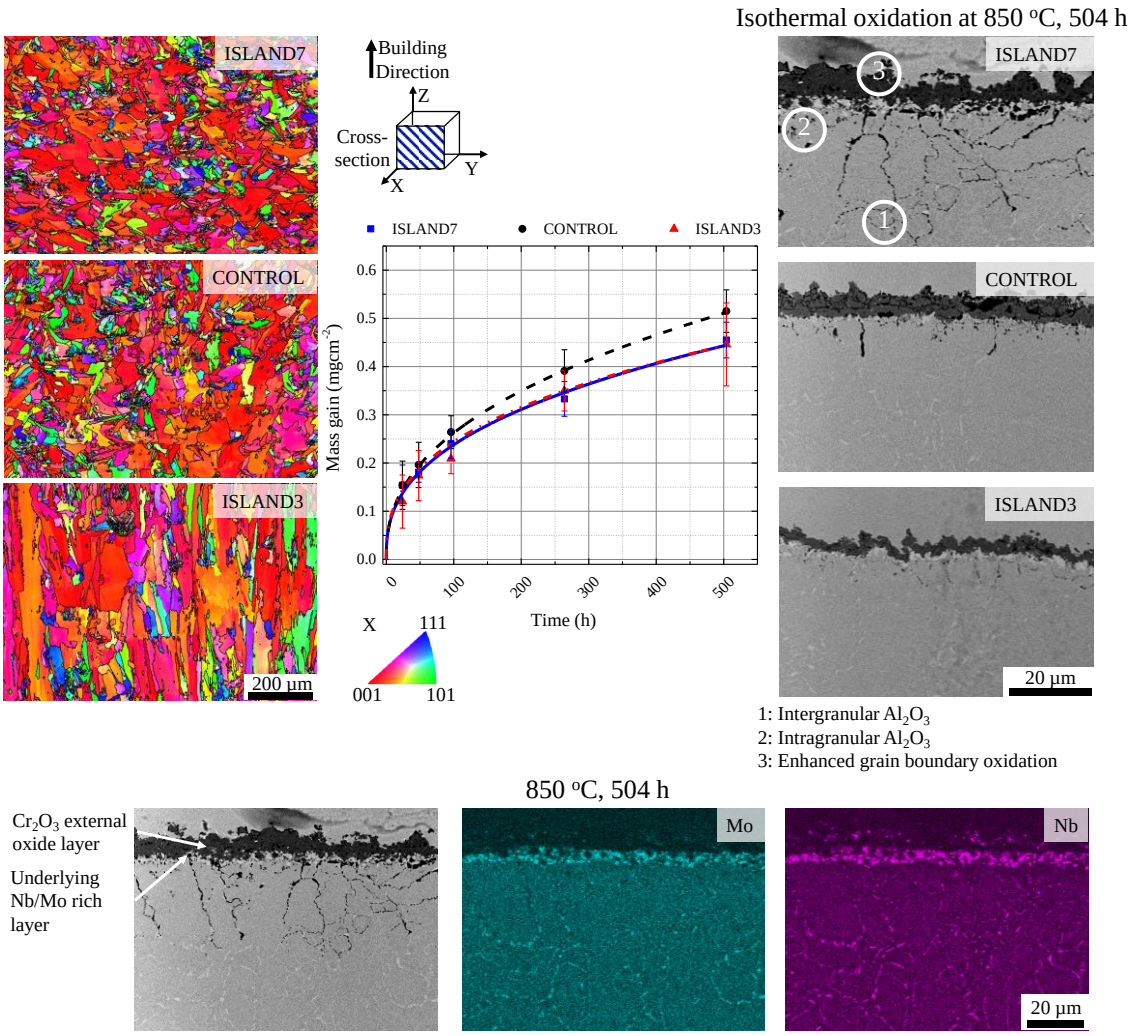
Highlights

Microstructural control of Inconel718 to create varying grain sizes and textures.
Similar mass gain for different conditions after isothermal oxidation at 850 ºC, 504 h.
Oxidation kinetics of all conditions are comparable to wrought Inconel718.
Conditions with smaller grain sizes resulted in deeper Al_2O_3 penetration.

Keywords

Inconel 718, oxidation, laser powder bed fusion, internal oxidation

Graphical Abstract



7.1 Introduction

Inconel718 is used in demanding environments such as aeroengines and nuclear reactors due to its good mechanical properties and resistance to elevated temperatures. The slow precipitation kinetics make IN718 weldable and relatively crack resistant thus a good candidate for additive manufacturing techniques such as laser powder bed fusion [1].

Oxidation properties are one of the more important factors affecting the high temperature performance. IN718 consists of ~19 wt.% of Cr which forms an adherent and protective Cr_2O_3 scale at the alloy surface during transient and steady-state oxidation below 1000°C. The formation of the protective chromia outer layer is the main reason behind the good oxidation resistance of IN718. However, due to the preferential oxidation of Cr, under the oxide a Cr depleted zone will form which means that the oxidation resistance of such a zone is inferior to the bulk metal [263]. Spallation or cracking of the chromia film mean that this underlying Cr-depleted region is then rapidly attacked [263]. Furthermore the loss of cross-sectional area through oxidation of the surface can result in a reduction in fatigue life and has the potential to aid the formation of fatigue cracks at the oxide surface and their propagation through the formation of brittle oxide compounds at the grain boundaries [181].

The microstructure produced after a solidification process such as L-PBF is primarily dependent on the thermal gradient and solidification rate [42,54,55]. The microstructures produced during L-PBF will be vastly different from those normally observed for wrought and heat-treated components. This difference translates to both a difference in grain size and texture. L-PBF is also a rapid solidification process, characterised by a high degree of elemental segregation which also contributes to make the microstructure produced distinctly different from wrought components. The layer-by-layer building strategy fundamental to L-PBF means that during the process the heat input and therefore the thermal gradient and cooling rate can be altered modifying the solidification rate. Thus, features such as grain size and predominant orientation can be modified during AM by altering deposition parameters such as the heat input parameters or the scanning strategies [56,91,92,134,153,155,158,166,264,265]. Previous work by these authors (discussed in Chapter 4) has been focused on the successful control of the microstructure after L-PBF through specific scanning strategies which forms the basis of the specimens investigated here.

Grain boundaries act as short-circuit diffusion pathways for oxygen in Cr and grain boundary diffusion is faster than lattice diffusion below 1000ºC [190,266]. Thus, the amount of grain boundaries impinging the surface should influence the oxidation rate. The initial transient oxidation rates on Ni based superalloys have been observed to also be affected by the orientation of the surface grains [186,192,193]. This effect is thought to be related to the planar density of the different orientations; resulting in the formation of large oxide grains which reduce the oxidation rate for orientations close to 〈111〉 or small oxide grains which yield a high number of boundaries accelerating the oxidation rate for orientations close to 〈001〉 [192]. This has also been observed for Cr, where the oxide thickness was found to be different between individual grains with a different orientation [190]. It has not yet been elucidated whether these variations in initial oxide thickness can be effectively used to reduce the oxidation rate over long term exposures at elevated temperatures and how this is affected by changes in tandem of grain size.

The scope of this study is to determine whether the modification of the microstructural morphology through L-PBF to alters the oxidation performance of IN718 under elevated temperatures.

7.2 Material and Methods

An M2 Concept Laser L-PBF system using pre-alloyed gas atomised IN718 powder (Ø 10 to 45 µm, ASTM B637-18 [104]) was used to create cuboids with dimensions of 20 mm by 20 mm by 10 mm using different scanning strategies. The powder chemical composition conformed to ASTM B637-18 [104] and consisted of Ni 52.08, Cr 19.57, Fe 18.22, Nb 5.23, Mo 3.04, Ti 0.99, Al 0.5, O 0.02 and C 0.05 wt.%. All processing was done under a continuous feed of argon (< 0.1% O_2).

The power, scan speed and hatch spacing were kept constant at 263 W, 1500 mm/s and 0.075 mm respectively, together with a layer thickness of 30 µm, selected for optimised density (>99.5%). The island scanning strategy was used to manufacture the specimens used in this work and is described in detail elsewhere [166]. The island size was varied from to 3 mm for the ISLAND3 condition to 5 mm for the CONTROL condition to 7 mm for the ISLAND7 condition.

Coupons were removed from the substrate and solution treated at 980ºC for 1 h to retain the initial

microstructure as confirmed in Chapter 4, followed by water quenching and double-ageing at 720ºC for 8 h, followed by furnace cooling to 620ºC, for 10 h and air cooled as per ASTM B637-18 [104]. After heat treatment, the specimens were sliced to 1 mm thick slices parallel to the build direction as depicted in Figure 7.1. The specimens were then metallographically polished on both sides to a mirror-like finish using 0.04 μm colloidal silica solution. Corners and edges were chamfered to reduce stress concentrations and polished.

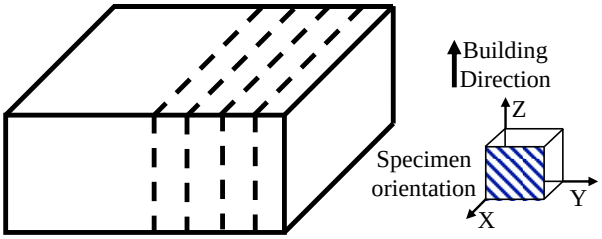


Figure 7.1: Coupon orientation with respect to the build direction.

Isothermal oxidation tests in laboratory air were performed using a Nabertherm horizontal metal tube furnace at 850 ± 5ºC for times up to 504 h. Prior to starting the tests, the furnace was calibrated using a K-type thermocouple over a period of 24 h at the oxidation temperature. Between intervals the specimens were furnace cooled at a cooling rate between 6 to 8ºC/min. The specimens were placed in dehydrated covered alumina boats after the test.

The sample dimensions (length, width, and thickness) were measured thrice using a Vernier caliper followed by degreasing in ethanol and drying. A high precision Sartorius Me5 micro-balance (±0.001 mg) was used to obtain mass gain measurements at intervals of 0 h, 24 h, 48 h, 96 h, 264 h and 504 h to determine the oxidation kinetics.

Scanning electron microscopy was performed using a field emission Zeiss Merlin Gemini SEM using both secondary electron and backscatter electron signals. Energy dispersive spectroscopy was used for chemical analysis of areas of interest and chemical mapping. Electron backscatter diffraction measurements were performed using a step size of 1.5 μm and a scan size of 1000 μm by 800 μm to generate inverse pole figure maps using a field emission Tescan Mira 3 SEM of the surface area prior to oxidation. The surfaces before and after oxidation were investigated using X-ray diffraction with a Rigaku Ultima IV diffractometer with CuK_{α} radiation operated in the Glancing Incidence Asymmetric Bragg configuration. An angle of incidence of 3º was used with a

step size of 0.05° and a scan speed of 1° per minute in the range of 30° to 100°. The tube acceleration voltage and tube current were set at – 40 kV and 40 mA respectively. Cross-sectional analysis of the oxide scale thickness and chemical composition was performed for each condition at 504 h. Specimens were sputter coated with a thin gold layer followed by Ni-plating using a Watt's bath electrolyte solution (710 ml deionised water, 30 g boric acid, 190 g Ni sulphate and 40 g Ni chlorate). The temperature was between 30 and 60°C with a current density between 1-10 $A.dm^{-2}$ for 20 minutes. Once plated, coupons were mounted using Struers Durocit-3 resin and sectioned using a Struers Accutom 5 precision cut-off machine and metallographically polished to a 0.04 μm finish. SEM together with EDS map measurements were performed.

7.3 Results and Discussion

7.3.1 Initial microstructure

The microstructures for the three conditions investigated here are shown in Figure 7.2 (a to c). The grain morphology for the ISLAND7 condition is less elongated when compared to the grain morphology obtained for the ISLAND3 condition. This change in morphology translates to a change in grain size with the grain size increasing with a reduction in the island size as shown in Figure 7.2 (d). The mechanism behind this behaviour is elucidated in Chapter 4. For the images shown in Figure 7.2 (a to c) for the ISLAND3 condition, the percentage of area covered by grain boundaries was 17%, while for the CONTROL condition this increased to 25% and then for ISLAND7 this was at 26%. Due to the relatively large step size used in this work (1.5 μm) compared to the actual expected grain boundary thickness (~0.5 nm [267]), the values obtained are overestimated. A correction factor was applied to obtain values which are more indicative considering the expected grain boundary thickness giving percentages of 5.7% for the ISLAND3 condition, 8.3% for the CONTROL condition and 8.7% for the ISLAND7 condition. These values are for indicative purposes and further measurement using transmission electron microscopy would give a more accurate but also more localised indication of the grain boundary percentage. The cubic unit cell for the different conditions has one of the 〈001〉 directions predominantly aligned to the build direction. For the ISLAND3 condition it was observed that the other two 〈001〉 directions were predominantly also aligned with the XY movement of the laser which resulted in a higher area percentage of grains oriented with their {001} faces parallel to the surface being oxidised as shown

in Figure 7.2 (e). For the ISLAND7 and CONTROL condition the alignment of the ⟨001⟩ axes along both the building direction and the XY direction was not as pronounced. This meant that the percentage of grains oriented with their {001} faces parallel to the surface being oxidised was lower overall compared to ISLAND3 as shown in Figure 7.2 (e).

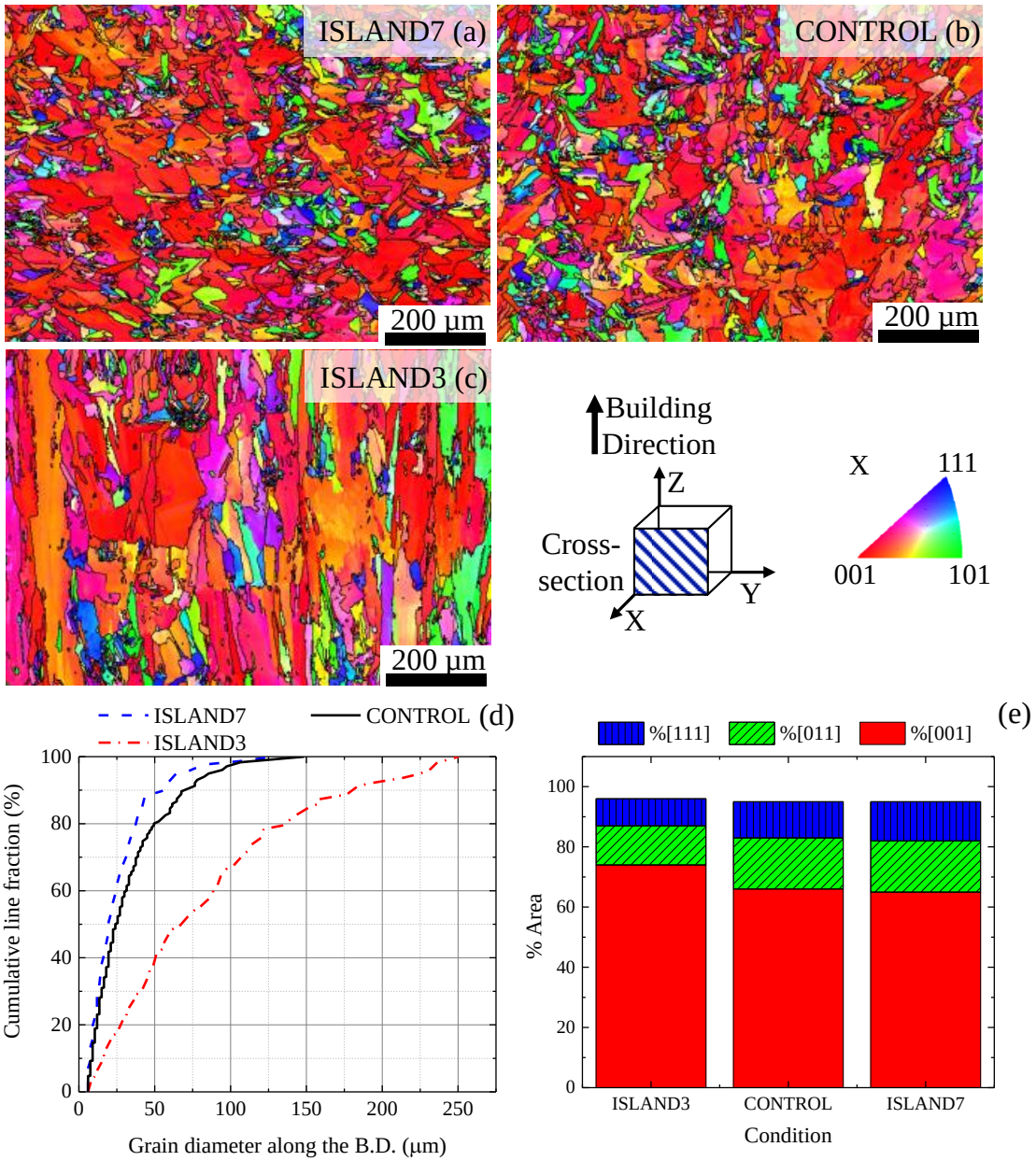


Figure 7.2: IPF maps for (a) ISLAND7, (b) CONTROL and (c) ISLAND3 together with (d) cumulative grain size distribution along the build direction for the different conditions and (e) orientation directions perpendicular to the surface being oxidised.

7.3.2 Oxidation Kinetics

The mass gain curves for all conditions are shown in Figure 7.3. Wrought IN718 has been observed to have a relatively low oxidation rate below 950ºC [185]. Surprisingly, despite the ISLAND7 condition having the smallest grain size overall, the CONTROL condition seems to exhibit the highest mass gain, however the differences are within the scatter range of the data.

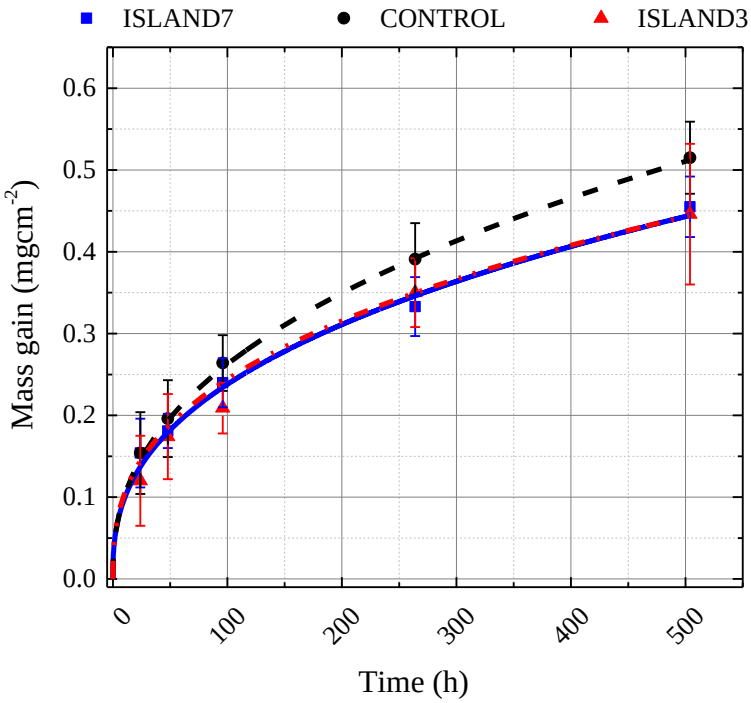


Figure 7.3: Mass gain values for the different conditions.

The oxidation kinetics observed follow a parabolic trend as shown in Figure 7.3. This behaviour can be described through the classical Wagner equation [185] in Equation 7.1:

$$(\Delta m)^n = K_n t \qquad \textit{(Equation 7.1)}$$

where:

Δm is the oxidation mass gain per unit surface area ($mgcm^{-2}$),
K_p is the oxide growth rate constant,
n is the rate exponent

and t is the oxidation time (s).

The rate exponent was found to be 2.6 for the ISLAND7 condition, 2.4 for the CONTROL condition and 2.7 for the ISLAND3 condition with adjusted R^2 values between 0.97 and 0.99 indicating a very good fit. The rate exponents obtained here are sub-parabolic and fall between parabolic ($n = 2$) and cubic ($n = 3$) behaviour. The ISLAND3 and ISLAND7 conditions exhibit a value closer to cubic behaviour while that for CONTROL condition tends to be closer to that for parabolic oxidation. Values from literature are typically approximated to parabolic behaviour, however for Inconel 625 manufactured using L-PBF, Lewis et al. [188] observe cubic oxidation kinetics. It is thought that the cubic kinetics observed in [188] are influenced by Nb enrichment resulting in the rapid formation of a delta phase (Ni_3Nb) layer occurring beneath the Cr_2O_3 scale contributing to a reduction in the initial oxidation rate.

A comparison of both the cubic and parabolic oxidation rate constants obtained for this work is shown in Table 7.1. The K_p values shown here are close to those observed for as-built IN718 manufactured using L-PBF [268]. The microstructure (grain size, preferred orientation, and type of grain boundaries) after solution treatment was not changed thus the constants obtained for as-built IN718 are of similar magnitude. There is a small difference in K_p between the ISLAND3 and ISLAND7 compared to the CONTROL conditions, with both the former oxidising at a slightly slower rate compared to results for as-built L-PBF IN718 reported in [268]. The mass gain values observed here, are slightly lower to what has been observed for wrought IN718 at similar durations and temperatures in cyclic oxidation [187]. This can be attributed to the fact that cyclic oxidation tends to be more aggressive due to the repeated heating and cooling cycles applied to the specimens.

Table 7.1: Parabolic K_p and cubic K_c oxidation rate constants for the different condition compared to other work on AM IN718. Adjusted R^2 values for this work were all above 0.97.

Condition	K_p ($mg^2cm^{-4}s^{-1}$) n =2	K_c ($mg^3cm^{-6}s^{-1}$) n =3
ISLAND7	1.16×10^{-7}	4.09×10^{-8}
CONTROL	1.51×10^{-7}	6.81×10^{-8}
ISLAND3	1.14×10^{-7}	4.77×10^{-8}
L-PBF IN718 as-built, oxidised at 850ºC, 1000 h [268]	1.4×10^{-7}	-
L-PBF IN718 ST at 1065ºC for 2 h, oxidised at 850ºC, 351 h, [79]	0.75×10^{-7}	-
Wrought IN718, cyclic oxidation at 850ºC, 168 h [187]	2.13×10^{-7}	
Wrought IN718, ST at 980ºC, DA 720ºC /8 h, 620ºC /8 h, AC, oxidised at 850ºC, 1000 h [268]	0.7×10^{-7}	-
EB-PBF IN718 as-built, oxidised at 850ºC, 1000 h [268]	0.62×10^{-7}	-
21Cr ferritic stainless steel at 850ºC [269]	2.50×10^{-7}	-
Pure Cr_2O_3 on Cr at 850ºC in pure O_2 [270]	1.18×10^{-9}	

ST: solution treated, DA: double-aged, AC: air cooled

Compared to L-PBF specimens which have been solution treated at 1065ºC for 2 h [79], the oxidation rates obtained in this work oxidise faster overall by 1.5 to 2 times as much. The solution treatment applied in [79] is at a higher temperature than the one applied in this work and would result in recrystallisation of the as-built microstructure. Recrystallisation of the structure would increase the percentage of twinned grain boundaries for fcc material through the formation of recrystallisation twins [271]. The authors [79] also report significant grain growth to have occurred after this high temperature solution treatment which would affect oxidation by presenting a lower number of grain boundaries while increasing the number of grain growth coherent twin grain boundaries [271]. Such grain boundaries have been linked to a reduced oxidation rate [272]. The low temperature of the solution treatment performed here could be affecting the oxidation kinetics of the alloy compared to performance after a solution treatment at temperatures above the recrystallisation temperature. While a low temperature solution treatment is beneficial in removing most elemental segregation, some Nb-rich carbides may remain or delta phases may form [79]. This could mean that the Nb element would not be able to diffuse to the near-surface region, which may slow down the formation of a delta phase layer at the interface affecting the oxidation kinetics

observed here somewhat. Longer oxidation periods for wrought IN718 in an identical heat treated condition have yielded a lower oxidation rate [268] which may be attributed to a similar effect; for IN718 in the wrought condition it would be expected that the grain size and grain boundary types would be different. Furthermore, it would not be expected that such structures have any residual elemental segregation as it would have been removed during the forming process.

A comparison of the performance of the specimens created in this work to other superalloys together with oxidation kinetics for pure Cr at various temperatures is shown in Figure 7.4. The oxidation rate of L-PBF IN718 compared to pure chromia is faster at 850ºC. The fact that IN718 oxidises faster than pure chromia forming alloys is due to the fact that other elements in addition to Cr such as Ti and Al will oxidise internally at the grain boundaries at faster rates accelerating the overall oxidation kinetics [189].

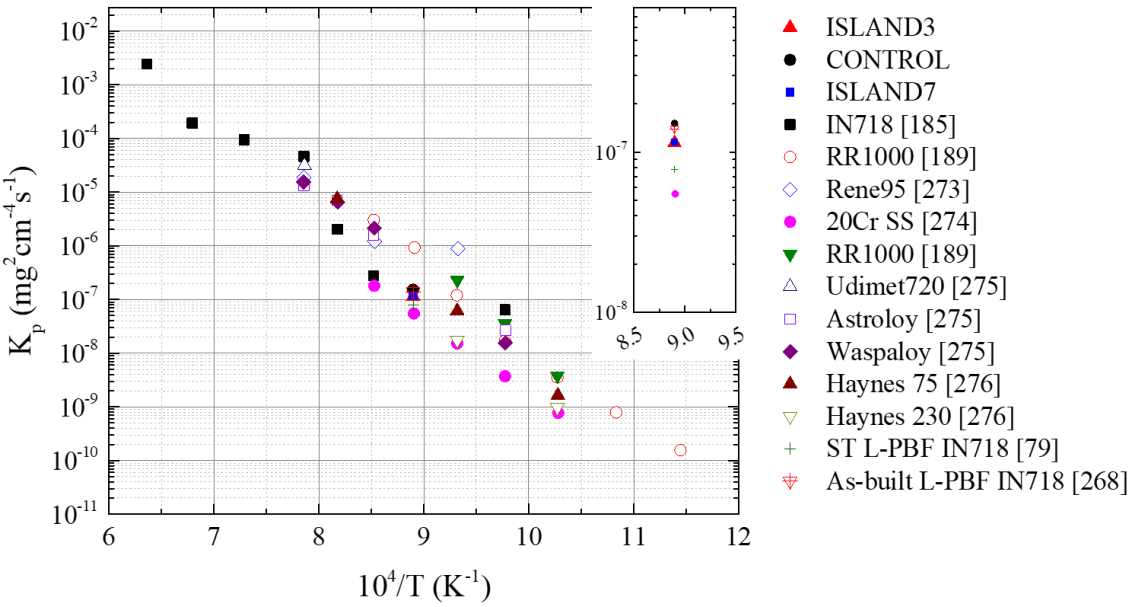


Figure 7.4: Arrhenius plot of parabolic K_p values comparing various superalloys from literature to the K_p values obtained in this work. Insert shows a high resolution of the points at 850 ºC. Adapted from [189].

7.3.3 Surface oxidation

The surface oxide morphology for the different conditions is shown in Figure 7.5. After 24 h, all conditions appear to exhibit a degree of grain boundary enhancement with the grain boundaries appearing to be delineated as grains elongated along the build direction of variable length and an irregular grain shape. Similar enhancement has been observed for Ni-base superalloys with a low

surface roughness [187,268] and for chromia on Cr [277]. The grain boundary enhancement remained evident even after 504 h. This enhancement is thought to occur due to a faster oxidation rate at the grain boundaries due to the grain boundaries acting as a short-circuit diffusion pathway [268]. The surface scale composition consisted primarily of chromium and oxygen, with varying quantities of Fe and Ni detected in specific areas and minor quantities of Ti, Al and Nb detected at the surface as well as shown in Figure 7.6 (a). The Fe and Ni elements might be due to the formation of an Fe or Ni based spinel forming. The EDS data presented in Figure 7.6 (a) was collected from an area which was likely a grain boundary thus the small amounts of Ti, Al and Nb may be reflections from elemental enrichment under the oxide scale or oxidation of Ti and Al along the grain boundaries rather than at the surface of the scale. The formation of small particles of elongated plate-like oxides was also evident for the ISLAND7 condition at 96 h, the CONTROL condition and ISLAND3 conditions after 264 h. The ISLAND7 condition (i.e. smallest grain size) exhibited spallation after 96 h, while the specimens with a larger grain size (CONTROL, ISLAND3) exhibited spallation after 264 h as seen in Figure 7.5. The integrity of the oxide scale and the duration of the steady state period are important aspects in oxidation resistance [278]. The scale will protect the underlying material by limiting the oxidation rate over long periods of time by acting as a diffusion barrier therefore earlier spallation is detrimental.

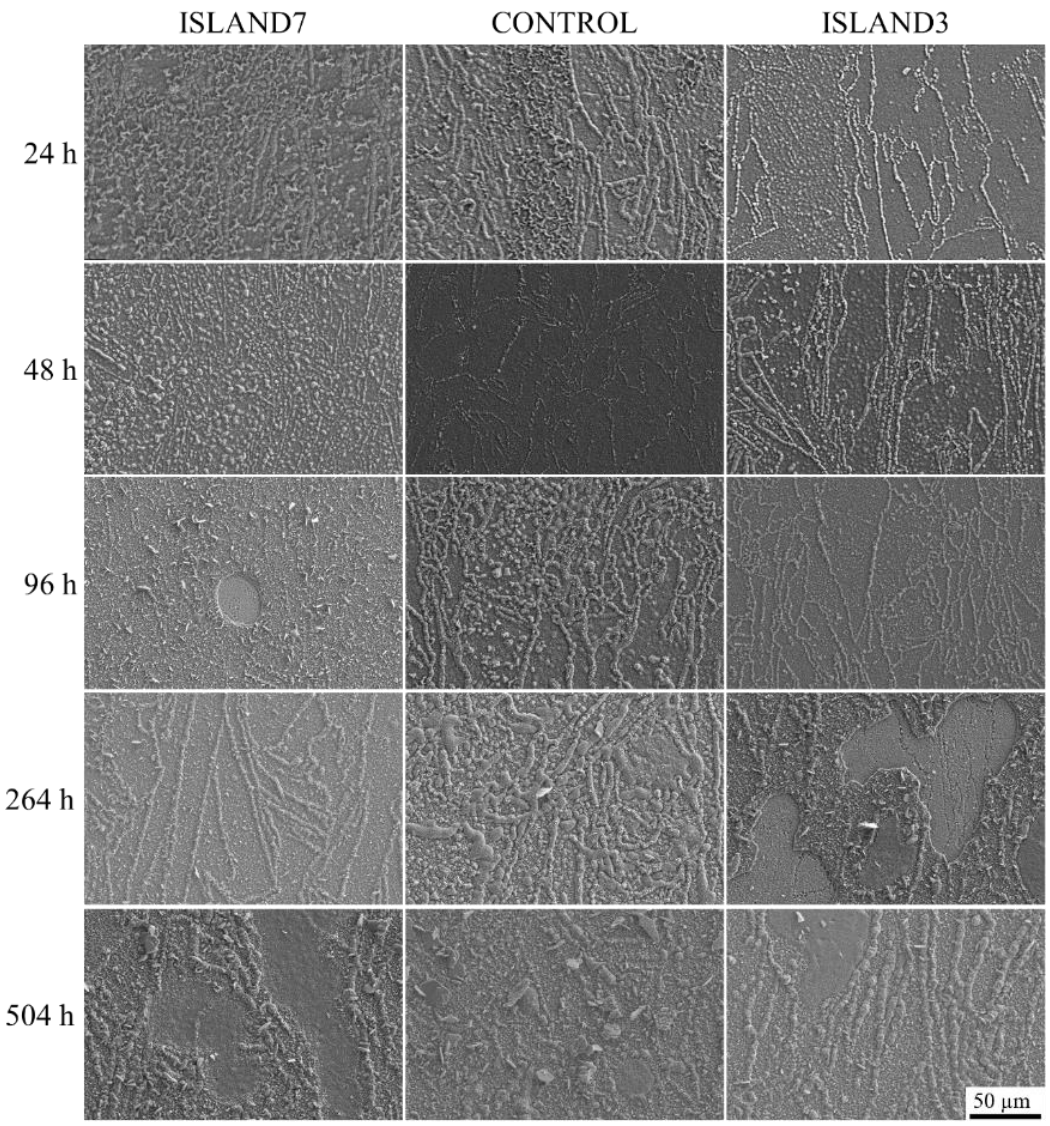
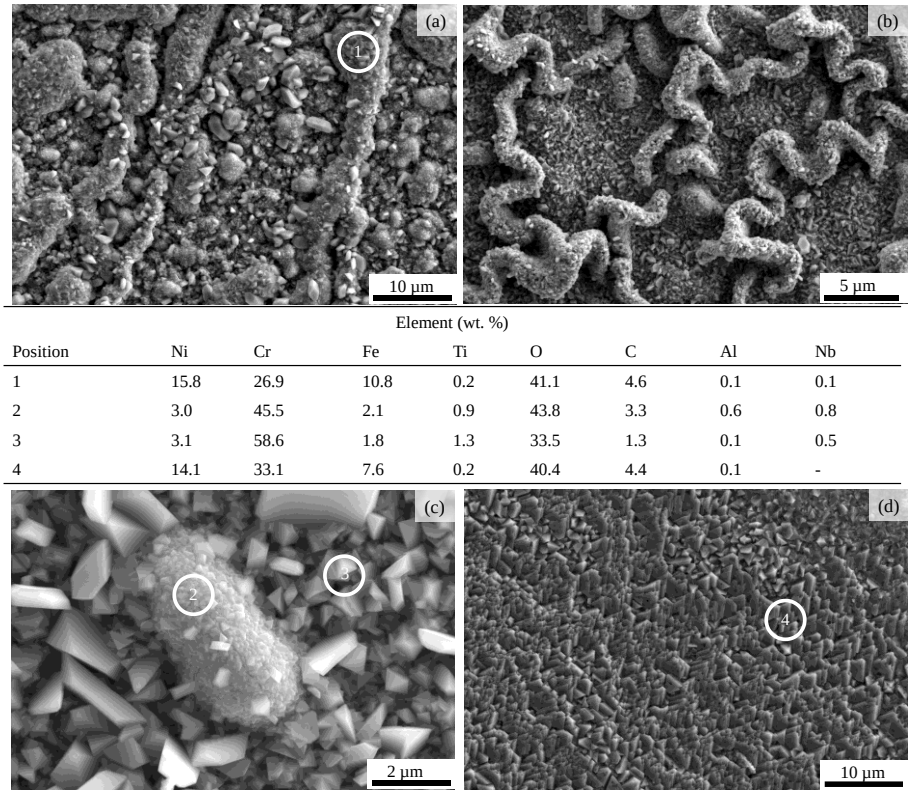


Figure 7.5: SE micrographs for the surface oxide morphology of IN718 oxidised in air at 850ºC for time intervals between 24 h to 504 h for the ISLAND7, CONTROL and ISLAND3 conditions.

On the surface for the ISLAND7 and CONTROL conditions, wrinkled oxide features were visible after 24 h as shown in Figure 7.5 and in Figure 7.6 (b). These were evident for the ISLAND3 condition in small quantities slightly later at 48 h. These wrinkled structures are evidence of compressive stresses within the forming oxide [190]. At 96 h for the ISLAND7 condition some areas were observed exhibiting spallation of small areas of oxide. The ISLAND7 condition also exhibited the formation of small areas consisting of very fine chromia grains as shown in Figure 7.6 (c). A crack is evident running through one such protruding area indicating fracturing of the oxide layer. The much smaller crystallite size (< 1 µm) in the protruding area is also evident which would

mean there is a high concentration of short circuit diffusion pathways. Evidence of further spallation was observed for all conditions following 264 h and 504 h. It was clear that after further exposure to oxidising environment, the areas undergoing spall were being re-oxidised. One such area is shown in Figure 7.6 (d). Despite reoxidation, the amount of Cr detected here is less than that detected in areas which had not spalled at shorter durations such as position 3 in Figure 7.6 (c). This would indicate that the oxide layer being formed here was still relatively thin as evidenced by the faceted appearance of the individual crystals in the area in Figure 7.6 (d) and the considerable contribution to the signal of Ni and Fe from the substrate. Possible reasons for this might be that the previous oxide had just spalled off and therefore the oxide was still relatively young.



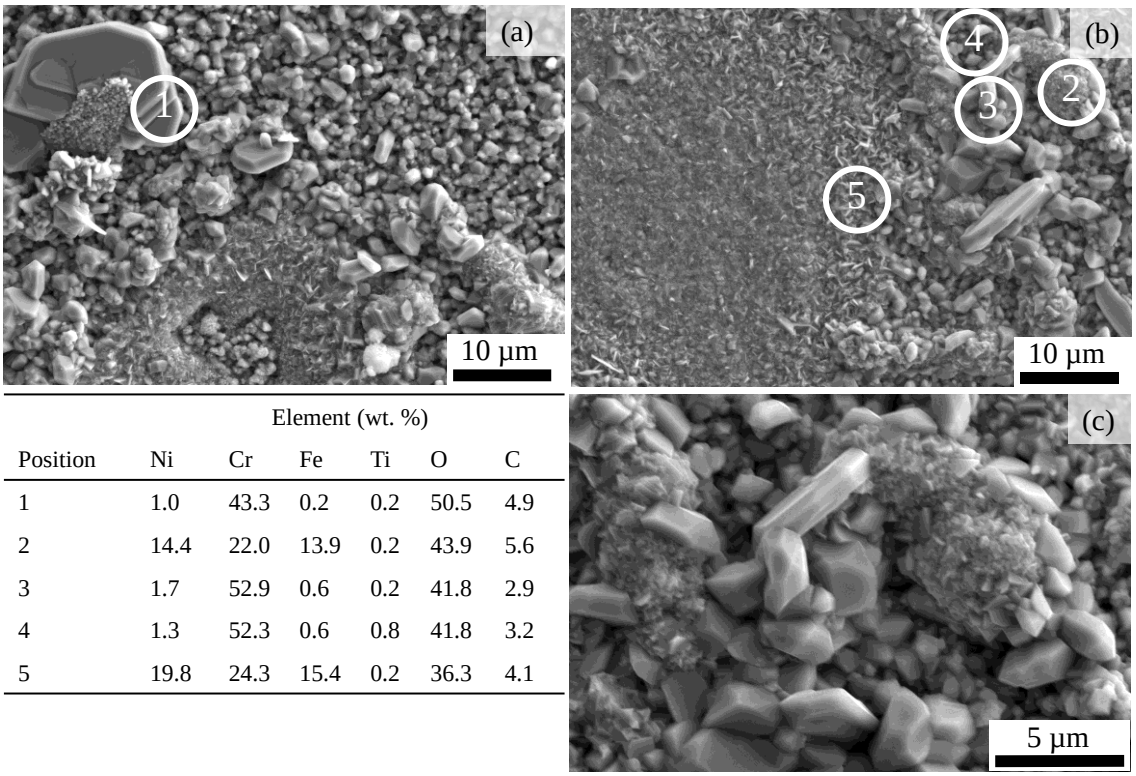
	Element (wt. %)							
Position	Ni	Cr	Fe	Ti	O	C	Al	Nb
1	15.8	26.9	10.8	0.2	41.1	4.6	0.1	0.1
2	3.0	45.5	2.1	0.9	43.8	3.3	0.6	0.8
3	3.1	58.6	1.8	1.3	33.5	1.3	0.1	0.5
4	14.1	33.1	7.6	0.2	40.4	4.4	0.1	-

Figure 7.6: SE micrographs of (a) Fe and Ni rich area for the CONTROL after 264 h (b) the wrinkled oxide structures after 24 h for the CONTROL specimen together with (c) Cr rich oxide nodule observed for ISLAND7 after 96 h and (d) faceted structures after 264 h on the CONTROL specimen after spallation and the chemical composition of specific areas of interest.

High resolution representative SE micrographs of the oxide grain morphology after 504 h for the different conditions are shown in Figure 7.7 (a and b) and Figure 7.8 (a). The surface consisted of a mixture of different structures and grain sizes. The observed elongated oxide platelets observed for

all conditions in Figure 7.5, were analysed as shown in Figure 7.7 (a) and found to consist of large amounts of Cr and oxygen – most likely large chromia grains growing outward from the surface. The platelets were mostly observed in the regions at the grain boundaries where the oxide growth was more evident. These platelets were found to have a relatively higher concentration of oxygen than the surrounding oxide surface. The elemental concentration approached that for stoichiometric Cr_2O_3.

For all conditions, globular oxide grains of differing sizes were observed. The chemical composition of these grains shown in position 3 and 4 in Figure 7.7 (b) is high in Cr and O with traces of other elements detected, notably Ni, Fe and Ti. Apart from these globular Cr rich grains, oxide nodules enriched in Cr, Fe and Ni were also observed as shown in position 2 and elongated oxide minute grains in position 5 in Figure 7.7 (b). These are most likely spinels based on $(Ni,Fe)(Cr,Fe)_2O_4$, further supported by the ratios of the percentages in which the elements have been detected. The formation of such spinels has been documented for oxidation of IN718 [71,279]. The formation of Fe rich areas in the external scale has also been observed for oxidation of IN718 made using EB-PBF at 750ºC and associated with potentially increased oxidation rates [280]. The morphology of the grains in position 2 and more specifically in position 5 also appears different from the surrounding chromia based grains; the structure of chromia is trigonal which is also apparent from the elongated crystals visible in Figure 7.7 (b) while the spinel structure is orthorhombic. The spinel grains are much smaller than the surrounding chromia grains as shown in Figure 7.7 (c) further presenting a high density of short circuit diffusion pathways through the increase in grain boundaries.



Position	Element (wt. %) Ni	Cr	Fe	Ti	O	C
1	1.0	43.3	0.2	0.2	50.5	4.9
2	14.4	22.0	13.9	0.2	43.9	5.6
3	1.7	52.9	0.6	0.2	41.8	2.9
4	1.3	52.3	0.6	0.8	41.8	3.2
5	19.8	24.3	15.4	0.2	36.3	4.1

Figure 7.7: High resolution SE micrographs for the surface oxide grain structure of IN718 oxidised in air at 850ºC for 504 h for the (a) CONTROL and (b)ISLAND7 conditions with (c) showing a higher magnification of position 2 which is thought to consist of $(Ni,Fe)Cr_2O_4$ spinel structures.

Extensive regions which appeared to have a faceted morphology rich in Cr and lower amounts of Ni and Fe were also observed as shown in Figure 7.6 (d), and then adjacent to them typically the elongated spinel structures observed in Figure 7.7 (b) and in higher resolution in Figure 7.8. Caplan et al. [190] observed that for Cr some of the surface may form single crystal areas appearing faceted and having a plane parallel inner and outer surface which is very similar to what is being observed here in Figure 7.6 (d) and Figure 7.7 (b). These crystals may form in the initial oxidation period after spallation. The chemical composition over these areas seems to vary with the internal parts of the area being rich in Cr as shown in Figure 7.8 (b), and the outer edges being rich in Fe and Ni as shown in Figure 7.8 (c and d). It is likely that these regions are a result of spallation occurring near the 264 h mark, followed by reoxidation of the surface, with the oxide layer being thinner in the centre region resulting in the detection of Ni and Fe from the substrate at 264 h with spinels rapidly forming on the outer edges of the area.

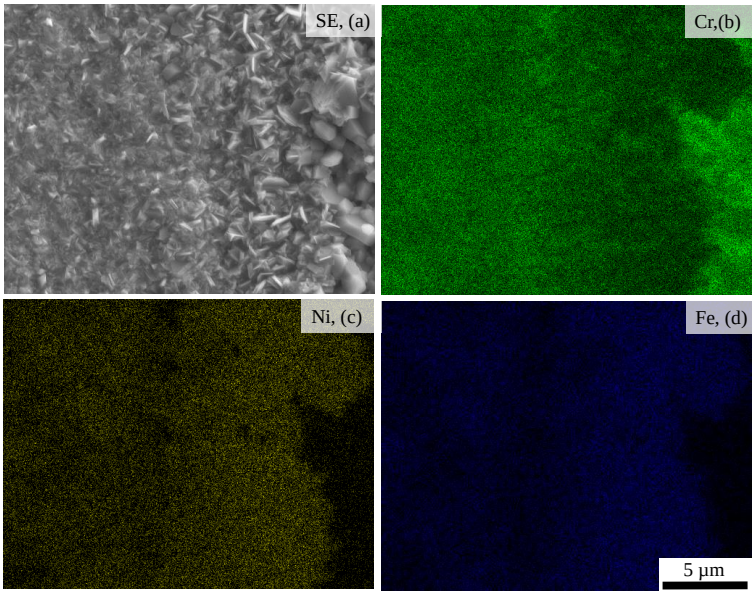


Figure 7.8: High resolution SE micrograph for the surface oxide grain structure of IN718 oxidised in air at 850°C for 504 h for the (a) ISLAND7 condition together with corresponding EDS maps for (b) Cr, (c) Ni and (d) Fe.

In areas where spallation occurred after 264 h, compositional differences were also observed between the surface oxide and underlying material. These are shown in Figure 7.9 (a to h). Within the spalled area a grain boundary is visible together with a rougher appearance in the spalled area. Scale spallation normally occurs upon cooling to room temperature. The roughened "thermally etched" appearance under the scale is attributed to the detachment of the scale during the oxidation process for instance by wrinkling, while where the scale maintained contact and then spalled off, textured oxide grain imprints can remain as are also seen within the spalled area [278]. Oxygen and chromium are not abundant in the region underlying the spall as shown in Figure 7.9 (b and h). Enrichment of Al and Ti is visible at the grain boundary due to the intergranular Al and Ti oxides forming. The spalled area is rich in both Nb and seemingly Mo. Areas with a denser concentration of both elements are also visible.

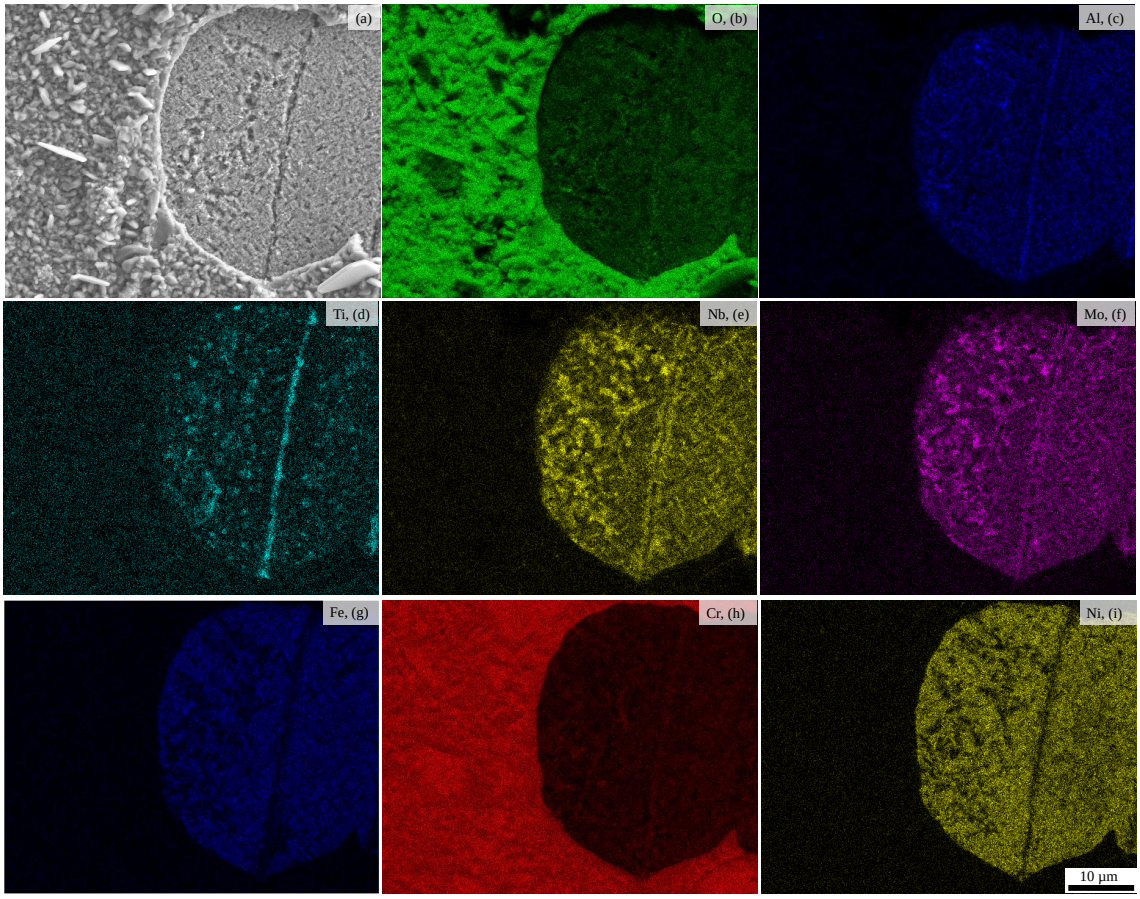


Figure 7.9: EDS maps for an area of spall in the ISLAND3 condition after 264 h, showing in (a) the SE micrograph with a grain boundary passing through the spalled region together with elemental composition maps for (b) O, (c) Al, (d) Ti, (e) Nb, (f) Mo, (g) Fe (h) Cr and (i) Ni.

Representative X-ray diffractographs for the different scanning strategies at the different oxidation time intervals are shown in Figure 7.10 (a to c). After 24 h, the reflections for the ISLAND7 and CONTROL conditions were mostly identical. For the ISLAND3 condition a very predominant reflection for the Ni substrate is still visible at 51.45º for the (200) orientation, indicating that chromia oxide formed after this interval is not as thick initially as that formed on the ISLAND7 and CONTROL conditions. This difference is not retained after 48 h. The phases formed between the different conditions were nearly identical after 504 h, thus the changes in grain size and preferred orientation were not enough to promote the growth of different structures at the surfaces in quantities appreciable through XRD. The differences in texture prior to starting the oxidation tests did not result in any differences between the different conditions in the preferential growth of the oxide over long exposure times.

After 24 h for all conditions, numerous reflections corresponding to Cr_2O_3 were observed as shown in Figure 7.10. After 24 h the oxide formed is still relatively thin as rapid transient growth is still occurring, and thus weak reflections corresponding to the underlying substrate were still visible (except for the ISLAND3 condition where this reflection was still strong). Some contribution from the substrate was still detected at 504 h for all conditions as shown in Figure 7.10 (a to c). In addition to chromia, several low intensity peaks corresponding to $FeCr_2O_4$, $NiCr_2O_4$ and $NiFe_2O_4$ spinel phases were also detected after 24 h. These reflections support the observations made using EDS of the surface where areas with enrichment in Ni and Fe had been quantified through EDS as shown in Figure 7.7 (b) and Figure 7.8 (a). After long oxidation times, the reflections for the spinel phases are reduced in intensity and frequency. No reflections for rutile TiO_2 or alumina were detected here which can be attributed to the shallow GIAB technique used and the relatively small quantities of these expected oxides and their expected position below the chromia scale.

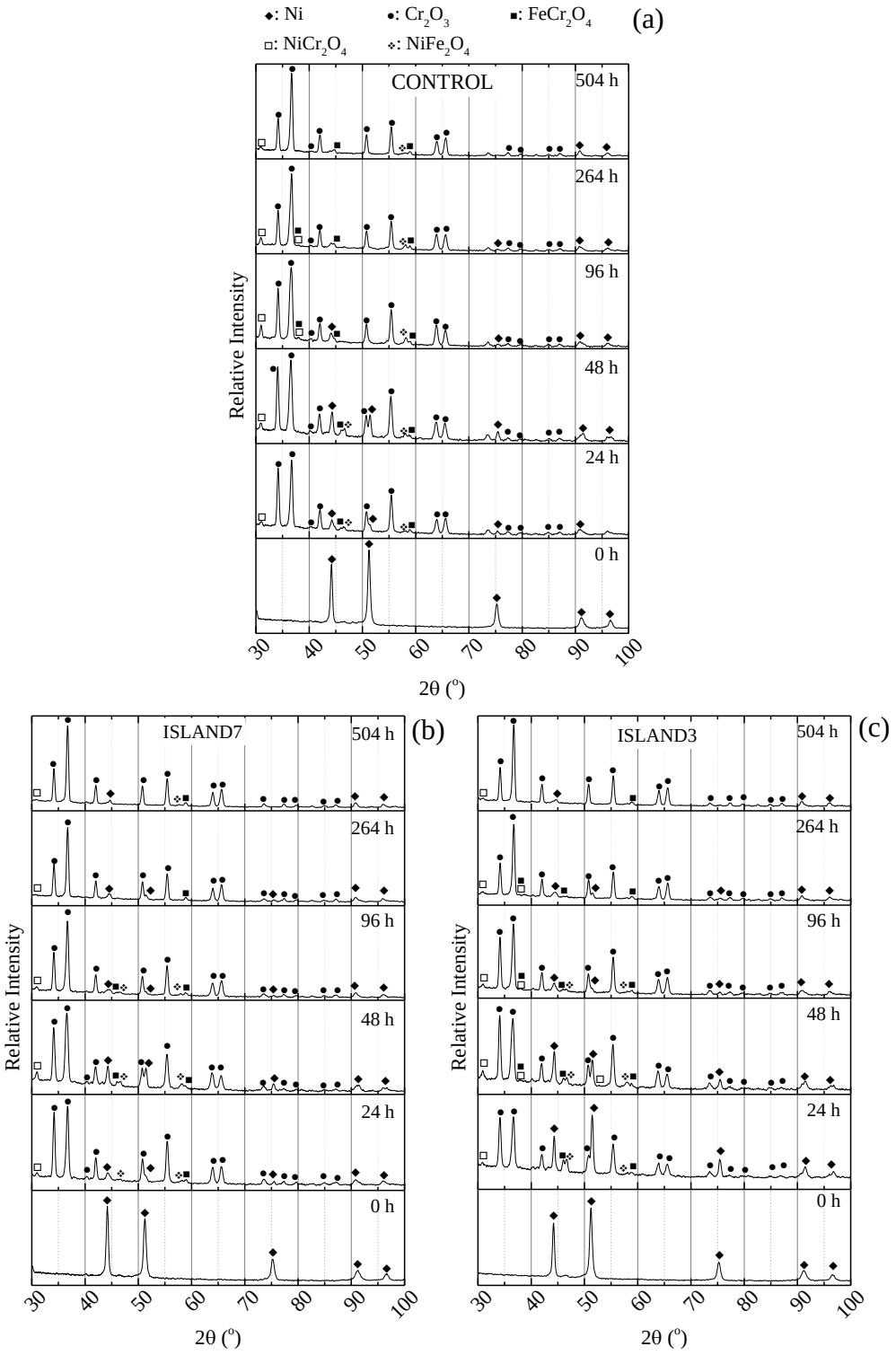


Figure 7.10: Representative diffractographs for (a) the CONTROL condition at each oxidation interval, together with representative diffractographs for the (b) ISLAND7 and (c) ISLAND3 conditions at all time intervals.

7.3.4 Cross-sectional analysis

Representative figures of the oxide cross-sections after 504 h of oxidation for each condition are shown in Figure 7.11. An external Cr rich oxide scale is formed over the surfaces. For the ISLAND7 condition the scale was found to be ~8 ± 2 μm thick, while for the CONTROL condition this was found to be ~5 ± 1 μm and for the ISLAND3 condition it was ~3 ± 1 μm thick. While there is a small reduction in thickness of the chromia oxide formed between the different conditions, the difference is not very high and the fact that spallation occurred may also have contributed some uncertainty to these measurements. Spallation at 850ºC for IN718 was not reported by other authors [79,185] thus it was surprising to observe it in this work. In work done by Calandri et al. [79] and by Greene et al. [185], the specimens were in the solution treated condition or mill-certified condition and not aged as is the case here. It may be possible that the precipitate formation is increasing the tendency towards spallation of the oxide film through altering the stresses in the oxide or that the delta phase layer is forming earlier than in the annealed condition affecting the mismatch between the oxide and the substrate. Further investigation is required to ascertain the active mechanism behind the spallation observed.

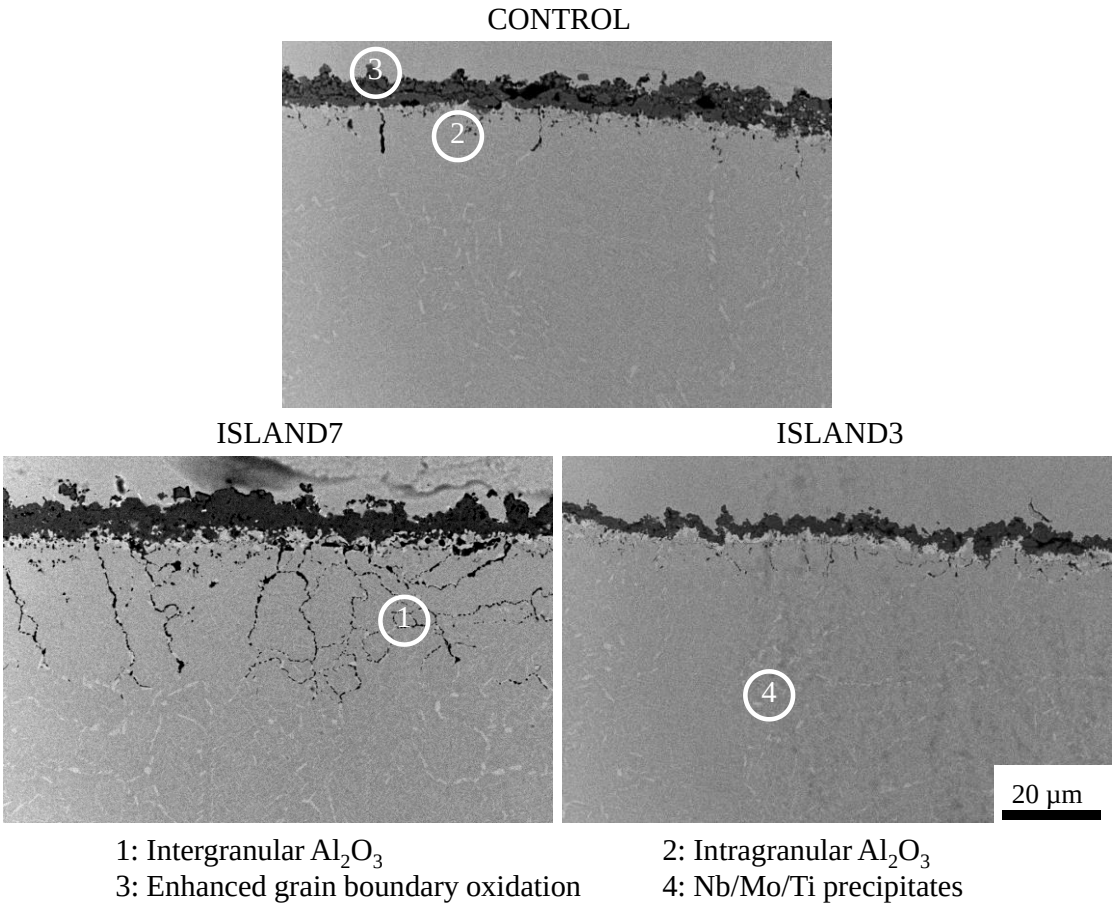


Figure 7.11: Representative BS micrographs for the ISLAND7, CONTROL and ISLAND3 conditions following oxidation in laboratory air at 850°C for 504 h. Features of interest are marked.

The interface between the oxide scale and the bulk material was observed to become irregular for all conditions; but specifically, for the ISLAND3 condition, the irregularity of the interface was very pronounced. The wrinkled oxide surfaces indicate the formation of initial compressive stresses forming on the oxide surface. Some cracking was observed on the surfaces in localised areas as previously observed. Cracking is also evident in the cross-sections of the oxide scale. Cracks were observed in the scale due to spalling being initiated. Pores were also evident in the cross-sections after 24 h for all conditions and cracking in the oxide being observed for the ISLAND7 condition after 96 h of oxidation and after 264 h for the CONTROL and ISLAND3 conditions.

For spallation to occur the oxide film must fracture internally to produce cracks through the thickness and the adherence at the oxide-metal interface must be lost [263]. For the case of a chromium oxide growing on a Ni metal substrate, the co-efficient of thermal expansion will be less

than that of the metal [263]. The growing oxide is typically under compressive stress arising from the constraints of the lateral growth strain in the film from the underlying alloy substrate. Pilling and Bedworth [281] and later Rhines and Wolf [282] both account for the generation of such stress; the former through the volume increase associated with forming the oxide molecules and the latter through the formation of oxides along grain boundaries lying perpendicular to the interface through concurrent inward diffusion of oxygen ions and outward diffusion of metal ions. The growth stresses are further augmented by thermal stresses occurring during the cooling stage after oxidation [283]. The Pilling Bedworth ratio (PBR) of Cr_2O_3 on Cr is 2.07, which means that a compressive stress will be formed in the scale. Other factors such as the scale composition, thickness and thermal cycling will also affect the strain generated in the scale.

This stress can be relaxed through either a shape change of the underlying substrate or wrinkling of the oxide film [266]. Wrinkling such as that seen on the surface images in Figure 7.6 (b) is significant as its onset indicates that the oxide will tend to spall upon cooling. Evans and Lobb [263] described the processes leading to initial spallation; for oxides where the oxide-metal interface is more resistant to fracture than the oxide, angled shear cracks will form in the oxide and with more stress build up the oxide particle is spalled off [263]. For situations where the interface has a lower strength than the oxide layer, the film will wrinkle and buckle and decohesion occurs between the scale and the substrate [263]. As oxidation progresses and the scale grows, the decohesion will increase and thus more of the scale will wrinkle [283]. Once the oxide scale becomes too thick to release the stresses through decohesion and wrinkling, tensile cracks will initiate typically at defects or where the film is curved which can result in spallation [263,283]. The slow cooling between testing intervals may also have re-oxidised the tips of any formed cracks, though it is expected that the thermal stresses generated would be less after a relatively sluggish cooling rate compared to rapid air cooling.

The compressive stress in the oxide scale was calculated as per [283], using a PBR of 2.07 for Cr_2O_3 on Cr [284] and a modulus for Cr_2O_3 calculated as 233 GPa at 850°C [285] to obtain a growth stress of around 63 GPa in the scale which is much higher than the bending strength of Cr_2O_3 at 400 MPa [286]. This would contribute to the generation of cracking in the oxide scale as the growth of the scale proceeds combined with wrinkling from decohesion between the oxide and metal interface during the process. The thermal stress was calculated by Zheng et al. [283] for a Ni based superalloy

and was found to be much lower than the growth stress. Thus, while thermal stress will contribute, the main factor behind spallation would be the growth stress. The fact that spallation occurred means that the K_p values after 264 h for ISLAND3 and CONTROL and for ISLAND7 after 96 h could be higher than those measured.

Even though the specimens were highly polished, the scale exhibits areas which have a higher thickness in specific locations as observed in Figure 7.11 which are thought to be due to enhanced grain boundary oxidation. For all conditions, formation of Al_2O_3 under the scale was visible as shown in Figure 7.11 and Figure 7.12; both intergranular; along the grain boundaries and intragranular; through the grains. For the ISLAND7 condition, the intergranular oxidation was observed to be very prevalent, with significant grain boundaries being highlighted by alumina oxides along the grain boundaries to depths of around 28 ± 4 μm. For the CONTROL and ISLAND3 conditions, the depth of alumina penetration was also observed but to a much lower extent; at around 8 ± 4 μm for both conditions. The CONTROL and ISLAND3 conditions had a similar oxide thickness and alumina penetration to what has been observed for solution treated L-PBF IN718 [79], while the ISLAND7 condition has a slightly higher Cr oxide thickness and a much deeper alumina penetration. The smaller initial grain size of ISLAND7 condition would mean that there is a higher percentage of short circuit diffusion pathways for oxygen to diffuse into the bulk of the material and for Al and Ti to diffuse towards the oxide scale. Apart from more intergranular oxidation, the depth of penetration of the intergranular oxides for this condition is also much higher compared to the other conditions which would indicate that oxygen was able to penetrate deeper into the substrate. The earlier spallation of this condition could have affected this behaviour, providing short windows where oxygen diffusion into the substrate was facilitated considerably resulting in the deeper oxygen penetration observed. While the degree of spallation was not very high before 504 h, there were some areas of oxide which were removed which could have resulted in this behaviour. Further investigation in the stress state at the top of the surface needs to be performed to confirm this. The degree of alumina penetration at the grain boundaries has been observed to accelerate fatigue failure within certain stress ranges, although the behaviour is very complex and dependent on the stresses induced in the base metal underneath the oxide film [181]. From an application perspective, extensive intergranular oxidation could present an uncertainty and loading limitation, making it difficult to predict the failure life of a component accurately.

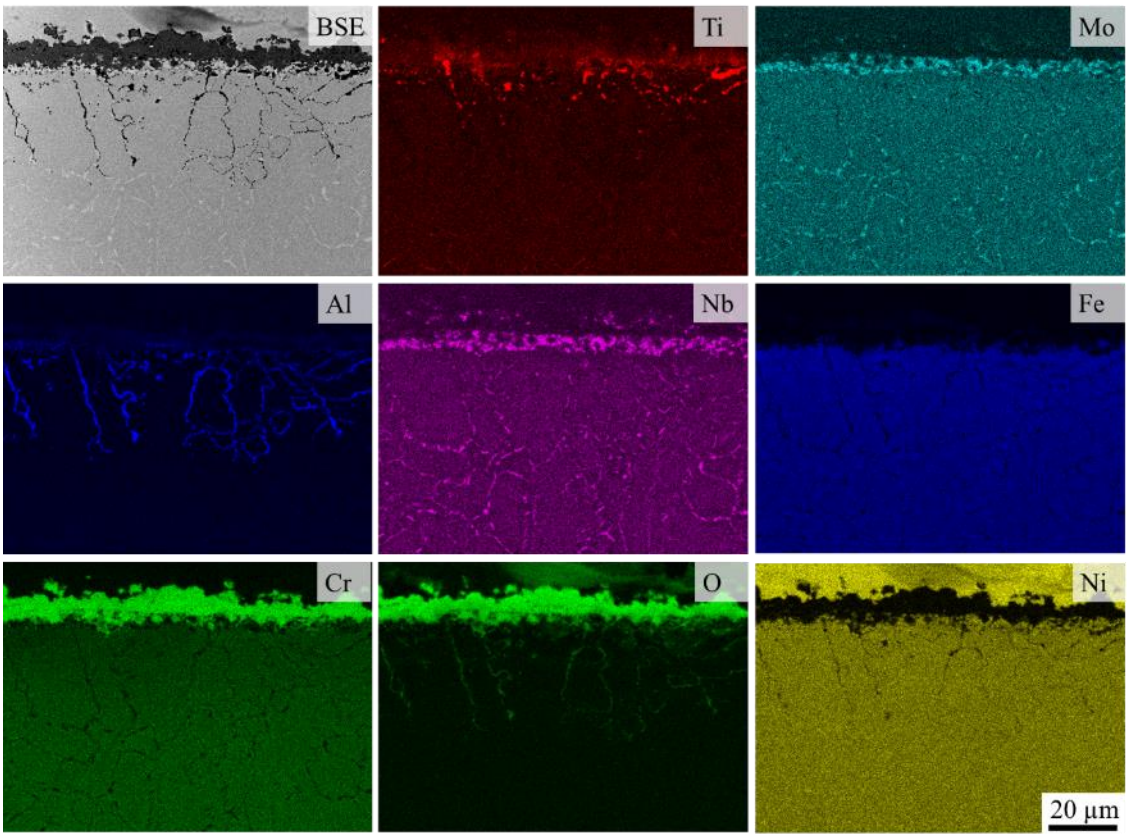


Figure 7.12: BSE micrograph and EDS maps for the ISLAND7 condition after 504 h, showing the elemental distribution of the oxides and underlying segregation.

The internal oxides observed in Figure 7.12 are predominantly rich in Al, but some Ti based oxides or Ti based nitrides are also visible closer to the surface. Formation of rutile (TiO_2) phases in the oxide scale for RR1000 has been detected by Cruchley et al. [189] and formation of TiO_2 intergranular phases have also been observed for IN718 by Calandri et al. [79]. The deeper alumina penetration at the grain boundaries as opposed to through the grains supports the fact that the boundaries are acting as short circuit diffusion pathways.

Furthermore, the near surface region beneath the chromia scale is exhibiting a higher amount of Nb and, interestingly Mo. The enrichment of the near surface in Nb has been previously observed for Inconel 625 [188] oxidised at 950ºC and for IN718 at 850 ºC [79,187] although in this case the Mo enrichment observed here was not documented, but visible in EDS results by Calandri et al. [79] while the Mn enrichment observed for IN625 was not detected here. The Nb enrichment was observed for all conditions after 24 h, forming a quasi-continuous layer under the chromium oxide

at around 96 h for all conditions. The Nb enrichment for IN718 has been confirmed to be δ-phase (Ni_3Nb) [287]. It is thought that this Nb layer at the interface between the Cr oxide and parent metal contributes to slowing down the oxidation rate [188,287].

A region depleted in Cr is also visible confirmed through EDS line scans in Figure 7.13 (a) due to the Cr being used to form the external Cr_2O_3 scale. For the ISLAND3 condition this depletion zone was around 20 μm while for the ISLAND7 condition the Cr depletion zone was around 26 μm deep. Nb enrichment can be observed in Figure 7.13 (b). The enrichment of Nb right under the oxide scale is evident with a corresponding increase in Ni content. This has been attributed to the formation of Ni_3Nb phases under the oxide scale [79]. Enrichment of Ni and Nb is also evident at the grain boundaries beyond the depth at which the alumina intergranular oxides form in Figure 7.12 and in Figure 7.13 (b and c) attributable to δ Ni_3Nb phases precipitating at the grain boundaries [79]. Upon closer inspection in Figure 7.13 (b), the Mo enrichment under the scale observed in Figure 7.12 appears to be close to the base chemical composition which may indicate that rather than enrichment occurring for this element, the lack of other elements due to diffusion means that the signal for Mo in the EDS map in Figure 7.12, appears magnified. Interestingly, the top surface composition of the oxide has some enrichment in Fe and Ni shown in Figure 7.13 (c) supporting the spinel formation already discussed. The intergranular oxidation of Al can be observed occurring at 40 μm in Figure 7.13 (c), while at the near surface Ti, Al and O enrichment is visible likely due to intragranular oxides or in the case of Ti potentially nitride phases forming in the vicinity as shown in Figure 7.13 (d). A schematic representation of these oxide phases is shown in Figure 7.13 (e).

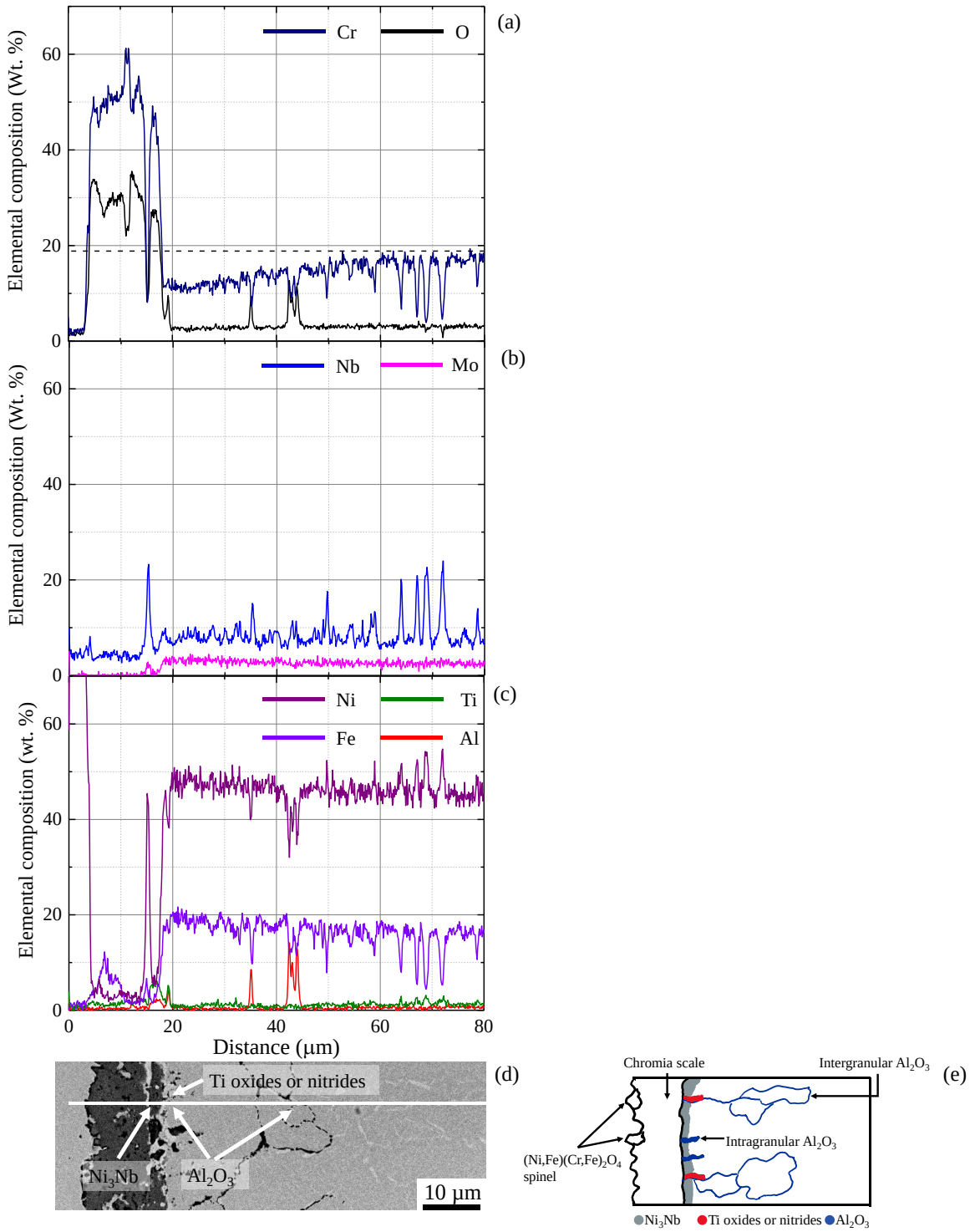


Figure 7.13: Variation in chemical composition along the cross-section for (a) Cr and O where dotted line indicates base material Cr composition, (b) Nb and Mo, (c) Fe, Ni Al and Ti together with (d) the respective BS micrograph and (e) a schematic representation of the phases present on oxidised IN718. Specimen under consideration was ISLAND7 after 504 h.

The fact that the differences in grain size and prevalent orientations did not significantly alter the oxidation rates over long exposure time is interesting. Over long exposures the differences in microstructure do not translate into a significant difference between conditions and do not alter the preferred orientation of the oxide being formed or the type of oxide being formed. When considering parts produced through AM, the grain size overall is still going to be much larger than an equivalent wrought condition (hundreds of microns compared to tens of microns). While there is a difference in grain size between the conditions seen here, this difference is still between conditions where the grains are overall very large. While the larger grain size investigated here overall probably did result in a small reduction in the initial oxidation rate, this is not enough to be significant especially after 504 h. During the oxidation process the oxide will also undergo recrystallisation which will further contribute to a reduction in the effect initial grain size has for long oxidation durations. This was especially visible for regions at the surface forming minute oxide grains. The difference in initial grain size and orientation does lead to a different degree of intergranular oxide penetration which may have implications for the fatigue performance. From an application perspective, these results are interesting as it means that specimens can be optimised to have smaller grain sizes or optimised for high density through L-PBF without having consequences on the high temperature oxidation performance. Further investigation into the reason behind the deeper intergranular oxide penetration is required focusing on the stresses generated at the oxide surface and investigating the nature of the parent metal grain boundaries in the near surface area as due to local recrystallisation in the near surface area the grain boundaries may be changing in nature also affecting the oxidation behaviour [272].

7.4 Conclusion

In this work the behaviour of L-PBF IN718 upon exposure to high temperature oxidising conditions was investigated. Three different conditions with different grain size and predominant grain orientations were analysed with the aim of determining whether microstructural control though different scanning strategies applied in L-PBF would affect the oxidation resistance.

The mass gain behaviour was broadly similar between the different conditions after long durations and comparable to wrought IN718. Even though the grain size and preferred texture for the conditions are different, after long exposure times the mass gain values are statistically similar

following sub-parabolic oxidation kinetics.

After 96 h, the specimen with the smallest grain size exhibited spallation, while the specimens with a larger grain size exhibited spallation after 264 h. The smaller grained condition also exhibited a higher degree of intergranular alumina penetration compared to the other conditions. All the conditions investigated here formed an underlying Nb rich layer which has been associated with a reduction of the oxidation rate moving from parabolic to cubic oxidation kinetics.

Further investigation is required to understand the stress states generated on the oxide surface during oxidation through for instance XRD stress measurements at different time intervals and to investigate the reason behind the early unexpected spallation observed here together with a more detailed characterisation of the near-surface sections under the oxide to determine whether the grain boundary character affected the oxidation behaviour. Furthermore, short term oxidation studies using EBSD would be useful in isolating the effect of surface grain orientation from the initial grain size.

CHAPTER 8. Conclusion and future work

8.1 Conclusion

The main findings of this doctoral work are summarised as follows:

i. Effect of laser heat input parameters compared to laser scanning strategy on the microstructure

The effects of laser heat input parameters together with different combinations of the island scanning parameters on the grain size, morphology and texture along the build direction were quantified. Increases in power and decreases in hatch spacing both resulted in a larger, more aligned grain structure along the building direction. Both power and hatch spacing were less effective at modifying the texture than changes in speed due to the short interaction times characterising the L-PBF process limiting effective heat transfer. Furthermore, changes in the heat input parameters can result in porosity from lack of consolidation or overheating. It was found that the scanning strategy was more effective at modifying the texture along the build direction compared to laser heat input parameters. A smaller island size, smaller island shift, and a higher island overlap all resulted in more alignment and larger grains along the B.D. The specimens obtained were still nominally dense. Smaller islands meant that the laser needed less time to arrive at the initial position increasing the pre-heat of the subsequent raster and inducing more epitaxial growth. Specimens with a smaller island size also yielded a larger cell size equated to a lower cooling rate ($G{\cdot}R$). Island shift values close to the build volume size interrupted the scanning order of the island and thus interrupted epitaxial growth; reducing it, while changes in the movement path such as a parallel island strategy could be used to increase epitaxial growth. Rather than changing the heat input into the melt pool and directly affecting the thermal gradient and solidification rate, changes in laser movement change how fast the layer cools down (affecting both G and R) and the heat flow direction. Using such an approach is indirect but viable when it is not desired to modify the heat input parameters for instance to minimise porosity or impact on cracking without modifying part orientation on a substrate.

ii. Effect of cross-sectional area

The build volume is often overlooked when considering parametric studies. This is especially important when the scanning strategy is being modified as the cross-sectional area being scanned will affect the movement path. Changing the island size was still an effective way at modifying the grain size and preferred alignment to the build direction regardless of the cross-sectional area. While the changes in scanning strategy were very effective for small cross-sectional areas, some scanning strategy modifications were not as effective when moving to larger cross-sectional areas. This was observed for both large volumes used for tensile bar manufacture and proof-of-concept hollow turbine blades (a complex structure). Changing the island shift was less effective at randomising and reducing the texture when compared to results obtained for small build volumes where this was the most successful strategy. As the scanning strategy is directly affected by the cross-sectional area being scanned, when considering scanning strategies as a route towards microstructural modifications the design of the components needs to be taken into consideration.

iii. Effect of baseplate heating

The feasibility of a heated baseplate in L-PBF of Inconel 718 was briefly investigated as an alternate method induce the columnar to equiaxed transition. This has not been previously applied specifically to L-PBF. In EB-PBF and DED such a concept has been investigated and while the idea is similar, the thermal gradient, solidification rate, heat source interaction and amount of heating in L-PBF are different. Baseplate heating at 400ºC appeared to reduce the thermal gradient, which together with the relatively fast solidification rates characterising the process led to differences compared to specimens not manufactured using a heated base plate. Numerous small globular grains formed in the mixed growth regime which could have been a result of either equiaxed nucleation and growth within the melt pool or recrystallisation of the existing grain structure as the specimen was being built. Through the application of a heated baseplate, an overall decrease in grain size was observed coupled with a reduction in the preferred alignment along the build direction together with an increase in the local misorientation. This contributed to an increase in hardness along the build direction for specimens processed on the heated baseplate compared to specimens which were not processed with a heated baseplate.

iv. Variation in mechanical properties and microstructural grading with scanning strategies

The feasibility of using laser scanning strategies to purposefully modify the microstructure and thus mechanical properties was further investigated using strategy parameters which yielded the most optimal density for small build volumes together with the highest degree of modification along the build direction. Room temperature mechanical testing demonstrated that the scanning strategy can be used in generating monolithic conditions with varying properties and functionally graded specimens with varying microstructures/properties. Specimens having larger grains and higher amounts of [001] predominant orientation to the loading direction exhibited a lower Young's modulus, a lower strength and locally more micro-strain. As observed in DIC, in a functionally graded component, consisting of two types of grain morphology, meant that the smaller grained, more randomly oriented side restrained the deformation of the overall component and that most of the strain occurred in the larger grained side. The junction of these functionally graded specimens was sound with a gradual change in grain size over the junction and failure occurring away from the junction.

v. Oxide films in L-PBF

The ductility for the mechanical test bars investigated here was relatively low and exhibited significant variability. Surprisingly, fractography revealed that even though full consolidation was obtained, failure of the specimens was still defect driven due to the entrainment of Al oxide films in the melt reducing wettability and affecting consolidation between subsequent layers. All the lack of consolidation defects exhibited aluminium enrichment and showed surface features such as wrinkling and slip bands associated with the folding and entrainment of thin Al films in the melt pool. Such defects have been observed in casting of Ni superalloys but have not been discussed in depth in the context of L-PBF for IN718. They are thought to occur due to the vaporisation and subsequent deposition of Al on the surface of newly formed melt pools. The smaller island size conditions in this work were observed to have a particularly high incidence of such defects. These conditions were also hotter than larger islands supporting the fact that vaporisation combined with melt pool flow dynamics could be contributing to the entrainment of the oxide films generated.

vi. Oxidation

The behaviour of L-PBF IN718 exposed to oxidising conditions at 850ºC with different initial microstructures was investigated to determine whether microstructural control through different scanning strategies would affect the oxidation resistance. Surprisingly, even though for L-PBF the grain size is larger compared to mill-annealed IN718, the oxidation rates after durations of 504 h were comparable those observed in literature for IN718 in this condition. Even though the grain size and preferred texture of the various conditions were both different, after 504 h the mass gain values were statistically similar following sub-parabolic oxidation kinetics. After 96 h the specimen with the smallest grain size exhibited spallation, while the specimens with a larger grain size exhibited spallation after 264 h. The smaller grained condition also exhibited a higher degree of intergranular alumina penetration compared to the other conditions. As the grain size for such specimens was smaller, intergranular oxidation is expected to be more prevalent. The deeper penetration of the oxides may be attributable to the earlier spallation occurring in these conditions resulting in very rapid attack when the base metal is exposed. All the conditions investigated here formed an underlying Nb rich layer which has been associated with a reduction of the oxidation rate moving from parabolic to sub-parabolic oxidation kinetics. From an application perspective, these results mean that specimens can be optimised to have smaller grain sizes for mechanical performance, optimised for high density or made using parameters favourable to avoid cracking without having negative consequences on their high temperature oxidation behaviour.

8.2 Future work

The use of laser heat parameters and more effectively laser scanning strategies has been demonstrated to be a promising tool which could be used to functionally vary mechanical properties or create graded components with no negative correlations for oxidation resistance. The following section will discuss further work to complement this research and potential areas for further investigation.

vii. Parametric improvements

While several scanning strategies were investigated, these were analysed using a constant set of laser heat input parameters. The amalgamation of heat input parameters aimed at reducing columnar growth together with scanning strategies known to reduce columnar growth or the opposite

approach to obtain a structure close to a directionally solidified microstructure would be valuable to further optimise mechanical properties. Modifying the scanning strategies was found to be affected by the cross-sectional area for parameters such as the island shift – applying an appropriate change to island shift in view of the cross-sectional area being scanned might be an effective way in which to induce the randomisation effect for larger areas. The properties considered here were related to grain size and orientation; investigating methods to modify the grain boundary character such as by inducing serrated grain boundaries or coincident site lattice boundaries would provide further improvements to those described here. While the heat treatment applied here was suitable in removing most brittle intercellular compounds, the use of such a heat treatment results in the recovery of dislocation structures at cell boundaries. Optimising the heat treatment to reduce recovery could be used in tandem with changes in microstructure to further strengthen IN718. IN718 also relies primarily on the formation of γ' and γ" for the strengthening effect; it would be useful to investigate to what degree microstructural control can improve the properties for alloys where precipitate strengthening is not used or alloys which are prone to solidification cracking. Further testing at elevated temperature such as creep and tensile testing together with fatigue testing would also provide a more accurate idea of how such components would behave in their intended application.

viii. Heated baseplate

The further optimisation of deposition with a heated baseplate could be used in tandem with parametric improvements to generate a fully equiaxed microstructure. While the results obtained from the preliminary investigation are quite promising, further work is needed to optimise the parameters to obtain a fully equiaxed structure and characterise the effect of a heated baseplate on the surface finish and density. Variations in melt pool size and shape together with its solidification behaviour could be investigated in more detail and the dislocation density could be measured to quantify the effect of the heated base plate on such structures. While the hardness measurements made along the build direction would indicate that the preferred alignment to the build direction is being modified, further mechanical testing could be done on specimens produced in different orientations to confirm this.

ix. Oxide film formation during processing

One of the limitations in this work was the oxidation of aluminium during fabrication. This formed aluminium oxide films entrained in the melt which were one of the major reasons behind the premature failure observed. Modelling of the melt pool motion and the melt pool temperatures, especially when the scanning strategy is changed would provide a vital tool in reducing the formation of such films. Transmission electron microscopy coupled with focused ion beam milling of such defects would provide further valuable characterisation opportunities to understand their formation mechanisms. The chemical composition of IN718 has not been specifically formulated for production using AM. Alloy design for additive manufacturing could also be a viable route towards reducing the formation of such films and ensuring that the ductility of components generated through AM is acceptable. Such powder design could involve the use of elements designed to react preferentially with the oxygen traces within the chamber during processing.

x. High temperature oxidation resistance

Oxidation resistance was investigated at 850ºC. Limited spallation initiated after 96 h which was unexpected when compared to other work in literature. Stress analysis of the oxide as it is forming together with an investigation of the changes in the near-surface area would be valuable additions to this work to understand the reason behind the unexpected spallation. Further investigation would be valuable at a lower temperature to gain a more accurate idea of the K_p values as these values would have been affected by the spallation occurring during the test. Furthermore, investigation into the effect of texture on the initial transient oxidation stages would be very valuable to determine whether the texture is affecting the oxide thickness for short durations. Short term oxidation studies using EBSD would be useful in isolating the effect of surface grain orientation from the initial grain size. In practice IN718 is used up to 650ºC, thus investigating the transient oxidation stage at a higher temperature would still offer a viable benefit to components used at lower temperatures. The mechanical testing of components which have been subjected to an oxidising environment would also provide further depth to these investigations and provide a full picture of practical application. Further investigation could assist in elucidating whether the different degree of intergranular oxide penetration has negative consequences for fatigue life of L-PBF IN718 components. Investigation

of the effect of different cross-section orientations e.g. XY cross-sections would also provide a more complete picture of the performance. Quantitative modelling could be performed to rationalise the relationship between the chromium oxide and the chromium concentration gradient moving into the IN718 substrate. This could be coupled with more accurate chemical analysis techniques such as electron probe microanalysis to further improve the accuracy in percentages of elements observed.

REFERENCES

[1] R.E. Schafrik, D.D. Ward, J.R. Groh, Application of Alloy 718 in GE Aircraft Engines: Past, Present and Next Five Years, Proc. Int. Symp. Superalloys Var. Deriv. (2001) 1–11. https://doi.org/10.7449/2001/Superalloys_2001_1_11.

[2] M.J. Donachie, S.J. Donachie, Superalloys A Technical Guide, 2002. https://doi.org/10.1016/B978-0-444-43022-9.50017-1.

[3] E. Akca, A. Gürsel, A Review on Superalloys and IN718 Nickel-Based INCONEL Superalloy, Period. Eng. Nat. Sci. 3 (2015). https://doi.org/10.21533/pen.v3i1.43.

[4] M.B. Henderson, D. Arrell, R. Larsson, M. Heobel, G. Marchant, Nickel based superalloy welding practices for industrial gas turbine applications, Sci. Technol. Weld. Join. 9 (2004) 13–21. https://doi.org/10.1179/136217104225017099.

[5] C. Tong, Advanced Materials Enable Energy Production from Fossil Fuels, in: C. Tong (Ed.), Intorduction to Mater. Adv. Energy Syst., 1st ed., Springerlink, Chicago, USA, 2018: pp. 171–230.

[6] D.R. Greatrix, Turbofan engines, in: Powered Flight Eng. Aerosp. Propuls., 1st ed., Springer, 2012: pp. 1–519. https://doi.org/10.1007/978-1-4471-2485-6.

[7] T. Trosch, J. Strößner, R. Völkl, U. Glatzel, Microstructure and mechanical properties of selective laser melted Inconel 718 compared to forging and casting, Mater. Lett. 164 (2016) 428–431. https://doi.org/10.1016/j.matlet.2015.10.136.

[8] Y. Kaynak, E. Tascioglu, Post-processing effects on the surface characteristics of Inconel 718 alloy fabricated by selective laser melting additive manufacturing, Prog. Addit. Manuf. 5 (2020) 221–234. https://doi.org/10.1007/s40964-019-00099-1.

[9] K. Prasad, R. Sarkar, P. Ghosal, V. Kumar, Simultaneous creep-fatigue damage accumulation of forged turbine disc of IN 718 superalloy, Mater. Sci. Eng. A. 572 (2013) 1–7. https://doi.org/10.1016/j.msea.2013.02.003.

[10] W.E. Frazier, Metal additive manufacturing: A review, J. Mater. Eng. Perform. 23 (2014)

1917–1928. https://doi.org/10.1007/s11665-014-0958-z.

[11] M. Brandt, S. Sun, M. Leary, S. Feih, J. Elambasseril, Q. Liu, High-value SLM aerospace components: From design to manufacture, Adv. Mater. Res. 633 (2013) 135–147. https://doi.org/10.4028/www.scientific.net/AMR.633.135.

[12] R.C. Reed, The superalloys, fundamentals and applications, Cambridge University Press, 2006. https://doi.org/10.1017/CBO9781107415324.004.

[13] M. Rahman, W.K.H. Seah, T.T. Teo, The machinability of Inconel 718, J. Mater. Process. Technol. 63 (1997) 199–204. https://doi.org/10.1016/S0924-0136(96)02624-6.

[14] T. DebRoy, H.L. Wei, J.S. Zuback, T. Mukherjee, J.W. Elmer, J.O. Milewski, A.M. Beese, A. Wilson-Heid, A. De, W. Zhang, Additive manufacturing of metallic components – Process, structure and properties, Prog. Mater. Sci. 92 (2018) 112–224. https://doi.org/10.1016/j.pmatsci.2017.10.001.

[15] X. Yu, X. Lin, F. Liu, L. Wang, Y. Tang, J. Li, S. Zhang, W. Huang, Influence of post-heat-treatment on the microstructure and fracture toughness properties of Inconel 718 fabricated with laser directed energy deposition additive manufacturing, Mater. Sci. Eng. A. 798 (2020) 140092. https://doi.org/10.1016/j.msea.2020.140092.

[16] A. Keshavarzkermani, M. Sadowski, L. Ladani, Direct metal laser melting of Inconel 718: Process impact on grain formation and orientation, J. Alloys Compd. 736 (2018) 297–305. https://doi.org/10.1016/j.jallcom.2017.11.130.

[17] S. Azadian, L.Y. Wei, R. Warren, Delta phase precipitation in inconel 718, Mater. Charact. 53 (2004) 7–16. https://doi.org/10.1016/j.matchar.2004.07.004.

[18] B. Hassan, J. Corney, Grain boundary precipitation in Inconel 718 and ATI 718Plus, Mater. Sci. Technol. (United Kingdom). 33 (2017) 1879–1889. https://doi.org/10.1080/02670836.2017.1333222.

[19] J. Gayda, T.P. Gabb, P.T. Kantzos, the Effect of Dual Microstructure Heat Treatment on an Advanced Nickel-Base Disk Alloy, Superalloys 2004 (Tenth Int. Symp. Superalloys). (2004) 323–329. https://doi.org/10.7449/2004/Superalloys_2004_323_329.

[20] T.P. Gabb, P.T. Kantzos, J. Telesman, J. Gayda, C.K. Sudbrack, B. Palsa, Fatigue resistance of the grain size transition zone in a dual microstructure superalloy disk, Int. J. Fatigue. 33 (2011) 414–426. https://doi.org/10.1016/j.ijfatigue.2010.09.022.

[21] T.D. Ngo, A. Kashani, G. Imbalzano, K.T.Q. Nguyen, D. Hui, Additive manufacturing (3D printing): A review of materials, methods, applications and challenges, Compos. Part B Eng. 143 (2018) 172–196. https://doi.org/10.1016/j.compositesb.2018.02.012.

[22] S. Singh, S. Ramakrishna, R. Singh, Material issues in additive manufacturing: A review, J. Manuf. Process. 25 (2017) 185–200. https://doi.org/10.1016/j.jmapro.2016.11.006.

[23] J. Strößner, M. Terock, U. Glatzel, Mechanical and Microstructural Investigation of Nickel-Based Superalloy IN718 Manufactured by Selective Laser Melting (SLM), Adv. Eng. Mater. 17 (2015) 1099–1105. https://doi.org/10.1002/adem.201500158.

[24] W.J. Sames, F.A. List, S. Pannala, R.R. Dehoff, S.S. Babu, The metallurgy and processing science of metal additive manufacturing, Int. Mater. Rev. 61 (2016) 315–360. https://doi.org/10.1080/09506608.2015.1116649.

[25] J. Allen, An Investigation into the Comparative Costs of Additive Manufacture vs. Machine from Solid for Aero Engine Parts, in: Cost Eff. Manuf. via Net-Shape Process., 2006: pp. 1–10. https://doi.org/10.14339/RTO-MP-AVT-139-17.

[26] J.P. Kruth, G. Levy, F. Klocke, T.H.C. Childs, Consolidation phenomena in laser and powder-bed based layered manufacturing, CIRP Ann. - Manuf. Technol. 56 (2007) 730–759. https://doi.org/10.1016/j.cirp.2007.10.004.

[27] C. Qiu, C. Panwisawas, M. Ward, H.C. Basoalto, J.W. Brooks, M.M. Attallah, On the role of melt flow into the surface structure and porosity development during selective laser melting, Acta Mater. 96 (2015) 72–79. https://doi.org/10.1016/j.actamat.2015.06.004.

[28] S.A. Khairallah, A. Anderson, Mesoscopic simulation model of selective laser melting of stainless steel powder, J. Mater. Process. Technol. 214 (2014) 2627–2636. https://doi.org/10.1016/j.jmatprotec.2014.06.001.

[29] S. Das, Physical Aspects of Process Control in Selective Laser Sintering of Metals, Adv. Eng.

Mater. 5 (2003) 701–711. https://doi.org/10.1002/adem.200310099.

[30] D.R. Eo, S.H. Park, J.W. Cho, Controlling inclusion evolution behavior by adjusting flow rate of shielding gas during direct energy deposition of AISI 316 L, Addit. Manuf. 33 (2020) 101119. https://doi.org/10.1016/j.addma.2020.101119.

[31] J.P. Kruth, L. Froyen, J. Van Vaerenbergh, P. Mercelis, M. Rombouts, B. Lauwers, Selective laser melting of iron-based powder, J. Mater. Process. Technol. 149 (2004) 616–622. https://doi.org/10.1016/j.jmatprotec.2003.11.051.

[32] D.R. Eo, S.G. Chung, J.M. Jeon, J.W. Cho, Melt pool oxidation and reduction in powder bed fusion, Addit. Manuf. 41 (2021) 101982. https://doi.org/10.1016/j.addma.2021.101982.

[33] R. Li, J. Liu, Y. Shi, L. Wang, W. Jiang, Balling behavior of stainless steel and nickel powder during selective laser melting process, Int. J. Adv. Manuf. Technol. 59 (2012) 1025–1035. https://doi.org/10.1007/s00170-011-3566-1.

[34] N.K. Tolochko, T. Laoui, Y.V. Khlopkov, S.E. Mozzharov, V.I. Titov, M.B. Ignatiev, Absorptance of powder materials suitable for laser sintering, Rapid Prototyp. J. 6 (2000) 155–160. https://doi.org/10.1109/CCNC.2017.7983268.

[35] S.A. Khairallah, A.T. Anderson, A. Rubenchik, W.E. King, Laser powder-bed fusion additive manufacturing: Physics of complex melt flow and formation mechanisms of pores, spatter, and denudation zones, Acta Mater. 108 (2016) 36–45. https://doi.org/10.1016/j.actamat.2016.02.014.

[36] D. Wang, C. Song, Y. Yang, Y. Bai, Investigation of crystal growth mechanism during selective laser melting and mechanical property characterization of 316L stainless steel parts, Mater. Des. 100 (2016) 291–299. https://doi.org/10.1016/j.matdes.2016.03.111.

[37] H.E. Helmer, C. Körner, R.F. Singer, Additive manufacturing of nickel-based superalloy Inconel 718 by selective electron beam melting: Processing window and microstructure, J. Mater. Res. 29 (2014) 1987–1996. https://doi.org/10.1557/jmr.2014.192.

[38] J.P. Oliveira, T.G. Santos, R.M. Miranda, Revisiting fundamental welding concepts to improve additive manufacturing: From theory to practice, Prog. Mater. Sci. 107 (2020)

100590. https://doi.org/10.1016/j.pmatsci.2019.100590.

[39] D. Wang, S. Li, G. Deng, Y. Liu, M.M. Attallah, A melt pool temperature model in laser powder bed fabricated CM247LC Ni superalloy to rationalize crack formation and microstructural inhomogeneities, Metall. Mater. Trans. A. (2021). https://doi.org/10.1007/s11661-021-06457-5.

[40] J.P. Oliveira, A.D. LaLonde, J. Ma, Processing parameters in laser powder bed fusion metal additive manufacturing, Mater. Des. 193 (2020) 1–12. https://doi.org/10.1016/j.matdes.2020.108762.

[41] D. Dai, D. Gu, Effect of metal vaporization behavior on keyhole-mode surface morphology of selective laser melted composites using different protective atmospheres, Appl. Surf. Sci. 355 (2015) 310–319. https://doi.org/10.1016/j.apsusc.2015.07.044.

[42] S.A. David, J.M. Vitek, Correlation between solidification parameters and weld microstructures, Int. Mater. Rev. 34 (1989) 213–245. https://doi.org/10.1179/imr.1989.34.1.213.

[43] D.D. Gu, W. Meiners, K. Wissenbach, R. Poprawe, Laser additive manufacturing of metallic components: Materials, processes and mechanisms, Int. Mater. Rev. 57 (2012) 133–164. https://doi.org/10.1179/1743280411Y.0000000014.

[44] I.A. Roberts, C.J. Wang, R. Esterlein, M. Stanford, D.J. Mynors, A three-dimensional finite element analysis of the temperature field during laser melting of metal powders in additive layer manufacturing, Int. J. Mach. Tools Manuf. 49 (2009) 916–923. https://doi.org/10.1016/j.ijmachtools.2009.07.004.

[45] Y. Li, D. Gu, Parametric analysis of thermal behavior during selective laser melting additive manufacturing of aluminum alloy powder, Mater. Des. 63 (2014) 856–867. https://doi.org/10.1016/j.matdes.2014.07.006.

[46] W. Kurz, C. Bezençon, M. Gäumann, Columnar to equiaxed transition in solidification processing, Sci. Technol. Adv. Mater. 2 (2001) 185–191. https://doi.org/10.1016/S1468-6996(01)00047-X.

[47] X. Wang, T. Keya, K. Chou, Build Height Effect on the Inconel 718 Parts Fabricated by Selective Laser Melting, Procedia Manuf. 5 (2016) 1006–1017. https://doi.org/10.1016/j.promfg.2016.08.089.

[48] L. Thijs, K. Kempen, J.P. Kruth, J. Van Humbeeck, Fine-structured aluminium products with controllable texture by selective laser melting of pre-alloyed AlSi10Mg powder, Acta Mater. 61 (2013) 1809–1819. https://doi.org/10.1016/j.actamat.2012.11.052.

[49] V. Ocelík, I. Furár, J.T.M. De Hosson, Microstructure and properties of laser clad coatings studied by orientation imaging microscopy, Acta Mater. 58 (2010) 6763–6772. https://doi.org/10.1016/j.actamat.2010.09.002.

[50] H.L. Wei, J.W. Elmer, T. Debroy, Origin of grain orientation during solidification of an aluminum alloy, Acta Mater. 115 (2016) 123–131. https://doi.org/10.1016/j.actamat.2016.05.057.

[51] B. AlMangour, D. Grzesiak, J.-M. Yang, Scanning strategies for texture and anisotropy tailoring during selective laser melting of TiC/316L stainless steel nanocomposites, J. Alloys Compd. 728 (2017) 424–435. https://doi.org/10.1016/j.jallcom.2017.08.022.

[52] Q. Jia, D. Gu, Selective laser melting additive manufacturing of Inconel 718 superalloy parts: Densification, microstructure and properties, J. Alloys Compd. 585 (2014) 713–721. https://doi.org/10.1016/j.jallcom.2013.09.171.

[53] E.L. Stevens, J. Toman, A.C. To, M. Chmielus, Variation of hardness, microstructure, and Laves phase distribution in direct laser deposited alloy 718 cuboids, Mater. Des. 119 (2017) 188–198. https://doi.org/10.1016/j.matdes.2017.01.031.

[54] N. Nadammal, S. Cabeza, T. Mishurova, T. Thiede, A. Kromm, C. Seyfert, L. Farahbod, C. Haberland, J.A. Schneider, P.D. Portella, G. Bruno, Effect of hatch length on the development of microstructure, texture and residual stresses in selective laser melted superalloy Inconel 718, Mater. Des. 134 (2017) 139–150. https://doi.org/10.1016/j.matdes.2017.08.049.

[55] C.H. Zhang, H. Zhang, C.L. Wu, S. Zhang, Z.L. Sun, S.Y. Dong, Multi-layer functional graded stainless steel fabricated by laser melting deposition, Vacuum. 141 (2017) 181–187. https://doi.org/10.1016/j.vacuum.2017.04.020.

[56] X. Wang, J.A. Muñiz-Lerma, O. Sánchez-Mata, M. Attarian Shandiz, M. Brochu, Microstructure and mechanical properties of stainless steel 316L vertical struts manufactured by laser powder bed fusion process, Mater. Sci. Eng. A. 736 (2018) 27–40. https://doi.org/10.1016/j.msea.2018.08.069.

[57] J. DuPont N., Fundamentals of weld solidification, in: T.J. Lienert, S.S. Babu, T.A. Siewert, V.L. Acoff (Eds.), ASM Handb. Weld. Fundam. Process. Vol. 06A, 1st ed., ASM International, 2011: pp. 102–121.

[58] R. Casati, J.N. Lemke, A. Tuissi, M. Vedani, Aging behaviour and mechanical performance of 18-Ni 300 steel processed by selective laser melting, Metals (Basel). 6 (2016) 1–13. https://doi.org/10.3390/met6090218.

[59] J.A. Dantzig, M. Rappaz, Solidification, 2nd ed., EPFL Press, 2017.

[60] D. Deng, R.L. Peng, H. Brodin, J. Moverare, Microstructure and mechanical properties of Inconel 718 produced by selective laser melting: Sample orientation dependence and effects of post heat treatments, Mater. Sci. Eng. A. 713 (2018) 294–306. https://doi.org/10.1016/j.msea.2017.12.043.

[61] N. Raghavan, R.R. Dehoff, S. Pannala, S. Simunovic, M.M. Kirka, J. Turner, N. Carlson, S.S. Babu, Numerical modelling of heat transfer and influence of process parameters on tailoring the grain morphology of in718 in EBM, Acta Mater. 112 (2016) 303–314.

[62] P. Nie, O.A. Ojo, Z. Li, Numerical modeling of microstructure evolution during laser additive manufacturing of a nickel-based superalloy, Acta Mater. 77 (2014) 85–95. https://doi.org/10.1016/j.actamat.2014.05.039.

[63] Y. Tian, D. McAllister, H. Colijn, M. Mills, D. Farson, M. Nordin, S. Babu, Rationalization of microstructure heterogeneity in INCONEL 718 builds made by the direct laser additive manufacturing process, Metall. Mater. Trans. A Phys. Metall. Mater. Sci. 45 (2014) 4470–4483. https://doi.org/10.1007/s11661-014-2370-6.

[64] J.L. Bennett, O.L. Kafka, H. Liao, S.J. Wolff, C. Yu, P. Cheng, G. Hyatt, K. Ehmann, J. Cao, Cooling rate effect on tensile strength of laser deposited Inconel 718, Procedia Manuf. 26 (2018) 912–919. https://doi.org/10.1016/j.promfg.2018.07.118.

[65] A. Yadollahi, N. Shamsaei, S.M. Thompson, D.W. Seely, Effects of process time interval and heat treatment on the mechanical and microstructural properties of direct laser deposited 316L stainless steel, Mater. Sci. Eng. A. 644 (2015) 171–183. https://doi.org/10.1016/j.msea.2015.07.056.

[66] L.L. Parimi, M.M. Attallah, J.C. Gebelin, R.C. Reed, Direct Laser Fabrication of Inconel-718: Effects on Distortion and Microstructure, Superalloys 2012. (2012) 509–519. https://doi.org/10.1002/9781118516430.ch56.

[67] C. Guévenoux, S. Hallais, A. Charles, E. Charkaluk, A. Constantinescu, Influence of interlayer dwell time on the microstructure of Inconel 718 Laser Cladded components, Opt. Laser Technol. 128 (2020) 106218. https://doi.org/10.1016/j.optlastec.2020.106218.

[68] X. Wang, K. Chou, Electron Backscatter Diffraction Analysis of Inconel 718 Parts Fabricated by Selective Laser Melting Additive Manufacturing, Jom. 69 (2017) 402–408. https://doi.org/10.1007/s11837-016-2198-1.

[69] A. Chamanfar, L. Sarrat, M. Jahazi, M. Asadi, A. Weck, A.K. Koul, Microstructural characteristics of forged and heat treated Inconel-718 disks, Mater. Des. 52 (2013) 791–800. https://doi.org/10.1016/j.matdes.2013.06.004.

[70] M.J. Donachie, S.J. Donachie, Understanding superalloy metallurgy, in: Superalloys a Tech. Guid., 2 nd, ASM International, 2002: pp. 25–39.

[71] S. Vernier, E. Andrieu, L. Laffont, Flash oxidation tests to evidence the segregation of boron at the grain boundaries of superalloy Inconel 718, Materialia. 15 (2021). https://doi.org/10.1016/j.mtla.2020.100989.

[72] Systems EOS GmbH - Electro Optical, Material Data Sheet IN718, (2014) 7.

[73] R.Y. Zhang, Z.N. Bi, H.L. Qin, J. Zhang, A.D. Fortes, H.B. Dong, Constrained Lattice Misfit Measurement in Bulk Inconel 718 Using High Resolution Neutron Diffraction, in: Proc. 9th Int. Symp. Superalloy 718 Deriv. Energy, Aerospace, Ind. Appl., The Minerals, Metals & Materials Society, 2018: pp. 439–448. https://doi.org/10.1007/978-3-319-89480-5.

[74] R.C. Reed, C.M.F. Rae, Physical Metallurgy of the Nickel-Based Superalloys, 5th ed.,

Elsevier, 2014. https://doi.org/10.1016/B978-0-444-53770-6.00022-8.

[75] X. You, Y. Tan, S. Shi, J.M. Yang, Y. Wang, J. Li, Q. You, Effect of solution heat treatment on the precipitation behavior and strengthening mechanisms of electron beam smelted Inconel 718 superalloy, Mater. Sci. Eng. A. 689 (2017) 257–268. https://doi.org/10.1016/j.msea.2017.01.093.

[76] V.A. Popovich, E.V. Borisov, A.A. Popovich, V.S. Sufiiarov, D.V. Masaylo, L. Alzina, Impact of heat treatment on mechanical behaviour of Inconel 718 processed with tailored microstructure by selective laser melting, Mater. Des. 131 (2017) 12–22. https://doi.org/10.1016/j.matdes.2017.05.065.

[77] S. Sui, H. Tan, J. Chen, C. Zhong, Z. Li, W. Fan, A. Gasser, W. Huang, The influence of Laves phases on the room temperature tensile properties of Inconel 718 fabricated by powder feeding laser additive manufacturing, Acta Mater. 164 (2019) 413–427. https://doi.org/10.1016/j.actamat.2018.10.032.

[78] Z.S. Yu, J.X. Zhang, Y. Yuan, R.C. Zhou, H.J. Zhang, H.Z. Wang, Microstructural evolution and mechanical properties of Inconel 718 after thermal exposure, Mater. Sci. Eng. A. 634 (2015) 55–63. https://doi.org/10.1016/j.msea.2015.03.004.

[79] M. Calandri, D. Manfredi, F. Calignano, E.P. Ambrosio, S. Biamino, R. Lupoi, D. Ugues, Solution Treatment Study of Inconel 718 Produced by SLM Additive Technique in View of the Oxidation Resistance, Adv. Eng. Mater. 20 (2018). https://doi.org/10.1002/adem.201800351.

[80] M. Anderson, A.L. Thielin, F. Bridier, P. Bocher, J. Savoie, δ Phase precipitation in Inconel 718 and associated mechanical properties, Mater. Sci. Eng. A. 679 (2017) 48–55. https://doi.org/10.1016/j.msea.2016.09.114.

[81] X. Li, J.J. Shi, C.H. Wang, G.H. Cao, A.M. Russell, Z.J. Zhou, C.P. Li, G.F. Chen, Effect of heat treatment on microstructure evolution of Inconel 718 alloy fabricated by selective laser melting, J. Alloys Compd. 764 (2018) 639–649. https://doi.org/10.1016/j.jallcom.2018.06.112.

[82] R.G. Thompson, J.R. Dobbs, D.E. Mayo, Effect of Heat Treatment on Microfissuring in Alloy

718., Weld. J. Res. Suppl. 65 (1986) 299s-304s.

[83] Y.C. Lin, X.Y. Jiang, S.C. Luo, D.G. He, Study on the structural transition and thermal properties of Ni3Nb-D022 phase: First-principles calculation, Mater. Des. 139 (2018) 16–24. https://doi.org/10.1016/j.matdes.2017.10.065.

[84] K.N. Amato, S.M. Gaytan, L.E. Murr, E. Martinez, P.W. Shindo, J. Hernandez, S. Collins, F. Medina, Microstructures and mechanical behavior of Inconel 718 fabricated by selective laser melting, Acta Mater. 60 (2012) 2229–2239. https://doi.org/10.1016/j.actamat.2011.12.032.

[85] P. Krakhmalev, G. Fredriksson, K. Svensson, I. Yadroitsev, I. Yadroitsava, M. Thuvander, R. Peng, Microstructure, solidification texture, and thermal stability of 316 L stainless steel manufactured by laser powder bed fusion, Metals (Basel). 8 (2018). https://doi.org/10.3390/met8080643.

[86] J. Wu, X.Q. Wang, W. Wang, M.M. Attallah, M.H. Loretto, Microstructure and strength of selectively laser melted AlSi10Mg, Acta Mater. 117 (2016) 311–320. https://doi.org/10.1016/j.actamat.2016.07.012.

[87] M. Wang, M.H. Fan, S. Cruchley, Y. Chiu, Effect of Cellular Dislocation Structure on the Strength of Additively Manufactured 316L Stainless Steel, in: Int. Conf. Process. Manuf. Adv. Mater. Fabr. Prop. Appl., Trans Tech Publications Ltd, 2020: pp. 1–9.

[88] Y. Zhong, L. Liu, S. Wikman, D. Cui, Z. Shen, Intragranular cellular segregation network structure strengthening 316L stainless steel prepared by selective laser melting, J. Nucl. Mater. 470 (2016) 170–178. https://doi.org/10.1016/j.jnucmat.2015.12.034.

[89] L. Liu, Q. Ding, Y. Zhong, J. Zou, J. Wu, Y.L. Chiu, J. Li, Z. Zhang, Q. Yu, Z. Shen, Dislocation network in additive manufactured steel breaks strength–ductility trade-off, Mater. Today. 21 (2018) 354–361. https://doi.org/10.1016/j.mattod.2017.11.004.

[90] A. Piglione, B. Attard, V. Vieira Rielli, C.T. Santos Maldonado, M.M. Attallah, S. Primig, M.S. Pham, On the constitutive relationship between solidification cells and the fatigue behaviour of IN718 fabricated by laser powder bed fusion, Addit. Manuf. 47 (2021) 102347. https://doi.org/10.1016/j.addma.2021.102347.

[91] L. Thijs, F. Verhaeghe, T. Craeghs, J. Van Humbeeck, J.P. Kruth, A study of the microstructural evolution during selective laser melting of Ti-6Al-4V, Acta Mater. 58 (2010) 3303–3312. https://doi.org/10.1016/j.actamat.2010.02.004.

[92] B. Dovgyy, A. Piglione, P. Hooper, M.-S. Pham, Comprehensive assessment of the printability of CoNiCrFeMn in Laser Powder Bed Fusion, Mater. Des. 194 (2020) 108845. https://doi.org/10.1016/j.matdes.2020.108845.

[93] H. Helmer, A. Bauereiß, R.F. Singer, C. Körner, Grain structure evolution in Inconel 718 during selective electron beam melting, Mater. Sci. Eng. A. 668 (2016) 180–187. https://doi.org/10.1016/j.msea.2016.05.046.

[94] M. Sundararaman, S. Banerjee, H. Mori, The Stability of γ" and γ’ phases in Alloy 718 under electron irradiation, Superalloys 718, 625, 706 Var. Deriv. 19 (2001) 379–387. https://doi.org/10.7449/2001/Superalloys_2001_379_387.

[95] P.J.P. Kañetas, L.A.R. Osorio, M.P.G. Mata, M.D. La Garza, V.P. López, Influence of the Delta Phase in the Microstructure of the Inconel 718 subjected to “Delta-processing” Heat Treatment and Hot Deformed, Procedia Mater. Sci. 8 (2015) 1160–1165. https://doi.org/10.1016/j.mspro.2015.04.180.

[96] A. Oradei-Basile, J.F. Radavich, A Current T-T-T Diagram for Wrought Alloy 718, Superalloys 718, 625 Var. Deriv. (1991) 325–335. https://doi.org/10.7449/1991/Superalloys_1991_325_335.

[97] N.Y. Ye, M. Cheng, S.H. Zhang, H.W. Song, H.W. Zhou, P.B. Wang, Effect of δ Phase on Mechanical Properties of GH4169 Alloy at Room Temperature, J. Iron Steel Res. Int. 22 (2015) 752–756. https://doi.org/10.1016/S1006-706X(15)30068-6.

[98] Y.L. Kuo, S. Horikawa, K. Kakehi, The effect of interdendritic δ phase on the mechanical properties of Alloy 718 built up by additive manufacturing, Mater. Des. 116 (2017) 411–418. https://doi.org/10.1016/j.matdes.2016.12.026.

[99] M.J. Sohrabi, H. Mirzadeh, M. Rafiei, Solidification behavior and Laves phase dissolution during homogenization heat treatment of Inconel 718 superalloy, Vacuum. 154 (2018) 235–243. https://doi.org/10.1016/j.vacuum.2018.05.019.

[100] Y. Idell, L.E. Levine, A.J. Allen, F. Zhang, C.E. Campbell, G.B. Olson, J. Gong, D.R. Snyder, H.Z. Deutchman, Unexpected δ-Phase Formation in Additive-Manufactured Ni-Based Superalloy, Jom. 68 (2016) 950–959. https://doi.org/10.1007/s11837-015-1772-2.

[101] H. Yu, S. Hayashi, K. Kakehi, Y.L. Kuo, Study of formed oxides in IN718 alloy during the fabrication by selective laser melting and electron beam melting, Metals (Basel). 9 (2019) 1–15. https://doi.org/10.3390/met9010019.

[102] Y. Chen, F. Lu, K. Zhang, P. Nie, S.R. Elmi Hosseini, K. Feng, Z. Li, Dendritic microstructure and hot cracking of laser additive manufactured Inconel 718 under improved base cooling, J. Alloys Compd. 670 (2016) 312–321. https://doi.org/10.1016/j.jallcom.2016.01.250.

[103] H. Xiao, S.M. Li, W.J. Xiao, Y.Q. Li, L.M. Cha, J. Mazumder, L.J. Song, Effects of laser modes on Nb segregation and Laves phase formation during laser additive manufacturing of nickel-based superalloy, Mater. Lett. 188 (2017) 260–262. https://doi.org/10.1016/j.matlet.2016.10.118.

[104] ASTM International, B637-18: Standard Specification for Precipitation-Hardening and Cold Worked Nickel Alloy Bars, Forgings, and Forging Stock for Moderate or High Temperature Service, (2019) 1–7. https://doi.org/10.1520/B0637-18.2.

[105] X. Wei, W. Zheng, Z. Song, T. Lei, Q. Yong, Q. Xie, Static recrystallization behaviour of Inconel 718 alloy during thermal deformation, J. Wuhan Univ. Technol. Mater. Sci. Ed. 29 (2014) 379–383. https://doi.org/10.1007/s11595-014-0925-4.

[106] M.C. Chaturvedi, Y. Han, Strengthening mechanisms in Inconel718 superalloy, Met. Sci. 17 (1983) 145–149.

[107] D. Zhang, W. Niu, X. Cao, Z. Liu, Effect of standard heat treatment on the microstructure and mechanical properties of selective laser melting manufactured Inconel 718 superalloy, Mater. Sci. Eng. A. 644 (2015) 32–40. https://doi.org/10.1016/j.msea.2015.06.021.

[108] L. Chen, M. Koizumi, M. Niino, R.G. Ford, Introduction, in: Y. Miyamoto, W.A. Kaysser, B.H. Rabin, A. Kawasaki, R.. Ford (Eds.), Funct. Graded Mater. Des. Process. Appl., 1st ed., Springer Science+Business Media, LLC, 1999: pp. 1–6.

[109] B.H. Rabin, R.L. Williamson, Graded Microstructures, in: Y. Miyamoto, W.A. Kaysser, B.H. Rabin, A. Kawasaki, R.. Ford (Eds.), Funct. Graded Mater. Des. Process. Appl., 1st ed., Springer Science+Business Media, LLC, 1999: pp. 29–62.

[110] F. Nogata, Lessons from nature, in: Y. Miyamoto, W.A. Kaysser, B.H. Rabin, A. Kawasaki, R.. Ford (Eds.), Funct. Graded Mater. Des. Process. Appl., 1st ed., Springer Science+Business Media, LLC, 1999: pp. 7–27.

[111] V. Popovich, E. Borisov, V. Heurtebise, T. Riemslag, A.A. Popovich, V.S. Sufiiarov, Creep and Thermomechanical Fatigue of Functionally Graded Inconel 718 Produced by Additive Manufacturing, Miner. Met. Mater. Ser. TMS 2018 1 (2018) 85–97. https://doi.org/10.1007/978-3-319-72526-0.

[112] J.D. Hunt, Steady state columnar and equiaxed growth of dendrites and eutectic, Mater. Sci. Eng. 65 (1984) 75–83. https://doi.org/10.1016/0025-5416(84)90201-5.

[113] M. Gäumann, R. Trivedi, W. Kurz, Nucleation ahead of the advancing interface in directional solidification, Mater. Sci. Eng. A. 226–228 (1997) 763–769. https://doi.org/10.1016/s0921-5093(97)80081-0.

[114] J.A. Koepf, M.R. Gotterbarm, M. Markl, C. Körner, 3D multi-layer grain structure simulation of powder bed fusion additive manufacturing, Acta Mater. 152 (2018) 119–126. https://doi.org/10.1016/j.actamat.2018.04.030.

[115] L. Wang, N. Wang, W.J. Yao, Y.P. Zheng, Effect of substrate orientation on the columnar-to-equiaxed transition in laser surface remelted single crystal superalloys, Acta Mater. 88 (2015) 283–292. https://doi.org/10.1016/j.actamat.2015.01.063.

[116] M. Gäumann, C. Bezençon, P. Canalis, W. Kurz, Single-crystal laser deposition of superalloys: Processing-microstructure maps, Acta Mater. 49 (2001) 1051–1062. https://doi.org/10.1016/S1359-6454(00)00367-0.

[117] L. Wang, N. Wang, Effect of substrate orientation on the formation of equiaxed stray grains in laser surface remelted single crystal superalloys: Experimental investigation, Acta Mater. 104 (2016) 250–258. https://doi.org/10.1016/j.actamat.2015.11.018.

[118] H.L. Wei, T. Mukherjee, T. Debroy, Grain Growth Modeling for Additive Manufacturing of Nickel Based Superalloys, in: Proc. 6th Int. Conf. Recryst. Grain Growth (ReX&GG 2016), 2016: pp. 265–270. https://doi.org/10.1007/978-3-319-48770-0_39.

[119] T.M. Rodgers, J.D. Madison, V. Tikare, Simulation of metal additive manufacturing microstructures using kinetic Monte Carlo, Comput. Mater. Sci. 135 (2017) 78–89. https://doi.org/10.1016/j.commatsci.2017.03.053.

[120] A. Rai, M. Markl, C. Körner, A coupled Cellular Automaton–Lattice Boltzmann model for grain structure simulation during additive manufacturing, Comput. Mater. Sci. 124 (2016) 37–48. https://doi.org/10.1016/j.commatsci.2016.07.005.

[121] P. Liu, Z. Wang, Y. Xiao, M.F. Horstemeyer, X. Cui, L. Chen, Insight into the mechanisms of columnar to equiaxed grain transition during metallic additive manufacturing, Addit. Manuf. 26 (2019) 22–29. https://doi.org/10.1016/j.addma.2018.12.019.

[122] L.N. Carter, X. Wang, N. Read, R. Khan, M. Aristizabal, K. Essa, M.M. Attallah, Process optimisation of selective laser melting using energy density model for nickel based superalloys, Mater. Sci. Technol. 0836 (2016) 1–5. https://doi.org/10.1179/1743284715Y.0000000108.

[123] U. Scipioni Bertoli, A.J. Wolfer, M.J. Matthews, J.P.R. Delplanque, J.M. Schoenung, On the limitations of volumetric energy density as a design parameter for selective laser melting, Mater. Des. 113 (2017) 331–340. https://doi.org/10.1016/j.matdes.2016.10.037.

[124] K.G. Prashanth, S. Scudino, T. Maity, J. Das, J. Eckert, Is the energy density a reliable parameter for materials synthesis by selective laser melting?, Mater. Res. Lett. 5 (2017) 386–390. https://doi.org/10.1080/21663831.2017.1299808.

[125] A.M. Rubenchik, W.E. King, S.S. Wu, Scaling laws for the additive manufacturing, J. Mater. Process. Technol. 257 (2018) 234–243. https://doi.org/10.1016/j.jmatprotec.2018.02.034.

[126] A. Paraschiv, G. Matache, M.R. Condruz, T.F. Frigioescu, I. Ionică, The influence of laser defocusing in selective laser melted in 625, Materials (Basel). 14 (2021) 1–14. https://doi.org/10.3390/ma14133447.

[127] M.C. Sow, T. De Terris, O. Castelnau, Z. Hamouche, F. Coste, R. Fabbro, P. Peyre, Influence of beam diameter on Laser Powder Bed Fusion (L-PBF) process, Addit. Manuf. 36 (2020) 101532. https://doi.org/10.1016/j.addma.2020.101532.

[128] Q. Guo, C. Zhao, M. Qu, L. Xiong, L.I. Escano, M.H. Hojjatzadeh, N.D. Parab, K. Fezzaa, W. Everhart, T. Sun, L. Chen, In-situ characterization and quantification of melt pool variation under constant input energy density in laser powder bed fusion additive manufacturing process, Addit. Manuf. 28 (2019) 600–609. https://doi.org/10.1016/j.addma.2019.04.021.

[129] V.A. Popovich, E. V. Borisov, A.A. Popovich, V.S. Sufiiarov, D. V. Masaylo, L. Alzina, Functionally graded Inconel 718 processed by additive manufacturing: Crystallographic texture, anisotropy of microstructure and mechanical properties, Mater. Des. 114 (2017) 441–449. https://doi.org/10.1016/j.matdes.2016.10.075.

[130] C. Körner, H. Helmer, A. Bauereiß, R.F. Singer, Tailoring the grain structure of IN718 during selective electron beam melting, MATEC Web Conf. 14 (2014) 08001. https://doi.org/10.1051/matecconf/20141408001.

[131] Y. Yang, S. Wen, Q. Wei, W. Li, J. Liu, Y. Shi, Effect of scan line spacing on texture , phase and nanohardness of TiAl / TiB 2 metal matrix composites fabricated by selective laser melting, J. Alloys Compd. 728 (2017) 803–814. https://doi.org/10.1016/j.jallcom.2017.09.053.

[132] Z. Dong, Y. Liu, W. Wen, J. Ge, J. Liang, Effect of hatch spacing on melt pool and as-built quality during selective laser melting of stainless steel: Modelling and experimental approaches, Materials (Basel). 12 (2018). https://doi.org/10.3390/ma12010050.

[133] L.N. Carter, M.M. Attallah, R.C. Reed, Laser Powder Bed Fabrication of Nickel-Base Superalloys: Influence of Parameters; Characterisation, Quantification and Mitigation of Cracking, Superalloys 2012. (2012) 577–586. https://doi.org/10.1002/9781118516430.ch64.

[134] X. Zhou, K. Li, D. Zhang, X. Liu, J. Ma, W. Liu, Z. Shen, Textures formed in a CoCrMo alloy by selective laser melting, J. Alloys Compd. 631 (2015) 153–164. https://doi.org/10.1016/j.jallcom.2015.01.096.

[135] P. Karimi, E. Sadeghi, J. Ålgårdh, A. Keshavarzkermani, R. Esmaeilizadeh, E. Toyserkani, J.

Andersson, Columnar-to-equiaxed grain transition in powder bed fusion via mimicking casting solidification and promoting in situ recrystallization, Addit. Manuf. 46 (2021) 102086. https://doi.org/10.1016/j.addma.2021.102086.

[136] L.L. Parimi, G. Ravi, D. Clark, M.M. Attallah, Microstructural and texture development in direct laser fabricated IN718, Mater. Charact. 89 (2014) 102–111. https://doi.org/10.1016/j.matchar.2013.12.012.

[137] K. Shah, I. ul Haq, A. Khan, S.A. Shah, M. Khan, A.J. Pinkerton, Parametric study of development of Inconel-steel functionally graded materials by laser direct metal deposition, Mater. Des. 54 (2014) 531–538. https://doi.org/10.1016/j.matdes.2013.08.079.

[138] S. Bontha, N.W. Klingbeil, P.A. Kobryn, H.L. Fraser, Effects of process variables and size-scale on solidification microstructure in beam-based fabrication of bulky 3D structures, Mater. Sci. Eng. A. 513–514 (2009) 311–318. https://doi.org/10.1016/j.msea.2009.02.019.

[139] R.J. Moat, A.J. Pinkerton, L. Li, P.J. Withers, M. Preuss, Crystallographic texture and microstructure of pulsed diode laser-deposited Waspaloy, Acta Mater. 57 (2009) 1220–1229. https://doi.org/10.1016/j.actamat.2008.11.004.

[140] J. Metelkova, Y. Kinds, K. Kempen, C. De Formanoir, A. Witvrouw, On the influence of laser defocusing in Selective Laser Melting of 316L, Addit. Manuf. 23 (2018) 161–169. https://doi.org/10.1016/j.addma.2018.08.006.

[141] M. Sadowski, L. Ladani, W. Brindley, J. Romano, Optimizing quality of additively manufactured Inconel 718 using powder bed laser melting process, Addit. Manuf. 11 (2016) 60–70. https://doi.org/10.1016/j.addma.2016.03.006.

[142] O. Gokcekaya, T. Ishimoto, T. Narushima, T. Nakano, Unique crystallographic texture formation in Inconel 718 by laser powder bed fusion and its effect on mechanical anisotropy, Acta Mater. (2020) In press. https://doi.org/10.1016/j.actamat.2021.116876.

[143] W.J. Suder, S.W. Williams, Investigation of the effects of basic laser material interaction parameters in laser welding, J. Laser Appl. 24 (2012) 032009. https://doi.org/10.2351/1.4728136.

[144] R.R. Dehoff, M.M. Kirka, W.J. Sames, H. Bilheux, A.S. Tremsin, L.E. Lowe, S.S. Babu, Site specific control of crystallographic grain orientation through electron beam additive manufacturing, Mater. Sci. Technol. 31 (2015) 931–938. https://doi.org/10.1179/1743284714Y.0000000734.

[145] K.A. Sofinowski, S. Raman, X. Wang, B. Gaskey, M. Seita, Layer-wise engineering of grain orientation (LEGO) in laser powder bed fusion of stainless steel 316L, Addit. Manuf. 38 (2021) 101809. https://doi.org/10.1016/j.addma.2020.101809.

[146] P. Barriobero-Vila, J. Gussone, J. Haubrich, S. Sandlöbes, J.C. Da Silva, P. Cloetens, N. Schell, G. Requena, Inducing stable α + β microstructures during selective laser melting of Ti-6Al-4V using intensified intrinsic heat treatments, Materials (Basel). 10 (2017) 1–14. https://doi.org/10.3390/ma10030268.

[147] B. AlMangour, M.S. Baek, D. Grzesiak, K.A. Lee, Strengthening of stainless steel by titanium carbide addition and grain refinement during selective laser melting, Mater. Sci. Eng. A. 712 (2018) 812–818. https://doi.org/10.1016/j.msea.2017.11.126.

[148] P. Krakhmalev, I. Yadroitsava, G. Fredriksson, I. Yadroitsev, In situ heat treatment in selective laser melted martensitic AISI 420 stainless steels, Mater. Des. 87 (2015) 380–385. https://doi.org/10.1016/j.matdes.2015.08.045.

[149] H. Yang, J. Yang, W. Huang, G. Jing, Z. Wang, X. Zeng, Controllable in-situ aging during selective laser melting: Stepwise precipitation of multiple strengthening phases in Inconel 718 alloy, J. Mater. Sci. Technol. 35 (2019) 1925–1930. https://doi.org/10.1016/j.jmst.2019.05.024.

[150] J.-P. Kruth, J. Deckers, E. Yasa, R. Wauthlé, Assessing and comparing influencing factors of residual stresses in selective laser melting using a novel analysis method, Proc. Inst. Mech. Eng. Part B J. Eng. Manuf. 226 (2012) 980–991. https://doi.org/10.1177/0954405412437085.

[151] P. Mercelis, J. Kruth, Residual stresses in selective laser sintering and selective laser melting, Rapid Prototyp. J. 12 (2006) 254–265. https://doi.org/10.1108/13552540610707013.

[152] B. Cheng, S. Shrestha, K. Chou, Stress and deformation evaluations of scanning strategy effect in selective laser melting, Addit. Manuf. 12 (2016) 240–251.

https://doi.org/10.1016/j.addma.2016.05.007.

[153] F. Geiger, K. Kunze, T. Etter, Tailoring the texture of IN738LC processed by selective laser melting (SLM) by specific scanning strategies, Mater. Sci. Eng. A. 661 (2016) 240–246. https://doi.org/10.1016/j.msea.2016.03.036.

[154] K. Kunze, T. Etter, J. Grässlin, V. Shklover, Texture, anisotropy in microstructure and mechanical properties of IN738LC alloy processed by selective laser melting (SLM), Mater. Sci. Eng. A. 620 (2015) 213–222. https://doi.org/10.1016/j.msea.2014.10.003.

[155] G.P. Dinda, A.K. Dasgupta, J. Mazumder, Texture control during laser deposition of nickel-based superalloy, Scr. Mater. 67 (2012) 503–506. https://doi.org/10.1016/j.scriptamat.2012.06.014.

[156] F. Liu, X. Lin, C. Huang, M. Song, G. Yang, J. Chen, W. Huang, The effect of laser scanning path on microstructures and mechanical properties of laser solid formed nickel-base superalloy Inconel 718, J. Alloys Compd. 509 (2011) 4505–4509. https://doi.org/10.1016/j.jallcom.2010.11.176.

[157] W. Li, M. Soshi, Modelling analysis of grain morphologies in Directed energy deposition (DED) coating with different laser scanning patterns, Mater. Lett. 251 (2019) 8–12. https://doi.org/10.1016/j.matlet.2019.05.027.

[158] H.L. Wei, J. Mazumder, T. DebRoy, Evolution of solidification texture during additive manufacturing, Sci. Rep. 5 (2015) 1–7. https://doi.org/10.1038/srep16446.

[159] S. Sun, K. Hagihara, T. Nakano, Effect of scanning strategy on texture formation in Ni-25 at.% Mo alloys fabricated by selective laser melting, Mater. Des. 140 (2018) 307–316. https://doi.org/10.1016/j.matdes.2017.11.060.

[160] L.N. Carter, C. Martin, P.J. Withers, M.M. Attallah, The influence of the laser scan strategy on grain structure and cracking behaviour in SLM powder-bed fabricated nickel superalloy, J. Alloys Compd. 615 (2014) 338–347. https://doi.org/10.1016/j.jallcom.2014.06.172.

[161] R.R. Dehoff, M.M. Kirka, F.A. List, K.A. Unocic, W.J. Sames, Crystallographic texture engineering through novel melt strategies via electron beam melting: Inconel 718, Mater. Sci.

Technol. 31 (2015) 939–944. https://doi.org/10.1179/1743284714Y.0000000697.

[162] M.M. Kirka, Y. Lee, D.A. Greeley, A. Okello, M.J. Goin, M.T. Pearce, R.R. Dehoff, Strategy for Texture Management in Metals Additive Manufacturing, JOM. 69 (2017) 523–531. https://doi.org/10.1007/s11837-017-2264-3.

[163] M. Shao, S. Vijayan, P. Nandwana, J.R. Jinschek, The effect of beam scan strategies on microstructural variations in Ti-6Al-4V fabricated by electron beam powder bed fusion, Mater. Des. 196 (2020) 109165. https://doi.org/10.1016/j.matdes.2020.109165.

[164] Y. Lei, K. Aoyagi, A. Chiba, A method to manipulate non-steady-state columnar-to-equiaxed transition in powder bed fusion additive manufacturing using an electron beam, Acta Mater. (2022) 117717. https://doi.org/10.1016/j.actamat.2022.117717.

[165] I. Tabernero, A. Lamikiz, S. Martínez, E. Ukar, J. Figueras, Evaluation of the mechanical properties of Inconel 718 components built by laser cladding, Int. J. Mach. Tools Manuf. 51 (2011) 465–470. https://doi.org/10.1016/j.ijmachtools.2011.02.003.

[166] B. Attard, S. Cruchley, C. Beetz, M. Megahed, Y.L. Chiu, M.M. Attallah, Microstructural control during laser powder fusion to create graded microstructure Ni-superalloy components, Addit. Manuf. 36 (2020) 101432. https://doi.org/10.1016/j.addma.2020.101432.

[167] A. Rai, H. Helmer, C. Körner, Simulation of grain structure evolution during powder bed based additive manufacturing, Addit. Manuf. 13 (2017) 124–134. https://doi.org/10.1016/j.addma.2016.10.007.

[168] N.J. Petch, The cleavage strength of polycrystals, J. Iron Steel Inst. 174 (1953) 25–28. https://doi.org/10.1007/BF01972547.

[169] A. Kudzal, B. McWilliams, C. Hofmeister, F. Kellogg, J. Yu, J. Taggart-Scarff, J. Liang, Effect of scan pattern on the microstructure and mechanical properties of Powder Bed Fusion additive manufactured 17-4 stainless steel, Mater. Des. 133 (2017) 205–215. https://doi.org/10.1016/j.matdes.2017.07.047.

[170] W.J. Sames, K.A. Unocic, G.W. Helmreich, M.M. Kirka, F. Medina, R.R. Dehoff, S.S. Babu, Feasibility of in situ controlled heat treatment (ISHT) of Inconel 718 during electron beam

melting additive manufacturing, Addit. Manuf. 13 (2017) 156–165. https://doi.org/10.1016/j.addma.2016.09.001.

[171] D. Thomas, S. Gilbert, Costs and Cost Effectiveness of Additive Manufacturing - A Literature Review and Discussion, NIST Spec. Publ. 1176 (2014) 1–77. https://doi.org/10.6028/NIST.SP.1176.

[172] H.M. Ledbetter, R.P. Reed, Elastic properties of metals and Alloys , I . iron, nickel and iron-nickel alloys, J. Phys. Chem. Ref. Data. 531 (1973) 531–617.

[173] D. Dye, H.J. Stone, R.C. Reed, A two phase elastic-plastic self-consistent model for the accumulation of microstrains in Waspaloy, Acta Mater. 49 (2001) 1271–1283. https://doi.org/10.1016/S1359-6454(01)00003-9.

[174] M. Yamamoto, The elastic constants of nickel single crystals, J. Japan Inst. Met. 6 (1942) 331–338. https://doi.org/10.2320/jinstmet1937.6.7_331.

[175] A. Harte, M. Atkinson, M. Preuss, J. Quinta da Fonseca, A statistical study of the relationship between plastic strain and lattice misorientation on the surface of a deformed Ni-based superalloy, Acta Mater. 195 (2020) 555–570. https://doi.org/10.1016/j.actamat.2020.05.029.

[176] S.Y. Im, S.Y. Jun, J.W. Lee, J.H. Lee, B.S. Lee, H.J. Lee, H.U. Hong, Unidirectional columnar microstructure and its effect on the enhanced creep resistance of selective electron beam melted Inconel 718, J. Alloys Compd. 817 (2020). https://doi.org/10.1016/j.jallcom.2019.153320.

[177] P. Caron, T. Kan, Y.G. Nakagawa, Effect of orientation on the intermediate temperature creep behaviour of Ni-base single crystal superalloys, Scr. Metall. 20 (1986) 499–502.

[178] A.A. Popovich, V.S. Sufiiarov, E. V Borisov, I.A. Polozov, D. V. Masaylo, A. V. Grigoriev, Anisotropy of Mechanical Properties of Products Manufactured Using Selective Laser Melting of Powdered Materials, Russ. J. Non-Ferrous Met. 58 (2017) 389–395. https://doi.org/10.3103/S1067821217040149.

[179] G.E. Bean, T.D. McLouth, D.B. Witkin, S.D. Sitzman, P.M. Adams, R.J. Zaldivar, Build Orientation Effects on Texture and Mechanical Properties of Selective Laser Melting Inconel

718, J. Mater. Eng. Perform. 28 (2019) 1942–1949. https://doi.org/10.1007/s11665-019-03980-w.

[180] Y.C. Wang, L.M. Lei, L. Shi, H.Y. Wan, F. Liang, G.P. Zhang, Scanning strategy dependent tensile properties of selective laser melted GH4169, Mater. Sci. Eng. A. 788 (2020) 139616. https://doi.org/10.1016/j.msea.2020.139616.

[181] S. Cruchley, H.Y. Li, H.E. Evans, P. Bowen, D.J. Child, M.C. Hardy, The role of oxidation damage in fatigue crack initiation of an advanced Ni-based superalloy, Int. J. Fatigue. 81 (2015) 265–274. https://doi.org/10.1016/j.ijfatigue.2015.08.016.

[182] S. Cruchley, M.P. Taylor, H.Y. Li, H.E. Evans, P. Bowen, D.J. Child, M.C. Hardy, Effect of prior oxidation on high cycle fatigue performance of RR1000 and role of oxidation in fatigue crack initiation, Mater. High Temp. 32 (2015) 68–73. https://doi.org/10.1179/0960340914Z.00000000064.

[183] S. Cruchley, H. Evans, M. Taylor, An overview of the oxidation of Ni-based superalloys for turbine disc applications: surface condition, applied load and mechanical performance, Mater. High Temp. 33 (2016) 465–475. https://doi.org/10.1080/09603409.2016.1171952.

[184] C.S. Giggins, F.S. Pettit, Oxidation of Ni-Cr-Al Alloys Between 1000° and 1200°C, J. Electrochem. Soc. 118 (1971) 1782. https://doi.org/10.1149/1.2407837.

[185] G.A. Greene, C.C. Finfrock, Oxidation of Inconel 718 in air at high temperatures, Oxid. Met. 55 (2001) 505–521. https://doi.org/10.1023/a:1010359815550.

[186] L. Li, X. Gong, X. Ye, J. Teng, Y. Nie, Y. Li, Q. Lei, Influence of building direction on the oxidation behavior of Inconel 718 alloy fabricated by additive manufacture of electron beam melting, Materials (Basel). 11 (2018). https://doi.org/10.3390/ma11122549.

[187] K.A. Al-Hatab, M.A. Al-Bukhaiti, U. Krupp, M. Kantehm, Cyclic oxidation behavior of in 718 superalloy in air at high temperatures, Oxid. Met. 75 (2011) 209–228. https://doi.org/10.1007/s11085-010-9230-6.

[188] E.R. Lewis, M.P. Taylor, B. Attard, N. Cruchley, A.P.C. Morrison, M.M. Attallah, S. Cruchley, Microstructural Characterisation and High-Temperature Oxidation of Laser Powder Bed

Fusion Processed Inconel 625, Mater. Lett. 311 (2021) 131582. https://doi.org/10.1016/j.matlet.2021.131582.

[189] S. Cruchley, H.E. Evans, M.P. Taylor, M.C. Hardy, S. Stekovic, Chromia layer growth on a Ni-based superalloy: Sub-parabolic kinetics and the role of titanium, Corros. Sci. 75 (2013) 58–66. https://doi.org/10.1016/j.corsci.2013.05.016.

[190] D. Caplan, G.I. Sproule, Effect of oxide grain structure on the high-temperature oxidation of Cr, Oxid. Met. 9 (1975) 459–472. https://doi.org/10.1007/BF00611694.

[191] V. Trindade, H.J. Christ, U. Krupp, Grain-size effects on the high-temperature oxidation behaviour of chromium steels, Oxid. Met. 73 (2010) 551–563. https://doi.org/10.1007/s11085-010-9192-8.

[192] X. Wang, F. Fan, J.A. Szpunar, L. Zhang, Influence of grain orientation on the incipient oxidation behavior of Haynes 230 at 900 °C, Mater. Charact. 107 (2015) 33–42. https://doi.org/10.1016/j.matchar.2015.06.029.

[193] F. Czerwinski, J.A. Szpunar, The influence of crystallographic orientation of nickel surface on oxidation inhibition by ceria coatings, Acta Mater. 46 (1998) 1403–1417. https://doi.org/10.1016/S1359-6454(97)00240-1.

[194] E.G. Wagenhuber, V.B. Trindade, U. Krupp, The role of oxygen-grain-boundary diffusion during intercrystalline oxidation and intergranular fatigue crack propagation in alloy 718, Proc. Int. Symp. Superalloys Var. Deriv. (2005) 591–600. https://doi.org/10.7449/2005/superalloys_2005_591_600.

[195] B822-17 Standard Test Method for Particle Size Distribution of Metal Powders and Related Compounds by Light Scattering 1, (2017) 1–4. https://doi.org/10.1520/B0822-17.2.

[196] ASTM, B213-17: Standard test methods for flow rate of metal powders using the hall flowmeter funnel, ASTM Stand. B213 − 20 Stand. (2017). https://doi.org/10.1520/B0213-17.2.

[197] R. Jennings, Hybrid Powder Metallurgy Processing for High Temperature Strength IN718 Superalloy, 2020.

[198] ASTM International, E8/E8M: Standard Test Methods for Tension Testing of Metallic Materials, (2018) 1–30. https://doi.org/10.1520/E0008.

[199] E. Chlebus, K. Gruber, B. Kuźnicka, J. Kurzac, T. Kurzynowski, Effect of heat treatment on the microstructure and mechanical properties of Inconel 718 processed by selective laser melting, Mater. Sci. Eng. A. 639 (2015) 647–655. https://doi.org/10.1016/j.msea.2015.05.035.

[200] ASTM B962-17: Standard Test Methods for Density of Compacted or Sintered Powder Metallurgy (PM) Products Using Archimedes' Principle, (2018) 1–7. https://doi.org/10.1520/B0962-17.2.

[201] J.J. Valencia, P.N. Quested, Thermophysical Properties, in: ASM Handbook, Vol. 15 Cast., 2008: p. 476. https://doi.org/10.1361/asmhba0005240.

[202] ASTM International, ASTM E112-13: Standard test methods for determining average grain size, ASTM Int. (2013) 1–28. https://doi.org/10.1520/E0112-13.1.4.

[203] F. Bachmann, R. Hielscher, H. Schaeben, Grain detection from 2d and 3d EBSD data-Specification of the MTEX algorithm, Ultramicroscopy. 111 (2011) 1720–1733. https://doi.org/10.1016/j.ultramic.2011.08.002.

[204] A. Forsey, S. Gungor, Demosaicing images from colour cameras for digital image correlation, Opt. Lasers Eng. 86 (2016) 20–28. https://doi.org/10.1016/j.optlaseng.2016.05.006.

[205] J. Gayda, D. Furrer, Dual-microstructure heat treatment, Adv. Mater. Process. 161 (2003) 36–39.

[206] H.Y. Wan, Z.J. Zhou, C.P. Li, G.F. Chen, G.P. Zhang, Effect of scanning strategy on grain structure and crystallographic texture of Inconel 718 processed by selective laser melting, J. Mater. Sci. Technol. 34 (2018) 1799–1804. https://doi.org/10.1016/j.polymer.2006.02.076.

[207] C.A. Gandin, M. Rappaz, A 3D cellular automaton algorithm for the prediction of dendritic grain growth, Acta Mater. 45 (1997) 2187–2195. https://doi.org/10.1016/S1359-6454(96)00303-5.

[208] C. Panwisawas, C. Qiu, M.J. Anderson, Y. Sovani, R.P. Turner, M.M. Attallah, J.W. Brooks, H.C. Basoalto, Mesoscale modelling of selective laser melting: Thermal fluid dynamics and

microstructural evolution, Comput. Mater. Sci. 126 (2017) 479–490. https://doi.org/10.1016/j.commatsci.2016.10.011.

[209] O. Lopez-Botello, U. Martinez-Hernandez, J. Ramírez, C. Pinna, K. Mumtaz, Two-dimensional simulation of grain structure growth within selective laser melted AA-2024, Mater. Des. 113 (2017) 369–376. https://doi.org/10.1016/j.matdes.2016.10.031.

[210] J.B. Wahl, K. Harris, Advanced Ni-Base superalloys for Small Gas turbines, Can. J. Metall. Mater. Sci. 50 (2011) 207–214.

[211] K. Harris, G.L. Erickson, R.E. Schwer, MAR M 247 Derivations - CM 247 LC DS Alloy CMSX single crystal alloys properties and performance, Superalloys. (1984) 221–230. https://doi.org/10.7449/1984/Superalloys_1984_221_230.

[212] S. Mosbah, Grain structure and segregation modeling using coupled FV and DP model, 8th Int. Symp. Superalloy 718 Deriv. 2014. (2014) 237–246. https://doi.org/10.1002/9781119016854.ch20.

[213] J. Kundin, L. Mushongera, H. Emmerich, Phase-field modeling of microstructure formation during rapid solidification in Inconel 718 superalloy, Acta Mater. 95 (2015) 343–356. https://doi.org/10.1016/j.actamat.2015.05.052.

[214] E.R. Denlinger, V. Jagdale, G. V. Srinivasan, T. El-Wardany, P. Michaleris, Thermal modeling of Inconel 718 processed with powder bed fusion and experimental validation using in situ measurements, Addit. Manuf. 11 (2016) 7–15. https://doi.org/10.1016/j.addma.2016.03.003.

[215] S. Li, H. Xiao, K. Liu, W. Xiao, Y. Li, X. Han, J. Mazumder, L. Song, Melt-pool motion, temperature variation and dendritic morphology of Inconel 718 during pulsed- and continuous-wave laser additive manufacturing: A comparative study, Mater. Des. 119 (2017) 351–360. https://doi.org/10.1016/j.matdes.2017.01.065.

[216] L. Thijs, M.L. Montero Sistiaga, R. Wauthle, Q. Xie, J.P. Kruth, J. Van Humbeeck, Strong morphological and crystallographic texture and resulting yield strength anisotropy in selective laser melted tantalum, Acta Mater. 61 (2013) 4657–4668. https://doi.org/10.1016/j.actamat.2013.04.036.

[217] I. Yadroitsev, P. Krakhmalev, I. Yadroitsava, S. Johansson, I. Smurov, Energy input effect on morphology and microstructure of selective laser melting single track from metallic powder, J. Mater. Process. Technol. 213 (2013) 606–613. https://doi.org/10.1016/j.jmatprotec.2012.11.014.

[218] J.P. White, N. Read, R.M. Ward, R. Mellor, M.M. Attallah, Prediction of melt pool profiles for selective laser melting of alsilomg alloy, Mater. Sci. Technol. Conf. Exhib. 2014, MS T 2014. 3 (2014) 1985–1992.

[219] J.N. Dupont, C. V. Robino, A.R. Marder, M.R. Notis, Solidification of Nb-bearing superalloys: Part II. Pseudoternary solidification surfaces, Metall. Mater. Trans. A Phys. Metall. Mater. Sci. 29 (1998) 2797–2806. https://doi.org/10.1007/s11661-998-0320-x.

[220] X. Wang, L.N. Carter, B. Pang, M.M. Attallah, M.H. Loretto, Microstructure and yield strength of SLM-fabricated CM247LC Ni-Superalloy, Acta Mater. 128 (2017) 87–95. https://doi.org/10.1016/j.actamat.2017.02.007.

[221] J.H. Martin, B.D. Yahata, J.M. Hundley, J.A. Mayer, T.A. Schaedler, T.M. Pollock, 3D printing of high-strength aluminium alloys, Nature. 549 (2017) pages365–369. https://doi.org/10.1038/nature23894.

[222] C. Hong, D. Gu, D. Dai, M. Alkhayat, W. Urban, P. Yuan, S. Cao, A. Gasser, A. Weisheit, I. Kelbassa, M. Zhong, R. Poprawe, Laser additive manufacturing of ultrafine TiC particle reinforced Inconel 625 based composite parts: Tailored microstructures and enhanced performance, Mater. Sci. Eng. A. 635 (2015) 118–128. https://doi.org/10.1016/j.msea.2015.03.043.

[223] I.T. Ho, Y.T. Chen, A.C. Yeh, C.P. Chen, K.K. Jen, Microstructure evolution induced by inoculants during the selective laser melting of IN718, Addit. Manuf. 21 (2018) 465–471. https://doi.org/10.1016/j.addma.2018.02.018.

[224] D. Carluccio, M.J. Bermingham, Y. Zhang, D.H. StJohn, K. Yang, P.A. Rometsch, X. Wu, M.S. Dargusch, Grain refinement of laser remelted Al-7Si and 6061 aluminium alloys with Tibor® and scandium additions, J. Manuf. Process. 35 (2018) 715–720. https://doi.org/10.1016/j.jmapro.2018.08.030.

[225] L. Xi, P. Wang, K.G. Prashanth, H. Li, H. V. Prykhodko, S. Scudino, I. Kaban, Effect of TiB2 particles on microstructure and crystallographic texture of Al-12Si fabricated by selective laser melting, J. Alloys Compd. 786 (2019) 551–556. https://doi.org/10.1016/j.jallcom.2019.01.327.

[226] F. Liu, X. Lin, G. Yang, M. Song, J. Chen, W. Huang, Microstructure and residual stress of laser rapid formed Inconel 718 nickel-base superalloy, Opt. Laser Technol. 43 (2011) 208–213. https://doi.org/10.1016/j.optlastec.2010.06.015.

[227] W.M. Tucho, P. Cuvillier, A. Sjolyst-Kverneland, V. Hansen, Microstructure and hardness studies of Inconel 718 manufactured by selective laser melting before and after solution heat treatment, Mater. Sci. Eng. A. 689 (2017) 220–232. https://doi.org/10.1016/j.msea.2017.02.062.

[228] P. Promoppatum, S.C. Yao, P.C. Pistorius, A.D. Rollett, A Comprehensive Comparison of the Analytical and Numerical Prediction of the Thermal History and Solidification Microstructure of Inconel 718 Products Made by Laser Powder-Bed Fusion, Engineering. 3 (2017) 685–694. https://doi.org/10.1016/J.ENG.2017.05.023.

[229] M. Renderos, A. Torregaray, M.E. Gutierrez-Orrantia, A. Lamikiz, N. Saintier, F. Girot, Microstructure characterization of recycled IN718 powder and resulting laser clad material, Mater. Charact. 134 (2017) 103–113. https://doi.org/10.1016/j.matchar.2017.09.029.

[230] Y.S. Lee, M.M. Kirka, N. Raghavan, R.R. Dehoff, Simulation of SPOT melting scan strategy to predict columnar to equiaxed transition in metal additive manufacturing, Solid Free. Fabr. 2017 Proc. 28th Annu. Int. Solid Free. Fabr. Symp. - An Addit. Manuf. Conf. SFF 2017. (2020) 1005–1017.

[231] N. Suutala, Effect of solidification conditions on the solidification mode in austenitic stainless steels, Metall. Trans. A. 14A (1983) 191–197. https://doi.org/10.1007/BF02651615.

[232] M. Balbaa, S. Mekhiel, M. Elbestawi, J. McIsaac, On selective laser melting of Inconel 718: Densification, surface roughness, and residual stresses, Mater. Des. 193 (2020) 108818. https://doi.org/10.1016/j.matdes.2020.108818.

[233] M. Laleh, A.E. Hughes, M.Y. Tan, G.S. Rohrer, S. Primig, N. Haghdadi, Grain boundary

character distribution in an additively manufactured austenitic stainless steel, Scr. Mater. 192 (2021) 115–119. https://doi.org/10.1016/j.scriptamat.2020.10.018.

[234] C. Panwisawas, Y. Gong, Y.T. Tang, R.C. Reed, J. Shinjo, Additive manufacturability of superalloys: Process-induced porosity, cooling rate and metal vapour, Addit. Manuf. 47 (2021) 102339. https://doi.org/10.1016/j.addma.2021.102339.

[235] A. Basak, S. Das, Epitaxy and Microstructure Evolution in Metal Additive Manufacturing, Annu. Rev. Mater. Res. 46 (2016) 125–149. https://doi.org/10.1146/annurev-matsci-070115-031728.

[236] A.A. Antonysamy, J. Meyer, P.B. Prangnell, Effect of build geometry on the β-grain structure and texture in additive manufacture of Ti6Al4V by selective electron beam melting, Mater. Charact. 84 (2013) 153–168. https://doi.org/10.1016/j.matchar.2013.07.012.

[237] M.R. Gotterbarm, M. Seifi, D. Melzer, J. Džugan, A.A. Salem, Z.H. Liu, C. Körner, Small scale testing of IN718 single crystals manufactured by EB-PBF, Addit. Manuf. 36 (2020) 101449. https://doi.org/10.1016/j.addma.2020.101449.

[238] T.G. Gallmeyer, S. Moorthy, B.B. Kappes, M.J. Mills, B. Amin-Ahmadi, A.P. Stebner, Knowledge of process-structure-property relationships to engineer better heat treatments for laser powder bed fusion additive manufactured Inconel 718, Addit. Manuf. 31 (2020) 100977. https://doi.org/10.1016/j.addma.2019.100977.

[239] A.N. Forsey, Y.B. Das, T.H. Simm, D. Clarke, J. Boswell, S. Gungor, R.J. Moat, Mechanical property heterogeneity in additively manufactured nickel superalloy, Mater. Sci. Eng. A. 712 (2018) 681–684. https://doi.org/10.1016/j.msea.2017.12.025.

[240] M. Ni, C. Chen, X. Wang, P. Wang, R. Li, X. Zhang, K. Zhou, Anisotropic tensile behavior of in situ precipitation strengthened Inconel 718 fabricated by additive manufacturing, Mater. Sci. Eng. A. 701 (2017) 344–351. https://doi.org/10.1016/j.msea.2017.06.098.

[241] A.R. Balachandramurthi, J. Moverare, N. Dixit, D. Deng, R. Pederson, Microstructural influence on fatigue crack propagation during high cycle fatigue testing of additively manufactured Alloy 718, Mater. Charact. 149 (2019) 82–94. https://doi.org/10.1016/j.matchar.2019.01.018.

[242] C. Qiu, N.J.E. Adkins, M.M. Attallah, Microstructure and tensile properties of selectively laser-melted and of HIPed laser-melted Ti-6Al-4V, Mater. Sci. Eng. A. 578 (2013) 230–239. https://doi.org/10.1016/j.msea.2013.04.099.

[243] C. Qiu, N.J.E. Adkins, M.M. Attallah, Selective laser melting of Invar 36: Microstructure and properties, Acta Mater. 103 (2016) 382–395. https://doi.org/10.1016/j.actamat.2015.10.020.

[244] A.K.M.B. Rashid, J. Campbell, Oxide defects in a vacuum investment-cast Ni-based turbine blade, Metall. Mater. Trans. A Phys. Metall. Mater. Sci. 35 A (2004) 2063–2071. https://doi.org/10.1007/s11661-004-0155-z.

[245] Y.N. Zhang, X. Cao, P. Wanjara, M. Medraj, Oxide films in laser additive manufactured Inconel 718, Acta Mater. 61 (2013) 6562–6576. https://doi.org/10.1016/j.actamat.2013.07.039.

[246] O.D. Neikov, Atomization and granulation, in: O.D. Neikov, S.S. Naboychenko, I. V. Murashova, V.G. Gopienko, I. V. Frishberg, D. V. Lotsko (Eds.), Handb. Non-Ferrous Met. Powders Technol. Appl., 1st ed., Elsevier Ltd, 2009: pp. 102–142. https://doi.org/10.1016/B978-1-85617-422-0.00005-7.

[247] J. Campbell, Entrainment, in: Complet. Cast. Handb., Elsevier, 2015: pp. 17–90. https://doi.org/10.1016/B978-0-444-63509-9.00002-9.

[248] J. Campbell, M. Tiryakioğlu, Bifilm defects in Ni-based alloy castings, Metall. Mater. Trans. B Process Metall. Mater. Process. Sci. 43 (2012) 902–914. https://doi.org/10.1007/s11663-012-9655-1.

[249] H. Song, L. Zhang, F. Cao, H. Shen, Z. Ning, Y. Huang, X. Zhao, X. Gu, Z. Qiu, J. Sun, Three-dimensional reconstruction of bifilm defects, Scr. Mater. 191 (2021) 179–184. https://doi.org/10.1016/j.scriptamat.2020.09.040.

[250] L. Kunz, P. Lukáš, R. Konečná, High-cycle fatigue of Ni-base superalloy Inconel 713LC, Int. J. Fatigue. 32 (2010) 908–913. https://doi.org/10.1016/j.ijfatigue.2009.02.042.

[251] M. Alizadeh-Sh, S.P.H. Marashi, E. Ranjbarnodeh, R. Shoja-Razavi, J.P. Oliveira, Dissimilar laser cladding of Inconel 718 powder on A-286 substrate: Microstructural evolution, J. Laser

Appl. 32 (2020) 022048. https://doi.org/10.2351/1.5124932.

[252] E. Jelis, M. Clemente, S. Kerwien, N.M. Ravindra, M.R. Hespos, Metallurgical and Mechanical Evaluation of 4340 Steel Produced by Direct Metal Laser Sintering, Jom. 67 (2015) 582–589. https://doi.org/10.1007/s11837-014-1273-8.

[253] X. Yang, F. Tang, X. Hao, Z. Li, Oxide Evolution During the Solidification of 316L Stainless Steel from Additive Manufacturing Powders with Different Oxygen Contents, Metall. Mater. Trans. B Process Metall. Mater. Process. Sci. 52 (2021) 2253–2262. https://doi.org/10.1007/s11663-021-02191-w.

[254] J. Campbell, The consolidation of metals: the origin of bifilms, J. Mater. Sci. 51 (2016) 96–106. https://doi.org/10.1007/s10853-015-9399-9.

[255] H. Kim, W. Cong, H.C. Zhang, Z. Liu, Laser engineered net shaping of nickel-based superalloy inconel 718 powders onto aisi 4140 alloy steel substrates: Interface bond and fracture failure mechanism, Materials (Basel). 10 (2017). https://doi.org/10.3390/ma10040341.

[256] T. Sand, C. Geers, Y. Cao, J.E. Svensson, L.G. Johansson, Effective Reduction of Chromium-oxy-hydroxide Evaporation from Ni-Base Alloy 690, Oxid. Met. 92 (2019) 259–279. https://doi.org/10.1007/s11085-019-09935-9.

[257] P. André, M. Abbaoui, A. Augeard, P. Desprez, T. Singo, Study of Condensed Phases, of Vaporization Temperatures of Aluminum Oxide and Aluminum, of Sublimation Temperature of Aluminum Nitride and Composition in an Air Aluminum Plasma, Plasma Chem. Plasma Process. 36 (2016) 1161–1175. https://doi.org/10.1007/s11090-016-9704-7.

[258] C.L.A. Leung, S. Marussi, R.C. Atwood, M. Towrie, P.J. Withers, P.D. Lee, In situ X-ray imaging of defect and molten pool dynamics in laser additive manufacturing, Nat. Commun. 9 (2018) 1–9. https://doi.org/10.1038/s41467-018-03734-7.

[259] M.J. Matthews, G. Guss, S.A. Khairallah, A.M. Rubenchik, P.J. Depond, W.E. King, Denudation of metal powder layers in laser powder bed fusion processes, Acta Mater. 114 (2016) 33–42. https://doi.org/10.1016/j.actamat.2016.05.017.

[260] S. Ly, A.M. Rubenchik, S.A. Khairallah, G. Guss, M.J. Matthews, Metal vapor micro-jet controls material redistribution in laser powder bed fusion additive manufacturing, Sci. Rep. 7 (2017) 1–12. https://doi.org/10.1038/s41598-017-04237-z.

[261] A.N.D. Gasper, B. Szost, X. Wang, D. Johns, S. Sharma, A.T. Clare, I.A. Ashcroft, Spatter and oxide formation in laser powder bed fusion of Inconel 718, Addit. Manuf. 24 (2018) 446–456. https://doi.org/10.1016/j.addma.2018.09.032.

[262] R. Zhou, Y. Liu, B. Liu, J. Li, Q. Fang, Precipitation behavior of selective laser melted FeCoCrNiC0.05 high entropy alloy, Intermetallics. 106 (2019) 20–25. https://doi.org/10.1016/j.intermet.2018.12.001.

[263] H.E. Evans, R.C. Lobb, Conditions for the initiation of oxide-scale cracking and spallation, Corros. Sci. 24 (1984) 209–222. https://doi.org/10.1016/0010-938X(84)90051-9.

[264] V.A. Popovich, E. V Borisov, V.S. Sufiyarov, A.A. Popovich, Tailoring the properties in functionally graded alloy inconel 718 using additive technologies, Met. Sci. Heat Treat. 60 (2019) 701–709. https://doi.org/10.1007/s11041-019-00343-z.

[265] F. Brenne, A. Taube, M. Pröbstle, S. Neumeier, D. Schwarze, M. Schaper, T. Niendorf, Microstructural design of Ni-base alloys for high-temperature applications: impact of heat treatment on microstructure and mechanical properties after selective laser melting, Prog. Addit. Manuf. (2016) 141–151. https://doi.org/10.1007/s40964-016-0013-8.

[266] D.R. Clarke, Stress generation during high-temperature oxidation of metallic alloys, Curr. Opin. Solid State Mater. Sci. 6 (2002) 237–244. https://doi.org/10.1016/S1359-0286(02)00074-8.

[267] J. Ding, D. Neffati, Q. Li, R. Su, J. Li, S. Xue, Z. Shang, Y. Zhang, H. Wang, Y. Kulkarni, X. Zhang, Thick grain boundary induced strengthening in nanocrystalline Ni alloy, Nanoscale. 11 (2019) 23449–23458. https://doi.org/10.1039/c9nr06843k.

[268] T. Sanviemvongsak, D. Monceau, B. Macquaire, High temperature oxidation of IN 718 manufactured by laser beam melting and electron beam melting: Effect of surface topography, Corros. Sci. 141 (2018) 127–145.

[269] H. Falk Windisch, J. Froitzheim, J.E. Svensson, Influence of Chromium Evaporation and Oxidation on Interconnect Steels at 650-850°C, ECS Trans. 57 (2013) 2225–2233. https://doi.org/10.1149/05701.2225ecst.

[270] E.A. Gulbransen, K.F. Andrew, Kinetics of the Oxidation of Chromium, J. Electrochem. Soc. 104 (1957) 334. https://doi.org/10.1149/1.2428576.

[271] N. Bozzolo, M. Bernacki, Viewpoint on the Formation and Evolution of Annealing Twins During Thermomechanical Processing of FCC Metals and Alloys, Metall. Mater. Trans. A Phys. Metall. Mater. Sci. 51 (2020) 2665–2684. https://doi.org/10.1007/s11661-020-05772-7.

[272] M.P. Phaniraj, D.I. Kim, Y.W. Cho, Effect of grain boundary characteristics on the oxidation behavior of ferritic stainless steel, Corros. Sci. 53 (2011) 4124–4130. https://doi.org/10.1016/j.corsci.2011.08.020.

[273] L. Zheng, M. Zhang, J. Dong, Oxidation behavior and mechanism of powder metallurgy Rene95 nickel based superalloy between 800 and 1000 °C, Appl. Surf. Sci. 256 (2010) 7510–7515. https://doi.org/10.1016/j.apsusc.2010.05.098.

[274] H.E. Evans, D.A. Hilton, R.A. Holm, S.J. Webstert, The influence of a titanium nitride dispersion on the oxidation behavior of 20%Cr-25%Ni stainless steel, Oxid. Met. 12 (1978) 473–485. https://doi.org/10.1007/BF00603805.

[275] J.H. Chen, P.M. Rogers, J.A. Little, Oxidation behavior of several chromia-forming commercial nickel-base superalloys, Oxid. Met. 47 (1997) 381–410. https://doi.org/10.1007/BF02134783.

[276] B.R. Barnard, P.K. Liaw, R.A. Buchanan, D.L. Klarstrom, Affects of applied stresses on the isothermal and cyclic high-temperature oxidation behavior of superalloys, Mater. Sci. Eng. A. 527 (2010) 3813–3821. https://doi.org/10.1016/j.msea.2010.03.050.

[277] D. Mortimer, M.L. Post, The oxidation of Cr and an Fe-50% Cr alloy, Corros. Sci. 8 (1968) 499–512. https://doi.org/10.1016/s0010-938x(68)80005-8.

[278] H. Hindam, D.P. Whittle, Microstructure, adhesion and growth kinetics of protective scales on metals and alloys, Oxid. Met. 18 (1982) 245–284. https://doi.org/10.1007/BF00656571.

[279] Q. Jia, D. Gu, Selective laser melting additive manufactured Inconel 718 superalloy parts: High-temperature oxidation property and its mechanisms, Opt. Laser Technol. 62 (2014) 161–171. https://doi.org/10.1016/j.optlastec.2014.03.008.

[280] K.A. Unocic, L.M. Kolbus, R.R. Dehoff, S.N. Dryepondt, B.A. Pint, High-Temperature Performance of UNS N07718 Processed by Additive Manufacturing, in: Corrosion, 2014.

[281] N.B. Pilling, R.E. Bedworth, The oxidation of metals at high temperatures, J. Inst. Met. 29 (1923) 529–591.

[282] F.N. Rhines, J.S. Wolf, Role of Oxide Microstructure and Growth Stresses in the High-Temperature Scaling of Nickel, Metall. Mater. Trans. 1 (1970) 1701–1710. https://doi.org/10.1007/bf02642020.

[283] L. Zheng, M. Zhang, R. Chellali, J. Dong, Investigations on the growing, cracking and spalling of oxides scales of powder metallurgy Rene95 nickel-based superalloy, Appl. Surf. Sci. 257 (2011) 9762–9767. https://doi.org/10.1016/j.apsusc.2011.06.005.

[284] H.E. Evans, Stress effects in high temperature oxidation of metals, Int. Mater. Rev. 40 (1995) 1–40. https://doi.org/10.1179/imr.1995.40.1.1.

[285] I. Saeki, T. Ohno, D. Seto, O. Sakai, Y. Sugiyama, T. Sato, A. Yamauchi, K. Kurokawa, M. Takeda, T. Onishi, Measurement of Young's modulus of oxides at high temperature related to the oxidation study, Mater. High Temp. 28 (2011) 264–268. https://doi.org/10.3184/096034011X13182685579795.

[286] K. Hirota, H. Motono, M. Yoshinaka, O. Yamaguchi, Fabrication and mechanical properties of almost fully-densified Cr2O3 ceramics, J. Mater. Sci. Lett. 21 (2002) 853–854. https://doi.org/10.1023/A:1015766427172.

[287] F. Delaunay, C. Berthier, M. Lenglet, J.M. Lameille, SEM-EDS and XPS studies of the high temperature oxidation behaviour of Inconel 718, Mikrochim. Acta. 132 (2000) 337–343. https://doi.org/10.1007/s006040050027.